UNIVERSITY OF ZULULAND

CATALYTIC OXIDATION OF CRESOLS USING MOLECULAR OZONE

By

Zamani Siphephelo Ncanana

2010 5459 4

Submitted to the

Faculty of Science and Agriculture

In fulfillment of the requirements for the degree of

Master of Science

In the

Department of Chemistry

At the

University of Zululand

Supervisor: **Prof. V.S.R. Rajasekhar Pullabhotla**

April 2017

DECLARATION

I, Zamani Siphephelo Ncanana, declare that this dissertation is to the best of my knowledge, my own work. It has only been submitted (by myself) for the degree of Master of Science at the University of Zululand. It has never been submitted before for any degree or examination at any other University. I also state that all the sources that I have used herein have been duly acknowledged.

Signature (Student) : _____

This _____ day of _____ 2017

Signature (Supervisor) : _____

This _____ day of _____ 2017

DEDICATION

This study is dedicated to my late Mother, Bongiwe Cynthia Ngidi. I feel blessed, having been born and raised by you into a person I am today. I believe I am destined to achieve more good in life with all the lessons and love you gave to me and my beloved siblings.

'Ngiyabonga **mame**'

ACKNOWLEDGEMETS

I sincerely, would like to thank my Supervisor, Prof. Viswanadha Srirama Rajasekhar Pullabhotla, for offering me an opportunity to further my research-based studies in the work presented in this dissertation. I highly appreciate his mentorship, guidance and support.

Financial support received from the Sasol Inzalo Foundation (SIF), National Research Foundation (NRF) and research office of the University of Zululand (UZ) led to a successful completion of this study and thus it is wholeheartedly acknowledged. Specials thanks are further extended to Dr. Irene Kamara (SIF, Principal), Dr. Mike Sibiya (SIF, student Mentor) and Ms. Noma Shoba (NRF, research office, UZ) for their significant contributions during this study. I also thank Dr. Sandile Jali and Ms. Jeanine Williams for their selfless assistance during my visit to Sasol Technology (R&D) for HPLC analyses and i will never forget their inputs.

I would like to thank my seniors, peers and juniors from the Department of Chemistry (UZ) for their warm company, full of chemistry, humor and friendship. Special gratitude goes to Mr. Sibusiso Buthelezi and Mrs. Nompumelelo Sibiya for helping in some laboratory analyses and purchasing of chemicals, respectively. Ms. Eunice Maupa from Department of Agriculture (UZ) is also acknowledged herein. I thank the University of Kwa-Zulu Natal for BET and microscopy analyses.

How ungrateful would I be to forget Mr. Lonnie Van Zyl from the IMBM unit in the University of the Western Cape, his HPLC related input was heartfelt.

My special thanks go to Dr. Nick Sadgrove for assistance in chromatographic separations while visiting his lab in UJ, without his contribution I… I don't know. Uniquely, I would like to thank Miss Gugulethu 'Sdandane' Khumalo, you've been my best friend, family, encouragement and countless other characters, especially during the period of my Master's degree, *thank you*.

Lastly but far from least, I would like to give my profound gratitude to my parents, Gogo MaNcube (Dalo), Mrs. Rose Vilakazi (Koko), Ms. Lindile Mkhwanazi (Doma), Lungile Ngidi and my siblings, Thenjiswa, Sanele, Ayanda, Scelo, Lwandile, Sduduzo and Fanele. Your love and patience is beyond anything imaginable. Ngibonga nabo bonke abaKhwanazi abakhulu.

..Of all I am, I give credit to God for His servants on Earth..

ABSTRACT

The environment, both in general and specifically our habitable segment is currently under threat from surfacing chemical pollutants that are generated mostly from pharmaceutical and industrial sectors. The extended use of cresols (*meta*-, *ortho*-, and *para*-cresol) in these sectors makes them potential pollutants and yet they are of hazardous nature to human, plants and animals. Therefore, the necessity to efficiently degrade these compounds is heightened and one of the reliable tools would be chemical oxidation, mainly advanced oxidation processes, which in this work refers to heterogeneously catalyzed oxidation of cresols using molecular ozone. The main objective of this study was to catalytically oxidize various cresol isomers using ozone. All oxidation reactions were studied as a function of time.

Metal (Ni, Fe, Mn, V) loaded γ-Al_2O_3, SiO_2 and V_2O_5 catalysts were synthesized by wet impregnation method. These catalysts were further calcined (300 ^{o}C) in air and characterized using powder X-ray diffraction (XRD), Fourier Transform-Infrared (FT-IR), inductively coupled plasma-optical emission spectroscopy (ICP-OES), scanning electron microscopy (SEM), energy dispersive X-ray (EDX) spectroscopy, transmission electron microscopy (TEM) and Brunauer-Emmet-Teller (BET) surface area analyzer. These analytical techniques provided essential information about the catalysts, ranging from solid phase composition and purity, catalyst surface morphology, concentration of a loaded metal on a support to the specific surface area of the catalyst material. Prior to the application of these calcined catalysts in the oxidation of *meta*-, *ortho*- and *para*-cresol, a brief study of column mounted oxidation of cresols was done.

A volume of 3.0 mL for each cresol isomer was adsorbed on pure γ-Al_2O_3 and SiO_2, mounted on a vertical glass column and oxidized with O_3 (0.123 mg/L) for 1, 3 and 5 h intervals. After each oxidation reaction, the samples were collected and dissolved in absolute ethanol. The resultant oxidation products were characterized using FT-IR and gas chromatography coupled with mass spectrometer (GC-MS), which separately provided data on functional groups that were introduced in the reaction and both percentage conversions & selectivities. Specific products that were identified include *m*-tolyl acetate (***m*-TA**) and 2,3-dihydroxy toluene (**2,3-DT**) from *m*-cresol; *o*-tolyl acetate (***o*-TA**) and 2,5-dihydroxy toluene (**2,5-DT**) from *o*-cresol; *p*-tolyl acetate (***p*-TA**) and 3,4-dihydroxy toluene (**3,4-DT**) from *p*-cresol. Diethyl maleate (**DM**) and diethyl oxalate (**DO**) products were commonly found in all cresols oxidation.

Column and reactor reactions yielded the same products of the respective cresol (*m*-, *o*-, *p*-cresol). Of all the products that were obtained, dihydroxy toluenes are the direct oxidation products of cresol whereas the rest are ethanol derivatised oxidation products. *i.e*. **DM** and **DO** were esterification products of maleic acid and oxalic acid, respectively. However, all products are termed 'oxidation products' in this thesis for simplicity. Detection of these oxidation products laid preliminary grounds for the more traditional catalytic oxidation reactions.

In a glass reactor (impinger), 25.0 mL of each cresol was ozonated in absence of a catalyst for 24 h and the obtained percentage conversions and selectivity results were used as reference data in catalyzed oxidations. The economically friendly pure activated charcoal was initially used as a catalyst (1% w/v charged) followed by pure supports *viz.* γ-Al_2O_3, SiO_2 and V_2O_5 separately. Activated charcoal showed lowest efficiency than the pure supports and thus the attention was put on improving their activity by loading different metals on their surfaces. Catalytic activity of pure supports assumed the order of SiO_2 > V_2O_5 > γ-Al_2O_3, with silica as the most active support.

Moreover, the metal loaded catalysts were utilized in the oxidative degradation of cresols and 1% w/v of catalyst was used in all catalytic work. Of all γ-Al_2O_3 supported catalysts, Mn(2.5%)/γ-Al_2O_3 yielded highest conversion of *m*-cresol (70%) due to Mn species present on surface γ-Al_2O_3, whereas Ni(2.5%)/γ-Al_2O_3 showed highest percentage conversions of both *o*-(66%) and *p*-cresols (81%). Amongst metal loaded SiO_2 catalysts, Fe(2.5%)/SiO_2 was more active in the degradation of *m*- (81%) and *o*-cresol (70%) due to its relatively large surface area and presence of Fe in a form of catalytically active Fe_2O_3, while Ni(2.5%)/SiO_2 degraded *p*-cresol (85%) the most. Mn(2.5%)/V_2O_5 catalyst converted most of *m*- (71%) and *o*-cresol (67%) to oxidation products whereas Fe(7.5%)/V_2O_5 relatively converted most of *p*-cresol (64%) to products which was promoted by Fe_3O_4 presence on V_2O_5 surface. The efficiency of metal loaded catalysts was decreased from SiO_2 to V_2O_5 support.

When supports (γ-Al_2O_3, SiO_2, V_2O_5) were used as catalysts, there was an apparent improvement in product selectivity compared to uncatalyzed ozonation reactions. However, the use of metal (Ni, Fe, Mn, V) loaded supports as catalysts resulted in the decrease in product selectivities but significantly improved percentage conversions.

Table of contents

List of Figures

List of Tables

List of Schemes

Abbreviations

%T	– Percentage Transmittance
µL	– microliter(s)
µm	– micro meter(s)
ac. ch	– activated charcoal
AOPs	– Advanced Oxidation Processes
AR	– Analytical Reagent
ATR	– Attenuated Total Reflectance
BET	– Brunauer-Emmett-Teller surface area analyzer
cm^{-1}	– per centimeters
cm^3/g	– cubic centimeters per gram
cps	– counts per second
Cyhex	– Cyclohexane
d	– pore diameter
DCM	– Dichloromethane
DNPH	– 2,4-dinitrophenyl hydrazine
EA	– Ethyl Acetate
EDX	– Energy Dispersive X-ray spectroscopy
EtOH	– Ethanol
eV	– electron Volts
Fe	– Iron
Fe(2.5%)/γ-Al_2O_3	– 2.5% of iron (by weight) loaded on a γ-Al_2O_3 support
Fe(2.5%)/SiO_2	– 2.5% of iron (by weight) loaded on a SiO_2 support
Fe(2.5%)/V_2O_5	– 2.5% of iron (by weight) loaded on a V_2O_5 support
Fe(7.5%)/γ-Al_2O_3	– 7.5% of iron (by weight) loaded on a γ-Al_2O_3 support
Fe(7.5%)/SiO_2	– 7.5% of iron (by weight) loaded on a SiO_2 support
Fe(7.5%)/V_2O_5	– 7.5% of iron (by weight) loaded on a V_2O_5 support

FT-IR	– Fourier Transform Infrared spectroscopy
g	– gram(s)
GC	– Gas Chromatography
GR	– Reagent Grade
h	– hour(s)
HO·	– Hydroxyl radical
HPLC	– High Performance Liquid Chromatography
ICP	– Inductively Coupled Plasma
JCPDS	– Join Committee on Powder Diffraction Standards
kJ/mol	– kilo Joules per mole
kV	– kilo Volts
L	– Liters
LPM	– Liters per minute
M	– Molar
m-	– *meta*-
MeOH	– Methanol
m^2/g	– square meters per gram
mg	– milligram
mg/kg	– milligrams per kilogram
mg/L	– milligrams per Liter
min	– minute(s)
mL	– milliliter
mL/min	– milliliter per minute
Mn	– Manganese
Mn(2.5%)/γ-Al_2O_3	– 2.5% of manganese (by weight) loaded on a γ-Al_2O_3 support
Mn(2.5%)/SiO_2	– 2.5% of manganese (by weight) loaded on a SiO_2 support
Mn(2.5%)/V_2O_5	– 2.5% of manganese (by weight) loaded on a V_2O_5 support

$Mn(7.5\%)/\gamma\text{-}Al_2O_3$	– 7.5% of manganese (by weight) loaded on a $\gamma\text{-}Al_2O_3$ support
$Mn(7.5\%)/SiO_2$	– 7.5% of manganese (by weight) loaded on a SiO_2 support
$Mn(7.5\%)/V_2O_5$	– 7.5% of manganese (by weight) loaded on a V_2O_5 support
MS	– Mass Spectrometer (GC detector)
MXT 1	– mixture 1
Ni	– Nickel
$Ni(2.5\%)/\gamma\text{-}Al_2O_3$	– 2.5% of nickel (by weight) loaded on a $\gamma\text{-}Al_2O_3$ support
$Ni(2.5\%)/SiO_2$	– 2.5% of nickel (by weight) loaded on a SiO_2 support
$Ni(2.5\%)/V_2O_5$	– 2.5% of nickel (by weight) loaded on a V_2O_5 support
$Ni(7.5\%)/\gamma\text{-}Al_2O_3$	– 7.5% of nickel (by weight) loaded on a $\gamma\text{-}Al_2O_3$ support
$Ni(7.5\%)/SiO_2$	– 7.5% of nickel (by weight) loaded on a SiO_2 support
$Ni(7.5\%)/V_2O_5$	– 7.5% of nickel (by weight) loaded on a V_2O_5 support
nm	– nano meter
NMR	– Nuclear Magnetic Resonance
No.	– Number
o-	– *ortho-*
^oC	– degrees Celsius
OES	– Optical Emission Spectroscopy (ICP detector)
OFR	– Oxygen Flow Rate
p-	– *para-*
p./ pp.	– page/ pages
ppm	– parts per million
R & D	– Research and Development
Redox	– Reduction oxidation
SEM	– Scanning Electron Microscopy
TEM	– Transmission Electron Microscopy
TEMPO	– (2,2,6,6-Tetramethylpiperidin-1-yl)oxyl

TLC	– Thin Layer Chromatography
UV	– Ultraviolet
V	– Volts
Vanadium	– Vanadium
$V(2.5\%)/\gamma\text{-}Al_2O_3$	– 2.5% of vanadium (by weight) loaded on a $\gamma\text{-}Al_2O_3$ support
$V(2.5\%)/SiO_2$	– 2.5% of vanadium (by weight) loaded on a SiO_2 support
$V(7.5\%)/\gamma\text{-}Al_2O_3$	– 7.5% of vanadium (by weight) loaded on a $\gamma\text{-}Al_2O_3$ support
$V(7.5\%)/SiO_2$	– 7.5% of vanadium (by weight) loaded on a SiO_2 support
w/v	– weight per volume
wt.%	– weight percentage
XRD	– X-Ray Diffraction spectroscopy

Symbols

%	– Percent
γ	– Gamma
μ	– Mu
β	– Beta
≥	– Greater or equal to
≤	– Less or equal to
>	– Greater than
<	– Less than
=	– Equal to
±	– Plus or minus
Δ	– Delta (change)

Chapter 1
GENERAL INTRODUCTION

1.0. Background

For decades, research scientists and engineers have faced challenges pertaining to alleviating and/ or preventing the formation of by-products from synthetic processes. As much as new synthetic products and protocols are introduced both in research and industrial sectors, the identification and subsequent destruction of by-products still remains a major challenge. An ideal chemical reaction affords a product in quantitative yields, however, Green Chemistry has recently suggested that the starting materials, products and reaction protocols should be as environmentally-friendly as possible. This is essential since the biosphere is already confronted by adverse issues such as global warming and extinctions, as a result of by-products surfacing from man-made processes.

To date, containment and chemical-mediated treatment of unwanted by-products given off from a wide range of chemical reactions are still the preferred methods. Prior to waste management regulations such as The South African Waste Act No. 59 of 2008,[a] these methods would adversely leak by-products into the environment, where they would exist as hazardous contaminants in water streams, urban air and soils. This led to unparalleled global attention focused on introducing stringent chemical waste handling protocols and acts, per vulnerable nations [1].

Although inherent organic pollutants continue to be a major concern, early reports focused on inorganic-type pollutants. Lefohn and Tingey [2] measured co-occurrence of potentially phytotoxic concentrations of ozone, sulfur dioxide and nitrogen dioxide air pollutants in the atmosphere; this trio of pollutants reduces plant growth and instigates foliar injury [3]. However, persistent pollutants of organic nature, such as polychlorinated biphenyls among others may be relatively harsh, as they can result to reproductive impairment and malformations, altered liver enzyme function and increased risk of tumors on the organisms [4].

Organic waste and/ or pollutants are diverse. They range from halogenated aliphatic to simple cyclic/ aromatic organic compounds. Numerous waste treatment procedures have been proposed for these compounds, such as: decomposition by irradiation using gamma rays [5], direct

[a] To reform the law regulating waste management in order to protect health and the environment by providing reasonable measures for the prevention of pollution and ecological degradation and for securing ecologically sustainable development

electrochemical oxidation [**6**], activated sludge processes [**7**], oxidation by ozonation [**8,9,10**], chlorination [**11**] and photocatalysis method [**12,13**] among others. The choice of a suitable waste treatment method is strongly dependent on a number of factors such as the chemical nature of the by-product, recyclability and life-time of the employed reagents (if any). Amongst the aforementioned waste treatment methods, Getoff demonstrated a non-chemical decomposition of a halogenated saturated-hydrocarbon, 1.2-dichloroethane, by employing irradiation using gamma rays [**5**]. Regardless of this, chemical-based methods such as ammonia-assisted chlorination of water have widely been explored since the early 1900's [**14**].

Disinfection by chlorination has been exploited in aquaculture, mainly for the elimination of unwanted aquatic and other industrial/ chemical contaminants. Unfortunately, concerns over reactive capabilities of the chlorinating agents with electron-activated ring structures and amino-functionalized organic compounds to produce chlorinated products, have been identified [**15**]. The pioneering work of Rosenberg *et al*. [**16**] on the adverse effects of chlorinated by-products such as 1,2-dichloroethane on marine organisms, prompted an alternative use of relatively milder ClO_2, $KMnO_4$, NH_2Cl, H_2O_2 and O_3 as opposed to Cl_2 as a disinfectant [**17**].

A review work published by Fiessinger *et al*. [**18**] represented ozone, O_3, as the best disinfectant. Ozone generally forms less toxic substances or mutagens, and does not produce halogenated compounds. Furthermore, it has an enhanced biodegradability and decomposes faster in water with no signs of stable precipitates/ residues which form when Cl_2 and ClO_2 are used [**17,18**]. Despite of the shortcomings from Cl_2 disinfection, Mori *et al*. [**19**] demonstrated the disinfection of the by-then common tap water contaminant, tetracyclic aromatic hydrocarbons, thus forming mono- and di-chlorinated, as well as oxygenated products in water.

Owing to the relatively higher oxidative potential compared to its rival oxidants, O_3 has for many years been applied in the removal of unpleasant taste, appearance and odor in water [**20**]. However, some organic pollutants such as atrazine are refractory towards ozone treatment; advanced oxidation processes (AOPs) coupled with other treatment methods have been developed and used to achieve high levels of oxidation percentages [**21**]. Since its discovery in the early–19^{th} century, O_3 has been applied extensively in oxidation-type organic reactions [**22**]. Example of these reactions include: oxidation of aliphatic hydrocarbons such as ethane and ethene [**23**], aromatic hydrocarbons such as *m*-cresol acetate [**24**], aqueous ozonation of

ammonium surfactant [8] and oxidation of polyethoxylated alcohols [25]. Others are complex, such as the heterogeneously-catalyzed O_3 oxidation of aliphatic [10,26] and aromatic hydrocarbons [27].

Recent attention has focused on O_3-based heterogeneous catalysis, as means of highly efficient degradation, mineralization or conversion of hazardous aromatic by-products into value-added and/ or environmentally benign products [27]. However, there is still room pertaining to understanding the O_3-based catalytic oxidation mechanisms of aromatic compounds. Understanding the latter would be a major achievement in the field of environmental chemistry as it would certainly aid in fighting chemical pollution.

1.1. Chemical pollution

Chemical pollution is an environmental term which simply defines an introduction of chemical substances as contaminants into the natural environment. With South African population alone reportedly increasing at a rate of *ca.* 1.46% per year, [28] the industries supplying essentials like, detergents, beverages, body lotions, medicine, gas and so forth are pressurized to meet social demands. Consequently, the manufacturing processes undertaken, results in various by-products given-off in different forms, either as gases or solids and liquids. A local news blog, Business Day Live, published an article in early-2013 which quotes: "air quality across South Africa exceeded the country's, as well as the World Health Organization's limits for aerosols", based on reports by the Council for Scientific and Industrial Research, South Africa [29]. Generally, chemical pollutants can be divided into two categories: inorganic and organic pollutants.

1.1.1. Inorganic pollutants

Inorganic chemical pollutants mostly constitute of heavy metals, suspended solids and many gaseous substances. The basic prominent methods of treating these pollutants include filtration, modification and recycling, where possible. Most common examples of inorganic pollutants include arsenic, cadmium, mercury, and lead metal traces, which are known to easily form silicate-based composites present in soil and related sediments [30]. The inorganic pollutants are, in many instances, overshadowed by rapidly-developing organic pollutants due to their

restrictive chemical nature. As a result, there are more organic pollutants threatening the environmental well-being.

1.1.2. Organic pollutants

Organic chemical pollutants are composed of hydrocarbons-type compounds. Common examples are aromatic amines [31], sulfonated aromatic compounds [31], chlorinated-hydrocarbons [32], bisphenols [33] and substituted-phenols (Figure 1.1) [34].

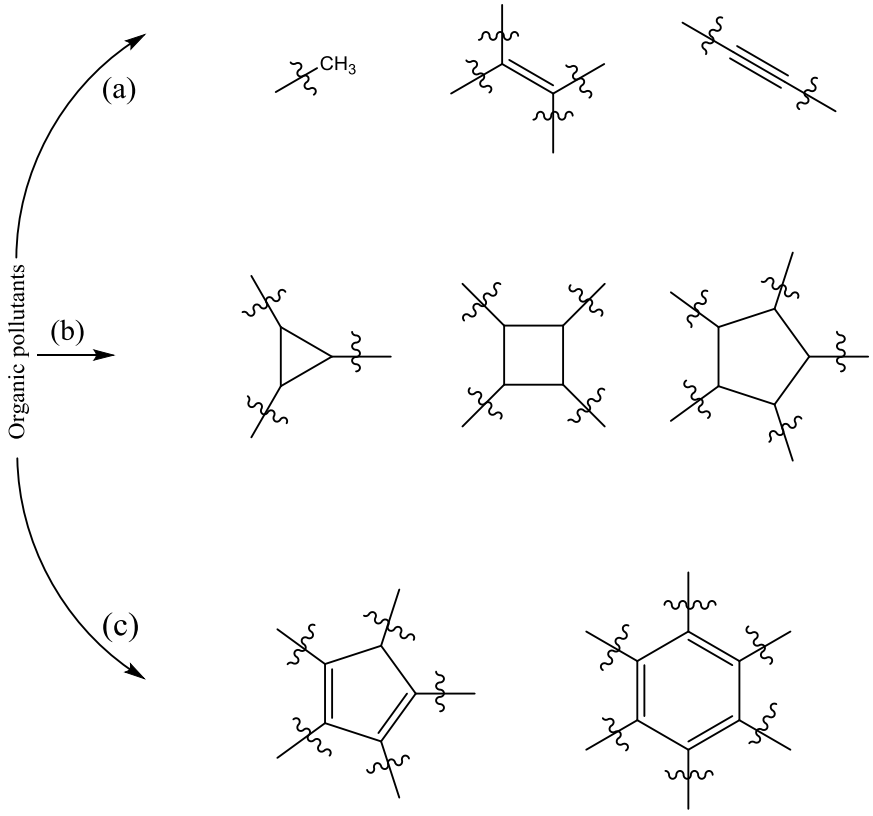

Figure 1.1. Generalized structural formulae of organic pollutants ranging from (a) saturated and unsaturated aliphatic, (b) saturated cyclic, to (c) aromatic hydrocarbon compounds.

The degree at which organic substances pose a threat to the environment is measured through their resistance to undergo chemical, biological and photolytic degradation. Persistent organic pollutants are characterized by their degree of solubility in water, which subsequently determines their bioaccumulation in fatty tissues. Most of them are semi-volatile in nature, which delays their decomposition in the atmosphere. Other determining factors on the fate of organic pollutants include mobility, bioavailability and toxicity [**35**].

- **Mobility**: The ability of the substance to be transported from one location to another and if critical concentrations are maintained, then acute effects may result.
- **Bioavailability**: This factor is determined by the substance's degree of lipophilicity, which may result in a biomagnification of a hazardous substance in organisms through the food chain.
- **Toxicity**: At relevant concentrations, the persistence, mobility and liphophilic nature of a substance may well fit a definition of a toxic material within an organism.

Environmental scientists have long used the aforementioned factors to identify potential organic pollutants which can be extracted, recycled, converted, degraded or mineralized into environmentally-friendly products. Organic pollutants can be classified into two groups: aliphatic and aromatic hydrocarbons, based on their intermolecular atomic arrangements.

1.1.2.1. *Aliphatic hydrocarbons*

An aliphatic hydrocarbon is a non-aromatic compound which can be straight, branched or cyclic in nature, *e.g.* butane, isobutene and cyclobutane, respectively. Aliphatic hydrocarbons may contain elements other than hydrogen and carbon, can also either be saturated or unsaturated bonded chemical structures.

Most common functional groups incorporated into aliphatic hydrocarbons include ketones, ethers, aldehydes, esters and alcohols. Oxidation of aromatic hydrocarbons in air may result in the formation of unsaturated aliphatic oxygenates in the atmosphere [**36**]. These oxygenates are thus exposed to further oxidation by oxidizing agents such as nitrates and hydroxyl radicals, as well as ozone [**37**]. The unsaturated carbon–carbon bond often initiates the chemical oxidation reaction. Thus, destruction of unsaturated aliphatic hydrocarbons through chemical oxidation is by far, an effective and cost efficient destructive method.

1.1.2.2. *Aromatic hydrocarbons*

Hydrocarbons that are classified as aromatic compounds are cyclic structures which have sigma bonds and delocalized π-electrons within the carbon-carbon bonds. Some of them consist of one or more heteroatoms within the ring which may participate in completing the aromaticity [38,39]. These compounds range from simple mono-cyclic to complex polycyclic aromatic compounds as shown in Figure 1.2. Aromatic compounds are stabilized by the delocalized cloud of electrons known as 'resonance energy'. A criterion for identifying a simple aromatic compound is: A molecule must satisfy Hückel's rule, having $4n+2$ electrons in the delocalized, conjugated p-orbital cloud. It must be cyclic, planar and every atom in the ring must be capable of participating in the delocalization of electrons by possessing unshared pair of electrons or a p-orbital.

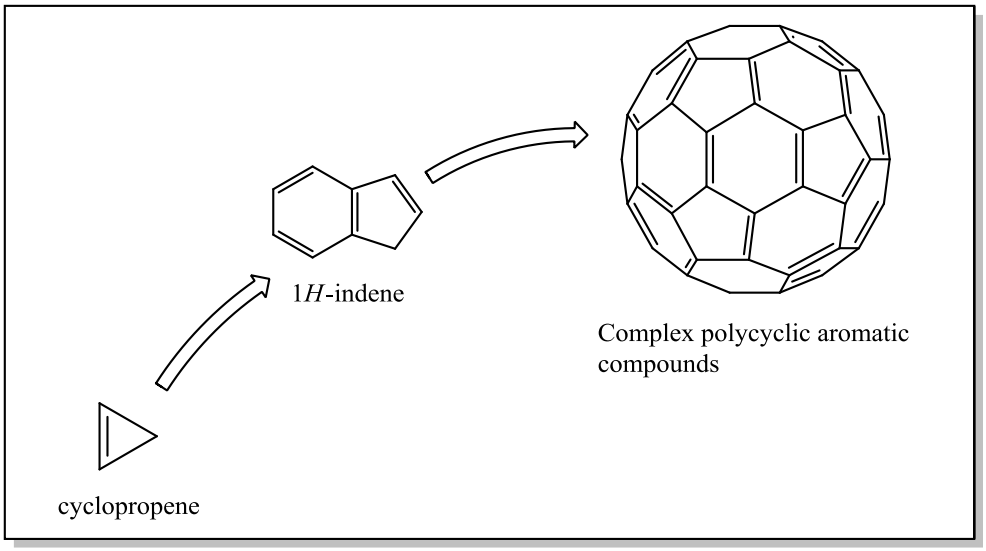

Figure 1.2. Illustration of the range of aromatic organic compounds from a simple mono-cyclic aromatic to a complex poly-cyclic aromatic hydrocarbon.

A compound need not necessarily be composed of only aromatic rings for it to be classified as aromatic [36]. For example, 1*H*-indene in Figure 1.2 is aromatic, mainly because of the aromatic benzene backbone.

The aromatic hydrocarbons have at least one C=C bond, which makes them unsaturated and classified as cycloalkenes. The C=C bond can be cleaved in the presence of a suitable oxidizing

agent, thus consequently introducing the carbonyl functional group within the structure. Furthermore, aromatic hydrocarbons possess different properties such solubility in either aqueous and/or organic solvents, carcinogenicity, mutagenicity, volatility, persistence towards biodegradability, toxicity and so forth. This enables most of them to be biologically and chemically active, which may react positively or negatively to certain organisms. Moreover, chemical oxidation is one of the key tools to destroy or convert environmentally unfriendly aromatic hydrocarbons [**6,9,20**].

1.2. Chemical oxidation

In chemistry terms, oxidation is known as the loss of electrons or an increase in oxidation state of an atom. Oxidation is a half reaction of a Redox reaction, opposite to its counterpart which is reduction. In a redox reaction, an oxidizing agent itself gets reduced, as a result of accepting electrons from the oxidized chemical species.

$$Fe^{3+} + Cu^{+} \rightarrow Fe^{2+} + Cu^{2+} \quad (1.1)$$

$$Cu^{+} \rightarrow Cu^{2+} + e- \quad (1.2)$$

$$Fe^{3+} + e^{-} \rightarrow Fe^{2+} \quad (1.3)$$

Redox reactions of inorganic species can be easily understood better than those of organic counterparts. An example of the former is illustrated in Equations 1.1–1.3; the Cu^{+} species get oxidized to Cu^{2+} by the Fe^{3+} oxidizing agent. The organic-type redox reactions, on the other hand, are generally observed through loss/ gain of proton and oxygen atoms, as well as an increase in multiple bond order on carbon atoms. One example is the oxidation of a secondary alcohol (through loss of the hydroxyl proton) to a ketone by a molecular oxygen (as oxidizing agent) in the presence of Mn(II) and Co(II) catalysts (Figure 1.3) [**40**].

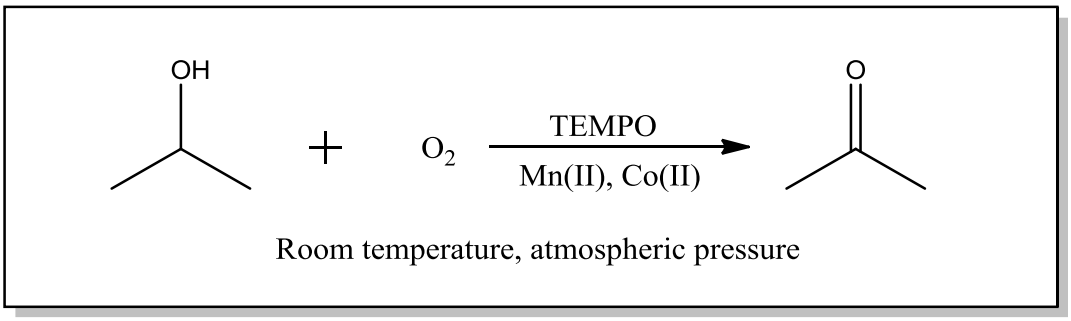

Figure 1.3. Oxidation reaction mechanism of a secondary alcohol oxidized into a ketone. [40]

The Cannizzaro reaction is another good example of an organic-type redox reaction (Figure 1.4). The products (b) and (c) are formed as a result of starting material (a) being oxidized and reduced, respectively. Other renowned examples include the synthesis of *m*-hydroxybenzyl alcohol diacetate from the oxidation of *m*-cresol acetate [24], and electrochemical oxidation of toluene to yield cresols [41].

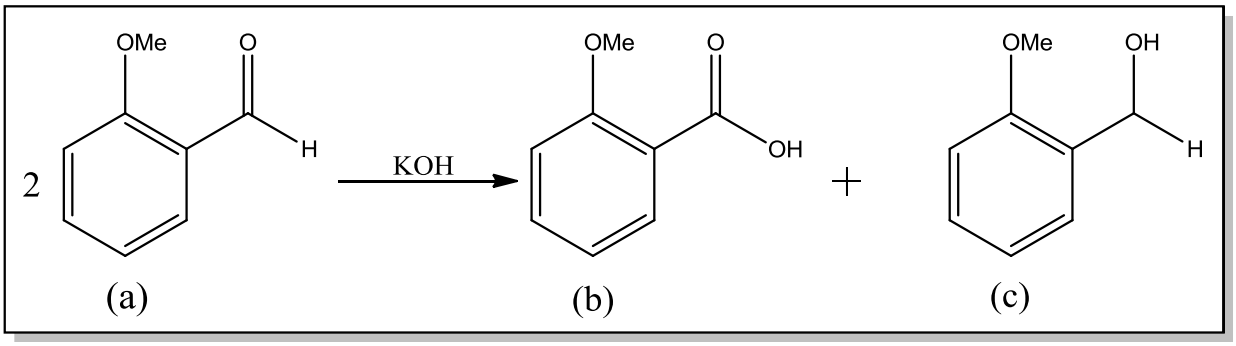

Figure 1.4. Disproportionation reaction of (a) non-enolizable aldehydes, to (b) carboxylic acids and (c) alcohols, under alkaline conditions.

Furthermore, in chemical oxidation, a vast number of oxidizing agents have been utilized (Table 1.1). Except the hydroxyl-radical and oxygen (atomic) oxidants which have shorter life-times, O_3 is mostly preferred due to its relatively high redox potential, as well as its fascinating physical and chemical properties.

Table 1.1. Summary of prominent oxidizing agents and their redox potentials.

Oxidizing agent	Formula	Redox potential (V)	References
Fluorine	F_2	2.87	[42]
Hydroxyl-radical	$OH^{\cdot}$	2.80	[43]
Oxygen (atomic)	O	2.42	[43]
Ozone	O_3	2.08	[31–33,43]
Hydrogen peroxide	H_2O_2	1.78	[43]
Lead (IV)	Pb^{4+}	1.67	[44]
Hypochloride	HOCl	1.49	[43]
Chlorine	Cl_2	1.36	[43]
Chlorine dioxide	ClO_2	1.27	[43]
Oxygen (molecular)	O_2	1.23	[43]
Iron (III)	Fe^{3+}	0.77	[45]
Copper (II)	Cu^{2+}	0.34	[46]

1.3. Ozone chemistry

Ozone is an allotrope of oxygen, discovered in 1839 by Schönbein [22,47]. It is composed of three oxygen atoms bonded together by two stable oxygen-oxygen bonds and one resonating bond which stabilizes the net charge of the molecule as a whole. There is no known natural standard-concentration of ozone in the atmosphere due to its shorter half-life. However, ozone is produced naturally by ultraviolet radiation[b] in the atmosphere, at different concentrations [48].

Ozone exists in two phases: gaseous and liquid, the former is less stable. The gaseous form has a pale-blue appearance at ambient temperature and pressure conditions. It is also highly soluble in water, compared to its parent allotrope, O_2 [49]. However, it is insoluble at pH levels of less than 7.0, while it decomposes under extreme alkaline conditions to form different, highly reactive free radicals such as $HO^{\cdot}$ (Equation 1.4) [25,49].

$$O_3 + H_2O\ (pH \geq 7.0) \rightarrow 2(HO^{\cdot}) + O_2 \qquad (1.4)$$

[b] The ultraviolet radiation from the sun splits the oxygen molecules into nascent oxygen atoms that are highly unstable unless they bind with nearby molecular oxygen to form ozone molecules.

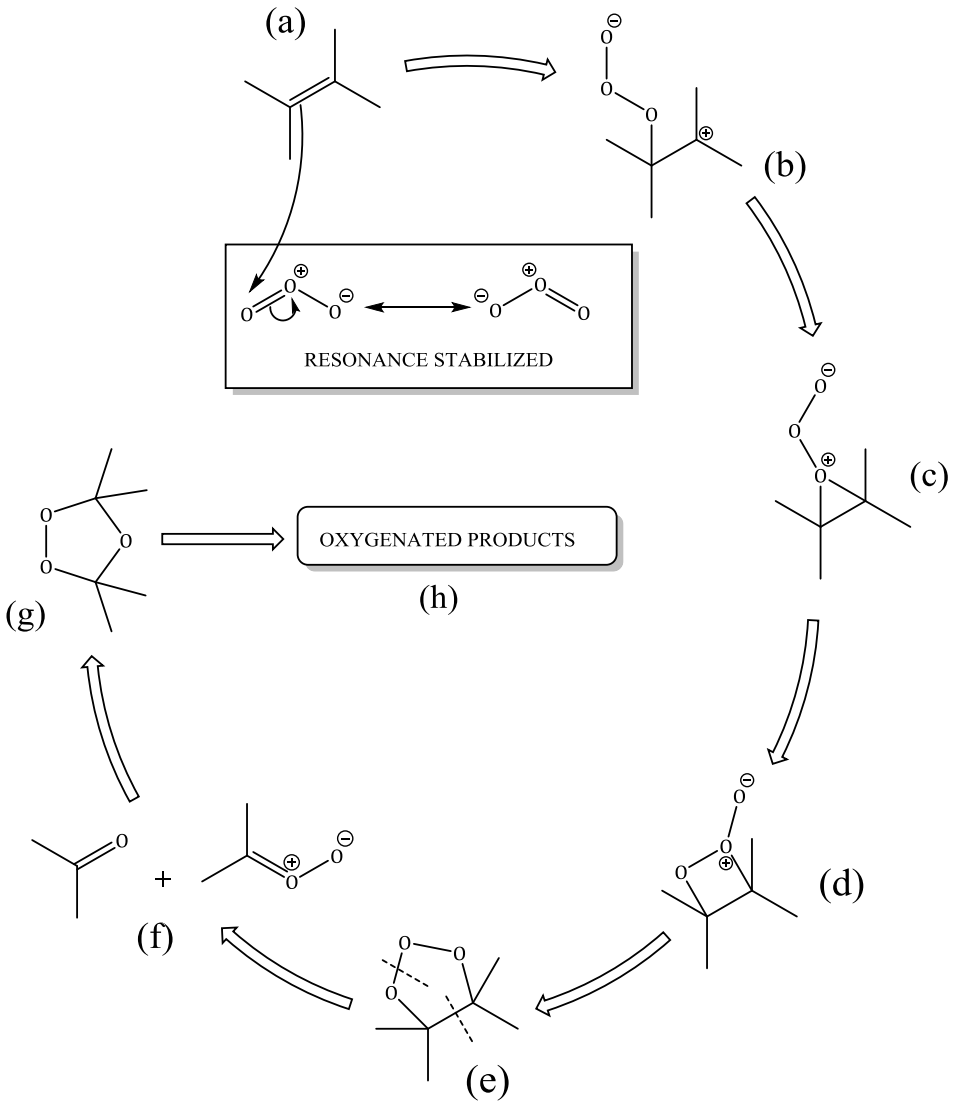

Figure 1.5. A schematic illustration of the Criegee ozone-alkene interaction mechanism [50].

According to Criegee [50], ozone reacts with unsaturated hydrocarbons through five prominent steps (Figure 1.5). In his proposed mechanism, an alkene (a) reacts with ozone to produce an σ-compound (b), which undergoes rearrangement to form a primary ozonide (e) through intermediates (c) and (d). The primary ozonide (e) dissociates into a carbonyl compound and carbonyl oxide intermediate in (f). The intermediates react to form the secondary ozonide (g) which further reacts with ozone to afford oxidation products which include aldehydes, ketones, and carboxylic acids, among others in (h). Moreover, understanding the latter mechanism and the

likes has encouraged the advancement of ozone generation methods, inclusively for domestic, industrial, commercial and research purposes.

1.3.1. Ozone generation

The ozone generation procedures can be classified into four, based on their intensive utilization in various research fields. The procedures involve UV radiation, electrolysis, radiochemical and corona discharge methods.

1.3.1.1. *Ultraviolet radiation method*

Basically, the formation of ozone from the feed gas (O_2) requires the precise amount of energy to break the existing O=O bonds that stabilize the O_2 compound. The resulting, unstable $O^{\cdot}$ radicals react with other O_2 molecules to form a relatively stable O_3 compound (Figure 1.6). Moreover, the enthalpy of formation of ozone is 143 kJ/mol. The energy provided by UV-radiation is sufficient to induce the required dissociation of O_2, thus forming the $O^{\cdot}$ radicals.

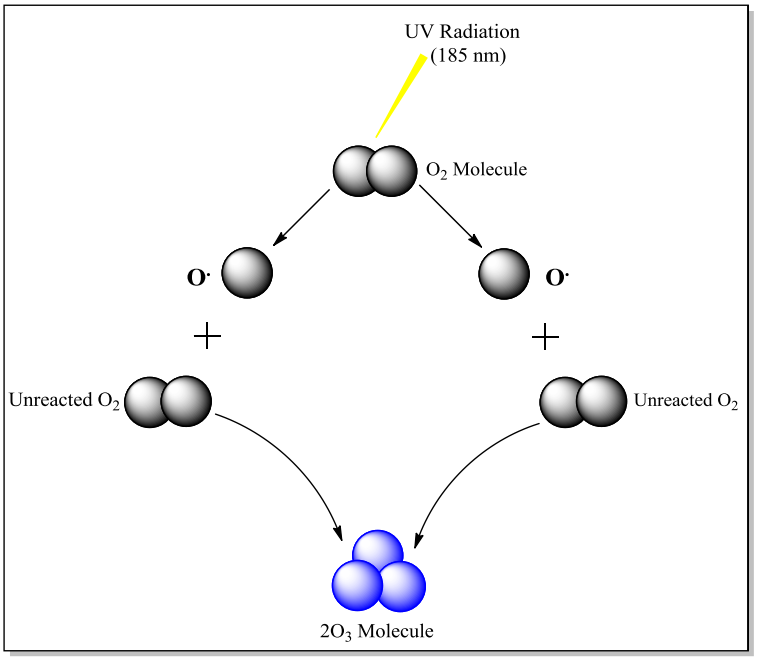

Figure 1.6. Ozone generation by UV-radiation method [47].

The high yield of ozone is achieved at UV-radiation of ≤ 200 nm (6.21 eV) wavelengths; radiation at 185 nm (6.71 eV) usually produces good results (Figure 1.6). Ozone dissociates at longer wavelength, meaning, its constituent oxygen atoms requires less energy to detach as

compared to that required for ozone formation. Contrarily, UV-radiation of 185 nm provides excessive energy for ozone formation, enough to effortlessly decompose the formed O_3 gas. But in actual sense, at 185 nm, the energy of formation is destructive to the deterioration of ozone production in the process. Although O_3 dissociates at longer UV wavelengths of between 200–308 nm, the 185 nm radiation provides sufficient energy to regenerate O_3 from the dissociated products, in addition to O_3 produced from O_2. Therefore, formation rate of O_3 exceed its dissociation.

1.3.1.2. *Electrolysis method*

Electrolysis is a chemical reaction which is aided by passing an electric current through a liquid solution, thus leading to the evolution of gaseous products. A similar procedure can also be used to generate O_3 gas from electrolytes such as water and dilute sulfuric acid [51], among others. In the presence of an electric current, O_2 is reduced at the cathode, and then evolves O_3 at the anode (Figure 1.7).

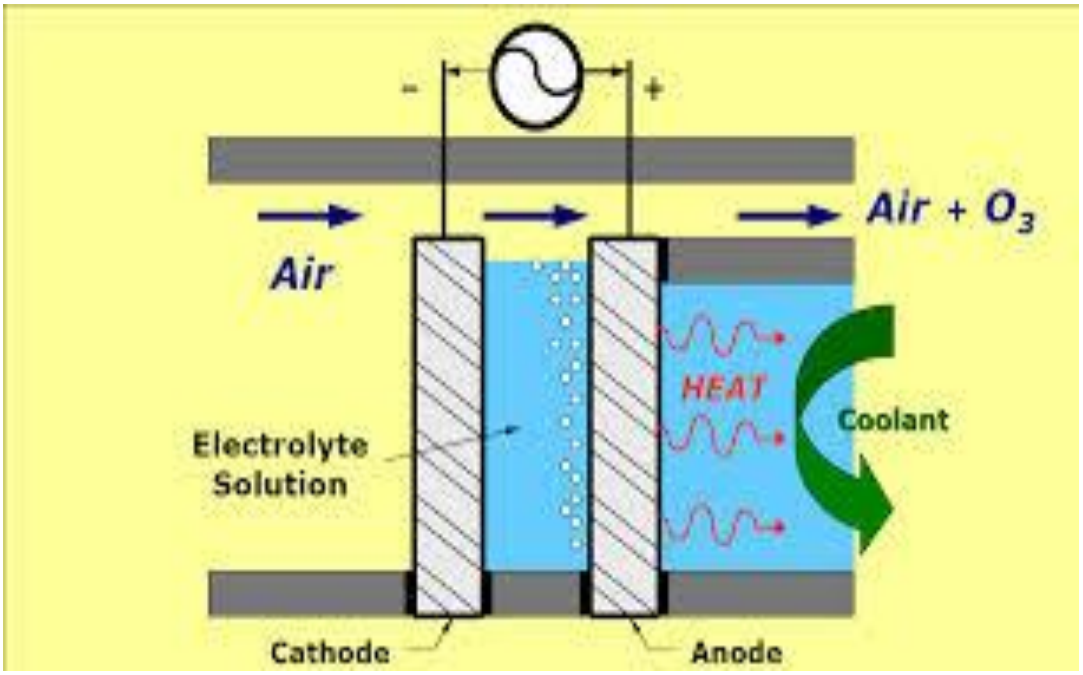

Figure 1.7. Ozone generation by electrolysis method [51].

1.3.1.3. *Radiochemical method*

Radiochemical-based method of forming O_3 includes irradiation of O_2 by high energy radioactive rays such as that of gamma, beta and high energy neutrons [48]. This method is rarely used due to expensive equipment and sophisticated application parameters. Moreover, this method requires a highly unstable, liquefied O_2 as the source.

1.3.1.4. *Corona discharge method*

Ozone production by the Corona discharge procedure is the most common and commercially viable method. The basic setup consists of two electrodes which are strategically placed at either sides of the reaction chamber to which an appropriate gas (commonly O_2) is fed (Figure 1.8). The high voltage is supplied to the electrodes, thus creating an electric field within the chamber. An electron ($\geq$ 5.1 eV) resonating between the two electrodes reacts with O_2 molecule, thus affording two $O^{\cdot}$ radicals. These radicals react with O_2 molecules, in the presence of body M molecule, to form the anticipated O_3 product (Equations 1.5 and 1.6) [48,52].

$$e^- + O_2 \rightarrow 2\,O^{\cdot} + e^- \qquad (1.5)$$

$$O^{\cdot} + O_2 + M \rightarrow O_3 + M \qquad (1.6)$$

Where M = O / O_2 / O_3 within the discharge (air flow) gap.

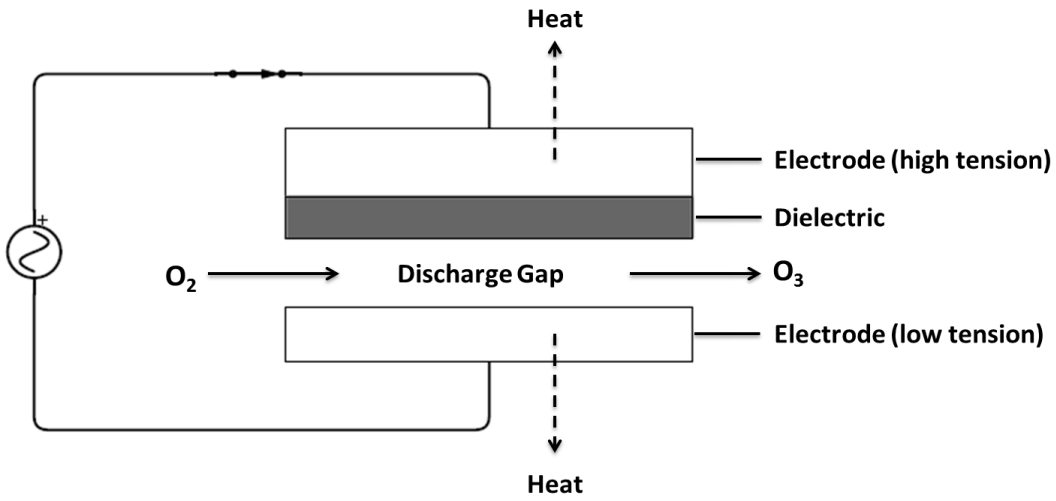

Figure 1.8. Ozone generation by Corona discharge method [52].

Amongst all four above-mentioned ozone production methods, a method that can be performed at low cost and yield high amounts of ozone per unit electrical input is paramount, which explains the common use of the Corona discharge method in ozone generation. As an oxidant, ozone has seen great consideration over the past years, however, ozone alone and/ or ozone with other reagents have gained significance from their utility in advanced oxidation processes [53].

1.3.2. Advanced oxidation processes

Advanced oxidation processes (AOPs) are defined as environmentally benign oxidation processes that practically rely on the production of the hydroxyl radical (2.8 V, redox potential). The hydroxyl radicals readily facilitate conversion of nearly all organic pollutants to harmless and/or value added products, through oxidative processes [53,54]. In comparison with other chemical and biological processes, AOPs have minor-to-none potential of altering the pollutants physical phase and producing large amounts of harmful waste products. These processes address the shortcomings common to conventional oxidants (*i.e.* H_2O_2 and O_3, among others) [53]. There are different reacting systems that achieve the production of active HO radicals and thus characterized as AOPs, Table 1.2 display some of the prominent systems.

Table 1.2. Advanced oxidation processes.

Entry no.	Reacting systems	Common terminology	References
1	H_2O_2 / Fe^{2+}	Fenton	[23,53,55]
2	H_2O_2 / Fe^{3+}	Fenton - like	[55,56]
3	H_2O_2 / Fe^{2+} (Fe^{3+}) / UV	Photo assisted Fenton	[55]
4	H_2O_2 / Fe^{3+} - Oxalate	-	[55]
5	Mn^{2+} / Oxalic acid / Ozone	-	[55]
6	TiO_2 / *hv* / O_2	Photocatalysis	[12,13,53,55,56]
7	H_2O_2 / UV	-	[55, 56]
8	O_3 / H_2O_2	-	[9,55,56]
8	O_3 / UV	-	[55, 56]
9	O_3	Ozonation	[9,17,18,20,37]
10	O_3 + heterogeneous catalysts	Catazone	[9,10,21,27,31]

Among the tabulated AOPs, Fenton, photocatalysis and ozonation based processes have been investigated and utilized to a significant extent and thus are briefly explained below.

- **Fenton processes:** The decomposition of H_2O_2 in the presence of Fe^{2+}, to produce a highly reactive hydroxyl radical. The generated hydroxyl radical further participates in oxidizing the targeted organic compounds [**23,53,55,56**]. Equations 1.7– .17 shows a typical mechanism of $HO^{\bullet}$ formation through Fenton process [**56**].

  Initial reactions:

  $H_2O_2 \rightarrow H_2O + ½\ O_2$ (1.7)

  $H_2O_2 + Fe^{2+} \rightarrow Fe^{3+} + HO^- + HO^{\bullet}$ (1.8)

  $H_2O_2 + Fe^{3+} \rightarrow Fe(OOH)^{2+} + H^+ \leftrightarrow Fe^{2+} + HO_2^{\bullet} + H^+$ (1.9)

  $HO^- + Fe^{3+} \rightarrow Fe(OH)^{2+} \leftrightarrow Fe^{2+} + HO^{\bullet}$ (1.10)

  Propagation step:

  $HO^{\bullet} + H_2O_2 \rightarrow HO_2^{\bullet} + H_2O$ (1.11)

  $HO_2^{\bullet} + H_2O_2 \rightarrow HO^{\bullet} + H_2O + O_2$ (1.12)

  $HO_2^{\bullet} + HO_2^- \rightarrow HO^{\bullet} + HO^- + O_2$ (1.13)

  Termination step:

  $Fe^{2+} + HO^{\bullet} \rightarrow Fe^{3+} + HO^-$ (1.14)

  $HO_2^{\bullet} + Fe^{3+} \rightarrow Fe^{2+} + H^+ + O_2$ (1.15)

  $HO^{\bullet} + HO_2^{\bullet} \rightarrow H_2O + O_2$ (1.16)

  $HO^{\bullet} + HO^{\bullet} \rightarrow H_2O_2 + O_2$ (1.17)

- **Photocatalysis:** A semiconductor material such as TiO_2 is bombarded with photonic energy, thus creating the electron-hole effect in the energy bands. These electrons and holes are thus responsible for the formation of the hydroxyl radicals, in the presence of appropriate scavengers [**12,13,53,55,56**]. Mechanistically, the formation of hydroxyl radicals through this process is rather complex and has been reviewed by Pera-Titus and co-workers among others [**56**].

- **Ozonation:** This process involves decomposing the targeted organic compound in the presence of ozone alone (direct ozonation) or in assistance by active $HO^{\bullet}$ species (indirect

ozonation) [9,17,18] that are produced during HO^- ions initiated decay of ozone [56]. The hydroxyl radical formation pathway (Eq. 1.18–1.26) can also be divided into three steps.

Initial reactions:

$$O_3 + HO^{\bullet} \rightarrow O_2^{\bullet-} + HO_2^{\bullet} \quad (1.18)$$

Propagation step:

$$O_3 + O_2^{\bullet-} \rightarrow O_3^{\bullet-} + O_2 \quad (1.19)$$

$$O_3^{\bullet-} + H^+ \leftrightarrow HO_3^{\bullet} \quad (1.20)$$

$$HO_3^{\bullet} \rightarrow HO^{\bullet} + O_2 \quad (1.21)$$

$$HO^{\bullet} + O_3 \rightarrow HO_4^{\bullet} \quad (1.22)$$

$$HO_4^{\bullet} \rightarrow HO_2^{\bullet} + O_2 \quad (1.23)$$

$$HO_2^{\bullet} \leftrightarrow O_2^{\bullet-} + H^+ \quad (1.24)$$

Termination step:

$$HO^{\bullet} + CO_3^{2-} \rightarrow HO^- + CO_3^{\bullet-} \quad (1.25)$$

$$HO^{\bullet} + HCO_3^- \rightarrow HO^- + CO_3^{\bullet} \quad (1.26)$$

However, a suitable catalyst may have to be employed, depending on the reactivity of the targeted organic matter towards ozone attack [9,10,21,27,31].

1.4. Catalysis

For the first time in 1836, Berzelius introduced the term ‘catalysis’, which defines a chemical material that increases the rate of product formation, at its low concentrations without being consumed in the process [57]. The mechanisms illustrating this phenomenon are unique per type of reaction performed. However, due to the complexity of the reactions, most catalytic mechanisms are still not well understood to date.

A catalyst provides an alternative, less energy-requiring protocol as compared to an uncatalyzed reaction (Figure 1.9), thus resulting in economically-friendly chemical production processes. In simpler and ideal terms, the catalyst forms a temporary bond with the substrate, so as to lower its

minimal activation energy necessary for a specific reaction to occur. The bond breaks after complete formation of the product(s), leaving the catalyst unaltered and ready for re-use [57]. Nowadays, there exists numerous types of catalysts and the corresponding research field is divided into three sub-divisions *i.e.* bio-catalysis, homogeneous and heterogeneous catalysis.

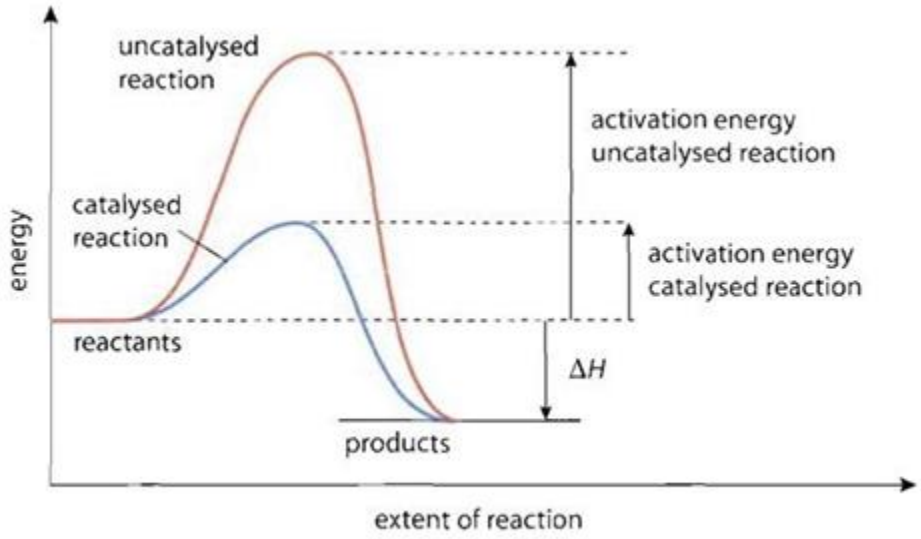

Figure 1.9. Potential energy diagram showing the activation energies of both the uncatalyzed and catalyzed reaction routes [58].

1.4.1. Bio-catalysis

Bio-catalysis or 'biological catalysis' is a biological-type catalysis which is known to utilize enzymes as catalysts in the targeted chemical reactions. They have been significantly applied in catalysis due to their high catalytic activities in certain chemical reactions, such as in production of anticarcinogenic conjugated linoleic acid from linoleic acid [59] and removal of phosphorus and nitrogen from the wastewater [60]. Although they are globular proteins which range from 62 to 2500 amino acids residue, only a small portion of their structures are directly involved in catalytic activities [61].

1.4.2. Homogeneous catalysis

Homogeneous catalysis is the opposite of heterogeneous catalysis; the catalyst is in the same physical phase/ form to that of the reactants, in a typical reaction. Despite their relatively high efficiency and selectivity towards the desired products as compared to heterogeneous catalysts, they usually require complex and time consuming separation from the products. Prakasham *et al.* [59] recently discussed examples of homogeneous catalysis which are the Suzuki–Miyaura and Kumada coupling reactions which utilize catalysts such as organometallic nickel *N*-heterocyclic carbine Ni-(NHC), soluble in common laboratory solvents (Figure 1.10).

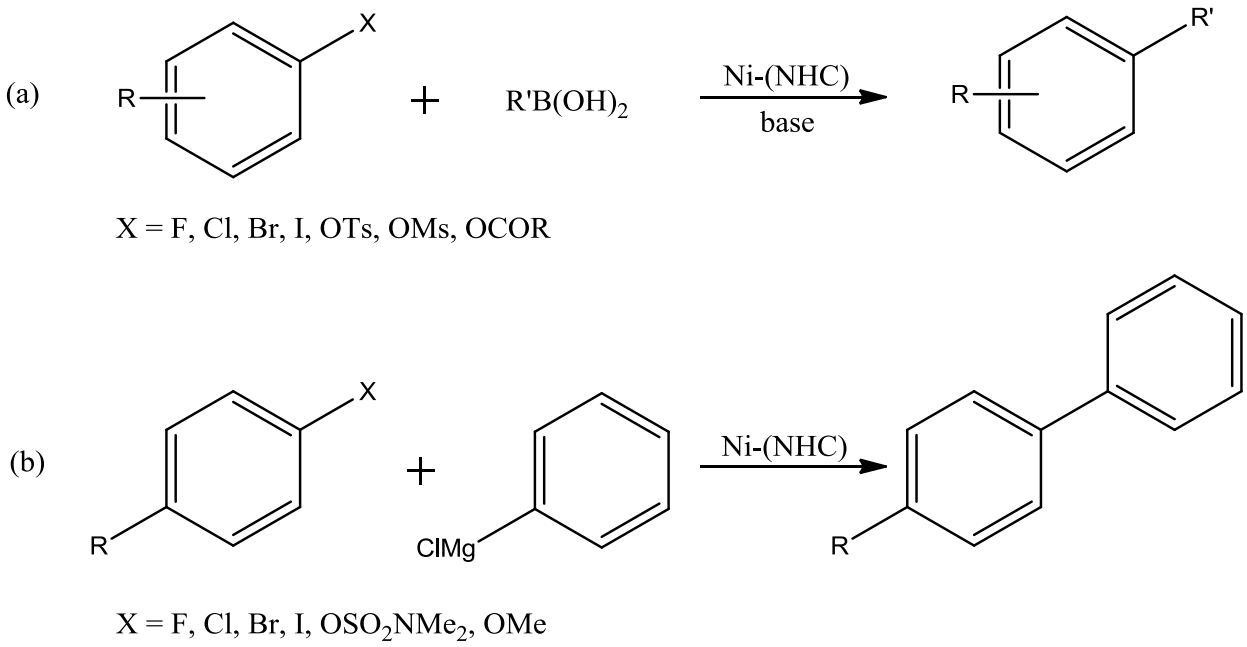

Figure 1.10. The nickel *N*-heterocyclic carbine-catalyzed Suzuki-Miyaura (a), and Kumada (b) coupling reactions [59].

1.4.3. Heterogeneous catalysis

Heterogeneous catalysis involves the use of catalysts which exist in a different physical phase to that of the reactants. In most cases, heterogeneous catalysts are solids in nature, and are employed in gaseous or liquid-mediated reactions. An important feature of such catalysts is the

surface area, which has a direct influence on the reaction rate; for a given mass of a particle: the smaller the particle size, the larger is the surface area [57].

A heterogeneous catalyst has characteristic active sites, which may have resulted from structural features such as crystal defects, and atomic features such as atoms located at the edges of the crystal structure. Active sites may plainly be a metal surface [57]. The mechanism at which the catalytic reaction proceeds depends on the active sites exposure towards the substrate. Therefore, in the absence of necessary active sites, a heterogeneous catalyst can be rendered catalytically-inactive, despite the employed quantity of a catalyst. As a result, the study on the nature of active sites in heterogeneous catalysts is a research field on its own.

Heterogeneous catalysis proceeds in seven prominent steps (Figure 1.11) [62], which are interpreted as follows:

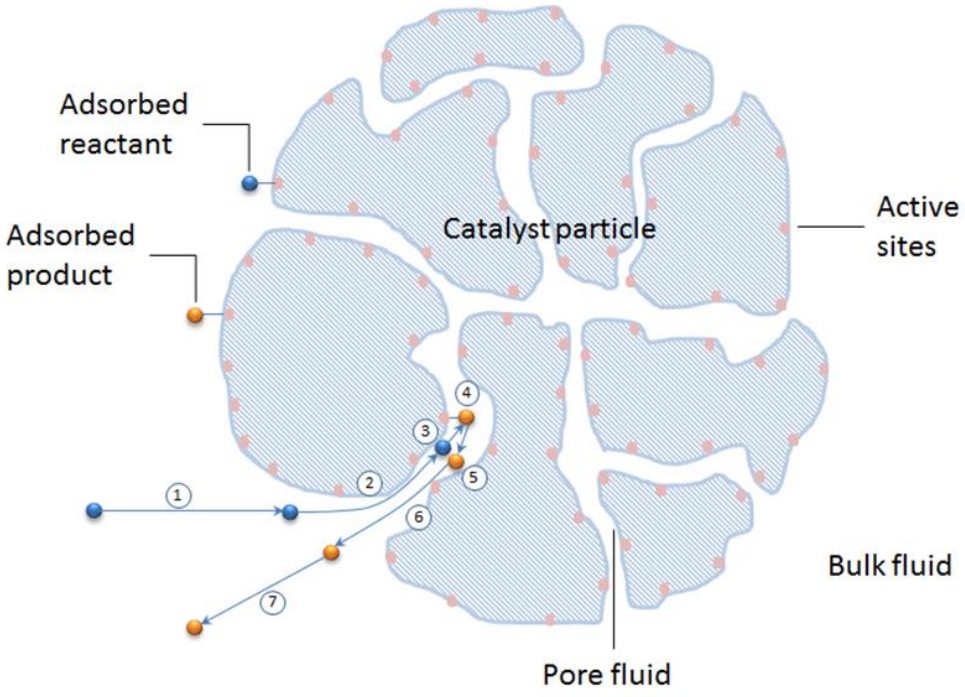

Figure 1.11. Schematic illustration of seven steps occurring in heterogeneous catalysis [62].

1) Transportation of the reactants from the bulk material's surface to an individual catalyst/ particle.
2) Transport of the reactants within the pores of the catalyst's active sites.

3) Adsorption of the reactants on the active site.
4) Conversion of reactants to products on the surface of the catalyst.
5) Desorption of the product from the active site.
6) Transportation of the products off the pores of the catalyst's active sites.
7) Transportation of the products from the individual particle to the bulk material.

Heterogeneous catalysts are well known for their extended recyclable nature, and can be easily separated from the products which are usually of different physical phase/ form. Typically, heterogeneous catalysts are composites, supported on secondary materials, such as high surface area metal oxides and highly porous zeolites [**63,64,65**].

Heterogeneous catalysis is still preferred over homogenous catalysis, due to reasons provided in Table 1.3.

Table 1.3. Advantages and disadvantages of homogeneous over heterogeneous catalysis [**66,67**].

Catalyst form	**Advantages**	**Disadvantages**
Homogeneous	Excellent selectivity (single active site)	Difficult to recover and mostly, not recyclable.
	–	Poor thermal stability
Heterogeneous	Easy to recover and recyclable	Poor to good selectivity (multiple active sites).
	Good thermal stability	–

This study however, intends to exploit heterogeneous catalytic ozonation of cresols to lay a brick in the wall of knowledge that yet remains under construction.

1.5. Scope and objectives of the study

In environmental and green chemistry aspects, an ideal goal would be to synthesize chemical substances that are environmentally benign, through greener synthetic procedures. Some of the most essential syntheses include that of plastics, dyes and pharmaceuticals, which mostly utilize compounds such as toxic cresols[c] as starting materials. Consequently to this, a staggering increase in detecting these compounds as contaminants in the environment will eventually become a serious issue. While in the process of finding alternative starting materials or synthetic protocols, investigations on more efficient and less time consuming treatment processes are of paramount importance.

Therefore, this study intends to explore alternative ways of degrading/ converting these toxic aromatic organic compounds into other value added compounds. These environmental-threatening, toxic compounds such as cresols will be degraded by both uncatalyzed and catalyzed oxidation reactions using molecular ozone (O_3) at ambient temperature and pressure conditions.

The prime objectives are:

- To investigate the new possible oxidative degradation techniques in the oxidation of cresols.
- Oxidative degradation of *m*-, *o*- and *p*-cresols adsorbed on alumina and silica packed column using ozone.
- Oxidative degradation of *m*-, *o*- and *p*-cresols in a glass reactor using ozone in the absence and presence of a catalyst.
- To synthesize the metal (Ni, Fe, Mn and V) doped supports (γ-Al_2O_3, SiO_2 and V_2O_5) and characterize the materials using Fourier-Transform Infrared Spectroscopy (FT-IR), powder X-Ray Diffraction (XRD), Brunauer-Emmett-Teller surface area analysis (BET), Scanning Electron Microscopy (SEM) and Transmission Electron Microscopy (TEM).
- To separate oxidation products obtained from catalytic ozonation using chromatographic techniques, and characterize them using FT-IR, Gas Chromatography coupled with Mass Spectrometry (GC-MS) and Nuclear Magnetic Resonance (NMR) techniques.

[c] When ingested, applied to skin or inhaled in large amounts, they may result in effects such as vomiting, heart damage, burning of skin, eyes and throat to both human and animals

- To study the mechanism involved in the organic transformations.
- To study the conversion and selectivity's involved in the uncatalyzed and catalyzed oxidation reactions.

In a quest to achieve the above mentioned objectives, it is necessary to detail the materials and methods that were utilized. These are presented in the following Chapter 2.

1.6. References

1. Number 59 of 2008: National Environmental Management: South African Waste Act, **2008** (Government Gazette). Retrieved from http://sawic.environment.gov.za/?menu=13. Accessed on 07/06/2014.
2. A. S. Lefohn, D. T. Tingey; The co-occurrence of potentially phytotoxic concentrations of various gaseous air pollutants. *Atmos. Environ.* 18 (11) (**1984**) 2521–2526.
3. R. A. Reinert, W. W. Heck; Effects of nitrogen dioxide in combination of sulfur dioxide and ozone on selected crops. *Studies in Environmental Science* 21 (**1982**) 533–546.
4. G. C. Di Renzo, J. A. Conry, J. Blake, M. S. DeFrancesco, N. DeNicola, J. N. Martin Jr., K. A. McCue, D. Richmond, Abid Shah, P. Sutton, T. J. Woodruff, S. Z. van der Poel, L. C. Giudice; International Federation of Gynecology and Obstetrics opinion on reproductive health impacts of exposure to toxic environmental chemicals. *Int. J. Gynecol. Obstet.* **Article in press**.
5. N. Getoff; Section 5.2. Solid and liquid waste treatment: Decomposition of biological resistant pollutants in water by irradiation. *Radiat. Phys. Chem*. 35 (1–3) (**1990**) 432–439.
6. J. A. Harrison, J. M. Mayne; The oxidation of aromatic organic compounds at a lead dioxide electrode. *Electrochim. Acta*. 28 (9) (**1983**) 1223–1228.
7. M. D. Fumi, G. Parodi, E. Parodi, A. Silva, R. Marchetti; Optimisation of long-term activated-sludge treatment of winery wastewater. *Bioresource Technol*. 52 (**1995**) 45–51.
8. C. Corless, G. Reynolds, N. Graham, R. Perry, T. M. Gibson, J. Haley; Aqueous ozonation of quaternary ammonium surfactant. *Water Res*. 23 (11) (**1989**) 1367–1371.
9. C. Volk, P. Roche, J. Joret, H. Paillard; Comparison of the effect of ozone, ozone-hydrogen peroxide system and catalytic ozone on the biodegradable organic matter of a fulvic acid solution. *Water Res.* 31(3) (**1997**) 650–656.
10. V. S. R. Rajasekhar Pullabhotla, C. Southway, S.B. Jonnalgadda; Ozone initiated oxidation of long chained *n*-alkanes in presence of activated charcoal or silica gel. *React. Kin. Catal. Lett*. 94 (**2008**) 289–299.
11. M. Fielding, J. Haley; Research note: Aqueous chlorination of permethrin. *Water Res*. 23 (4) (**1989**) 523–524.

12. R. Terzian, N. Serpone; Heterogenous photocatalyzed oxidation creosote components: mineralization of xylenols by illuminated TiO_2 in oxygenated aqueous media. *J. Photochem. Photobiol. A: Chem*. 89 (**1995**) 163–175.
13. J. C. Crittenden, R. P. S. Suri, D. L. Perram, D. W. Hand; Decontamination of water using adsorption and photocatalysis. *Water Res*. 31 (**1997**) 411–418.
14. J. Race; The use of ammonia in the chlorination of water. *The Lancet*. 88 (4845) (**1916**) 71–72.
15. K. L. Murphy, R. Zaloum, D. Fulford; Effects of chlorination practice on soluble organics. *Water Res*. 9 (**1975**) 389–396.
16. R. Rosenberg, O. Grahn, L. Johansson; Toxic effect of aliphatic chlorinated by-products from vinyl chloride production on marine animals. *Water Res*. 9 (**1975**) 607–612.
17. F. Fiessinger, J. J. Rook, J. P. Duguet; Alternative methods for chlorination. *Sci. Total Environ.* 47 (**1985**) 299–315.
18. F. Fiessinger, Y. Richard, A. Montiel, P. Musquere; Advantages and disadvantages of chemical oxidation and disinfection by ozone and chlorine. *Sci. Total Environ.* 18 (**1981**) 245–260.
19. Y. Mori, S. Goto, S. Onodera, S. Naito, H. Matsushita; Aqueous chlorination of tetracyclic aromatic hydrocarbons: Reactivity and product distribution. *Chemosphere* 22 (5-6) (**1991**) 495–501.
20. S. T. Summerfelt; Review of ozone processes and applications as an oxidizing agent in aquaculture. *Prog. Fish Cult*. 59 (**1997**) 94–105.
21. V. S. R. Rajasekhar Pullabhotla, S.B. Jonnalgadda; Oxidation of higher alkanes at moderate reaction conditions with ozone in presence of mesoporous materials. *J. Adv. Oxid. Technol*. 11 (**2008**) 445–454.
22. M. B. Rubin; The History Of Ozone. The Schönbein period, 1839-1868. *Bull. Hist. Chem.* 26(1) (**2001**) 40–56.
23. H. J. H. Fenton; Organic chemistry – aliphatic division: Action of ozone. *Annu. Rep. Prog. Chem*. 3 (**1906**) 74–79.
24. A. N. Bashkirov, I. V. Vygodskaya, V. Ya. Kugel, F. I. Novak; oxidation of *m*-cresol acetate in the presence of acetic anhydride (preparation of *m*-hydroxybenzyl alcohol diacetate). *Neftekhimiya* 16 (**1976**) 876–879.

25. A. M. Brambilla, L. Calvosa, A. Monteverdi, S. Polesello, B. Rindone; Ozone oxidation of polyethoxylated alcohols. *Water Res*. 27(8) (**1993**) 1313–1322.
26. P. C. C. Faria, J. J. M. Órfão, M. F. R. Pereira; Activated carbon ozonation of oxamic and oxalic acids. *Appl. Catal. B-Environ*. 79 (**2008**) 237–243.
27. S. Maddila, V. D. B. C. Dasireddy, S. B. Jonnalagadda; Ce-V loaded metal oxides as catalysts for dechlorination of chloronitrophenol by ozone. *Appl. Catal. B-Environ.* 150 – 151 (**2014**) 305–314.
28. P. Lehlola; South African Statistics, **2014/2015**. Retrieved from http://www.statssa.gov.za/wp-content/uploads/2015/10/Annual_Report_2015_Book_1.pdf. Accessed on 25/11/2015.
29. S. Wild, S. Blaine; Townships 'choking to death' on dirty air. http://www.bdlive.co.za/national/science/2013/02/06/townships-choking-to-death-on-dirty-air. Accessed on 06/02/2013.
30. R. S. Picoloto, H. Wiltsche, G. Knapp, P. A. Mello, J. S. Barin, E. M. M. Floresa; Determination of inorganic pollutants in soil after volatilization using microwave-induced combustion. *Spectrochim. Acta B* 86 (**2013**) 123–130.
31. P. C. C. Faria, D. C. M. Monteiro, J. J. M. Órfão, M. F. R. Pereira; Cerium, manganese and cobalt oxides as catalyst for the ozonation of selected organic compounds. *Chemosphere* 74 (**2009**) 818–824.
32. E. C. Chetty, V. B. Dasireddy, S. Maddila, S. B. Jonnalagadda; Efficient conversion of 1,2-dichlorobenzene to mucochloric acid with ozonation catalyzed by V_2O_5 loaded metal oxides. *Appl. Catal. B-Environ.* 117-118 (**2012**) 18–28.
33. M. Umar, F. Roddick, L. Fan, H. A. Aziz; Application of ozone for the removal of bisphenol A from water and wastewater – A review; *Chemosphere* 90 (**2013**) 2197-2207.
34. Y. Zheng, D. O. Hill, C. H. Kuo; Destruction of cresols by chemical oxidation. *J. Hazard. Mater.* 34 (**1993**) 245–260.
35. L. Ritter, K. R. Solomon, J. Forget, M. Stemeroff, C. O'Leary; A review of selected persistent organic pollutants: DDT-Aldrin-Dieldrin-Endrin-Chlordane, Heptachlor-Hexachlorobenzene-Mirex-Toxophene, Polychlorinated biphenyls, Dioxins and Furans. *PCS*. 95(39) (**1995**) 1–145.

36. L. Fomina, L. E. Sansores, R. Salcedo; On the aromaticity of a nanofulvene. *J. Mol. Struct-Theochem.* 362 (**1996**) 257–261.
37. E. Grosjean, D. Grosjean; The reaction of unsaturated aliphatic oxygenates with ozone. *J. Atmos. Chem*. 32 (**1999**) 205–232.
38. A. Moyano, J. C. Paniagua; Distortive properties of sigma and pi-electrons and aromaticity: a semiempirical localized molecular orbital approach. *J. Mol. Struct-Theochem.* 369 (**1996**) 39–52.
39. L. Nyulaszi, P. Varnai, T. Veszpremi; About the aromaticity of the five-membered heterocycles. *J. Mol. Struct-Theochem.* 358 (**1995**) 55–61.
40. A. Cecchetto, F. Fontana, F. Minisci, F. Recupero; Efficient Mn–Cu and Mn–Co–TEMPO-catalysed oxidation of alcohols into aldehydes and ketones by oxygen under mild conditions. *Tetrahedron Lett.* 42 (**2001**) 6651–6653.
41. K. Otsuka, K. Ishizuka, I. Yamanaka; Synthesis of cresols by applying H_2–O_2 fuel cell reaction. *Electrochim. Acta* 37(13) (**1992**) 2549–2552.
42. R. D. Chambers, D. Holling, A. J. Rees, G. Sandford; Microreactors for oxidations using fluorine. *J. Fluorine Chem.* 119 (**2003**) 81–82.
43. P. A. Balakrishnan , A. Arunagiri, P. G. Rao; Ozone generation by silent electric discharge and its application in tertiary treatment of tannery effluent. *J. Electrostat.* 56 (**2002**) 77–86.
44. N. I. Kapustina, G. I. Nikishin; Oxidation of 1-methylcyclobutanol by Pb (IV) and Mn (III) compounds. *Chem. Bull.*, 41 (**1992**) 2189–2192.
45. B. Winther-Jensen, J. Chen, K. West, G. Wallace; Vapor Phase Polymerization of Pyrrole and Thiophene Using Iron(III) Sulfonates as Oxidizing Agents. *Macromolecules* 37 (**2004**) 5930–5935.
46. M. Fontecave, J. L. Pierre; Oxidations by copper metalloenzymes and some biomimetic approaches. *Coordin. Chem. Rev.* 170 (**1998**) 125–140.
47. M. B. Rubin; The history of ozone (part III): *C. D. Harries* and the introduction of ozone into organic chemistry. *Helv. Chim. Acta* 86 (**2003**) 930–940.
48. W. Smith; Principles of ozone generation. Information sheet. Retrieved from http://watertecengineering.com. Accessed on 18/05/2014.
49. G. Gordon; The chemistry and reactions of ozone in our environment. *Prog. Nucl. Energ*. 29 (**1995**) 89–96.

50. R. Criegee; Mechanism of ozonolysis. *Angew. Chem. Int. Edit*. 14 (11) (**1975**) 745–752.
51. S. D. Han, J. D. Kim, K. S. Myung, R. K. Rana, K. C. Singh; Electro-chemical production of ozone using water electrolysis cell of solid polymer electrolyte (SPE). *Indian J. Chem. Technol.* 13 (**2006**) 156–161.
52. Z. B. Guzel-Seydim, A. K. Greene, A. C. Seydim; Use of ozone in the food industry. *Lebensm. Wiss. Technol*. 37 (**2004**) 453–460.
53. M. Cheng, G. Zeng, D. Huang, C. Lai, P. Xu, C. Zhang, Y. Liu; Hydroxyl radicals based advanced oxidation processes (AOPs) for remediation of soils contaminated with organic compounds: A review. *Chem. Eng. J*. 284 (**2016**) 582–589.
54. A. Karci; Degradation of chlorophenols and alkyphenol ethoxylates, two representative textile chemicals, in water by advanced oxidation processes: the state of the art transformation products and toxicity. *Chemosphere* 99 (**2014**) 1–18.
55. R. Andreozzi, V. Caprio, A. Insola, R. Marotta; Advanced oxidation processes (AOP) for water purification and recovery. *Catal. Today* 53 (**1999**) 51–59.
56. M. Pera-Titus, V. García-Molina, M. A. Baños, J. Giménez, S. Esplugas; Degradation of chlorophenols by means of advanced oxidation processes: a general review. *Appl. Catal. B-Environ.* 47 (**2004**) 219–256.
57. A. J. B. Robertson; The early history of catalysis. *Platinum Metals Rev.*, 19(2) (**1975**) 64–69.
58. M. Clugston, R. Flemming; Advanced Chemistry. *Textbook*. (**2001**) pp 270–271.
59. A. P. Prakasham, P. Ghosh; Nickel N-heterocyclic carbene complexes and their utility in homogeneous catalysis. *Inorg. Chim. Acta* 431 (**2015**) 61–100.
60. A. A. Khaskheli, F. N. Talpur, A. S. Demir, A. Cebeci, S. Jawaid; A highly selective whole cell biocatalysis method for the production of two major bioactive conjugated linoleic acid isomers. *Biocatalysis and Agricultural Biotechnology*. 2 (**2013**) 328–332.
61. S. Rasoul-Amini, N. Montazeri-Najafabady, S. Shaker, A. Safari, A. Kazemi, P. Mousavi, M. A. Mobasher, Y. Ghasemi; Removal of nitrogen and phosphorus from wastewater using microalgae free cells in bath culture system. *Biocatalysis and Agricultural Biotechnology*. 3 (**2014**) 126–131.

62. E. Fontes; Modeling approaches in heterogenous catalysis. COSMOL blog, (**2015**). Retrieved from https://www.comsol.com/blogs/modeling-approaches-in-heterogeneous-catalysis/. Accessed on 02/06/2016.
63. M. Sui, L. She; Review on research and application of mesoporous transitional metal oxides in water treatment. *Front. Environ. Scie. Eng*. 7(6) (**2013**) 795–802.
64. M. A. Vuurman, I. E. Wachs, D. J. Stufkens, A. Oskam; Characterization of chromium oxide supported on Al_2O_3, ZrO_2, TiO_2 and SiO_2 under dehydrated conditions. *J. Mol. Catal*. 80 (**1993**) 209–227.
65. W. W. Kaeding, L. B. Young, C. C. Chu; Shape-Selective Reactions with Zeolite Catalysts: IV. Alkylation of Toluene with Ethylene to Produce *p*-Ethyltoluene. *J. Catal*. 89 (**1984**) 267–273.
66. G. Arzamendi, I. Campo, E. Arguinarenã, M. Sancheź, M. Montes, L.M. Gandía; Synthesis of biodiesel with heterogeneous NaOH/alumina catalysts: Comparison with homogeneous NaOH. *Chem. Eng. J*. 134 (**2007**) 123–130.
67. G. Centi, S. Perathoner, T. Torre, M. G. Verduna; Catalytic wet oxidation with H_2O_2 of carboxylic acids on homogeneous and heterogeneous Fenton-type catalysts. *Catal. Today* 55 (**2000**) 61–69.

Chapter 2

MATERIALS AND METHODS

2.0. Reagents

The reagents employed in this study were, potassium iodide (KI, Merck, 99.0%, AR), starch soluble ($(C_6H_{10}O_5)_n$, Merck, GR), potassium dichromate ($K_2Cr_2O_7$, Merck, 99.5%), sodium thiosulphate pentahydrate ($Na_2S_2O_3 \cdot 5H_2O$, Saarchem, 99.5%, AR), vanadium pentoxide (V_2O_5, Merck, 99.0%, extra pure), vanadium(IV) oxide sulfate hydrate ($VOSO_4 \cdot xH_2O$, Aldrich, 97.0%), manganese(II) chloride tetrahydrate ($MnCl_2 \cdot 4H_2O$, Aldrich, 99.0%, Reagent grade), aluminum oxide (γ-Al_2O_3, Aldrich, nanopowder < 50 nm particle size), nickel(II) chloride hexahydrate ($NiCl_2 \cdot 6H_2O$, ACE, 98.0%, AR), Aluminum oxide anhydrous (Al_2O_3, ACE, 98.0%, AR), *m*-cresol (C_7H_8O, Merck, 99.0%, synthesis grade), *o*-cresol (C_7H_8O, Merck, 99.0%, synthesis grade), *p*-cresol (C_7H_8O, Merck, 98.0%, synthesis grade), iron(II) chloride tetrahydrate ($FeCl_2 \cdot 4H_2O$, Aldrich, 99.0%, Reagent plus), Charcoal (C^{12}, Merck, activated powder), Silica gel 60 (SiO_2, Merck, 70-230 mesh ASTM), oxygen gas (O_2, AFROX, 99.99%, medicinal grade), ICP multi-element standard solution IV (1000 mg/L, Merck, 23 elements in diluted nitric acid) and absolute ethanol (Merck, 99.5%).

2.1. Calibration of ozone generator

The ozone gas was produced using the Mighty zone (*mzpv* – 4000, input air pressure = 1 Bar Max.) ozone generator for all ozonation reactions. The iodometric titration was adopted to calibrate the generator and to determine the ozone concentration produced.

The oxygen flow rates and the electrical currents (10 to 100%) applied were the two parameters that were changed to get various outputs of ozone concentration. In the calibration experiments, one of the parameters is kept constant while the other is varied. For example, the oxygen flow rate was kept constant at 0.5 liters per minute (LPM) while varying the electric current from 10 to 100%. The ozone concentration data was further generated by changing the oxygen flow rates and applied currents.

The above mentioned iodometric titration involves potassium iodide (KI) oxidation by ozone, producing a yellow-brown potassium iodate (KIO_3) solution and oxygen (O_2) as shown in Equation 2.1. During the latter, the proportionality between the resultant amounts of KIO_3 to O_3 concentration within the ozone-oxygen mixture enabled determination of the ozone concentration separately. Under acidified conditions (pH = 2), the iodate ion is further oxidized

into an iodide and consequently releases iodine (eq. 2.2). The amount of iodine produced was then determined with sodium thiosulfate ($Na_2S_2O_3$) solution, since the produced iodine amount is proportional to the ozone concentration and can be calculated from the utilized thiosulfate amount during titration (eq. 2.3). The various solutions that were prepared and used in the iodometric titrations are summarized in the Table 2.1.

$$KI + 3\ O_3 \rightarrow KIO_3 + 3\ O_2 \quad (2.1)$$

$$KIO_3 + 5\ KI + 6\ HCl \rightarrow 3\ I_2 + 6\ KCl + 3\ H_2O \quad (2.2)$$

$$2\ Na_2S_2O_3 + I_2 \rightarrow 2\ NaI + Na_2S_4O_6 \quad (2.3)$$

Table 2.1. Summarized preparation of solutions that were used in iodometric titrations.

Solution/ standard	**Acid/ salt**	**Weight/ volume**	**Distilled water**[d]
2% KI	KI	20.0 g	1.0 L
1 M H_2SO_4	H_2SO_4	55.5 mL	1.0 L
Indicator solution	Starch	5.0 g	1.0 L
0.1 M $Na_2S_2O_3$ Stock solution	$Na_2S_2O_3 \cdot 5H_2O$	25.0 g	1.0 L, standardized against $K_2Cr_2O_7$

The sodium thiosulfate solution concentration was determined and verified prior each titrimetric determination of ozone concentration. A solution of 0.0045 M Sodium thiosulfate was prepared by dilution from the stock solution and standardized using standard potassium dichromate solution. Sodium thiosulfate solution was standardized using a dichromate method. Anhydrous potassium dichromate (4.904 g) was dissolved in distilled water and diluted to 1.0 L mark, making a 0.1 M primary standard. Then to 80 mL of distilled water, 10.0 mL of a dichromate standard, 1.0 mL of conc. sulfuric acid and 1.0 g of potassium iodide were added and immediately titrated with 0.1 M sodium thiosulfate solution until a brown-yellow color of the produced iodine almost disappeared, the starch indicator (1.0 mL) was then added and the titration was continued until the blue color (formed during the indicator addition) discharged.

$$Cr_2O_7^{2-} + 6\ I^- + 14\ H^+ \rightarrow 2\ Cr^{3+} + 3\ I_2 + 7\ H_2O \quad (2.4)$$

[d] During the preparation of solutions, distilled water was added up to a 1 L mark on a volumetric flask.

$$2\ S_2O_3^{2-} + I_2 \rightarrow S_4O_6^{2-} + 2\ I^- \quad (2.5)$$

In a glass reactor, typically that of a setup illustrated later in this Chapter, a gaseous mixture of ozone and oxygen from the ozone generator was bubbled for 2 min into an impinger containing 200 mL of KI solution and the oxygen flow rates of 0.5 to 5 LPM and currents of 10 to 100 % were used for this calibration. Then, the absorbed ozone in the KI solution was determined by adding 20.0 mL H_2SO_4 (1.0 M) to acidify the resultant KI solution. The acidified KI solution (20.0 mL) was then titrated with 0.0045 M sodium thiosulfate solution until the brown-yellow color almost disappeared and a starch indicator (2.0 mL) was added, followed by further titration until the blue color vanished. The final ozone concentration was calculated through a series of the following Equations:

Combining eq. 2.1 and 2.2, gives eq. 2.6

$$3\ O_3 + 6\ KI + 6\ HCl \rightarrow 3\ O_2 + 3\ I_2 + 6\ KCl + 3\ H_2O \quad (2.6)$$

Combining eq. 2.6 and 2.3, gives eq. 2.7

$$3\ O_3 + 6\ KI + 6\ HCl + 6\ Na_2S_2O_3 \rightarrow 3\ O_2 + 6\ NaI + 6\ KCl + 3\ H_2O + 3\ Na_2S_4O_6 \quad (2.7)$$

Since the stoichiometry (Eq. 2.7) of O_3 : $Na_2S_2O_3$ is 1 : 2, then

$$N_{(\text{sodium thiosulfate})} \text{ in mol.} = \frac{C\ (\text{Sodium thiosulfate}) \times V\ (\text{Sodium thiosulfate})}{1000} \quad (2.8)$$

$$N_{(\text{ozone})} \text{ in mol.} = \frac{N\ (\text{Sodium thiosulfate}) \times 10\ (\text{dilution factor})}{2} \quad (2.9)$$

$$M_{(\text{ozone})} \text{ in grams} = N_{(\text{ozone})} \times M_{w\ (\text{ozone})} \quad (2.10)$$

$$C_{(\text{ozone})} \text{ in ppm} = M_{(\text{ozone})} \times \textbf{OFR}\ (\text{Oxygen flow rate per 2 min}) \quad (2.11)$$

(**OFR** is 0.500, 0.250, 0.17, 0.125 and 0.100 for 1 to 5 LPM respectively)

Where: N = number of moles, C = concentration, V = volume, M = mass and M_w = molecular weight

The ozone generator calibration curves are shown in Figure 2.1. The optimum ozone concentration produced (0.123 mg/L) at minimum consumption of the oxygen feed gas (0.5 LPM) and electrical power (10%, electric current) was chosen for use in the current study. Figure 2.1(a) displays the various concentrations of ozone obtained when the oxygen flow rates (0.5–5 LPM) were varied against different electric currents (10 to 100%).

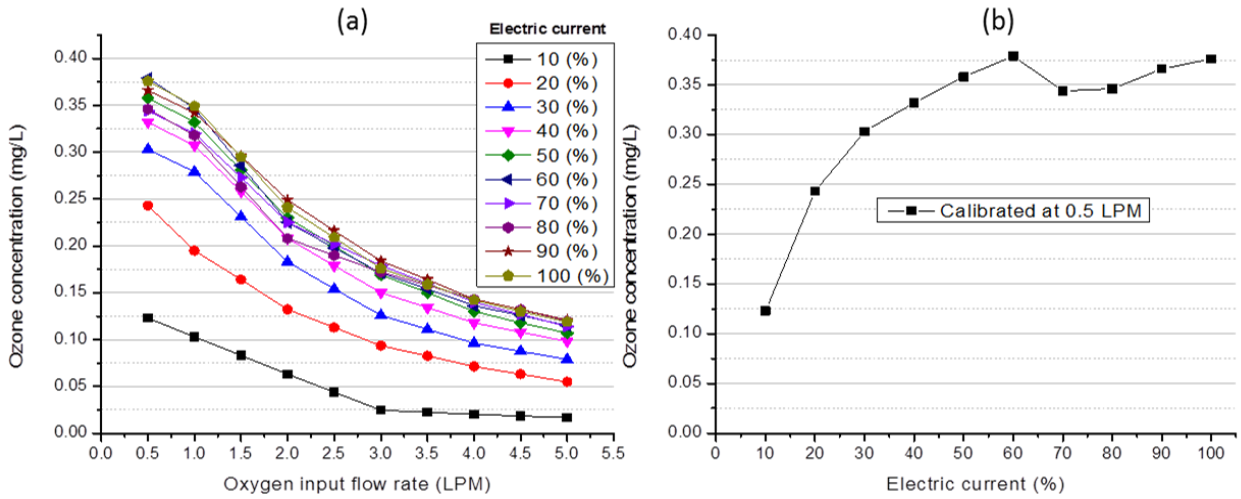

Figure 2.1. Ozone generator calibration results with (a) varied oxygen flow rates from 0.5 to 5 LPM for all percentages of electric currents, and (b) fixed oxygen flow rate at 0.5 LPM for all percentages of electric currents.

It can be noticed that, at low input oxygen flow rate, the ozone concentration is higher than when compared to the high input oxygen flow rate. This is due to the time spent by oxygen molecules inside a corona discharge tube. The lower the flow rate, the longer time the O_2 molecules spend within a tube and the more they react to form plenty of ozone molecules, and the alternative is also true. Figure 2.1(b) indicates the ozone concentrations determined at fixed oxygen flow rate of 0.5 LPM and varied electric currents (10 to 100%). At 0.5 LPM, the concentration of ozone increased with increasing electric currents up till 60% of current where thereafter a slight drop in concentration was observed which later recovered from 80–100% electric currents. The drop in ozone concentration (between 60 and 80% current units) is believed to mark the currents range where ozone dissociation rate is slightly higher than that of its formation.

2.2. Synthesis of catalysts

The metal loaded catalysts were prepared by the wet impregnation method [**1**]. For example, a manganese-loaded γ-alumina catalyst was prepared by dissolving manganese(II) chloride tetrahydrate (0.9005 g) in 25 mL of distilled water making a mixture labeled as MXT 1, and separately a slurry was prepared by dissolving γ-alumina (9.750 g) in 25 mL of distilled water based on the calculations presented from Equation 2.12 to 2.15. The γ-alumina slurry was kept under continuous stirring while MXT 1 was transferred onto it drop-wise and the resultant was stirred for 2 h to achieve a proper dispersion of the metal ions on the surface of the γ-alumina support, followed by evaporation of water at 90–100 ^{o}C. Evaporation step was continued until a thick paste was observed and the latter was further dried in the oven at 90 ^{o}C overnight under air flow. The total yield of the as-synthesized catalyst was 10.0 g and exactly half of it was calcined at 300 ^{o}C for 5 h. The same procedure was repeated for all the other catalyst preparations using different supports (γ-Al_2O_3/ SiO_2/ V_2O_5), changing only the metal precursor salt (Ni, Fe and V salts). The loaded amount of metal was varied from 2.5 to 7.5 wt%. The calculations used to get all the suitable reaction amounts for the catalyst preparation are given from Equation 2.12 to 2.15.

- Salt: $MnCl_2.4H_2O$
- Molecular weight (salt) = 197.90 g/mol.
- Molecular weight of metal (Mn) = 54.95 g/mol.

$$\%\ Mn\ in\ the\ salt = \frac{54.95\ g/mol}{197.90\ \text{g/mol}} \times 100\ \% \qquad (2.12)$$

% Mn = 27.76 %

- Preparation of a 10 g metal-loaded catalyst.
- *i.e.* 2.5 % loaded metal (0.250 g of metal + 9.750 g of support)
- Question: how much of the metal salt is required (RSM) to get 0.250 g of the Mn metal?

$$27.76\ \% = \frac{0.250g\ of\ Metal}{\text{RSM}} \times 100\% \qquad (2.13)$$

$$RSM = \frac{0.250}{27.76} \times 100\% \qquad (2.14)$$

$$RSM = 0.9005\ g\ of\ MnCl_2.4H_2O \quad (2.15)$$

Where **RSM** = required metal salt mass.

To prepare 7.5 % loaded metal catalyst, 0.250 g mass of a metal in equation 2.13 changes into 0.750 g. Thus, the RSM value solely depends on the metal precursor used and the targeted metal loading.

2.3. Characterization techniques

2.3.1. Catalysts characterization

All the catalysts, both as-synthesized and calcined were analyzed using different characterization techniques, such as X-ray diffraction spectroscopy (XRD), Fourier Transform-infrared spectroscopy (FT-IR), inductively coupled plasma-optical emission spectroscopy (ICP-OES), scanning electron microscopy-energy dispersive X-ray spectroscopy (SEM-EDX), transmission electron microscopy (TEM) and Brunauer-Emmet-Teller (BET) surface area analyses.

2.3.1.1. *X-Ray Diffraction Spectroscopy (XRD)*

The XRD characterization of all catalyst samples was performed using powder X-Ray Diffractometer (Bruker AXS Advance D8 diffractometer) with monochromatic Cu Kα (λ = 1.5406 Å) incident radiation at 40 kV and 40 mA at room temperature. The samples were ground into fine powder and placed on a sample holder. The samples were scanned within the high angle 2θ range (10 – 90^o) to get all characteristic diffraction peaks of the materials at 0.1 min^{-1} scan speed and 0.01314 step size increments.

2.3.1.2. *Fourier Transform-Infrared Spectroscopy (FT-IR)*

Fourier transform infrared (FT-IR) spectra were obtained using a Bruker instrument, Tensor 27 FT-IR spectrometer equipped with a standard attenuated total reflectance (ATR) crystal cell. A small amount of a powdered calcined catalyst [metal (Ni, Fe, Mn, and V) loaded γ-Al_2O_3, SiO_2 and/ or V_2O_5] sample was pressed over the crystal (23 units of pressure gauge) for optimal exposure to the evanescent wave. The samples were then scanned over the mid-IR region of 450–4000 cm^{-1}. A similar analytical procedure was repeated for determination of functionalities

within organic species (solvents, substrates and oxidation products) and only few drops of the liquid analyte were suspended over the crystal (no sample pressing required).

2.3.1.3. *Inductively Coupled Plasma-Optical Emission Spectroscopy (ICP-OES)*

The inductively coupled plasma – optical emission spectroscopy (ICP-OES), was used to determine the experimental metal concentration in each metal-loaded catalyst material. The Agilent 700 series ICP equipped with an Agilent 710 OES detector was used to perform the analyses. A multi-element ICP standard solution was diluted into sub-standard solutions of 5, 10, 25, 50 and 100 ppm in concentration. These sub-standard solutions were analyzed on the ICP-OES instrument to plot a calibration curve that was later used to extrapolate the experimental concentrations of the loaded metals within the catalyst samples. The sample preparation was done as follows; A Mn(2.5%)/γ-Al_2O_3 (0.3 g) catalyst sample was weighed and transferred onto a 100 mL volumetric flask, digested in 1:3 aqua regia (HNO_3 : HCl) for one hour and filled up to the mark with distilled water. Two sets of three blank solutions were also prepared, with one set of blanks (distilled water) associated with the standard solutions and the other (30% aqua regia) assigned to the digested catalyst samples. This method was repeated for all catalysts ICP-OES analyses.

2.3.1.4. *Scanning Electron Microscopy-Energy Dispersive X-ray Spectroscopy (SEM-EDX)*

The scanning electron microscope (SEM) analyses were performed using a Carl Zeiss instrument, FE-SEM Sigma VP system (VP-03-67). The SEM was coupled with the energy dispersive x-ray spectroscopy (EDX) detector, an X-Max^N 50, Model (51-XMX1003) from Oxford instruments. Each solid catalyst sample was ground into a very fine powder and a small quantity was pasted on the carbon tape that was placed on a stub (sample holder). The samples were then analyzed under 2.0–10 kV and 10–20 kV accelerating voltage for non-conductive and conductive catalyst samples respectively, to minimize charging. The working distance was varied between 5 and 10 mm. Lastly, the EDX detector was further used to probe into surface composition of each catalyst material, providing both qualitative and quantitative information through surface scanning, point mapping and line mapping analyses.

2.3.1.5. *Transmission Electron Microscopy (TEM)*

A transmission electron microscope (TEM) JEOL 1010 used was used with an accelerating voltage of 100 kV, equipped with Megaview III camera and Soft Imaging System iTEM was used to determine the morphology. The samples were ground into fine powder and dispersed in ethanol/ hexane solvent and sonicated for 20 minutes to minimize clustered particles. A drop of a catalyst sample was then placed over a Formvar-coated copper grid (150 mesh) and dried at room temperature before the analysis.

2.3.1.6. *Brunauer-Emmet-Teller surface area analyzer (BET)*

The surface areas of calcined catalyst samples were determined using a Brunauer-Emmet-Teller (BET) surface area analyzer [2]. The samples were first degassed at 250 ^{o}C overnight under N_2 flow in Micrometrics flow prep 060 as a form of pretreatment. The latter was then analyzed in a fully automated single and/ multiple-point Micrometrics Gemini 2360 BET instrument under liquid N_2 conditions. This analysis was done to relate the surface areas of herein used catalysts to the substrates conversion and product selectivities since the surface of a solid catalyst material is said to have an effect on its activity.

2.3.2. Oxidation products characterization

Different analytical techniques were used to separate and characterize the oxidation products. This includes gas chromatography coupled with mass spectrometry (GC-MS), thin layer chromatography (TLC), gravitational column chromatography, high performance liquid chromatography (HPLC-UV) and the Fourier Transform-infrared spectroscopy (FT-IR).

2.3.2.1. *Gas Chromatography coupled with Mass Spectrometer (GC-MS)*

An Agilent, 7890A GC system coupled with a 5975C VL MSD (with Triple-Axis Detector) was used to analyze the oxidation products and to calculate the selectivity and conversion percentages in the catalytic ozonation reactions. An Agilent 190915-433: 325 ^{o}C: 30 m × 250 μm × 0.25 μm GC column was used and programmed as follows: The initial temperature was kept at 60 ^{o}C for 4 min and then constantly increased by heating at a rate of 4 ^{o}C/min, all done at an injection temperature and pressure of 250 ^{o}C and 29.127 kPa, respectively. A sample volume of 1.0 μL was manually injected using a 10.0 μL Agilent syringe and a 5975 Data analysis software

was used to analyze both the mass spectra and gas chromatograms. The helium (He) and hydrogen (H_2) gases were used as a GC mobile phase and the MSD flame gas, respectively (both purchased from AFROX).

2.3.2.2. *High performance liquid chromatography (HPLC)*

The HPLC (reverse-phase chromatography) analyses were performed using an Ultimate 3000 HPLC system from Dionex, with a built-in degasser, pump, auto-sampler, column compartment and a diode array detector (UV). The chromatograms were plotted and analyzed using the Chromeleon software (version 6.8.0). An Accentis ® Express C18 column of 10.0 cm length, 4.6 mm width and 2.7 μm particle sizes was utilized and its temperature was set to 40 ^{o}C. The samples were first dissolved in 0.1% phosphoric acid (1.0 mL H_3PO_4 in 1000 mL of distilled water) with a dilution factor of 1:20 (0.05 mL sample: 0.95 mL acidified water), and then introduced into the HPLC column. The mobile phase used was composed of the acetonitrile and 0.1% phosphoric acid with the initial solvent composition of 5:95, respectively.

Table 2.2. The gradient-elution curve conditions used in the separation of oxidation products.

Retention time (min)	**Flow rate (mL/min)**	**0.1% phosphoric acid (%)**	**Acetonitrile (%)**
0.0	1	95.0	5.0
0.0	1	95.0	5.0
8.0	1	95.0	5.0
35.0	1	20.0	80.0
37.0	1	95.0	5.0

A gradient-elution curve was constructed through a series of trial and error separation experiments, and this was done to obtain the conditions (Table 2.2) that gives a proper chromatogram with clear peak separation of the oxidation products for all crude samples. The HPLC instrument was set-up to auto-inject 50.0 μL (from a 1.0 mL vial) per analysis during the analyses.

Table 2.3. A list of samples analyzed on the High Performance Liquid Chromatography.

Sample label	Parent substrate	Reaction type	Other details
Sample A	*m*-cresol	Column	Adsorbed on alumina, 3 h
Sample B	*o*-cresol	Column	Adsorbed on alumina, 3 h
Sample C	*p*-cresol	Column	Adsorbed on alumina, 3 h
Sample D	*m*-cresol	Column	Adsorbed on silica, 3 h
Sample E	*o*-cresol	Column	Adsorbed on silica, 3 h
Sample F	*p*-cresol	Column	Adsorbed on silica, 3 h
Sample G	*m*-cresol	Column	Adsorbed on alumina, 5 h
Sample H	*o*-cresol	Column	Adsorbed on alumina, 5 h
Sample I	*p*-cresol	Column	Adsorbed on alumina, 5 h
Sample J	*m*-cresol	Column	Adsorbed on silica, 5 h
Sample K	*o*-cresol	Column	Adsorbed on silica, 5 h
Sample L	*p*-cresol	Column	Adsorbed on silica, 5 h
Sample M	*m*-cresol	Reactor	Gamma alumina catalyzed, 24 h
Sample N	*o*-cresol	Reactor	Gamma alumina catalyzed, 24 h
Sample O	*p*-cresol	Reactor	Gamma alumina catalyzed, 24 h
Sample P	*o*-cresol	Reactor	Uncatalyzed, 24 h
Sample Q	*p*-cresol	Reactor	Uncatalyzed, 24 h

2.3.2.3. *Aldehydes and ketones test (Brady's test)*

The crude samples (Table 2.3) from all three substrates were further subjected to the test of aldehydes and ketones, referred to as Brady's test [3]. In the application of this test, the carbonyls contained in a product mixture were derivatised with 2,4-dinitrophenyl hydrazine (DNPH) in methanol and the resulting hydrazone complex (Figure 2.2) was analyzed using gradient elution reversed phase HPLC with a UV detector at 370 nm using a C18 column [3].

The instrument was pre-calibrated using isovaleraldehyde (3-methylbutanal) as an external standard prepared in ultrapure water containing different concentrations[e] of the compound.

Figure 2.2 illustrates the mechanism of the ketones and aldehydes test. A carbonyl component (A) from the product mixture gets attached to nitrogen (1) of DNPH, resulting in a hydrazone complex. The resultant complex is then eluted at a retention time characteristic to the number of carbons that makes up a component (A). The hydrazone complexes formed during this test varies in polarity based on the length of a newly attached carbon chain, *i.e.* C3, C4, C5 *etc*. are eluted at different times.

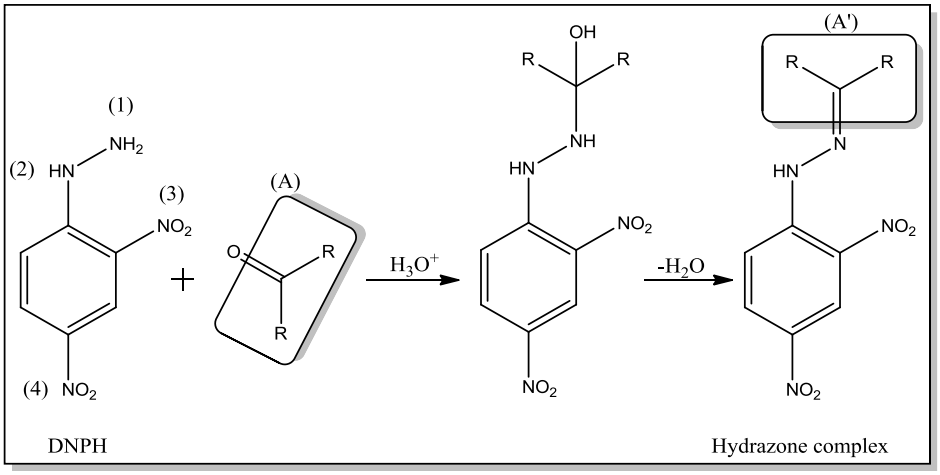

Figure 2.2. A typical ketones and aldehydes test (Brady's test) reaction mechanism.

This test was basically conducted in order to determine the presence of the aldehyde/ketone products in the sample and test results came out positive for all samples (Table 2.4), indicating the presence of aldehydes and ketones in the samples.

Table 2.4. Concentrations of carbonyl components detected from the product mixtures through Brady's method (on HPLC).

Sample	**Concentration (mg/kg as CO)**
Sample A	160.13

[e] The standard has specifically been design by Sasol R&D and we have no right to share the exact concentrations of isoveraldehyde within the standard.

Sample B	99.97
Sample C	61.60
Sample D	65.83
Sample E	94.58
Sample F	69.84
Sample G	130.43
Sample H	107.84
Sample I	56.83
Sample J	130.03
Sample K	96.26
Sample L	70.88
Sample M	78.50
Sample N	118.80
Sample O	86.62
Sample P	118.85
Sample Q	328.91

The Table 2.4 serves to confirm the presence and the concentrations of carbonyl functionalized components within the products mixtures. Based on the DNPH standard, the majority of the carbonyls detected were formaldehyde and acetaldehyde. There were other components that could not be identified; they were not acetone, propionaldehyde (propanal), C4 ketones/ aldehydes or C5 ketones/ aldehydes.

2.3.2.4. *Thin Layer and Column Chromatography*

The thin layer chromatography (TLC) technique was used to find a suitable solvent system that gives an adequate separation of the fractions from the product mixture's sample. A flow chart in the Figure 2.3 illustrates the typical order in which the separations were conducted. A product mixture (sample collected after 24 h of an oxidation reaction of *m*-cresol) was first concentrated by removing excess EtOH through rota-evaporation, this concentrate was then ran through a dry-

flash chromatogram, first using 100% MeOH to attain **concentrate 1** and later with 6 : 4 (Cyhex : EA) to get **concentrate 2** (with SiO_2 as a stationary phase).

Spotted on a silica coated TLC plate, products contained in **concentrate 1** were observed to be UV (254 and 366 nm, wavelengths) inactive whereas the oxidation products contained in **concentrate 2** showed high UV activity, suggesting the presence of molecules with conjugated double bonds. The **concentrate 1** was then put aside and the focus was turned to **concentrate 2** since the ozonation products of cresols that have been reported mainly contain compounds with Sp^2-carbons [**4**]. The suitable solvent systems (Table 2.5) that could separate the fractions contained in **concentrate 2** were found by a trial-and-error procedure. **Fractions 1**, **2** and **3** were collected, however, these fractions still contained a mixture of products and at this stage, fractions were too minute for further chromatographic separations. The same was also observed in an attempt to separate oxidation products of the *o*- and *p*-cresol.

The separation was then declared unsuccessful and thus the targeted NMR analyses of individual products could not be proceeded with. The experienced difficulty in separating oxidation products from the O_3 mediated oxidation of cresols could be the reason why approaches of identifying these products by techniques like GC-MS have been employed in literature [**4**]. Normally, the comparison of corresponding standards (purchased) with MS detected oxidation products is done. Thus, the GC-MS analysis was used to identify the oxidation products of cresols in the present work.

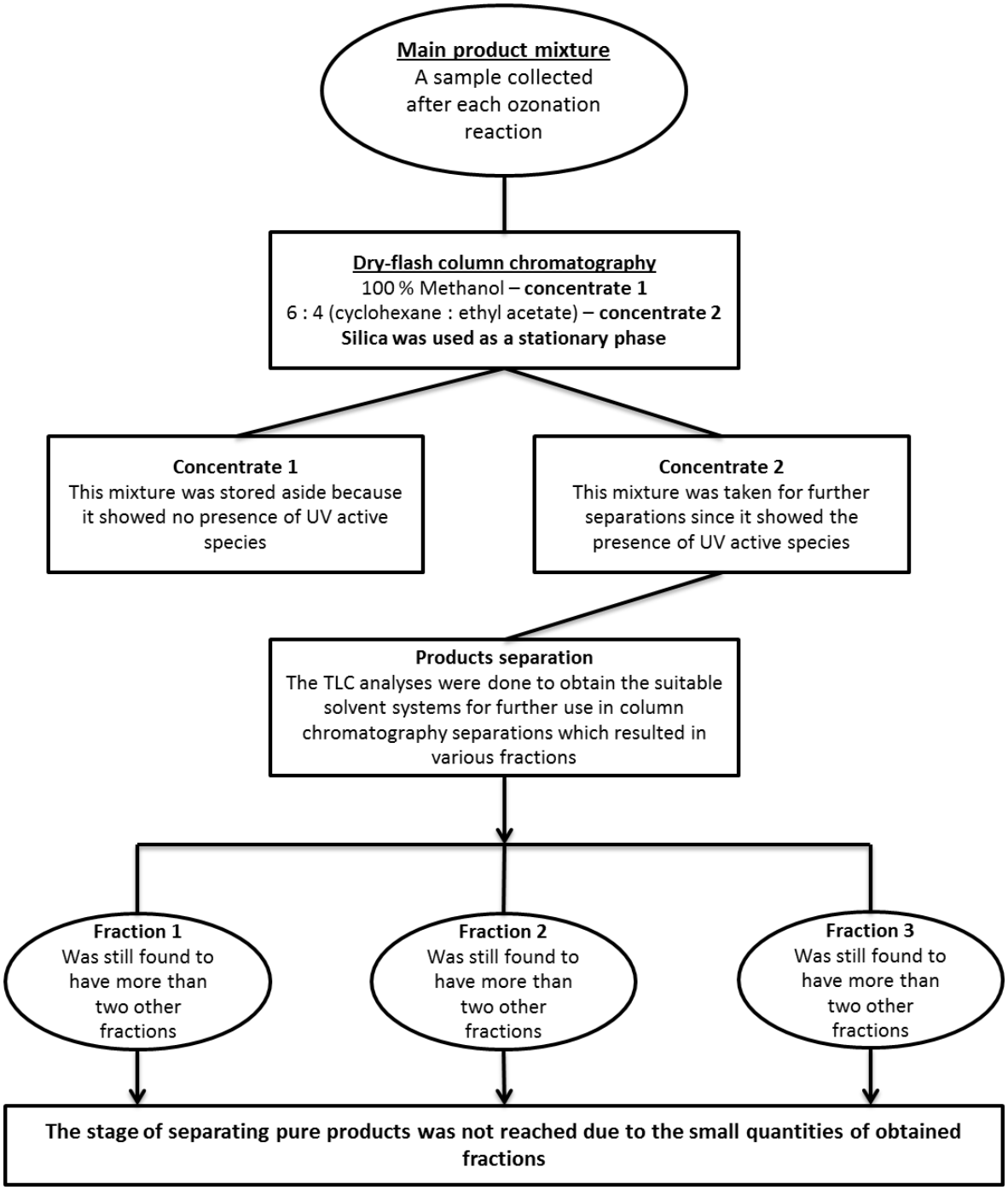

Figure 2.3. A flow chart showing a typical order in which a chromatographic separation of the oxidation products from each substrate was executed.

Up to two different solvent systems were required to separate each set of three fractions from the concentrates of both the *m*- and *o*-cresol, as shown in Table 2.5 (**entry 1** and **2**) whereas four

different solvent systems were required to achieve the same for the *p*-cresol (**entry 1–4**). The dashes (–) seen in **entry 3** and **4** under *m*- and *o*-cresol concentrates simply mean that, no other solvent system was further utilized than the ones presented in **entry 1** and **2**, during their products separation.

Table 2.5. The solvent systems that were used in column chromatography technique for each concentrate separation.

Entry No	***m*-cresol concentrate 1**	***o*-cresol concentrate 1**	***p*-cresol concentrate 1**
1	100% [f]DCM	100% DCM	1:9 (EA:Cyhex)
2	0.5:9.5 ([g]MeOH:DCM)	1:0.5:7.5 ([h]EA:MeOH:DCM)	2:8 (EA:Cyhex[i])
3	–	–	3:7 (EA:Cyhex)
4	–	–	5:2.5:2.5 (Cyhex:MeOH:EA)

2.4. Ozonation reactions

The character of O_3 as a highly reactive oxidant in the oxidation of most of the aromatic organic compounds prompted us to use O_3 as an oxidant in this study. The aromatic organic compounds (*m*-, *o*- and *p*-cresol) were ozonated in two different set-ups, glass column and glass reactor (without and with the use of a catalyst).

2.4.1. Glass column reactions

A dry metal oxide (γ-Al_2O_3/ SiO_2) adsorbent was charged onto a graduated glass column and measured to a height of 5.0 mL, and it was then discharged into a 50.0 mL glass beaker and mixed with 3.0 mL of a substrate (*m*-, *o*- or *p*-cresol). The semi-dry slurry-like mixture was then transferred back onto the glass column. The cotton wool was used as a plug at the bottom of the column to avoid leakage as illustrated in Figure 2.4. Ozone was introduced into the column

[f] Dichloromethane (DCM)
[g] Methanol (MeOH)
[h] Ethyl acetate (EA)
[i] Cyclohexane (Cyhex)

through the bottom of the column at room temperature. The substrate was oxidized for various time intervals (1, 3 and 5 h). The excess and/or unreacted ozone was allowed to pass through a series of KI traps, which consists of 2% KI solution. The series of potassium iodide solution (KI)-traps were used to convert the unreacted ozone back into its parent O_2 allotrope and this whole reaction setup was done in a fume hood.

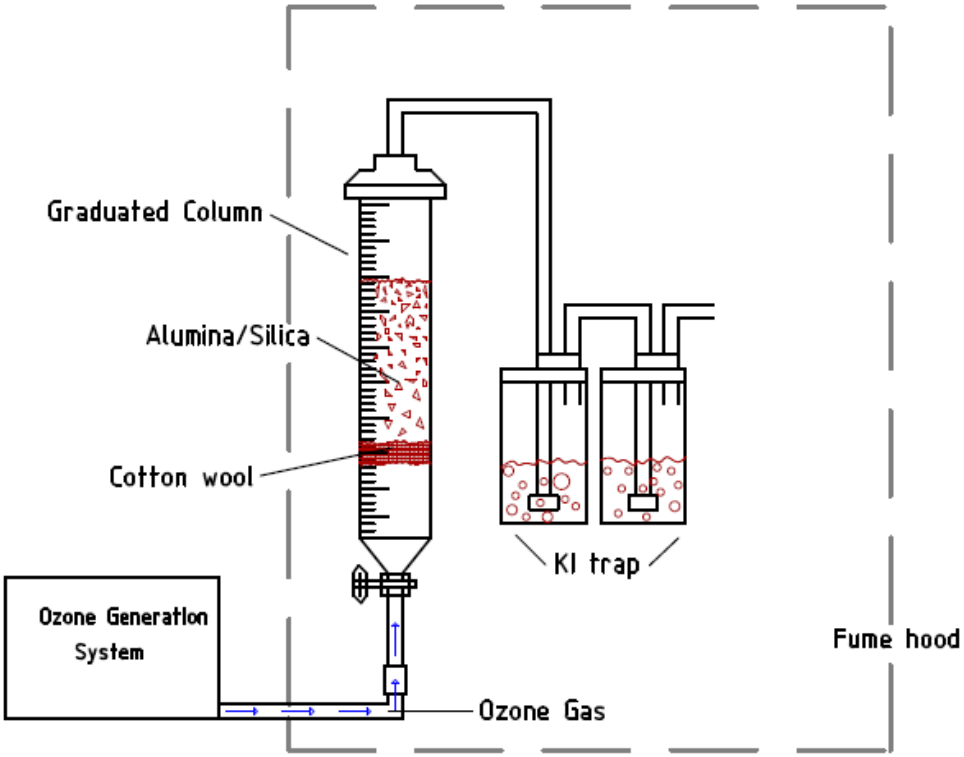

Figure 2.4. Reaction setup for the column based ozonation reactions.

2.4.2. Non-catalytic ozonation reactions using glass a reactor

The *m*-cresol substrate (25.0 mL) was ozonated under ambient reaction conditions in a glass reactor/ impinger (dimensions: height = 18.0 cm and outer diameter = 2.5 cm) equipped with a magnetic stirrer bar. The ozone gas was bubbled into the *m*-cresol substrate through a porous bubbler with porosity 2. The reaction setup is shown in Figure 2.5. The unreacted and/ or excess of ozone was destroyed in the series of KI-solutions traps (eq. 2.1). All the reactions were

performed in a fume hood. Samples from each reaction were drawn at various time intervals from 3, 6, 9, 12, 15, 18, 21 and 24 h. All the resultant products were dissolved in ethanol and stored in labeled glass vials for chromatographic separations and further analyses. The product mixture from each drawn sample was then analyzed using GC-MS. The similar procedure was adopted for the *o*- and *p*-cresol substrates in the absence and presence of different catalysts.

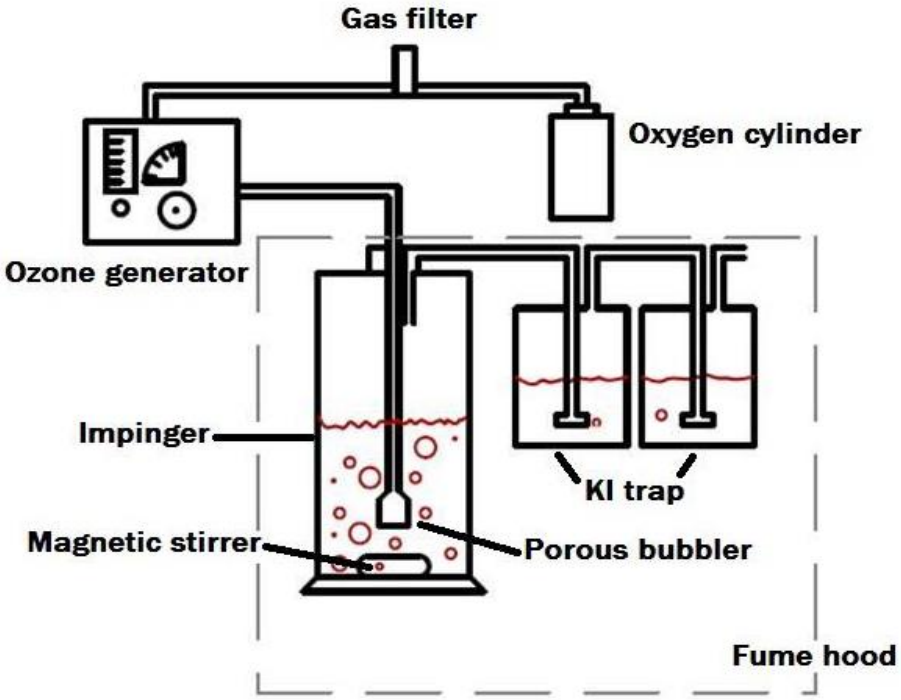

Figure 2.5. Reaction setup for the ozonation reactions in the glass reactor.

2.4.3. Catalytic ozonation reactions using glass reactor

Catalytic ozonation reactions, "catazone" were performed in the glass reactor set-up as shown in Figure 2.5. A mass of 0.250 g of activated charcoal catalyst was weighed and quantitatively transferred into a glass reactor equipped with a magnetic stirrer bar. A volume of 25.0 mL substrate was then added into the reactor. The ozone gas was bubbled into the substrate through a porous bubbler with porosity 2. The use of magnetic stirrer can facilitate the uniform distribution of a catalyst and the ozone gas within a substrate (*m*-, *o*-, and *p*-cresol). The sample aliquots were collected in every 3 h time intervals of a 24 h reaction. All the resultant product mixtures were dissolved in ethanol and stored in labeled glass vials for chromatographic separations and further

analyses. The similar procedure was repeated for all the catalytic ozonation reactions of cresol isomers (*m*-, *o*-, and *p*-cresol) using various supports (γ-Al_2O_3, SiO_2 and V_2O_5) and metal (Ni, Fe, Mn and V) loaded γ-Al_2O_3, SiO_2 and V_2O_5 catalyst materials. Each of the collected samples in absolute ethanol was filtered four times through a Whatman 42 filter paper to remove the solid catalyst from the crude sample.

2.5. Data presentation and statistical analysis

The current study is more on comparison basis, *i.e.* different metals loaded on one support for catalytic oxidation of three different cresol isomers, separately. Therefore, the spectroscopy (XRD & FT-IR) acquired data is herein presented graphically, where line graphs are used. These graphs (spectra) are normalized and then stacked for simplicity. Other spectroscopy results (ICP-OES & EDX) are tabulated and where possible, presented in images. Furthermore, the microscopy (SEM & TEM) results are herein reported in images and where necessary and possible, the particle sizes were measured using ImageJ software to get average/ mean particle sizes from the images.

In the catalysis Chapters (4 & 5), the line graphs were also used, providing essential information on both the activity of the employed catalyst and the reactivity of the cresol isomer towards ozone in the absence and/ or presence of a catalyst. The data used to plot the later graphs was acquired by GC-MS and is also tabulated in text and/ or Appendix Sections in this work. Key information gathered from GC-MS data include the amounts of oxidized cresol isomer per unit time (percentage conversion) and amounts of catalyst dependent oxidation products that are formed over time, per substrate (percentage selectivity).

As highlighted earlier, this study proceeds in a more comparison based approach, and determining the most active catalyst by comparing percentage conversions of a substrate yielded by different catalysts at a particular time seems statistically unmerited. For example, if catalyst A & B were used in the oxidation of *m*-cresol for 24 h and catalyst A outperformed B from 3–18 h in percentage conversions, B would be the most active catalyst at 24 h of reaction if it has converted more of the substrate than A. Some literature-based evidence of the latter example can be seen in a study done by Faria *et al*. [5], in a catalytic oxidation of sulfanilic acid (5–240 min), the Ce-Mn-O catalyst is dominantly efficient for more than half the reaction duration but credit

of high efficiency is given to the Ce-Co-O catalyst which outperforms the Ce-Mn-O catalyst at final stages of the reaction. However, this argument may be more subjective than objective.

Considering the later argument, the activity of each catalyst was first discussed at a specific reaction time (24 h) in comparison with other catalysts. Then, the activities of each catalyst at 3, 6, 9, 12, 15, 18 and 24 h were added and averaged to get the mean catalyst activity and deduce catalyst activity order in the oxidation of each cresol isomer. The average catalyst activities were surmised from average percentage conversion bar-graphs of cresol isomers. Though not intrinsically termed 'average percentage conversion' but, activities of different catalysts have previously been compared based on the catalysts ability to convert the substrate (on average). In the work of Chetty *et al*. [**6**], the 5% V_2O_5 loaded catalysts were concluded to be the most active in the oxidation of 1,2-dichlorobenzene compared to 1% V_2O_5 loaded catalysts, which was true, but only when the average percentage conversions of the substrate are considered.

Considering average percentage conversions/ catalytic activity could help simplify comparison discussions such as in comparing two catalysts/ catalytic routes that leads to complete mineralization of the substrate, the catalyst that gives a high average percentage conversion of the substrate can be credited as the most efficient. For example, the use of ozone with a catalyst can be concluded to be the most efficient combination to oxidize MeOH than the use of oxygen with catalyst under conditions studied by Almquist *et al*. [**7**], though both these combinations led to mineralization of MeOH. The later conclusion can be readily made if average percentage conversions of MeOH are considered.

The next Chapter, Chapter 3 shows the characterization catalyst materials that were synthesized using materials and methods that are presented in the current Chapter. It further discusses some significant findings obtained during different characterization techniques.

2.6. References

1. (a) G. Bruhns; Standardization of iodine and thiosulfate solutions. *Zeit. Anorg. Chem.*, 49 (**1906**) 277–283.
   (b) P. Jannasch, W. Gottschalk; Use of ozone in quantitative analysis. *J. pr. Chem.*, 73 (**1906**) 497–519.
2. S. Brunauer, P. H. Emmett, E. Teller; Adsorption of gases in multimolecular layers. *J. Am. Chem. Soc*. 60 (2) (**1938**) 309–319.
3. O. S. Brady, G. V. Elsmie; The use of 2:4-Dinitrophenylhydrazine as a reagent for aldehydes and ketones. *Analyst.* 51 (**1926**) 77–78.
4. M. C. Valsania, F. Fasano, S. D. Richardson, M. Vincenti; Investigation of the degradation of cresols in the treatment with ozone. *Water Res.* 46 (**2012**) 2795–2804.
5. P. C. C. Faria, D. C. M. Monteiro, J. J. M. Órfão, M. F. R. Pereira; Cerium, manganese and cobalt oxides as catalysts for the ozonation of selected organic compounds. *Chemosphere* 74 (**2009**) 818–824.
6. E. C. Chetty, V. B. Dasireddy, S. Maddila, S. J. Jonnalagadda; Efficient conversion of 1,2-dichlorobenzene to mucochloric acid with ozonation catalyzed by V_2O_5 loaded metal oxides. *Appl. Catal. B-Environ.* 117–118 (**2012**) 18 –28.
7. C. B. Almquist, E. Sahle-Demessie, S. C. Sehker, J. Sowash; Methanol oxidation using ozone on titanium-supported vanadia catalyst. *Environ. Sci. Technol*. 41 (**2007**) 4754–4760.

Chapter 3

CHARACTERIZATION OF CATALYST MATERIALS

3.0. Introduction

It is essential to understand both the physical and chemical nature of a catalyst, as these parameters determines its activity to a great extent. This chapter gives a discussion of both qualitative and quantitative analyses results that were attained using various spectroscopic and microscopic techniques. The characterization and analytical techniques used, range from powder X-ray diffraction (XRD), Fourier Transform-Infrared (FT-IR) spectroscopy, inductively coupled plasma-optical emission (ICP-OES) spectroscopy, scanning electron microscopy (SEM), energy dispersive X-ray (EDX) spectroscopy, transmission electron microscopy (TEM) to Brunauer-Emmet-Teller (BET) surface area analyzer. All the metal loaded γ-Al_2O_3, SiO_2 and V_2O_5 calcined catalysts were characterized, with metal dopants being Ni, Fe, Mn and V.

3.1. Powder X-ray diffraction results

The XRD characterization technique was used in order to understand the underlying compositional and structural information of the calcined metal (Ni, Fe, Mn, V) loaded γ-Al_2O_3, SiO_2 and V_2O_5 catalysts, the results are given below.

3.1.1. X-ray diffraction results for various metals loaded on γ-Al_2O_3 support

Aluminas, especially gamma alumina, have been widely used as an adsorbent, catalyst and catalyst support owing to its characteristically large surface area, pronounced acidity and high porosity [**1–3**]. Figure 3.1a, shows a diffractogram can be assigned to pure γ-Al_2O_3 with a cubic crystal structure (JCPDS 00-010-0425), space group *Fd-3m* and lattice constants $a = b = c =$ 0.5586 nm. This unique alumina form is reported to be based on an *fcc* structural arrangement with an ABCABC stacking of oxygen atoms, ideally, it is defined by a formula $Al_{21+1/3}X_{2+2/3}O_{32}$ where X is a vacancy [**4,5**]. The characteristic γ-Al_2O_3 diffraction peaks (111), (220), (311), (222), (400), (511) and (440) at 2θ angles of 19.13^o, 32.37^o, 37.47^o, 40.92^o, 45.86^o, 62.65^o and 67.20^o, respectively were observed. Furthermore, at 2.5 wt.% loading of Ni, Fe, Mn and V metal loadings (Figure 3.1a), there were no diffraction peaks distinguishing the metals or their oxides that were detectable (even though these metals or their oxides are there). However, at 7.5 wt.% of metal loading on γ-Al_2O_3 (Figure 3.1b), the Fe-loaded catalyst revealed the presence of the iron oxide phase through diffraction peaks (104), (110), (024), (116), (214) and (300) at 2θ

values equal to 33.53°, 36.00°, 49.77°, 54.29°, 62.67° and 64.12° respectively. This diffraction pattern can be assigned to Fe_2O_3 called Hematite (JCPDS 01-089-8104), with a rhombohedral crystal structure and a space group of *R-3c* [6,7]. In both sets of catalysts (Figure 3.1a-b), two diffraction peaks (111) and (222) from the γ-Al_2O_3 support seem to have vanished in all other calcined metal-loaded catalysts. These peaks however, were not lost on the uncalcined counterparts (Figure A1, p. 132) which strongly suggests the significant sensitivity of the γ-Al_2O_3 crystalline phase towards the calcination temperature chosen in this work (300 °C).

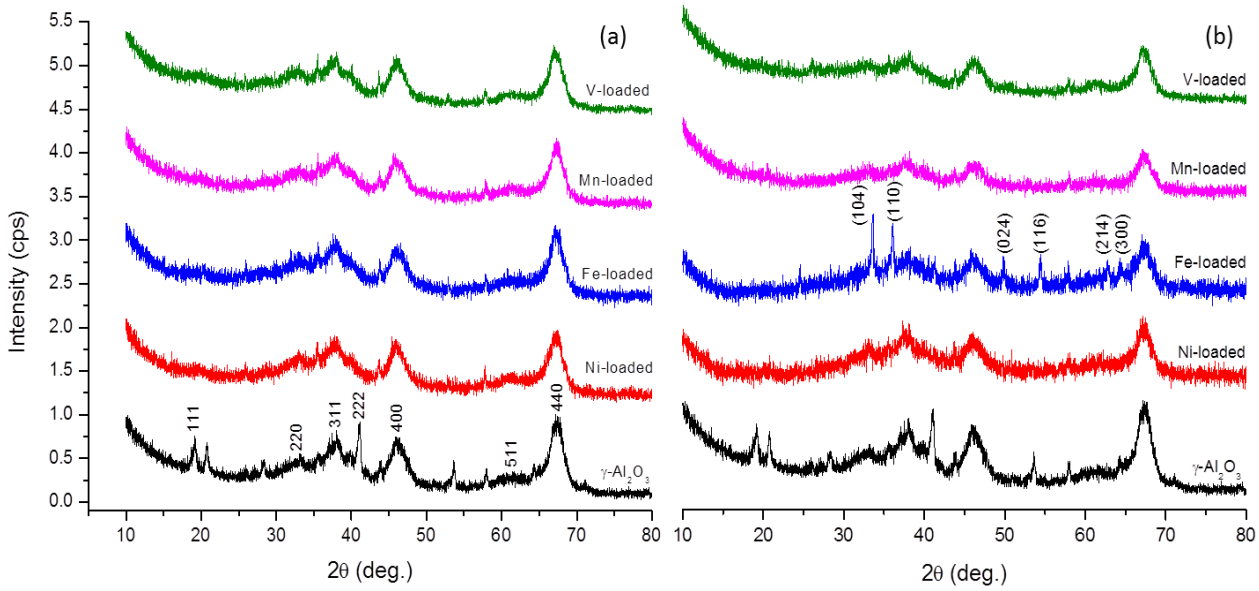

Figure 3.1. X-ray diffractograms of (a) γ-Al_2O_3 support, Ni(2.5%)/γ-Al_2O_3, Fe(2.5%)/γ-Al_2O_3, Mn(2.5%)/γ-Al_2O_3, V(2.5%)/γ-Al_2O_3 and (b) γ-Al_2O_3 support, Ni(7.5%)/γ-Al_2O_3, Fe(7.5%)/γ-Al_2O_3, Mn(7.5%)/γ-Al_2O_3, V(7.5%)/γ-Al_2O_3 calcined catalysts.

3.1.2. X-ray diffraction results for various metals loaded on SiO_2 support

Silica supported catalysts were also studied, and the subsequent X-ray diffractograms are shown in Figure 3.2. In both Figures 3.2a and 3.2b, the amorphous silica support with a characteristic broad diffraction band at 2θ = 23.23° was observed [8]. It can be noticed that, at 2.5 wt.% of loaded Ni, Mn and V metal contents (Figure 3.2a), there were no detectable crystalline phases on the surface of the support except for the Fe-loaded SiO_2 catalyst. This is believed to be due to the

relatively low crystallinity of the resultant oxides of the aforementioned metals as compared to those of iron (Fe). The 2.5 wt.% Fe-loaded diffractogram displays diffraction peaks (104), (110), (024) and (116) at 2θ angles 33.39°, 35.80°, 48.63° and 54.28° respectively. This data can be indexed to the rhombohedral crystal phase of Fe_2O_3 (JCPDS 01-089-8104) with an *R-3c* space group and lattice constants *a* = 0.5023 nm, *b* = 0.5023 nm and *c* = 0.5421 nm [**6,7**]. The increase in the Fe content on the support resulted in more diffraction peaks being observed, this can be seen in Figure 3.2b of the Fe-loaded catalyst at 7.5 wt.% loading of Fe. Moreover, at 7.5 wt.% metal loadings (Figure 3.2b), an unidentified Ni_xO_n diffraction peak was detected and the Mn-loaded catalyst provided two peaks (101) and (103), supposedly representing a tetragonal hausmannite Mn_3O_4 (JCPDS 00-24-0734) [**9**]. No diffraction peaks were recorded for both vanadium (V) and its oxides in all V-loaded SiO_2 catalysts.

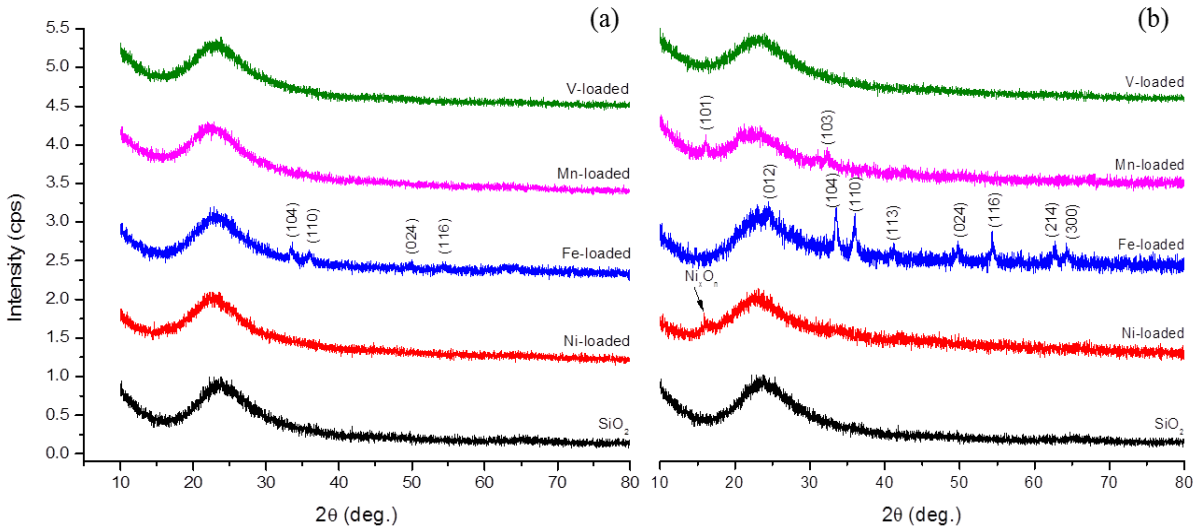

Figure 3.2. X-ray diffractograms of (a) SiO_2 support, Ni(2.5%)/SiO_2, Fe(2.5%)/SiO_2, Mn(2.5%)/SiO_2, V(2.5%)/SiO_2 and (b) SiO_2 support, Ni(7.5%)/SiO_2, Fe(7.5%)/SiO_2, Mn(7.5%)/SiO_2, V(7.5%)/SiO_2 calcined catalysts.

3.1.3. X-ray diffraction results for various metals loaded on V_2O_5 support

The phase composition and purity of both the pure and metal loaded V_2O_5 calcined catalysts were characterized using XRD and the results are shown in Figure 3.3. The diffraction patterns of V_2O_5 support can be seen in Figure 3.3a, and it was found to possess an orthorhombic

crystalline phase (JCPDS 00-041-1426). The latter phase was determined from the V_2O_5 diffraction peaks detected at 2θ of 15.80°, 20.82°, 22.15°, 26.64°, 31.51°, 32.82°, 34.75°, 41.65°, 41.69°, 45.85°, 47.81°, 49.44°, 51.71° and indexed as (200), (001), (101), (110), (400), (011), (310), (002), (102), (411), (600), (012) and (020) planes respectively [**10,11**]. This crystalline vanadium support has a space group *Pmmn* with lattice constants a = 0.3565 nm, b = 0.4372 nm and c = 1.151 nm.

At 2.5 wt.%, Ni and Mn metal-loaded catalysts were observed to have retained the crystalline phase of the V_2O_5 support (Figure 3.3a). However, the Fe-loaded catalyst was an exception, due to the diffraction peak detected at 2θ = 27.89°, which is supposedly (220) indexed from Fe_3O_4 (JCPDS 01-079-0416) [**6**]. The Ni-loaded catalyst retained the V_2O_5 phase character whereas the Fe-loaded catalyst saw a slight intensity increase of the Fe_3O_4 phase and two diffraction peaks were observed on the 7.5 wt.% of Mn-loaded catalyst (Figure 3.3b). The Mn metal (Figure 3.3b) significantly introduced a crystal plane (112) onto the support, detected at 2θ angle of 27.59°. Even though detecting a single diffraction peak hardly serves as positive identification, the latter plane is believed to be from a tetragonal hausmannite Mn_3O_4 (JCPDS 00-24-0734) [**9**].

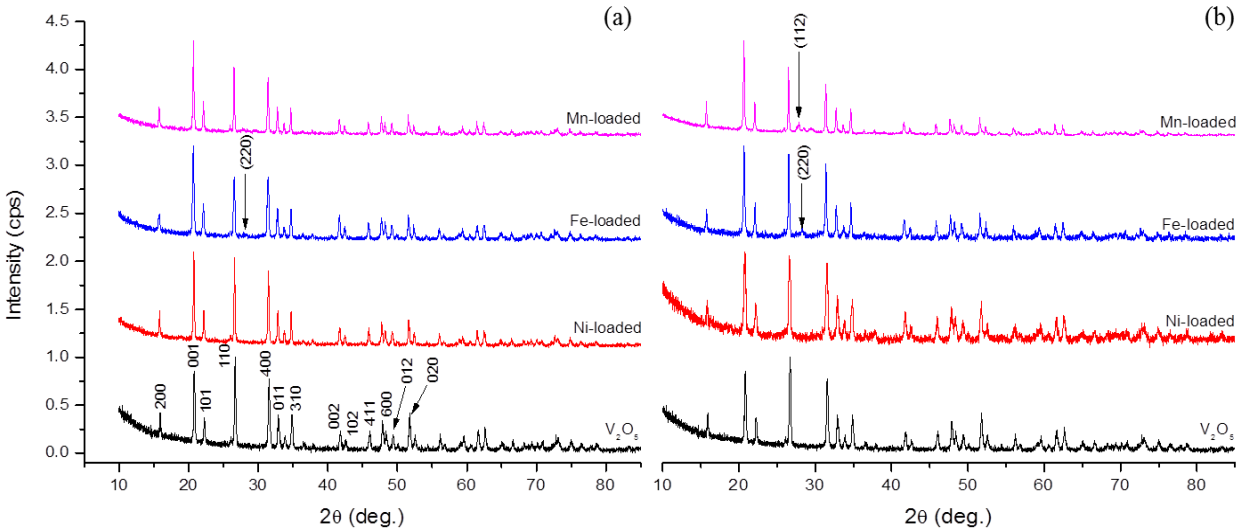

Figure 3.3. X-ray diffractograms of (a) V_2O_5 support, Ni(2.5%)/V_2O_5, Fe(2.5%)/V_2O_5, Mn(2.5%)/V_2O_5, V(2.5%)/V_2O_5 and (b) V_2O_5 support, Ni(7.5%)/V_2O_5, Fe(7.5%)/V_2O_5, Mn(7.5%)/V_2O_5 calcined catalysts.

3.2. Fourier Transform-Infrared spectroscopy results

The FT-IR analysis was done to characterize the catalyst materials by collecting infrared spectra that provides compositional and purity information about the catalysts.

3.2.1. FT-IR results for various metals loaded on γ-Al_2O_3 support

Figure 3.4 displays the FT-IR analysis results of γ-Al_2O_3 and metal-loaded γ-Al_2O_3 calcined catalysts. The spectrum of pure γ-Al_2O_3 (Figures 3.4a and 3.4b) was observed to have a very broad absorption band at 3450 cm^{-1}, which is characteristic to the stretching vibrations of the O–H bond of the physically adsorbed water molecules. The aforementioned is due to the tendency of γ-Al_2O_3 to adsorb the atmospheric moisture [**12**]. At 1059 cm^{-1}, a shoulder representing the Al–O bond inter-vibrational mode frequencies was spotted in the FT-IR spectrum of the support and the absorption shoulders within the β range (950–500 cm^{-1}) assigned to the tetrahedral AlO_4 and an octahedral AlO_6 that are known to reflect in the IR spectrum of γ-Al_2O_3 [**12,13**].

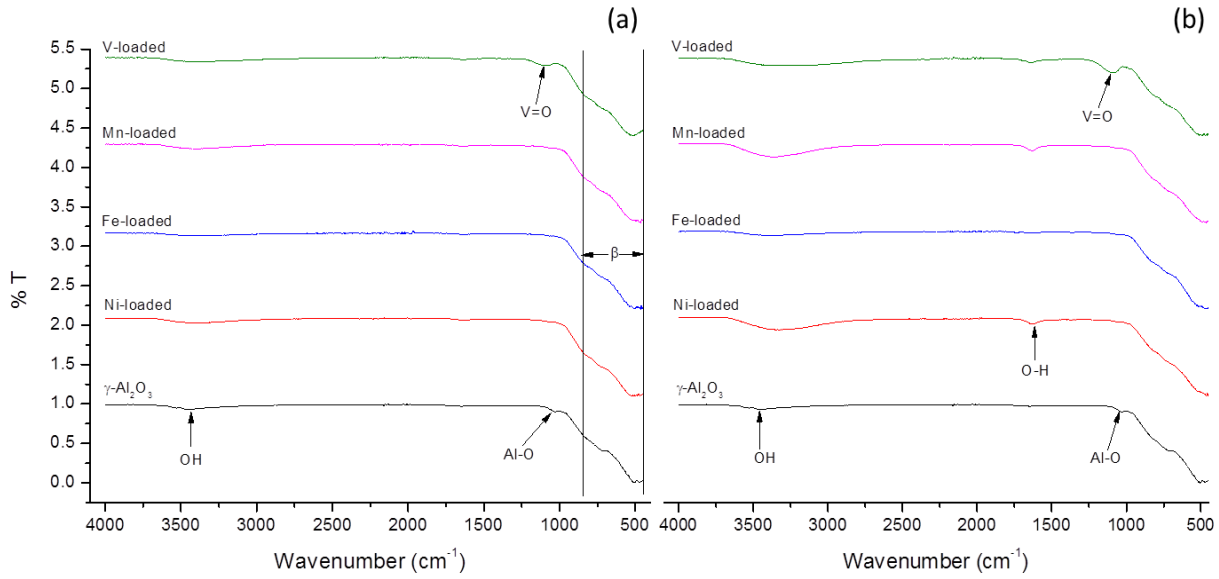

Figure 3.4. FT-IR spectra of (a) γ-Al_2O_3 support, Ni(2.5%)/γ-Al_2O_3, Fe(2.5%)/γ-Al_2O_3, Mn(2.5%)/γ-Al_2O_3, V(2.5%)/γ-Al_2O_3 and (b) γ-Al_2O_3 support, Ni(7.5%)/γ-Al_2O_3, Fe(7.5%)/γ-Al_2O_3, Mn(7.5%)/γ-Al_2O_3, V(7.5%)/γ-Al_2O_3 calcined catalysts.

The IR spectra of Ni, Fe and Mn metal-loaded catalyst at 2.5 wt.% (Figure 3.4a) resembled that of the support except the V-loaded catalyst which possesses an absorption band at 1023 cm^{-1}that accounts for the presence of V=O bond stretching [**11**]. This suggests that an oxide of vanadium was formed on the surface of the calcined catalyst. When the loaded metal content was changed to 7.5 wt.% (Figure 3.4b), a significant increase of the IR absorption bands was observed. The slight increase in the absorption band at 3450 cm^{-1} can be attributed to the difficulty of removing moisture from the surface of γ-Al_2O_3 at higher loadings of each metal dopant, probably due to the enhanced water entrapment on the surface of the catalysts. The latter is also believed to have resulted in the IR absorption peak at 1642 cm^{-1} which is characteristic to the bending mode of the O–H bond from the water molecule (Figure 3.4b) [**13**].

3.2.2. FT-IR results for various metals loaded on SiO_2 support

The FT-IR spectra of the pure SiO_2 support and calcined Ni, Fe, Mn and V-loaded SiO_2 catalysts are shown in Figure 3.5. The pure SiO_2 infrared spectrum (Figures 3.5a and 3.5b) was observed to consist of the absorption peaks at 1090 cm^{-1} and 815 cm^{-1}, which corresponds to the stretching of Si–O–Si and bending vibrations of the Si–O bonds, respectively [**14,15**]. The metal-loaded catalysts at 2.5 wt.% of metal content (Figure 3.5a) attained the similar infrared spectrum to that of the pure SiO_2 support. However, changing the amount of loaded metal to 7.5 wt.% (Figure 3.5b) resulted in the introduction of the peaks at 3440 and 1663 cm^{-1} which are respectively characteristic to the stretching and bending vibrations of the O–H bond found in the physically adsorbed H_2O in surface of the support. The aforementioned was observed for Ni, Mn and V-loaded SiO_2 at 7.5 wt.%.

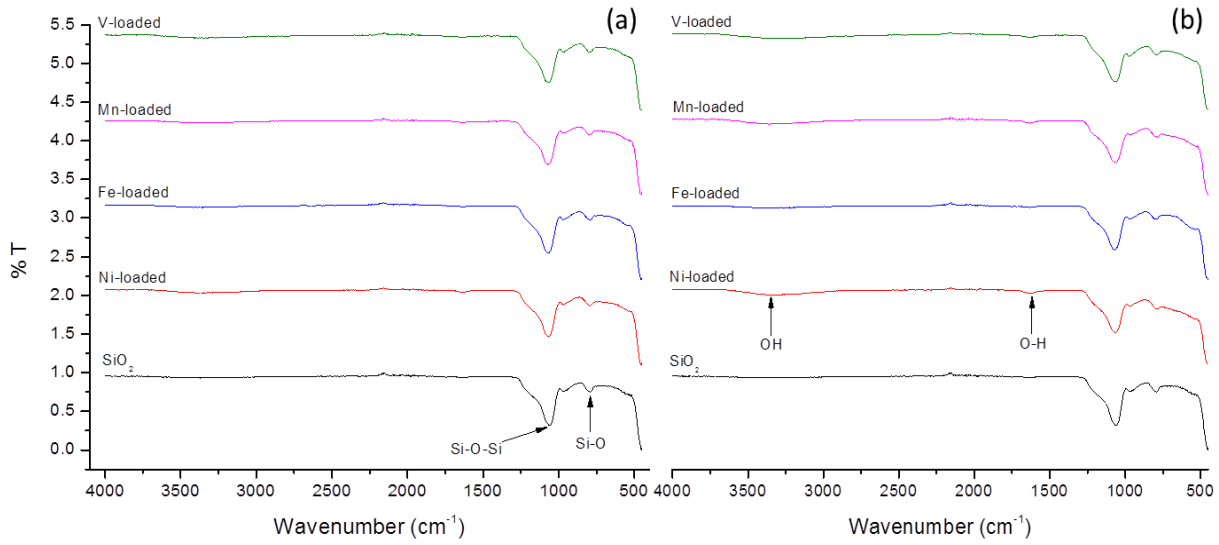

Figure 3.5. FT-IR spectra of (a) SiO_2 support, Ni(2.5%)/SiO_2, Fe(2.5%)/SiO_2, Mn(2.5%)/SiO_2, V(2.5%)/SiO_2 and (b) SiO_2 support, Ni(7.5%)/SiO_2, Fe(7.5%)/SiO_2, Mn(7.5%)/SiO_2, V(7.5%)/SiO_2 calcined catalysts.

3.2.3. FT-IR results for various metals loaded on V_2O_5 support

Figure 3.6 present two sets of FT-IR spectra of pure V_2O_5 support and calcined Ni, Fe and Mn-loaded V_2O_5 catalysts. The pure V_2O_5 support (Figures 3.6a and 3.6b) reflected two characteristic absorption peaks at 1024 and 825 cm^{-1} which accounts for the V=O bond stretching and symmetrical vibrations of the V–O–V bonds, respectively [**11**]. Both the Fe and Mn-loaded catalysts exhibited the IR spectrum similar to that of the V_2O_5 support (Figure 3.6a and 3.6b). The Ni-loaded (2.5 and 7.5 wt.%) V_2O_5 catalysts on the other hand, were observed to have exceptionally high affinity to adsorb and/ or retain water within their surfaces (Figure 3.6a and 3.6b). This was confirmed from the presence of the absorption peaks at 3443 and 1608 cm^{-1} that are attributed to the stretching and bending vibrations of the O–H bond.

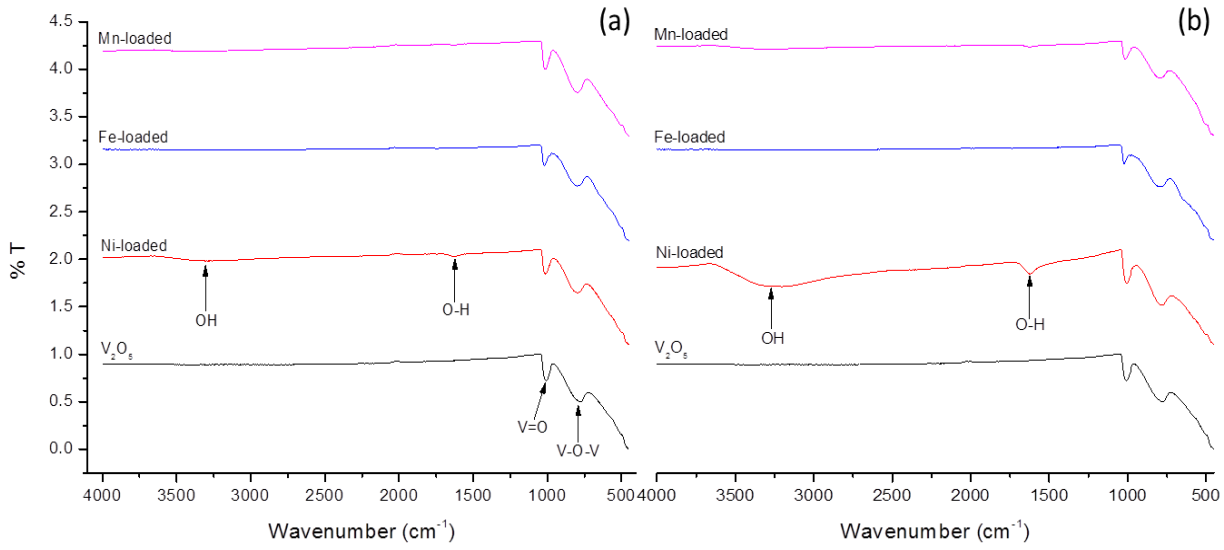

Figure 3.6. FT-IR spectra of (a) V_2O_5 support, Ni(2.5%)/V_2O_5, Fe(2.5%)/V_2O_5, Mn(2.5%)/V_2O_5, V(2.5%)/V_2O_5 and (b) V_2O_5 support, Ni(7.5%)/V_2O_5, Fe(7.5%)/V_2O_5, Mn(7.5%)/V_2O_5 calcined catalysts.

3.3. Inductively coupled plasma-optical emission spectroscopy (ICP-OES) results

The ICP-OES technique was used to determine the concentration of the loaded metal content within the calcined catalyst. The targeted theoretical loadings were 2.5 and 7.5% weight percentage of each metal (Ni, Fe, Mn, V) on γ-Al_2O_3, SiO_2 and V_2O_5 supports, separately. The ICP-OES analysis (Table 3.1) played a vital role in showing the achieved percentage loadings during the catalyst preparations. However, discrepancies were observed between theoretical and experimental metal contents (concentrations). For example, **entries 13** and **14** show very low metal loadings than expected and this suggests that the analyzed catalyst portions were very deficient in metals whereas other **entries** (*i.e.* **1**, **2** and more) gave good experimental concentrations. There was only one sample that was found to have an experimental concentration value that is bigger that the theoretical (**entry 16**). The calculations used to measure appropriate amounts of metal salts used during the catalyst preparations are detailed in Section 2.2 (eq. 2.12–2.15, p. 33).

Table 3.1. ICP-OES results for metal loadings (theoretical and experimental) on various supports.

Entry no.	Catalyst sample	Theoretical metal content (wt.%)	Experimental metal content (wt.%)
1	Ni(2.5%)/γ-Al_2O_3	2.5	2.42
2	Ni(7.5%)/γ-Al_2O_3	7.5	7.55
3	Fe(2.5%)/γ-Al_2O_3	2.5	2.28
4	Fe(7.5%)/γ-Al_2O_3	7.5	5.43
5	Mn(2.5%)/γ-Al_2O_3	2.5	2.45
6	Mn(7.5%)/γ-Al_2O_3	7.5	5.51
7	V(2.5%)/γ-Al_2O_3	2.5	2.40
8	V(7.5%)/γ-Al_2O_3	7.5	7.32
9	Ni(2.5%)/SiO_2	2.5	2.28
10	Ni(7.5%)/SiO_2	7.5	6.20
11	Fe(2.5%)/SiO_2	2.5	2.06
12	Fe(7.5%)/SiO_2	7.5	5.04
13	Mn(2.5%)/SiO_2	2.5	1.64
14	Mn(7.5%)/SiO_2	7.5	3.51
15	V(2.5%)/SiO_2	2.5	2.24
16	V(7.5%)/SiO_2	7.5	7.61
17	Ni(2.5%)/V_2O_5	2.5	2.33
18	Ni(7.5%)/V_2O_5	7.5	7.01
19	Fe(2.5%)/V_2O_5	2.5	2.34
20	Fe(7.5%)/V_2O_5	7.5	6.50
21	Mn(2.5%)/V_2O_5	2.5	2.70
22	Mn(7.5%)/V_2O_5	7.5	5.15

3.4. Scanning electron microscopy (SEM) results

The SEM analyses were conducted to obtain essential physical information about the metal (Ni, Fe, Mn and V) loaded catalyst samples; this includes surface morphology and surface composition.

3.4.1. SEM results for various metals loaded on γ-Al_2O_3 support

The Figure 3.7 provides the SEM images of the support (γ-Al_2O_3) and 2.5 wt.% metal loaded γ-Al_2O_3 catalysts. The γ-Al_2O_3 support appeared to have both the fine powdered and clustered particles (Figure 3.7a). The clusters are believed to have resulted from the adsorbed moisture present on the surface of the support and the FT-IR results are in agreement with this interpretation (Figure 3.4a). The introduction of the Ni dopant (Figure 3.7b) onto the surface of γ-Al_2O_3 resulted in dense and aggregated particles with no significant shape definition. Furthermore, Figure 3.7 (c–e) display agglomerated particles of different sizes and shapes, particles arranged in a layered form and irregular shaped particles, respectively. The images in Figure 3.7c and 3.7e both appears brighter, this could be due to the high yield of secondary electrons from the loaded metals, Fe and V, respectively. Figure 3.8 represents the SEM images for 7.5% metal loaded γ-Al_2O_3 catalysts. There were no major differences in the morphologies of these catalysts, in comparison with the lower metal loading percentage, 2.5 wt.% (Figure 3.7).

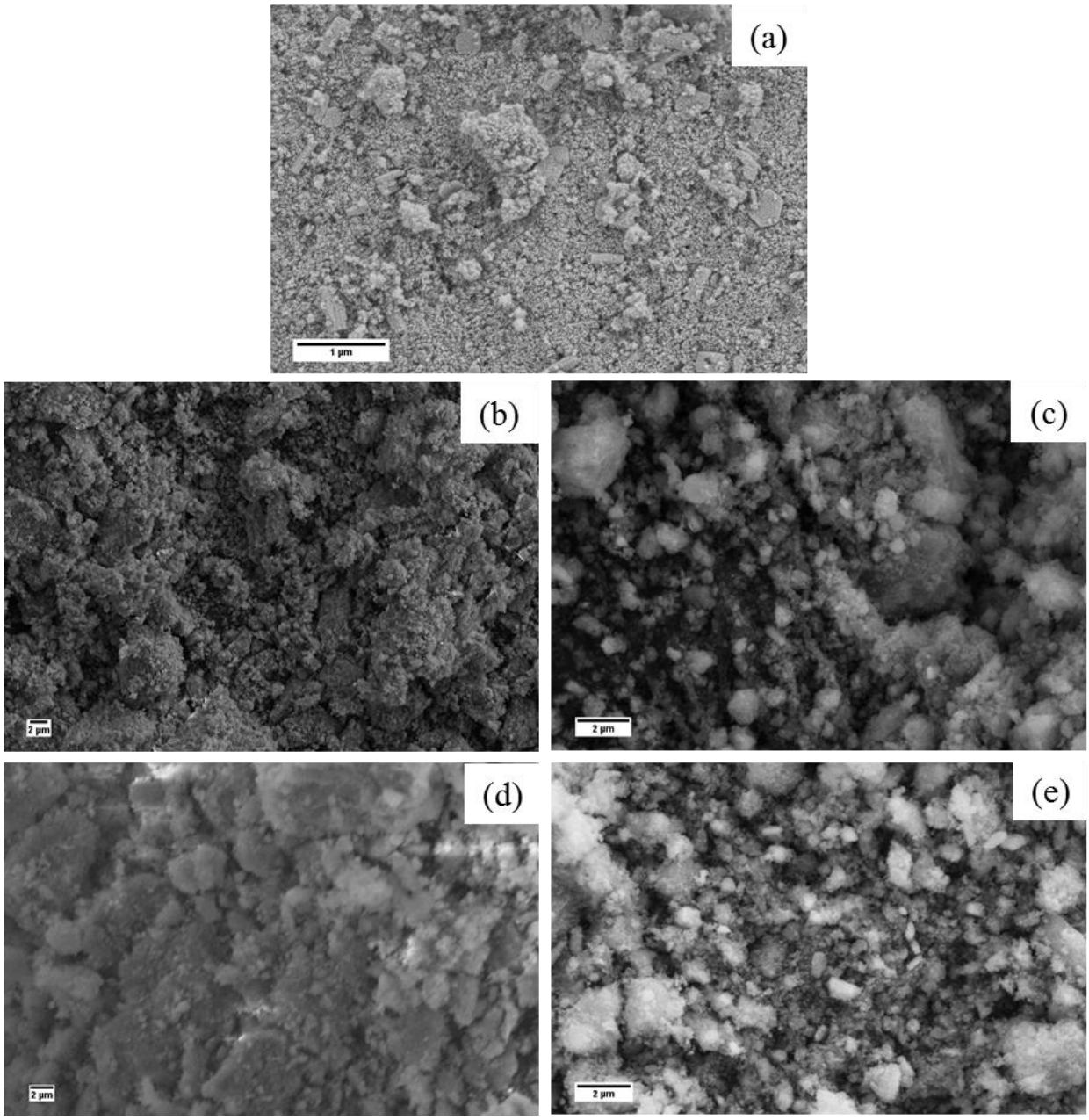

Figure 3.7. SEM images of (a) γ-Al_2O_3 support, (b) Ni(2.5%)/γ-Al_2O_3, (c) Fe(2.5%)/γ-Al_2O_3, (d) Mn(2.5%)/γ-Al_2O_3, (e) V(2.5%)/γ-Al_2O_3 calcined catalysts.

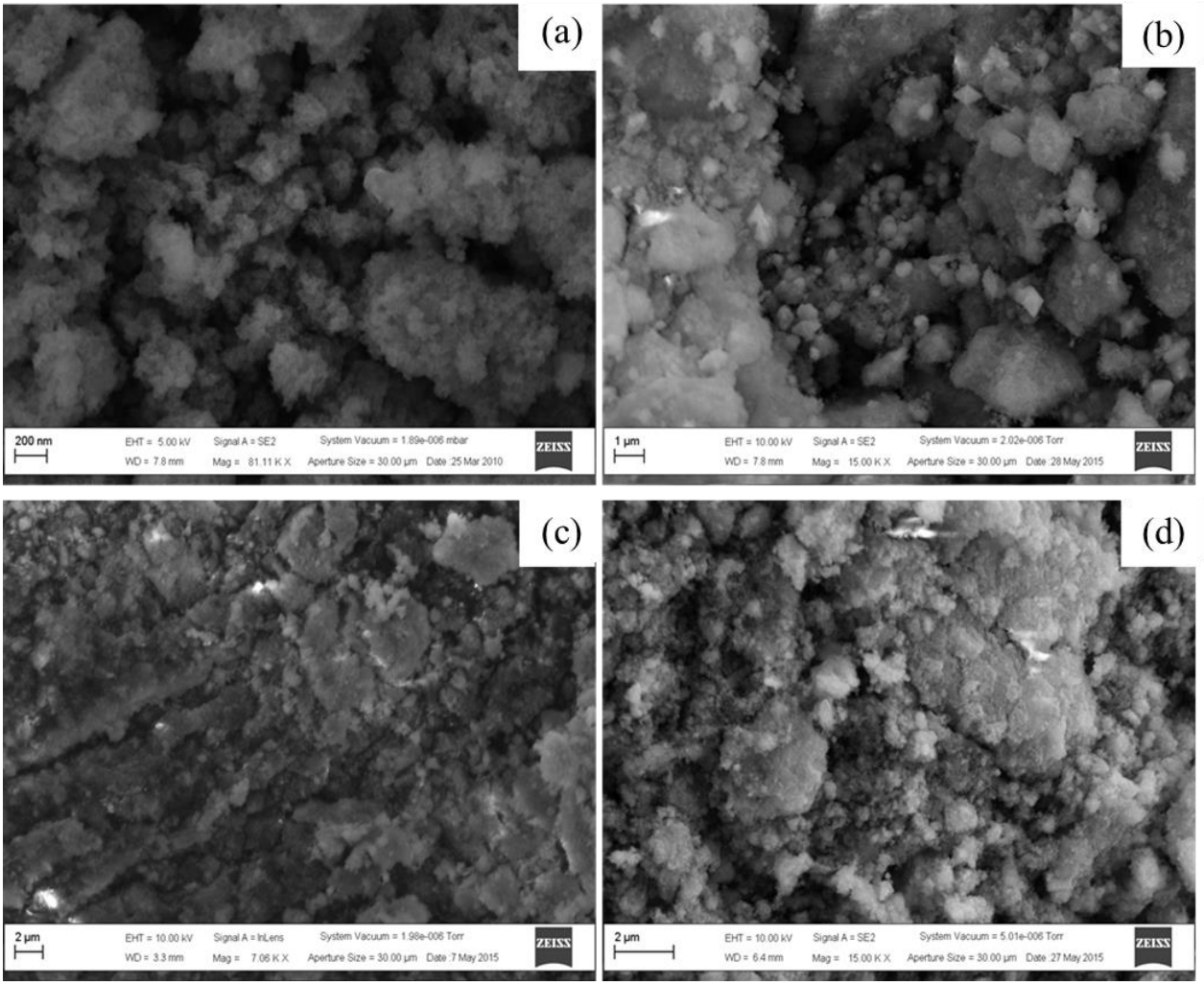

Figure 3.8. SEM images of (a) Ni(7.5%)/γ-Al_2O_3, (b) Fe(7.5%)/γ-Al_2O_3, (c) Mn(7.5%)/γ-Al_2O_3, (d) V(7.5%)/γ-Al_2O_3 calcined catalysts.

3.4.2. SEM results for various metals loaded on SiO_2 support

The SEM micrographs of SiO_2 supported metal (Ni, Fe, Mn & V) were obtained and they are displayed in Figures 3.9 and 3.10, with 2.5 and 7.5 wt.% of metal loadings, respectively. The pure SiO_2 support (Figure 3.9a) is observed to have aggregated particles and this is apparent in all metal-loaded silica catalysts (Figure 3.9b–e). However, the iron (Fe)-loaded SiO_2 catalyst (Figure 3.9c) reveal an exceptional case of the crystalline and irregular spherical particles agglomerated to form one particle (denoted by a circle, Figure 3.9c) on the surface of the SiO_2 support, typical of Fe_2O_3 [**16**].

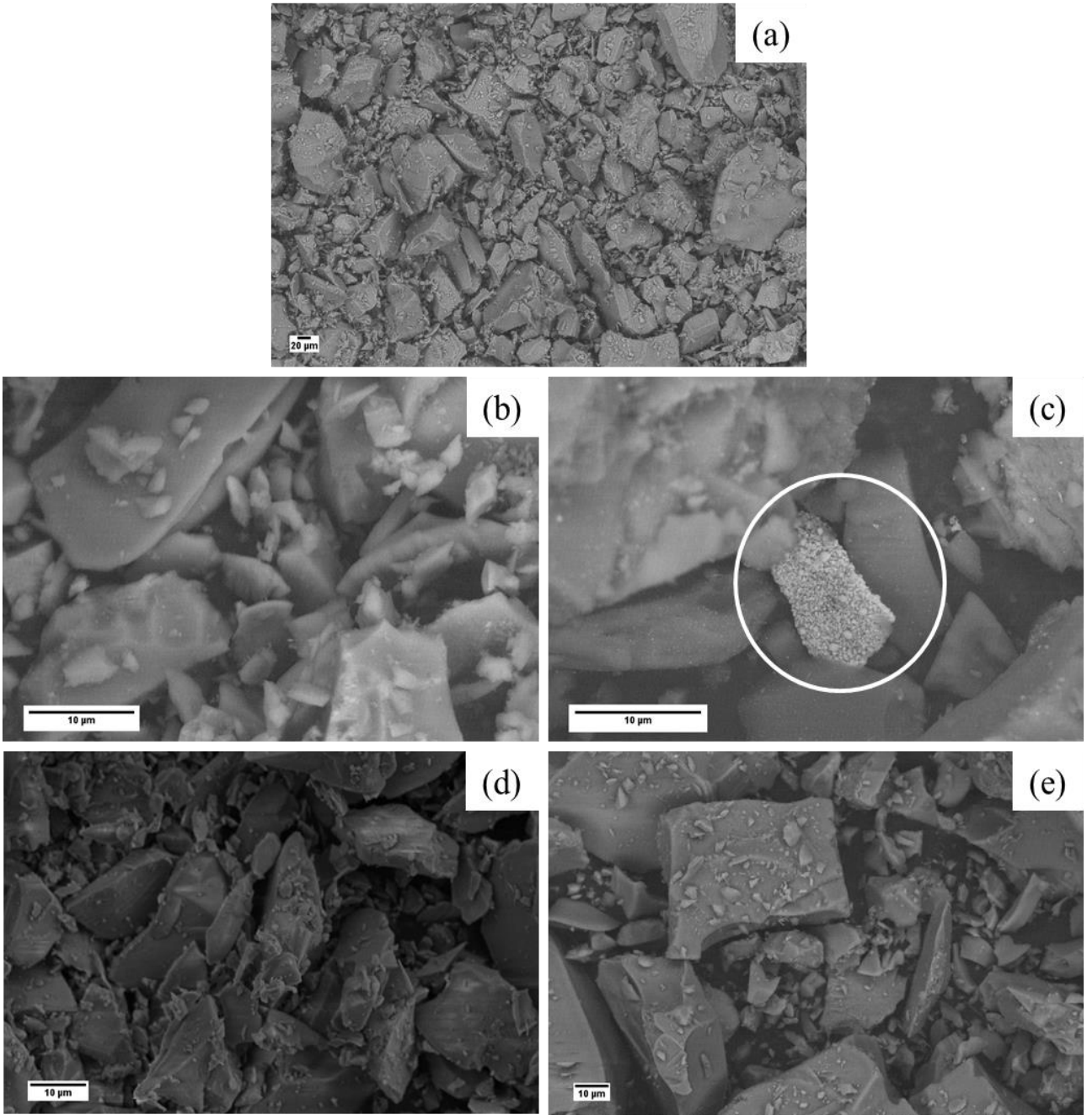

Figure 3.9. SEM images of (a) SiO_2 support, (b) Ni(2.5%)/SiO_2, (c) Fe(2.5%)/SiO_2, (d) Mn(2.5%)/SiO_2, (e) V(2.5%)/SiO_2 calcined catalysts.

The increase in the amount of the Fe dopant to 7.5 wt.% (Figure 3.10b) on the SiO_2 surface resulted in the Fe_2O_3 particles not only aggregated but loosely dispersed further as independent particles over the SiO_2 support. The Ni and Mn loaded catalysts (Figures 3.10a and 3.10c)

exhibit bulky and sharp-edged agglomerated amorphous particles whilst the V-loaded catalyst (Figure 3.10d) displayed the morphology of the parent SiO_2 support.

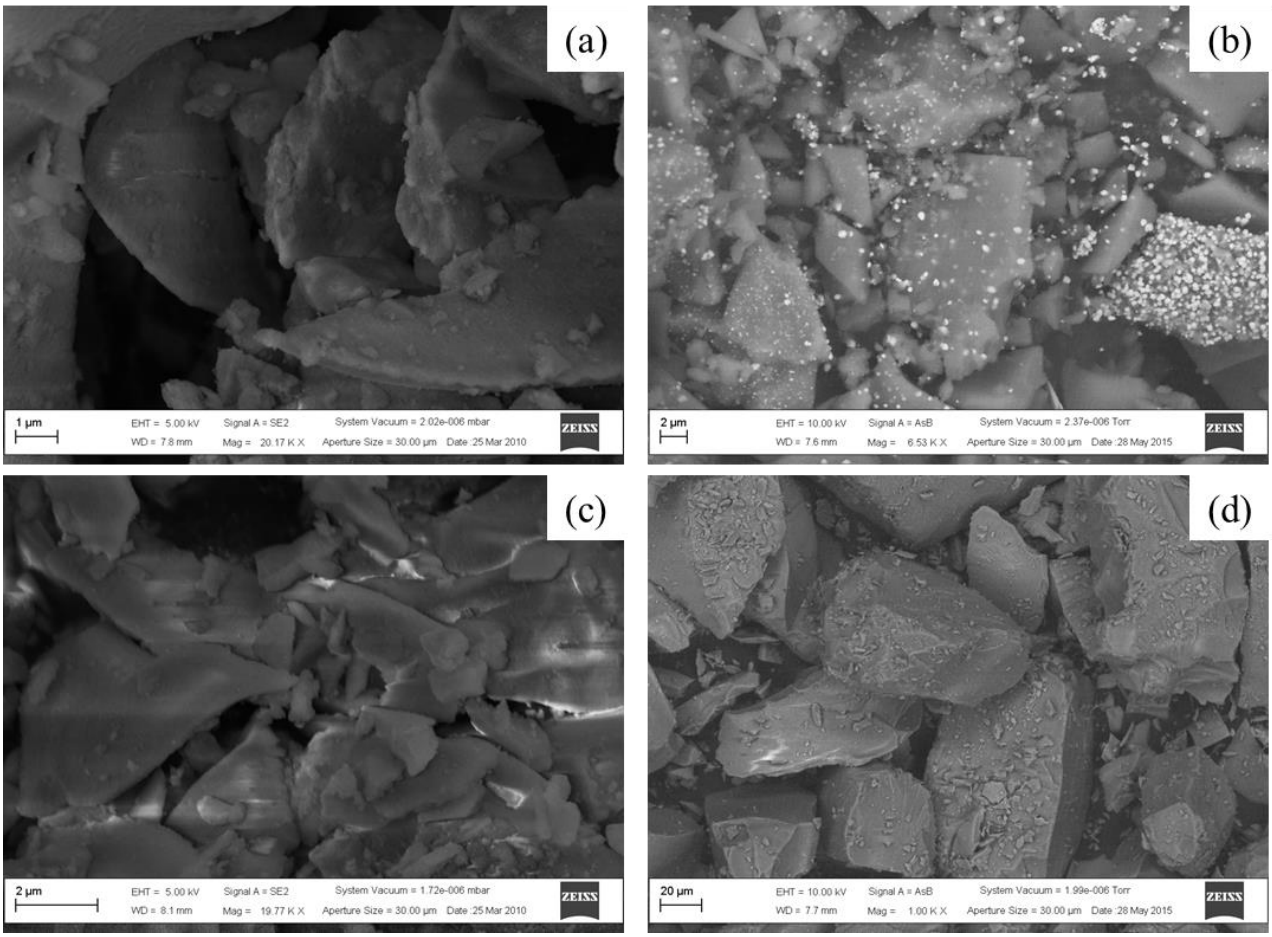

Figure 3.10. SEM images of (a) Ni(7.5%)/SiO_2, (b) Fe(7.5%)/SiO_2, (c) Mn(7.5%)/SiO_2, (d) V(7.5%)/SiO_2 calcined catalysts.

3.4.3. SEM results for various metals loaded on V_2O_5 support

Figure 3.11 and 3.12 presents the SEM micrographs of pure V_2O_5 and metal (Ni, Fe & Mn) loaded V_2O_5 support at varied metal contents, 2.5 and 7.5 wt.% respectively. The V_2O_5 support (Figure 3.11a) can be seen, possessing orderly assembled crystalline and bar-like particles of irregular shapes and sizes. These particles appear to have disintegrated after the 2.5 wt.% impregnation of Ni (Figure 3.11b), Mn (Figure 3.11d) and upon calcination. The latter may have been promoted by stirring and grinding during the catalyst preparation. The 2.5 wt.% Fe loaded

catalyst (Figure 3.11c) presents a combination of aggregated and isolated particles of irregular shapes.

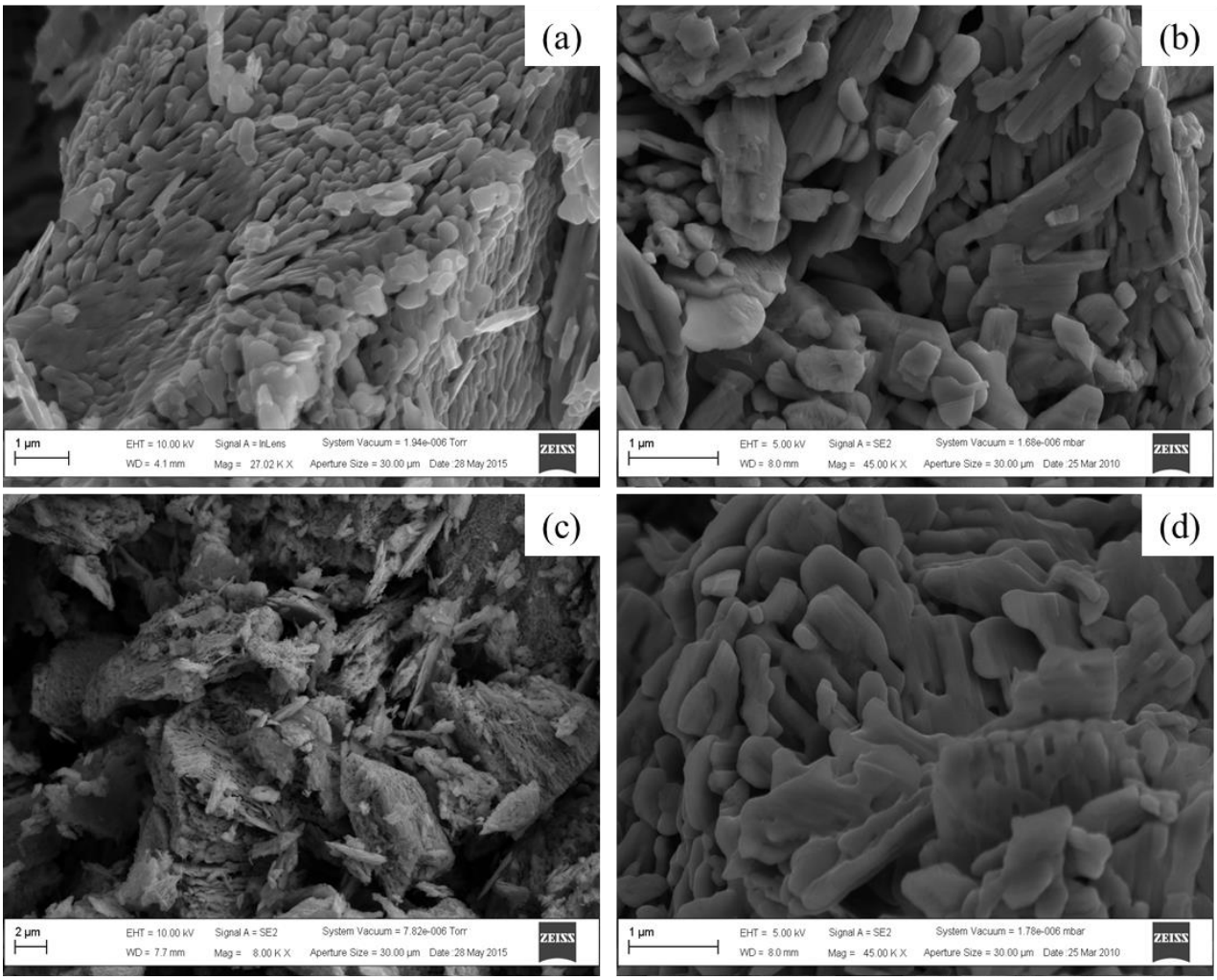

Figure 3.11. SEM images of (a) V_2O_5 support, (b) Ni(2.5%)/V_2O_5, (c) Fe(2.5%)/V_2O_5 and (d) Mn(2.5%)/ V_2O_5 calcined catalysts.

The 7.5 wt.% metal loaded V_2O_5 catalysts were observed to have wire-like particles covering the surfaces of larger particles and this is apparent in Figures 3.12b and 3.12c. The increased amount of Ni (Figure 3.12a) on the surface of V_2O_5 appear to have reduced the particle sizes as compared to the 2.5 wt.% loading (Figure 3.11b). The Mn loaded catalyst (Figure 3.12c) exceptionally has particles resembling the structure of flowers.

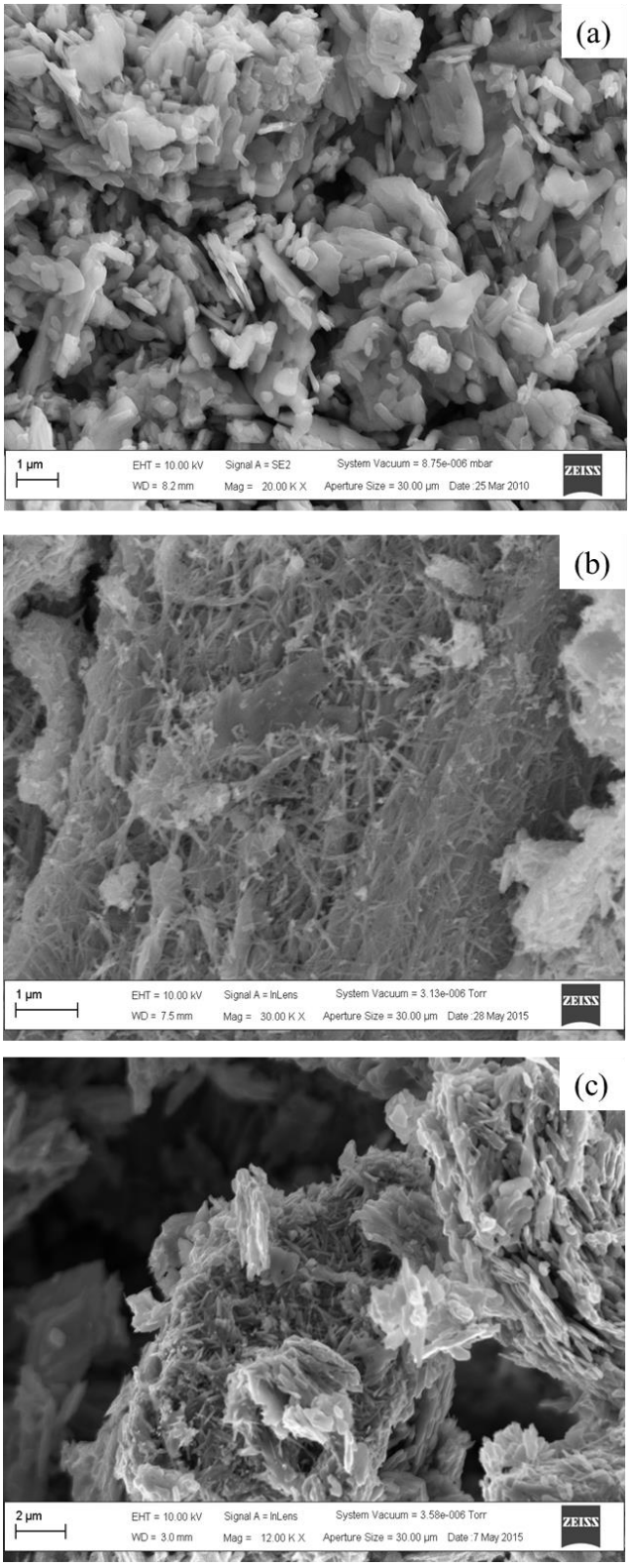

Figure 3.12. SEM images of (a) Ni(7.5%)/V_2O_5, (b) Fe(7.5%)/V_2O_5 and (c) Mn(7.5%)/ V_2O_5 calcined catalysts.

3.5. Energy dispersive X-ray spectroscopy (EDX) results

The representative EDX results for metal (Ni, Fe, Mn, V) loaded (γ-Al_2O_3, SiO_2, V_2O_5) catalysts is given in Figure 3.13. The Figure 3.13 (a–d) displays the EDX scanned surface of the Fe(2.5%)/SiO_2 catalyst, resultant spectrum, point-mapping and line-mapping analyses, respectively. The energy dispersive X-rays were able to provide qualitative results from the catalyst surface in Figure 3.13a and it can be seen from the EDX spectrum (Figure 3.13b) that the catalyst is composed of 55.8, 41.8 and 2.5 wt.% of oxygen, silicon and iron, respectively.

The point-mapping (Figure 3.13c) provides an insight in terms of metal dispersion over the SiO_2 surface and Fe was observed to be well dispersed, except at the circled point which appears to be rich in Fe. The aforementioned is typical of a rarely observed scenario in 2.5 wt.% metal-loaded catalysts that were prepared in this work, such that, the metal aggregation to form larger particles on the surface of a support was mostly observed in Fe-loaded catalysts herein (Appendix A, Figures A2, A4, A11, pp. 132–137). The line-mapping analysis revealed that the circled particle (Figure 3.13d) is composed of SiO_2 that is covered in a large amount of Fe_2O_3 particles. This is apparent in line-mapping signals (Figure 3.13d), the light blue spectrum represents the Fe metal and the red and green spectra represent Si and O, respectively.

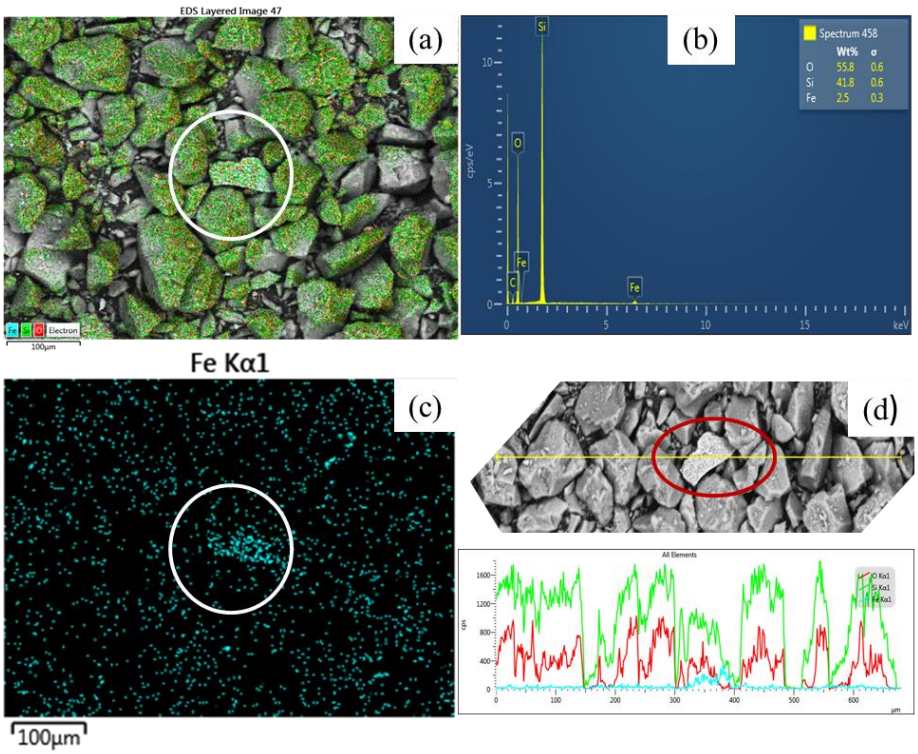

Figure 3.13. EDX results, showing the (a) scanned catalyst surface, (b) EDX spectrum, (c) point-mapping and (d) line-mapping of the calcined Fe(2.5%)/SiO_2 catalyst.

On other catalysts, metals (Ni, Mn and V) were observed to be well distributed on surfaces of the support (γ-Al_2O_3, SiO_2 and/ or V_2O_5) materials as seen in Appendix A (Figure A2–A12, pp. 132–137). The loaded metal concentrations according to EDX analyses were observed to be different from those obtained from ICP-OES. This may be a compositional effect of the selected portion of the catalyst sample for each analysis, the portion may either be rich in metal or deficient, provided that it does not give a theoretically expected concentration (2.5 or 7.5% of metal). The other reason may be a significant difference in sample sizes used during these two separate analyses as well as the distribution of the metals over the surface of the catalyst supports. The ICP-OES analyses required 0.3 g of the catalyst while the SEM-EDX analyses took less than 0.1 g.

The Table 3.2 shows the loaded metal (Ni, Fe, Mn and V) concentrations on supports (γ-Al_2O_3, SiO_2 and V_2O_5) according to EDX analyses. **Entries 5**, **9**, **11** and **14** show examples of catalyst samples that have experimental metal contents equal to the theoretically expected metal contents.

Other catalysts however, proved to either be rich in metal concentration or poor and this is evident in Table 3.2.

Table 3.2. The EDX results for metal (Ni, Fe, Mn and V) loadings on various supports (γ-Al_2O_3, SiO_2 & V_2O_5).

Entry no.	**Catalyst sample**	**Theoretical metal content (wt.%)**	**Experimental metal content (wt.%)**
1	Ni(2.5%)/γ-Al_2O_3	2.5	2.3
2	Ni(7.5%)/γ-Al_2O_3	7.5	8.1
3	Fe(2.5%)/γ-Al_2O_3	2.5	2.1
4	Fe(7.5%)/γ-Al_2O_3	7.5	7.3
5	Mn(2.5%)/γ-Al_2O_3	2.5	2.5
6	Mn(7.5%)/γ-Al_2O_3	7.5	6.7
7	V(2.5%)/γ-Al_2O_3	2.5	2.4
8	V(7.5%)/γ-Al_2O_3	7.5	8.7
9	Ni(2.5%)/SiO_2	2.5	2.5
10	Ni(7.5%)/SiO_2	7.5	7.4
11	Fe(2.5%)/SiO_2	2.5	2.5
12	Fe(7.5%)/SiO_2	7.5	7.8
13	Mn(2.5%)/SiO_2	2.5	3.1
14	Mn(7.5%)/SiO_2	7.5	7.5
15	V(2.5%)/SiO_2	2.5	2.1
16	V(7.5%)/SiO_2	7.5	7.1
17	Ni(2.5%)/V_2O_5	2.5	2.6
18	Ni(7.5%)/V_2O_5	7.5	6.1
19	Fe(2.5%)/V_2O_5	2.5	2.3
20	Fe(7.5%)/V_2O_5	7.5	7.2

21	Mn(2.5%)/V_2O_5	2.5	2.7
22	Mn(7.5%)/V_2O_5	7.5	7.7

3.6. Transmission electron microscopy (TEM) results

The transmission electron microscopy (TEM) analysis was employed to obtain detailed morphological results for the metal-loaded catalysts.

3.6.1. TEM results for various metals loaded on γ-Al_2O_3 support

The TEM micrographs for 2.5 and 7.5 wt.% of the metal loaded γ-Al_2O_3 catalysts are displayed in Figures 3.14 and 3.15 respectively. The particles of the pure γ-Al_2O_3 support (Figure 3.14a) were observed to possess high preference towards binding with one another and this was also evident in analogous metal loaded catalysts. The γ-Al_2O_3 support has an average particle size of 8.74 nm with irregularly shaped particles. The average particle size increased to 15.07 nm with 2.5 wt.% Ni loading (Figure 3.14b), 13.00 nm for Fe loading (Figure 3.14c), 10.26 nm for Mn loading (Figure 3.14d) and 8.82 nm for V loading (Figure 3.14e) on γ-Al_2O_3 supported catalysts. It is worth noticing the trend of average particle sizes that appear to decrease with the increase in atomic radii of the loaded metals (Ni – V) on the γ-Al_2O_3 support.

At the increased dopant amount, 7.5 wt.%, the catalysts were still observed to exhibit the morphology of the pure γ-Al_2O_3 support (Figure 3.15). The particle sizes were, on average found to be 9.61, 10.79, 10.55 and 11.91 nm (Figure 3.15a – d) for the Ni, Fe, Mn and V-loaded catalysts. Contrary to literature [**17,18**], average particle sizes of Ni and Fe loaded γ-Al_2O_3 material (Table 3.3) was observed to decrease from 2.5 to 7.5% of loadings. It is however plausible, that at 2.5%, the Ni and Fe particles grew on the surface of the support, resulting in larger particles [**17**].

Table 3.3. Mean particle sizes of metal loaded γ-Al_2O_3 catalysts, measured from TEM images.

Entry no.	**Catalyst**	**Mean particle size distribution (nm)**	
		2.5 wt.%	7.5 wt.%
1	γ-Al_2O_3 support	8.74	

2	Ni/γ-Al_2O_3	15.70	9.61
3	Fe/γ-Al_2O_3	13.00	10.79
4	Mn/γ-Al_2O_3	10.26	10.55
5	V/γ-Al_2O_3	8.82	11.91

Opposite to the former would be true for 7.5% Ni and Fe loadings on γ-Al_2O_3. This would mean that, a greater fraction of these metals and/ or their respective oxides have not grown on the surface of the support but distances away, resulting in smaller average particle sizes. Other than that, a greater number of loosely bound metal species on γ-Al_2O_3 surface may have been detached during sonication when the samples were being prepared from TEM analyses (Section 2.3.1.5, p. 36).

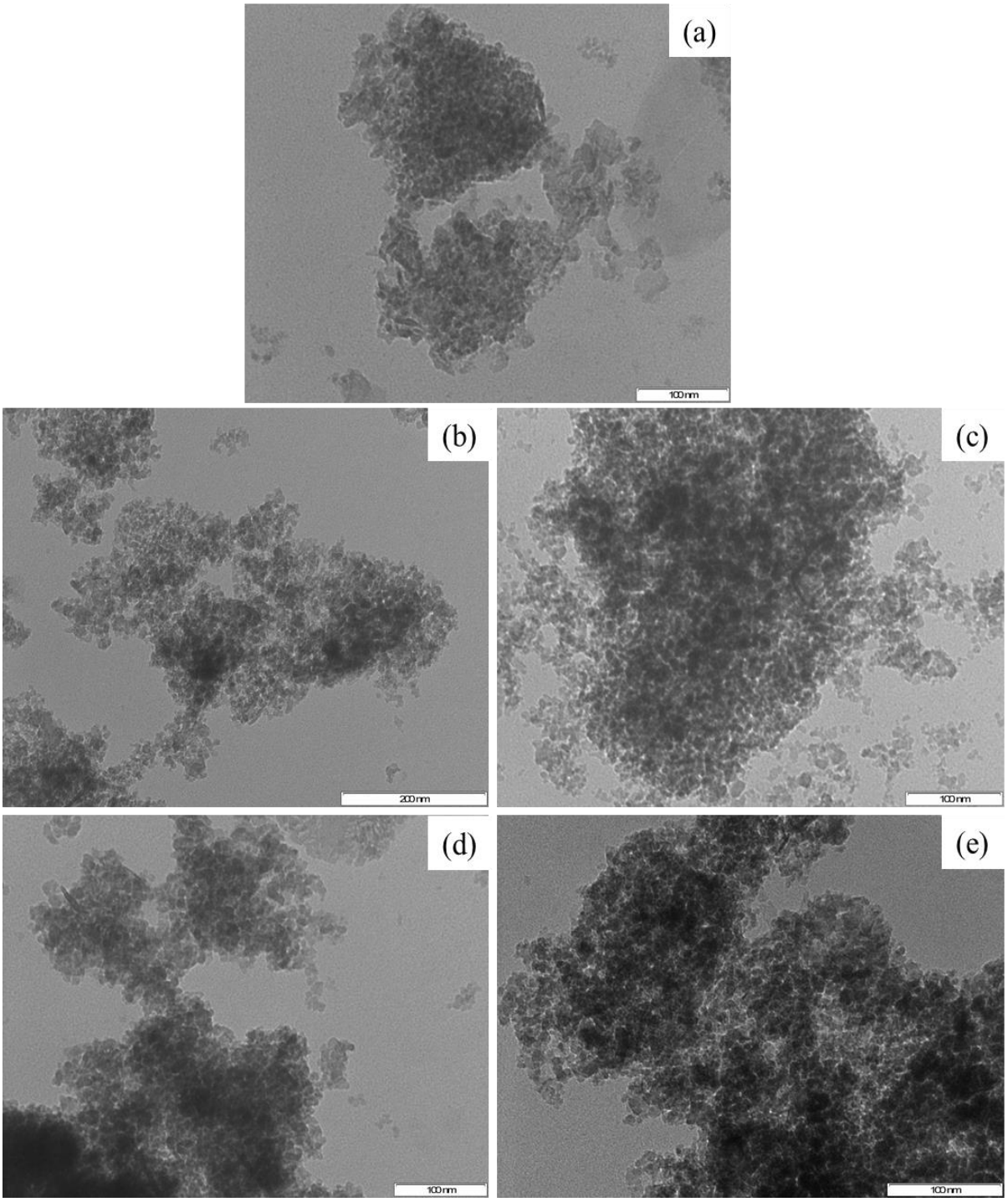

Figure 3.14. TEM images of (a) γ-Al_2O_3 support, (b) Ni(2.5%)/γ-Al_2O_3, (c) Fe(2.5%)/γ-Al_2O_3, (d) Mn(2.5%)/γ-Al_2O_3 and (e) V(2.5%)/γ-Al_2O_3 calcined catalysts.

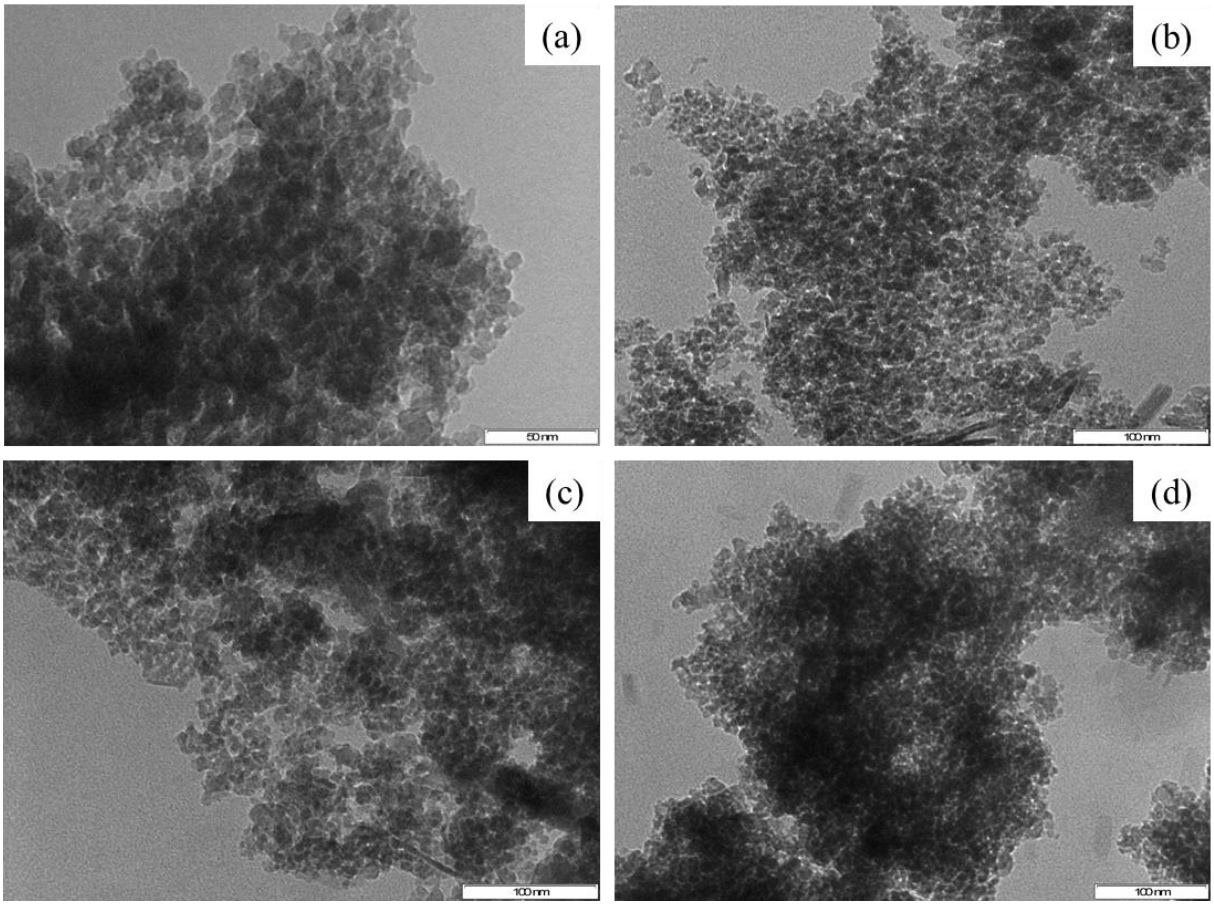

Figure 3.15. TEM images of (a) Ni(7.5%)/γ-Al_2O_3, (b) Fe(7.5%)/γ-Al_2O_3, (c) Mn(7.5%)/γ-Al_2O_3 and (d) V(7.5%)/γ-Al_2O_3 calcined catalysts.

3.6.2. TEM results for various metals loaded on SiO_2 support

The TEM micrographs of all the metal loaded SiO_2 catalysts (Figure 3.16 and 3.17) showed closely packed particles, resembling those of pure SiO_2 (Figure 3.16a). These particles were estimated to be in a nanometer range in sizes based on the scale bars. Measuring the particle sizes is vital but couldn't be accomplished due to the difficulty of taking the micrographs that show clear particle lengths and widths since the particles were highly aggregated. The Fe loaded catalyst in Figure 3.16c display evidence of loaded metal aggregation over the surface of a support, appearing as two dark particles. The later has been highlighted on the SEM results as well (Figure 3.9 and 3.10) and the aggregated particles were found to be Fe_2O_3 by XRD analysis (Figure 3.2). Li *et al*. [**16**] reported similar results, where the average particle size for Fe_2O_3 was

80 nm, which presents no major difference since the dark particles in Figure 3.16c were found to be 50.02 and 108.72 nm in size (79.4 nm in average). This comparison, however, holds if Fe_2O_3 particles (seen as dark spots in Figure 3.16c) in the current work are all between 50–110 nm of size range.

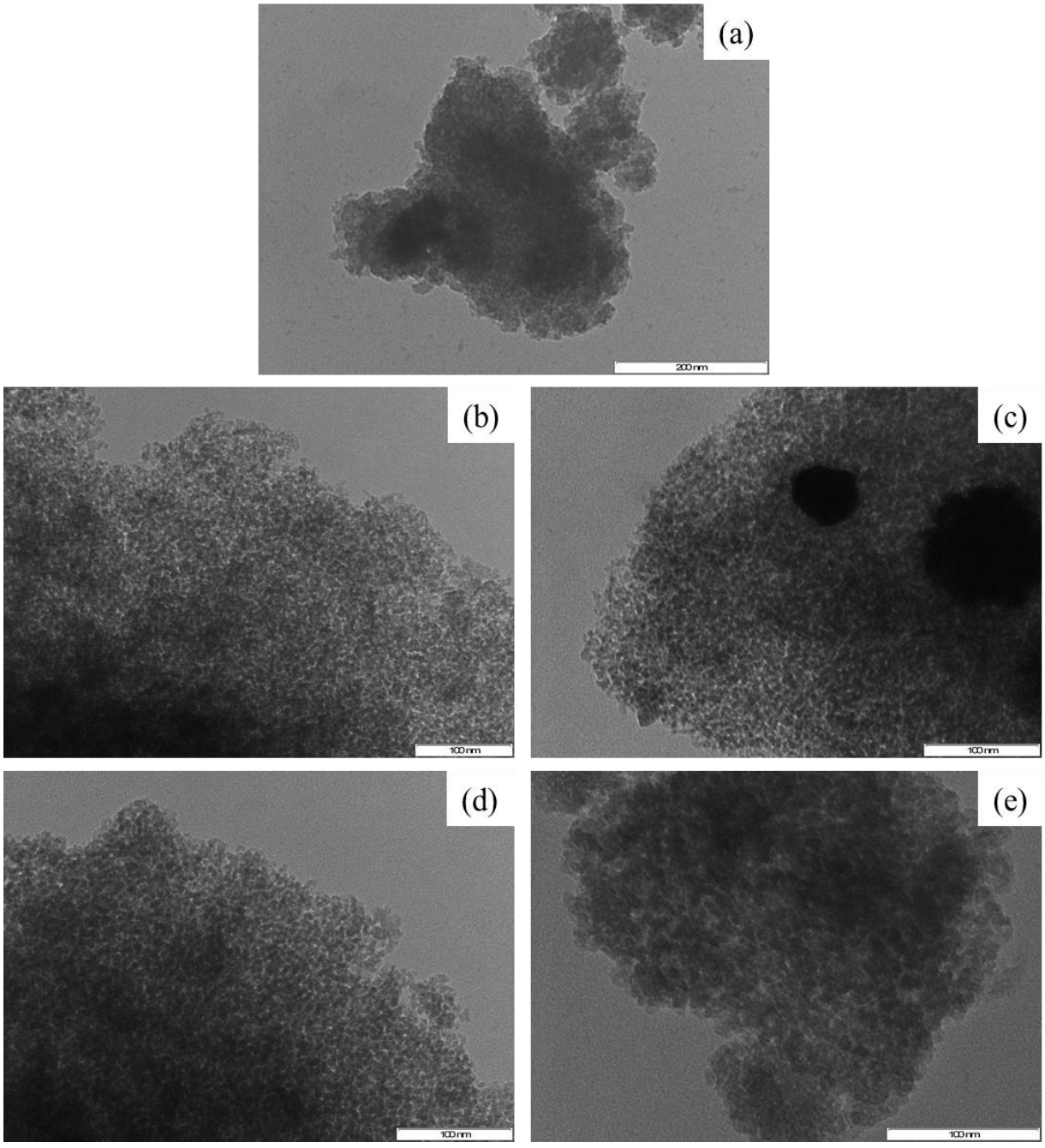

Figure 3.16. TEM images of (a) SiO_2 support, (b) Ni(2.5%)/SiO_2, (c) Fe(2.5%)/SiO_2, (d) Mn(2.5%)/SiO_2 and (e) V(2.5%)/SiO_2 calcined catalysts.

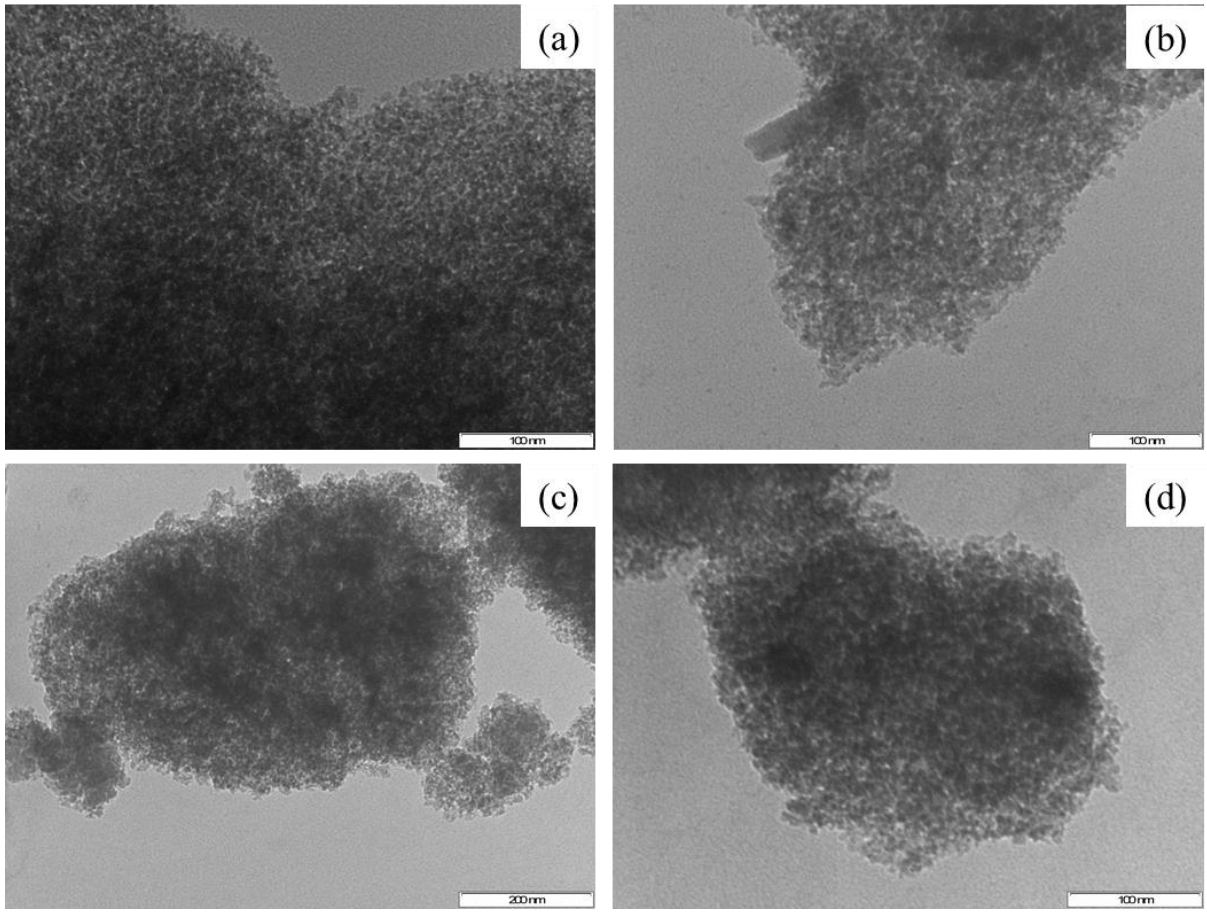

Figure 3.17. TEM images of (a) Ni(7.5%)/SiO_2, (b) Fe(7.5%)/SiO_2, (c) Mn(7.5%)/SiO_2 and (d) V(7.5%)/SiO_2 calcined catalysts.

3.6.3. TEM results for various metals loaded on V_2O_5 support

Presented in Figures 3.18 and 3.19, are the TEM micrographs of the pure V_2O_5 support followed by the metal loaded V_2O_5 calcined catalysts (Figure 3.18a). The aforementioned support was observed to have crystalline plate-like particles with average size of 62.67 nm and considerable shape homogeneity. The latter particle size is not far from the reported sizes of the V_2O_5, which were found to range between 30–60 nm [**19**]. A rather high level of aggregation was witnessed in the 2.5 and 7.5 wt.% Ni loaded (Figure 3.18b and 3.19a) catalysts, which instigated hindrance in measuring the particle sizes. The Fe-loaded catalyst (Figure 3.18c) produced both sheet-like and rod-like particles, with rods (50.07 nm thick) dominating the sheets in numbers. In literature, V_2O_5 is reportedly reducible into VO_2 which has rod-like particles in the presence of a suitable

reducing agent [20]. Consequently, the latter suggests that the elevated reducing ability of the Fe(II) salt was enough to reduce or partly reduce V_2O_5 to VO_2. However, the VO_2 crystalline phase could not be identified on the XRD results of Fe loaded V_2O_5 catalysts, certainly because they share a number of crystal planes and this means that Fe(II) was also a limiting reagent towards formation of VO_2 rod-like particles. This is further supported by the increase in the number of VO_2 rods with the increase of the Fe(II) content to 7.5 wt.% (Figure 3.19c).

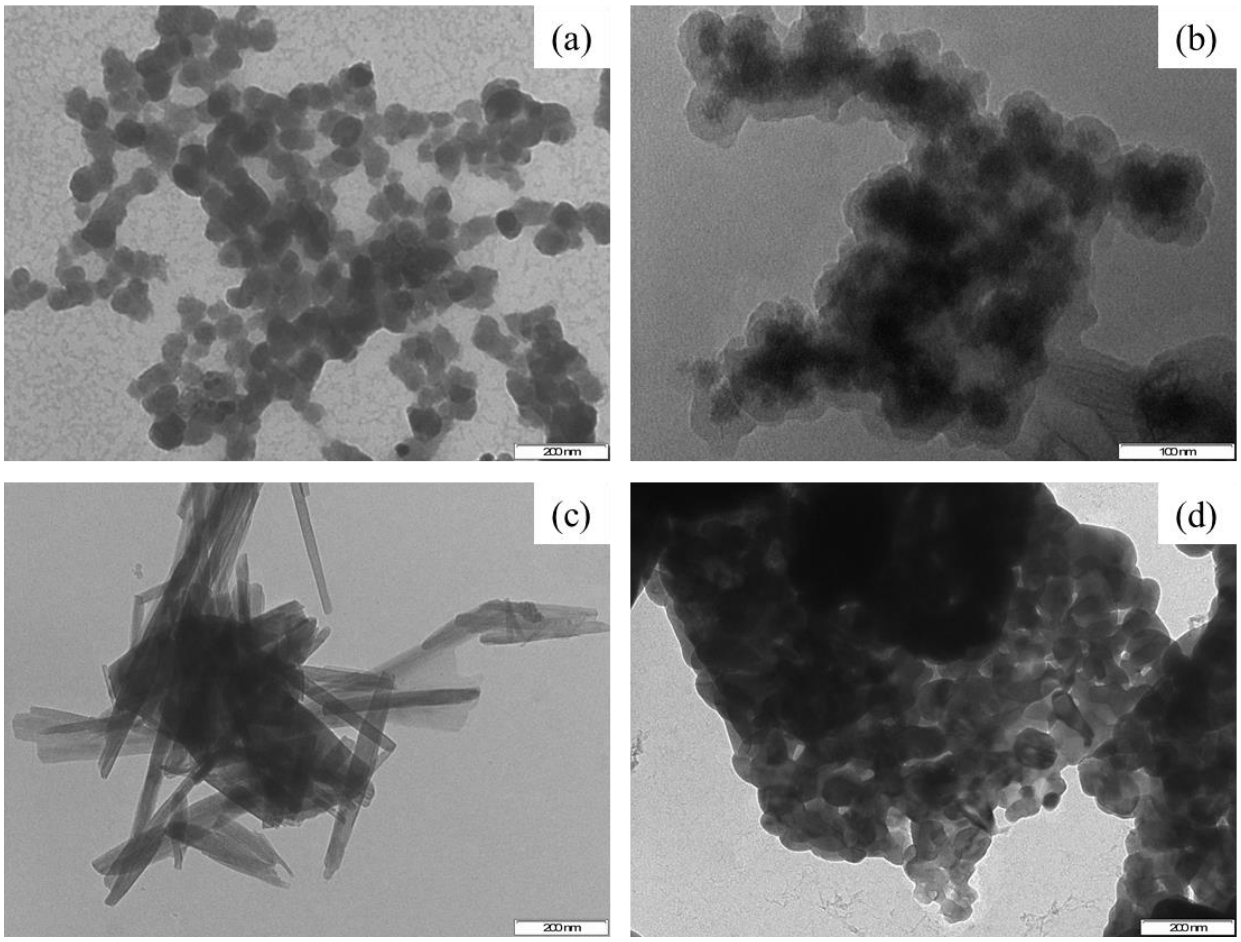

Figure 3.18. TEM images of (a) V_2O_5 support, (b) Ni(2.5%)/V_2O_5, (c) Fe(2.5%)/V_2O_5 and (d) Mn(2.5%)/ V_2O_5 calcined catalysts.

Agglomerated and dense looking particles were observed for 2.5 wt.% Mn loaded catalyst (Figure 3.18d) and the change in morphology is apparent in the 7.5 wt.% Mn content (3.19c) on the surface of the support. The Mn(7.5%)/V_2O_5 catalyst shows flake-like particles of irregular shapes and a few rod-like particles, probably that of VO_2. It is worth mentioning that, not only a

reducing agent can promote the reduction of V_2O_5 to VO_2 but the calcination does as well, up to a small extent [**20**]. This may explain the thin rod-like particles that can be seen in Figure 3.19c.

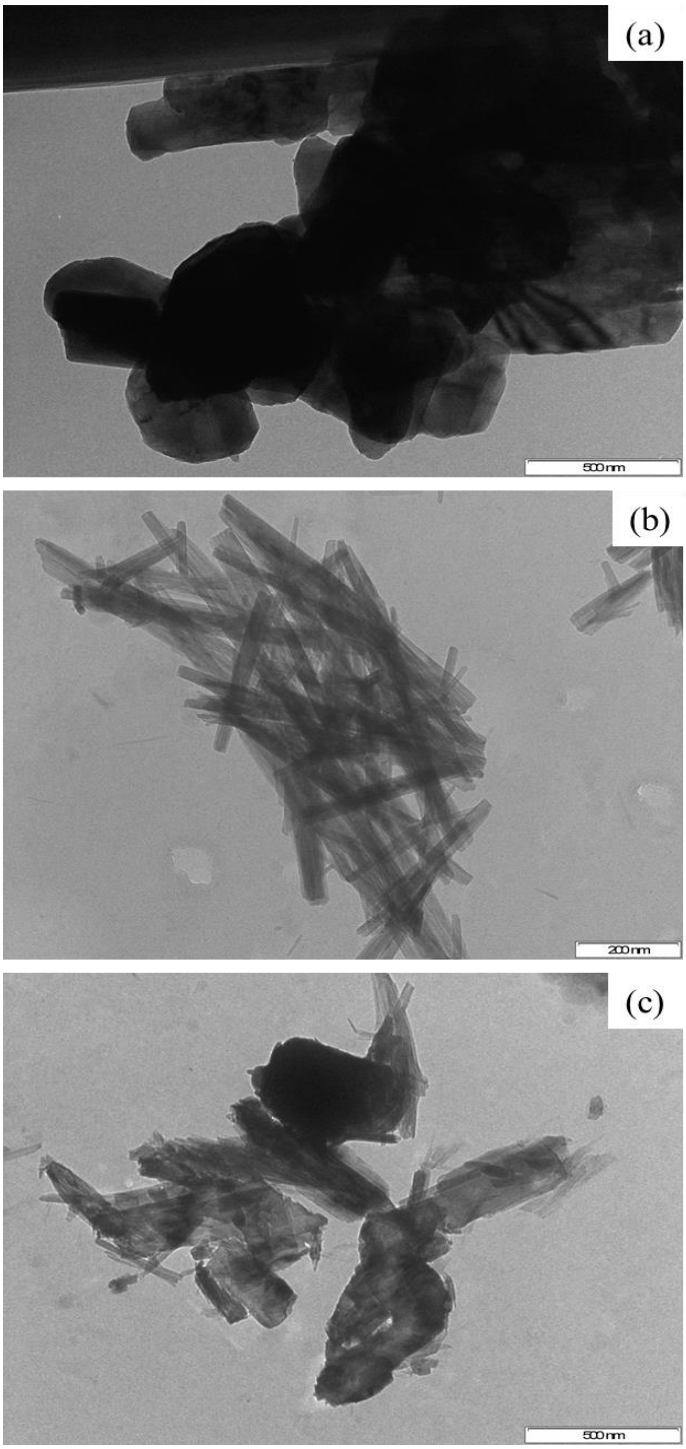

Figure 3.19. TEM images of (a) Ni(7.5%)/V_2O_5, (b) Fe(7.5%)/V_2O_5 and (c) Mn(7.5%)/V_2O_5 calcined catalysts.

3.7. Brunauer-Emmet-Teller (BET) surface area analysis results

The surface areas of metal-loaded γ-Al_2O_3 and SiO_2 catalysts were determined by the Brunauer, Emmett and Teller (BET) surface area analysis. The pure γ-Al_2O_3 and SiO_2 supports had the BET surface areas of 295.0 and 506.0 m^2/g, respectively. Their surface areas were anticipated to decrease with metal loadings and it was observed that when the 2.5 wt.% of Mn metal was loaded onto a γ-Al_2O_3 support, the obtained surface area was 167.6 m^2/g which further decreased to 107.8 m^2/g with increase in the loaded metal content on the support, to 7.5 wt.%. A similar trend was observed in both the Mn and V loaded SiO_2 catalysts (Table 3.4). Furthermore, an increase in pore sizes was recorded as the surface areas decreased, basically, increasing the loaded metal content led to an increase in pore sizes of the catalysts. This may be due to the tendency of metal particles to form aggregates leaving the measurable internal volume as pores [21]. The aggregation of metal particles was also confirmed herein, as seen in SEM, EDX and TEM analyses (Sections 3.4–3.6, pp. 58–68).

Table 3.4. BET surface areas for the various metal loaded γ-Al_2O_3 and SiO_2 supports.

Sample	**BET Surface Area (m^2/g)**	**Pore Volume (cm^3/g)**	**Pore Size (nm)**
Pure γ-Al_2O_3	**295.0**	–	–
Mn(2.5%)/γ-Al_2O_3 cal.	167.6	0.382646	9.13
Mn(7.5%)/γ-Al_2O_3 cal.	107.8	0.302151	11.21
Pure SiO_2	**506.0**	–	–
Mn(2.5%)/SiO_2 cal.	339.6	0.009591	7.28
Mn(7.5%)/SiO_2 cal.	279.9	0.007381	8.24
V(2.5%)/SiO_2 cal.	403.8	0.006261	6.25
V(7.5%)/SiO_2 cal.	322.5	0.531641	6.59
Fe(7.5%)/SiO_2 cal.	414.6	–	5.94

Figure 3.20 represents, N_2 adsorption-desorption isotherms of the metal-loaded γ-Al_2O_3 and SiO_2 calcined catalysts. The extension of Figure 3.20 can be found in Appendix A, (Figure A13, p. 138) showing the BET isotherm of the Fe(7.5%)/SiO_2 catalysts. Both the metal-loaded γ-Al_2O_3 and SiO_2 catalysts, according to IUPAC classification, were found to be of type-IV isotherms with H3 and H2 hysteresis loops, [**21**] respectively. This by default categorized them as mesopores with pore sizes ranging from 1.5–100 nm, which is also in good agreement with the obtained catalyst's BET pore size results (Table 3.4).

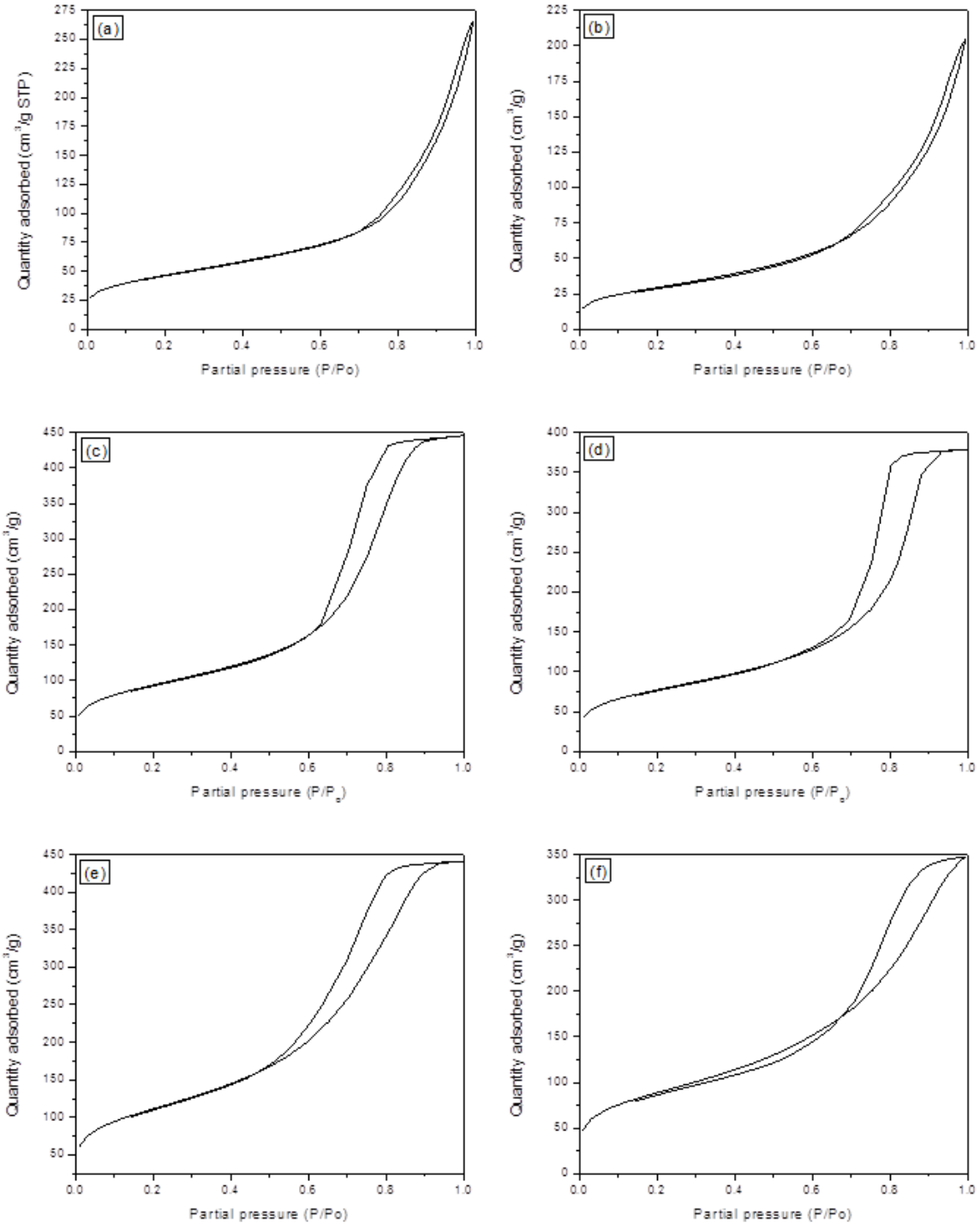

Figure 3.20. N_2 sorption isotherms of the (a) Mn(2.5%)/γ-Al_2O_3, (b) Mn(7.5%)/γ-Al_2O_3 (c) Mn(2.5%)/SiO_2, (d) Mn(7.5%)/SiO_2, (e) V(2.5%)/SiO_2 and (f) V(7.5%)/SiO_2 calcined catalysts.

3.8. References

1. D. S. Maciver, H. H. Tobin, R. T. Barth; Catalytic aluminas I. Surface chemistry of eta and gamma alumina. *J. Catal.*, 2 (**1963**) 485–487.
2. M. Sui, L. She; Review on research and application of mesoporous transitional metal oxides in water treatment. *Front. Environ. Scie. Eng.* 7(6) (**2013**) 795–802.
3. M. A. Vuurman, I. E. Wachs, D. J. Stufkens, A. Oskam; Characterization of chromium oxide supported on Al_2O_3, ZrO_2, TiO_2 and SiO_2 under dehydrated conditions. *J. Mol. Catal.* 80 (**1993**) 209–227.
4. Y. Rozita, R. Brydson, A. J. Scott; An investigation of commercial gamma-Al_2O_3 nanoparticles. *J. Phys:* Conference series 241 (**2010**) 1–4.
5. L. Samain, A. Jaworski, M. Eden, D. M. Ladd, D-K. Seo, F. J. Garcia-Garcia, U. Haussermann; Structural analysis of highly porous γ-Al_2O_3. *J. Solid State Chem*. 217 (**2014**) 1–8.
6. V. Zabarskas, S. Tamulevičius, I. Prosyčevas, J. Puišo; Analysis of Fe_2O_3 protective coatings thermally grown on color picture TV tube structural steel components. *Mater. Scie+.* 10 (2) (**2004**) 147–151.
7. S. K. Sahoo, K. Agarwai, A. K. Singh, B. G. Polke, K. C. Raha; Characterization of γ-Fe_2O_3 nano powders synthesized by emulsion precipitation-calcination route and rheological behavior of α-Fe_2O_3. *Int. J. Eng. Sci. Technol*. 2 (8) (**2010**) 118–126.
8. V. S. R. Rajasekhar Pullabhotla, A. Rahman, S. B. Jonnalagadda; Selective catalytic Knoevenagel condensation by Ni-SiO_2 supported heterogeneous catalysts: An environmental benign approach. *Catal. Commun*. 10 (**2009**) 365–369.
9. H. Xia, Y. Wan, F. Yan, L. Lu; Manganese oxide thin films prepared by pulsed laser deposition for thin film microbatteries. *Mater. Chem. Phys.* 143 (**2014**) 720–727.
10. Y. Shimizu, K. Nagase, N. Miura, N. Yamazoe; Electrochromic properties of spin-coated V_2O_5 thin films. *Solid state ionics* 53 – 56 (**1992**) 490–495.
11. Y. Chen, G. Yang, Z. Zhang, X. Yang, W. Hou, J.J. Zhu; Polyaniline-intercalated layered vanadium oxide nanocomposites – One-pot hydrothermal synthesis and application in lithium battery. *Nanoscale* 2 (**2010**) 2131–2138.

12. G. Paglia; Determination of the structure of γ-Alumina using empirical and first principles calculations combined with supporting experiments. *Curtin University of Technology*, *Perth*. (**2004**). Retrieved 2017-22-01.
13. C. J. Lucio-Ortiz, J. R. De la Rosa, A. H. Ramirez, J. A. De los Reyes Heredia, P. Del Angel. S. Munoz-Aguirre. L. M. De Leon-Covian; Synthesis and characterization of Fe doped mesoporous Al_2O_3 by sol-gel method and its use in trichloroethylene combustion. *J Sol-Gel Sci. Technol*. 58 (**2011**) 374–384.
14. A. Beganskiene, V. Sirutkaitis, M. Kurtinaitiene, R. Juskenas, A. Kareiva; FTIR, TEM and NMR investigations of Stöber silica nanoparticles. *Mater. Sci*. 10 (4) (**2004**) 287–290.
15. B. Shokri, M. Abbasi Firouzjah, S.I. Hosseini; FTIR analysis of silicon dioxide thin film deposited by metal organic-based PECVD. *Laser & plasma institute, Shahid Beheshti University, Tehran, Iran*.
16. R. Li, Q. Li, S. Gao, J. K. Shang; Enhanced Arsenite Adsorption onto Litchi-Like Al-Doped Iron Oxides. *J. Am. Ceram. Soc.* 94(2) (**2011**) 584–591.
17. G. C. Bond; The origins of particle size effects in heterogeneous catalysis. *Surf. Sci.* 156 (**1985**) 966–981.
18. M. Zangouei, A. Z. Moghaddam, M. Arasteh; The influence of Nickel loading on reducibility of NiO/Al_2O_3 catalysts synthesized by Sol-Gel method. *Chemical Engineering Research Bulletin* 14 (**2010**) 97–102.
19. S. H. Ng, T. J. Patey, R. Büchel, F. Krumeich, J. Z. Wang, H. K. Liu, S. E. Pratsinis, P. Novák; Flame spray-pyrolyzed vanadium oxide nanoparticles for lithium battery cathodes. *Phys. Chem. Chem. Phys.* 11 (**2009**) 3748–3755.
20. Y. Liu, E. Uchaker, N. Zhou, J. Li, Q. Zhanga, G. Cao; Facile synthesis of nanostructured vanadium oxide as cathode materials for efficient Li-ion batteries. *J. Mater. Chem.* 22 (**2012**) 24439–24445.
21. A. Teimouri, B. Najari, A. N. Chermahini, H. Salavati, M. Fazel-Najafabadi; Characterization and catalytic properties of molybdenum oxide catalysts supported on ZrO_2–γ-Al_2O_3 for ammoxidation of toluene. *RSC Adv.* 4 (**2014**) 37679–37686.

Chapter 4

CATALYTIC OXIDATION OF CRESOLS AND OPTIMIZATION OF REACTION CONDITIONS IN A COLUMN AND A GLASS REACTOR

4.0. Introduction

In catalysis, transition-metal oxides such as TiO_2, Fe_2O_3, Al_2O_3, SiO_2 and ZrO_2 have prominently been used as catalysts, adsorbents and catalyst supports [**1–2**]. These oxides often possess a network of pores that are categorized in terms of their diameters (d) *i.e.* ($d \leq 2$ nm), (2 nm > d < 50 nm) and ($d \geq 50$ nm) which are named microporous, mesoporous and macroporous, respectively. As catalysts, these materials tend to demand that the targeted substrate's molecular size be competent to their pore sizes, thus allowing it access onto the pores and exposure to inner catalytically active sites [**1**]. There also exists a variety of metal oxides with catalytic activity, such as Mn_2O_3, Cr_2O_3 and V_2O_5 that have been reported to be applicable in hydrogenation, dehydrogenation and oxidation of hydrocarbons [**1–3**]. However, prior to exploiting the aforementioned catalysts, the economically friendly approach would be to first test, to check the activity of conventional catalysts such as activated charcoal in the reaction of interest.

Activated charcoal is cheaper when compared to most catalysts, due to its ease of preparation. It can be prepared from raw materials such as charcoal, saw dust and coal [**4**]. Physico–chemical properties of activated charcoal are the reason of the extensive research covered on activated charcoal, both as an adsorbent and/ or a catalyst. As discussed by Lima *et al*. activated charcoal has elevated hardness, electrical conductivity, thermal and corrosion resistance towards acids and bases [**5**]. Furthermore, aluminas may be considered as the rivals of activated carbon, especially gamma alumina. The latter has been widely used as a catalyst, owing to its characteristically large surface area, pronounced acidity and high porosity [**6**]. It is more likely to find gamma alumina in a hydrated state and Maciver *et al*. reported a minimum time to evacuate physisorbed water from the materials pores to be from 8 to 10 hours under specific conditions [**6**]. Treating gamma alumina at elevated temperatures (> 600 ^{o}C) may lead to crystallite size growth and decline of surface hydroxyl groups present, which both would potentially inhibit its catalytic activity. Gamma alumina is also competitively analogous to silica.

Silica attracted great attention from many years ago, initially as a colloid system and to the recent past till to-date as a catalyst material, support, drying and reinforcing agent [**7**]. Similar to gamma alumina, silica physically adsorbs water vapor onto its surface, specifically on the silanols and not to the rest of the surface. However, heating the latter beyond complete dehydration (> 400 ^{o}C) may affect the surface silanols and consequently alter its catalytic activity

[7]. What the γ-Al_2O_3 and SiO_2 materials have in common is high surface area, thermal stability and ability to physisorb (physically adsorb) liquid substances onto their catalytically active surfaces. This make these oxides to be ideal for exploitation in oxidative degradation of some environmentally unfriendly organic substances.

In this chapter, we aim to explore and compare the catalytic activity of γ-Al_2O_3 and SiO_2 (when used as adsorbants) packed in a glass colum to activated charcoal and metal oxides (γ-Al_2O_3, SiO_2 and V_2O_5 supports) in the ozone initiated oxidation of three methyl phenols (*m*-, *o*-, and *p*-cresols). The results obtained hereafter will be used as preliminary results for the succeeding Chapter 5.

4.1. Ozonation of cresols adsorbed on γ-Al_2O_3 or SiO_2 packed in a glass column

The necessity of degrading and/ or converting cresol isomers into less harmful and value added products has been emphasized in this dissertation. In a quest to achieve the latter, *m*-, *o*- and *p*-cresols were oxidized using ozone, as illustrated in Section 2.5.1 (Figure 2.4, p. 44). Figure 4.1 display the line graphs which provide the relationships between the percentage conversion and ozonation time (1–5 h) of the three isomeric substrates, adsorbed separately on γ-Al_2O_3 and SiO_2 mesopores. The *m*-cresol (Figure 4.1a) was observed to reach the percentage conversion of above 50% when adsorbed on γ-Al_2O_3 and less than 40% on SiO_2. The maximum conversion of the *o*-cresol (Figure 4.1b) was recorded just below the 60% mark at 3 h of reaction time, which decrease to below 50% when adsorbed on SiO_2 while a linear increase can be seen for the γ-Al_2O_3 adsorbed substrate, reaching up to just below 40%. Moreover, up to 60% of *p*-cresol (Figure 4.1c) was converted to products when adsorbed on silica and only up to above 30% with γ-Al_2O_3 at 3 h, a drop in substrate conversion was noticed at 5 h, in both reaction sets. The aforementioned drop in substrate conversion over time could be due to the oxidation products being continuously oxidized until they turn into CO_2 gas [8].

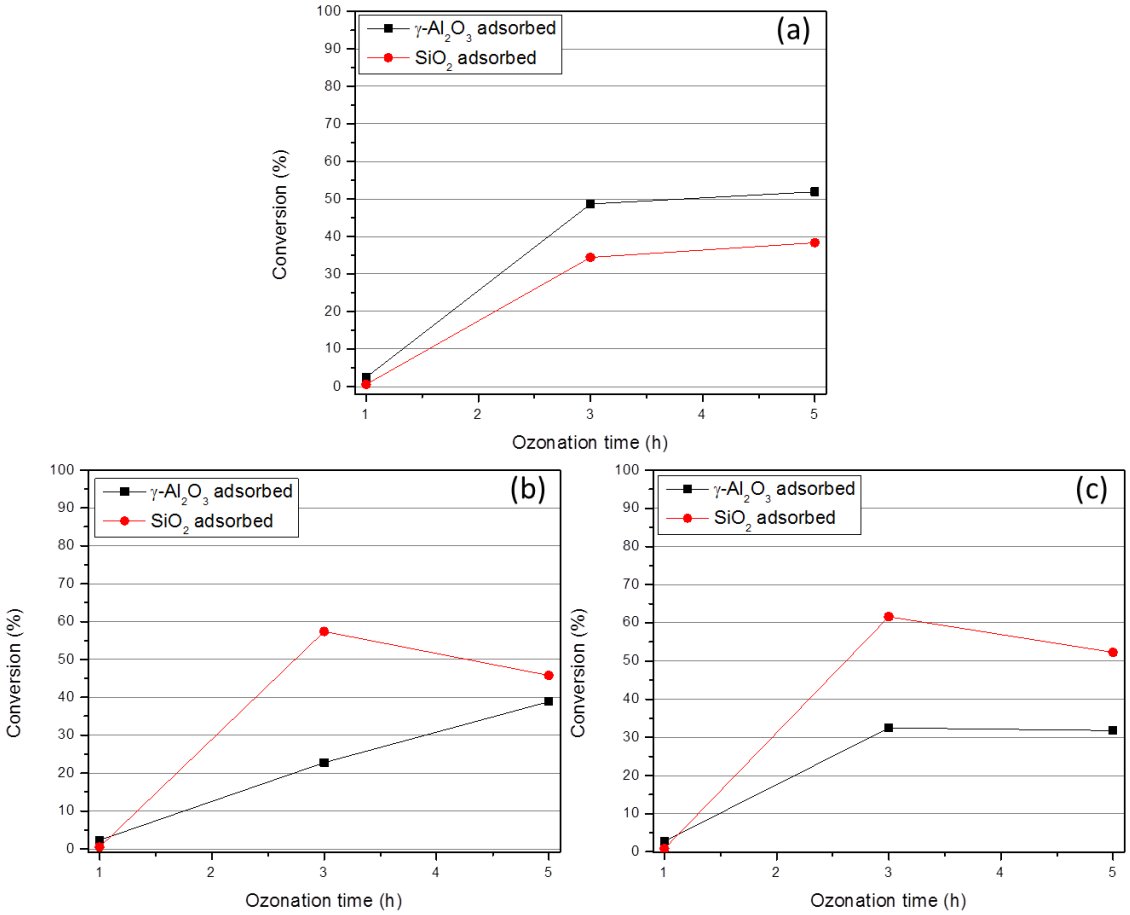

Figure 4.1. Conversion profiles of (a) *m*-cresol, (b) *o*-cresol and (c) *p*-cresol adsorbed on γ-Al_2O_3 and SiO_2 packed in a glass column.

A reactivity trend of the substrates when adsorbed on γ-Al_2O_3 at 3 h of reaction time, assumed the order of *m*- > *p*- > *o*-cresol and *p*- > *o*- > *m*-cresol on SiO_2 adsorbent. Interestingly, the drop in conversion percentages as the reaction progressed can be used to estimate the amount of oxidation products that turned into CO_2 gas, using the accurate values in Table 4.1.

Table 4.1. Percentage conversion results for the ozonation of various cresols adsorbed on γ-Al_2O_3 and SiO_2 packed in a glass column.

Entry no.	**Reaction time (h)**	***m*-cres. conv. (%)**		***o*-cres. conv. (%)**		***p*-cres. conv. (%)**	
		γ-Al_2O_3	**SiO_2**	**γ-Al_2O_3**	**SiO_2**	**γ-Al_2O_3**	**SiO_2**

1	1	2.50	0.55	2.31	0.49	2.80	0.82
2	3	48.67	34.45	22.76	57.42	32.51	61.60
3	5	51.88	38.35	38.90	45.79	31.78	52.28

The γ-Al_2O_3 adsorbent was observed to be more catalytically active towards the oxidative degradation of *m*-cresol whereas the SiO_2 adsorbent showed more prominent activity towards *o*-cresol and *p*-cresol degradation.

The oxidation products that could be identified, includes tolyl acetates (**TAs**), dihydroxy toluenes (**DTs**) and diethyl maleate (**DM**) as seen in Table 4.2. In particular, *m*-tolyl acetate (***m*-TA**), *o*-tolyl acetate (***o*-TA**) and *p*-tolyl acetate (***p*-TA**) were obtained from the *m*-, *o*- and *p*-cresol substrates, respectively. The **2,3-DT** and **3,4-DTs** were detected to be the favored oxidation products from the early ozonation stages of the *m*-cresol, whilst, *o*- and *p*-cresols respectively produced **2,5-DT** and **3,4-DT**. Diethyl maleate was produced nearly, in all ozonation reactions. Table 4.2 presents the substrates conversion and product selectivities from all the column mounted ozonation reactions. When *m*-cresol was adsorbed on γ-Al_2O_3, up to 40.8% of ***m*-TA** and 4.3% of **2,3-DT** were selectively produced in 1 h, however, these products decreased over time due to further reaction with ozone and plausibly, interaction with other reactive species within the reaction. The **DM** could not be detected in 1 h, which suggested the product to have resulted from extensive ozonation of other relative intermediate species. Furthermore, the selectivity towards **DM** was increased with time (**entry 1**).

The *m*-cresol adsorbed on SiO_2 (**entry 2**) produced **3,4-DT** of 27.4% in selectivity and no **DM** was detected in this reaction, proposing that, the stage of **DM** formation was never reached in a reaction, which could be explained by high selectivities of ***m*-TA** and **3,4-DT**. The *o*-cresol selectively got converted to 90.3% of ***o*-TA** and 7.4% of **2,5-DT** in 1 h when adsorbed on γ-Al_2O_3 (**entry 3**) and from 3–5 h, the selectivity of **DM** was observed to decrease, suggesting its low persistence towards O_3 attack due to Sp^2-carbons in its structure [9]. **Entry 4** (Table 4.2) displays a case that could draw some confusion, the SiO_2 adsorbed *o*-cresol gave 100% selectivity of ***o*-TA** in 1 h and the latter appears to decrease then increase again over time, however, this could be linked to the substrate conversion that significantly decreased from 3–5 h,

plausibly due to continuous ozone attack upon other oxidation products leading to their partial mineralization. The aforementioned would be true for percentage selectivities of **2,5-DT** and **DM** oxidation products in **entry 4**.

Table 4.2. Substrate conversion and product selectivity from ozonation reactions in a column.

Entry no.	Adsorbed substrate	Reaction time (h)	Conversion (%)	Selectivity (%)			
				Tolyl acetates	Dihydroxy Toluenes	Diethyl maleate	Unidentified products
1	*m*-cresol on γ-Al_2O_3	1	2.50	40.78	4.31	0	54.91
		3	48.67	23.68	3.36	5.33	67.63
		5	51.88	17.09	1.57	7.38	73.96
2	*m*-cresol on SiO_2	1	0.55	46.35	27.37	-	26.28
		3	34.45	34.49	14.22	-	51.29
		5	38.35	23.53	1.28	-	75.19
3	*o*-cresol on γ-Al_2O_3	1	2.31	90.29	7.41	-	2.30
		3	22.76	43.97	3.92	14.50	37.61
		5	38.90	17.75	3.81	5.36	73.08
4	*o*-cresol on SiO_2	1	0.49	100	0	0	0
		3	57.42	13.78	2.29	6.29	77.64
		5	45.79	46.20	7.48	34.72	11.60
5	*p*-cresol on γ-Al_2O_3	1	2.80	54.82	16.12	0	29.06
		3	32.51	17.63	11.86	4.65	65.86
		5	31.78	34.43	14.92	4.24	46.41
6	*p*-cresol on SiO_2	1	0.82	100	0	0	0
		3	61.60	21.34	17.04	18.67	42.95
		5	52.28	58.01	21.55	9.00	11.44

The following example could provide a logical reasoning regarding the increasing-then-decreasing percentage conversions with time as observed in **entries 4**, **5** and **6**: A hypothetical substrate A is oxidized and only 30% gets converted into products, before the unreacted 70% is converted to products, the oxidation products (making up 30%) are further oxidized to mineralization completely or in part. Hence, the percentage conversion of substrate A would first increase then decreases.

Despite the success of column ozonation in degrading cresol isomers to some extent, poor column packing resulted to uneven ozone distribution within the column and color differences that were visible on all sides of the column helped signify this observation.

4.2. Uncatalyzed and catalyzed ozonation of cresols in a glass reactor

The ozone-based oxidation of cresol isomers was conducted using a method that is herein detailed in Sections 2.4.2 (p. 44) and 2.4.3 (p. 45). Initially, the *m*-, *o*- and *p*-cresol were ozonated in the absence of a catalyst and subsequently in the presence of activated charcoal, γ-Al_2O_3, SiO_2 and V_2O_5 as heterogeneous catalysts (Figure 4.2). Notably, the uncatalyzed oxidation of the cresol isomers resulted in different substrate conversion percentages, assuming the order of *p*- > *o*- > *m*-cresol (Figures 4.2c, b and a, respectively) in terms of converted substrate amount at 24 h of reaction time. In contrast to some literature, the cresols reactivity order (*p*- > *m*- > *o*-cresol) was reported by Valsania *et al.* [**8**] in the absence of a catalyst. The activated charcoal catalyst was observed to have enhanced the degradation of cresol isomers as compared to the uncatalyzed reactions over 24 h periods. The differences in substrate conversions between uncatalyzed and activated charcoal catalyzed reactions are more significant in the oxidation of *m*-cresol from 15–24 h (Figure 4.2a) followed by that of *p*-cresol which starts from 9–24 h (Figure 4.2c) and the *o*-cresol appeared to be mostly converted when no catalyst was used than when activated charcoal was utilized. The reactivity order of the substrates changed to *p*- > *m*- > *o*-cresol when activated charcoal was used as a catalyst.

The γ-Al_2O_3 catalyst was found to be active in the ozonation of *m*-cresol (Figure 4.2a), reaching up to above 45% of *m*-cresol conversion, whereas, only about 30% of *o*- and *p*-cresol (Figure 4.2 b–c) was converted in 24 h, drawing the substrate reactivity order of *m*- > *o*- > *p*-cresol. Moreover, the SiO_2 catalyst outperformed the rest of the catalysts, explicitly from 21–24 h. Up to 57% of *p*-cresol (Figure 4.2c), 43% of *o*-cresol (Figure 4.2b) and 51% for *m*-cresol (Figure 4.2a) reacted with ozone to form oxidation products in 24 h. The logarithmic conversion curves obtained in both *o*- and *p*-cresol catalyzed by SiO_2 suggests a low increase in percentage conversion beyond 24 h while the exponential curve seen for *m*-cresol calculates the opposite. The SiO_2 catalyst led to a substrate reactivity order of *p*- > *m*- > *o*-cresol which is in agreement with literature [**8**].

The V_2O_5 catalyst formed logarithmic substrate conversion curves over time and it recorded relatively higher amounts of *m*-cresol converted to products between 3–18 h of reaction period. The catalyst achieved 40% conversion of *m*-cresol, 31% of *o*-cresol and 42% of *p*-cresol as shown in Figures 4.2a–c, respectively. The V_2O_5 catalyst resulted in the cresols reactivity order of *p*- > *m*- > *o*-cresol, with *p*-cresol being the most converted substrate and *o*-cresol being the least at 24 h of reaction.

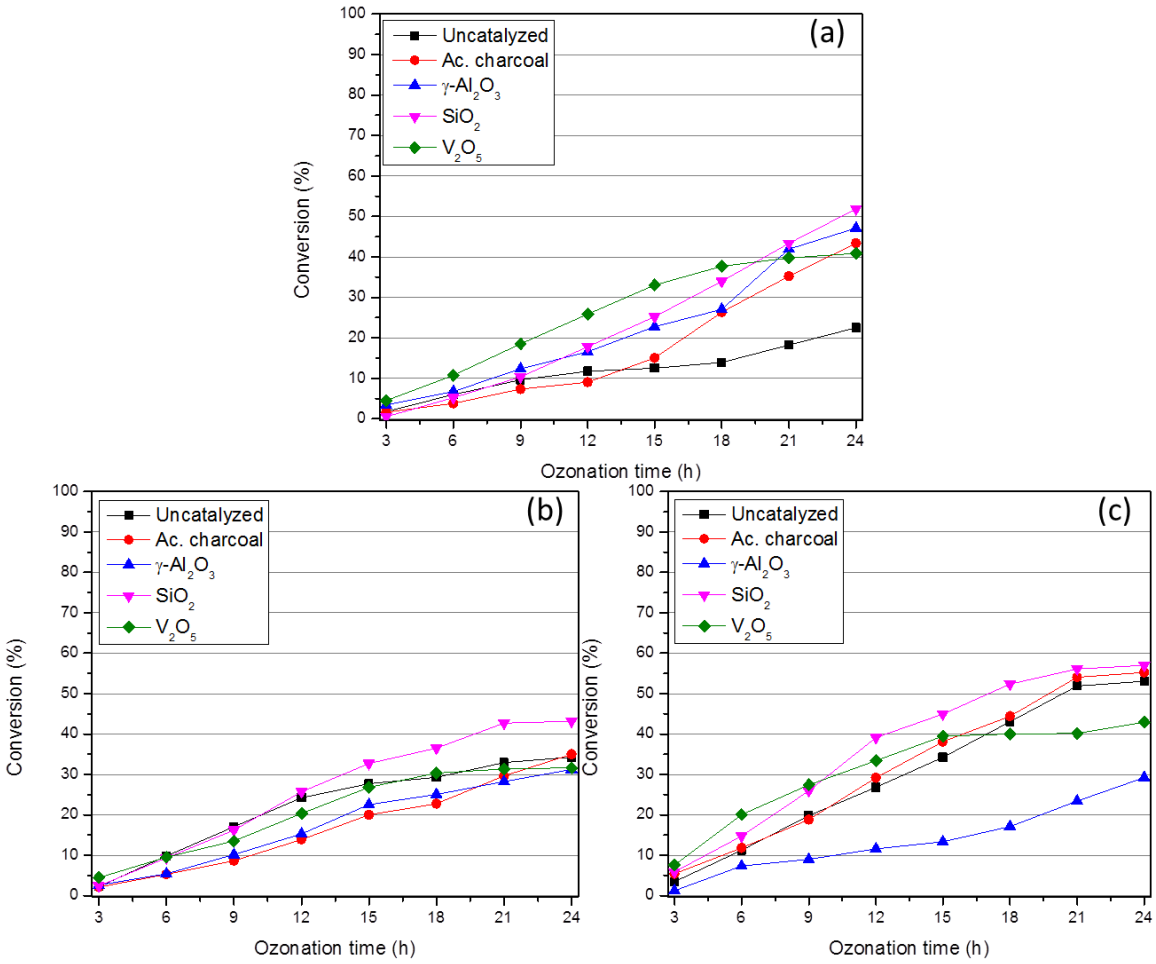

Figure 4.2. Percentage conversions of (a) *m*-cresol, (b) *o*-cresol and (c) *p*-cresol from uncatalyzed and activated charcoal, γ-Al_2O_3, SiO_2 and V_2O_5 catalyzed ozonation reactions.

The cresol isomers were observed to be separately discerning of catalysts used in their degradation, and thus the performance of each catalyst differs from substrate to substrate at a

specific reaction time. The order of catalyst performance in oxidation of *m*-cresol (Figure 4.2a) is apparently SiO_2 > γ-Al_2O_3 > activated charcoal > V_2O_5 which changes to SiO_2 > activated charcoal > V_2O_5 > γ-Al_2O_3 for *o*-cresol (Figure 4.2b) and SiO_2 > activated charcoal > V_2O_5 > γ-Al_2O_3 for *p*-cresol (Figure 4.2c) in 24 h of reaction time. Table 4.3 display accurate conversion values of cresol isomers from uncatalyzed and catalyzed ozonation reactions that are graphically represented in Figure 4.2.

Table 4.3. Conversion of cresols from uncatalyzed and catalyzed ozone–based oxidation.

Substrate Ozonized	**Uncatalyzed**	**Ac. charcoal**	**γ-Al_2O_3**	**SiO_2**	**V_2O_5**
m-cresol	Conv. %	Conv. %	Conv. %	Conv. %	Conv. %
3 h	1.79	1.66	3.48	0.51	4.50
6 h	5.99	3.81	6.76	5.25	10.75
9 h	9.62	7.37	12.35	10.32	18.53
12 h	11.76	9.05	16.56	17.84	25.87
15 h	12.53	15.07	22.76	25.26	33.03
18 h	13.91	26.37	27.06	33.98	37.72
21 h	18.23	35.23	41.95	43.33	39.77
24 h	22.54	43.42	47.11	51.87	40.86
o-cresol	Conv. %	Conv. %	Conv. %	Conv. %	Conv. %
3 h	2.23	2.14	2.64	2.42	4.46
6 h	9.83	5.29	5.39	9.32	9.54
9 h	17.04	8.66	10.16	16.21	13.53
12 h	24.25	13.87	15.30	25.72	20.33
15 h	27.72	20.00	22.50	32.69	26.81
18 h	29.27	22.77	25.07	36.51	30.37
21 h	32.92	29.67	28.22	42.72	31.32
24 h	34.29	35.01	31.24	43.17	31.66
p-cresol	Conv. %	Conv. %	Conv. %	Conv. %	Conv. %
3 h	3.45	5.39	1.23	5.86	7.57
6 h	11.23	11.80	7.32	14.77	20.07
9 h	19.79	18.82	8.99	25.94	27.38
12 h	26.84	29.19	11.56	39.09	33.42
15 h	34.23	38.12	13.34	44.92	39.45

18 h	43.06	44.41	17.12	52.34	39.97
21 h	51.90	54.03	23.43	56.14	40.16
24 h	53.06	55.26	29.24	57.01	42.93

For comparison purposes, average percentage conversions from all reactions were calculated (percentage conversions obtained in every 3 h of an oxidation reaction were added and averaged), mainly to best understand the overall activity of each catalyst on an average. Figure 4.3 displays the average percentage conversions of cresol isomers from uncatalyzed and catalyzed (activated charcoal, γ-Al_2O_3, SiO_2, V_2O_5) ozonation of each substrate. The lowest average conversion of *m*-cresol into oxidation products was observed in the uncatalyzed reaction and the use of catalyst materials improved the conversion of *m*-cresol. Activated charcoal was the least active of all catalyst in the oxidation of the latter substrate whereas V_2O_5 was the most active, on average, drawing a performance sequence of V_2O_5 > SiO_2 > γ-Al_2O_3> activated charcoal.

Notably, only the SiO_2 catalyst (Figure 4.3) was active towards degradation of *o*-cresol and the other catalysts were inactive, with activated charcoal as the most inactive and V_2O_5 the least, on average. Thus, the inactivity order of gamma alumina, vanadia and activated charcoal in the oxidation of *o*-cresol was V_2O_5 < γ-Al_2O_3 < activated charcoal. In the oxidation of *p*-cresol on the other hand, only a γ-Al_2O_3 catalyst was found to be inactive amongst the four catalysts and the activity sequence was in the order of SiO_2 > activated charcoal > V_2O_5 on average.

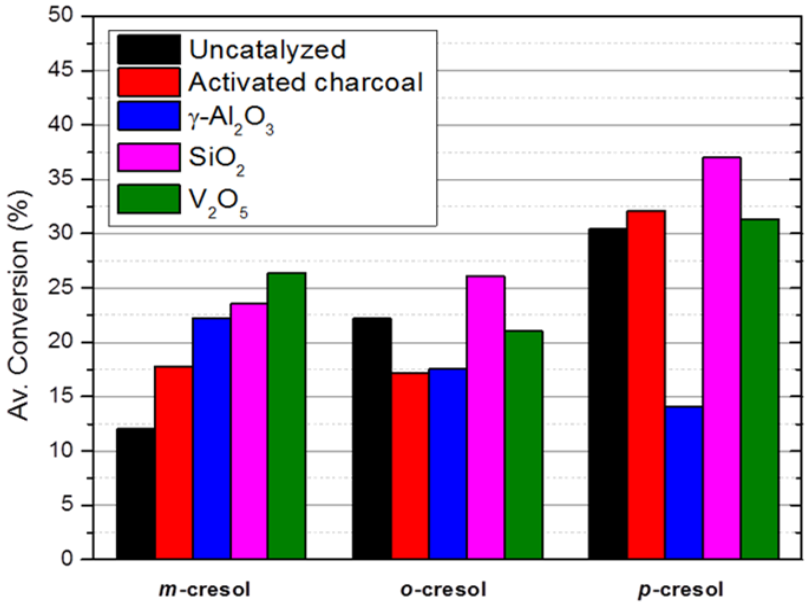

Figure 4.3. Average percentage conversions of cresol isomers from uncatalyzed and activated charcoal, γ-Al_2O_3, SiO_2, V_2O_5 catalyzed ozonation reactions.

The percentage selectivities of the resultant oxidation products that could be identified were recorded and calculated from the GC-MS peak integration data. Figure 4.4 display the *m*-cresol oxidation products and their selectivities in the uncatalyzed and in presence of activated charcoal, γ-Al_2O_3, SiO_2 and V_2O_5 as catalysts. The *m*-tolyl acetate (***m*-TA**) (Figure 4.4a) is produced the most in the absence of a catalyst, followed by activated charcoal, γ-Al_2O_3, V_2O_5 and the least with SiO_2 catalyst. Activated charcoal selectively favored the formation of 2,3-dihydroxy toluene (**2,3-DT**) (Figure 4.4b) slightly higher than the other catalysts. Moreover, activated charcoal displayed similar selectivities towards diethyl maleate (**DM**) formation to that of the uncatalyzed reaction within 3–24 h while the rest of the catalysts relatively produced less than 3% of the product (Figure 4.4c). Activated charcoal further outperformed the metal oxide catalysts (Figure 4.4d), producing above 20% of diethyl oxalate (**DO**) followed by SiO_2, γ-Al_2O_3 then a V_2O_5 catalyst and this product was hardly formed during the uncatalyzed oxidation of *m*-cresol.

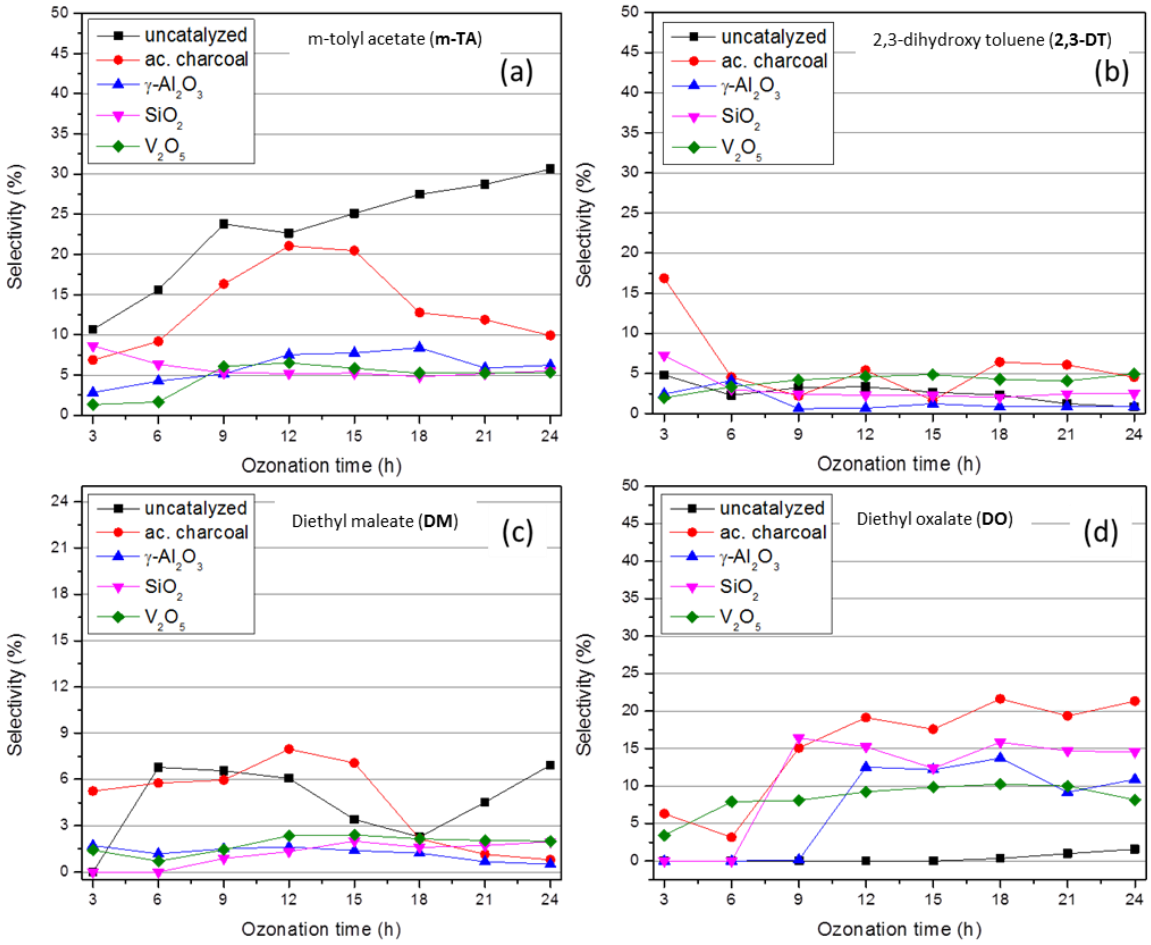

Figure 4.4. Percentage selectivities of the *m*-cresol products (a) ***m*-TA**, (b) **2,3-DT**, (c) **DM** and (d) **DO** from uncatalyzed and activated charcoal, γ-Al_2O_3, SiO_2 and V_2O_5 catalyzed ozonation reactions.

The uncatalyzed and catalyzed ozonation of the *o*-cresol yielded the *o*-tolyl acetate (***o*-TA**), 2,5-dihydroxy toluene (**2,5-DT**), diethyl maleate (**DM**), diethyl oxalate (**DO**) and a variety of unidentified oxidation products. The selectivities of aforementioned products are shown in Figure 4.5. It is apparent that activated charcoal highly promotes the formation of ***o*-TA** (Figure 4.5a) over the 24 h duration as compared to other catalysts followed by γ-Al_2O_3. The SiO_2 and V_2O_5 catalysts were observed to relatively inhibit the formation of ***o*-TA** even though SiO_2 displayed highest selectivity in the first 3 h of the reaction. The **2,5-DT** (Figure 4.5b) was the least formed oxidation product though significant selectivity improvements were introduced by

catalysts. Almost all four catalysts (Figure 4.5c), except for activated charcoal, presented low product selectivity towards **DM** within the first 12 h.

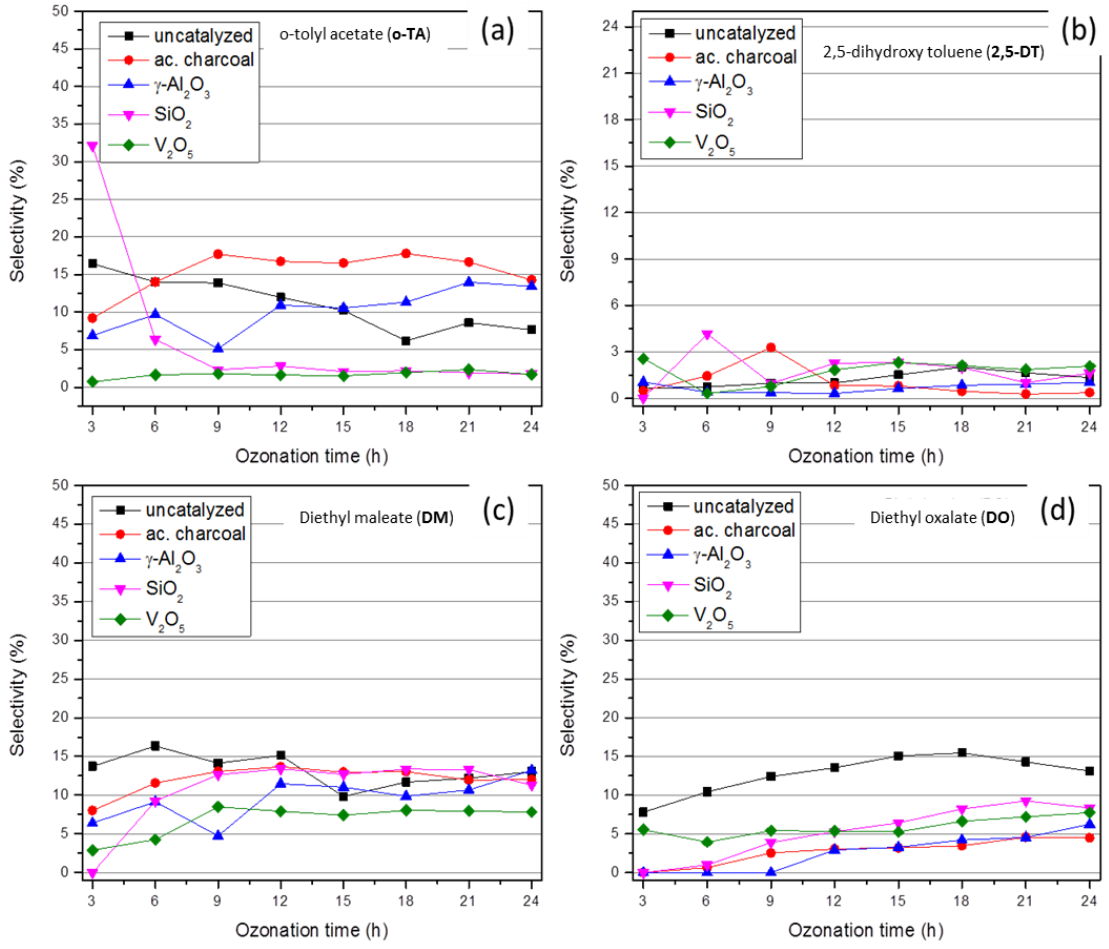

Figure 4.5. Percentage selectivities of the *o*-cresol products (a) ***o*-TA**, (b) **2,5-DT**, (c) **DM** and (d) **DO** from uncatalyzed and activated charcoal, γ-Al_2O_3, SiO_2 and V_2O_5 catalyzed ozonation reactions.

However, activated charcoal and SiO_2 selectively favours the **DM** formation from 12–24 h compared to the uncatalyzed *o*-cresol oxidation. Furthermore, less **DO** was formed (Figure 4.5d) during catalyzed oxidation of the *o*-cresol while more formation can be seen in the uncatalyzed reaction.

The *p*-cresol ozonation resulted in *p*-tolyl acetate (***p*-TA**), 3,4-dihydroxy toluene (**3,4-DT**), diethyl maleate (**DM**), diethyl oxalate (**DO**) and other unidentified oxidation products. Figure 4.6 illustrates the identified products and their selectivities under catalyzed and uncatalyzed reactions. The formation of ***p*-TA** and **DM** (Figures 4.6a and 4.6c) was promoted the most in activated charcoal catalyzed oxidation reactions of *p*-cresol, whereas γ-Al_2O_3, SiO_2 and V_2O_5 resulted in less formation of ***p*-TA** and **DM**.

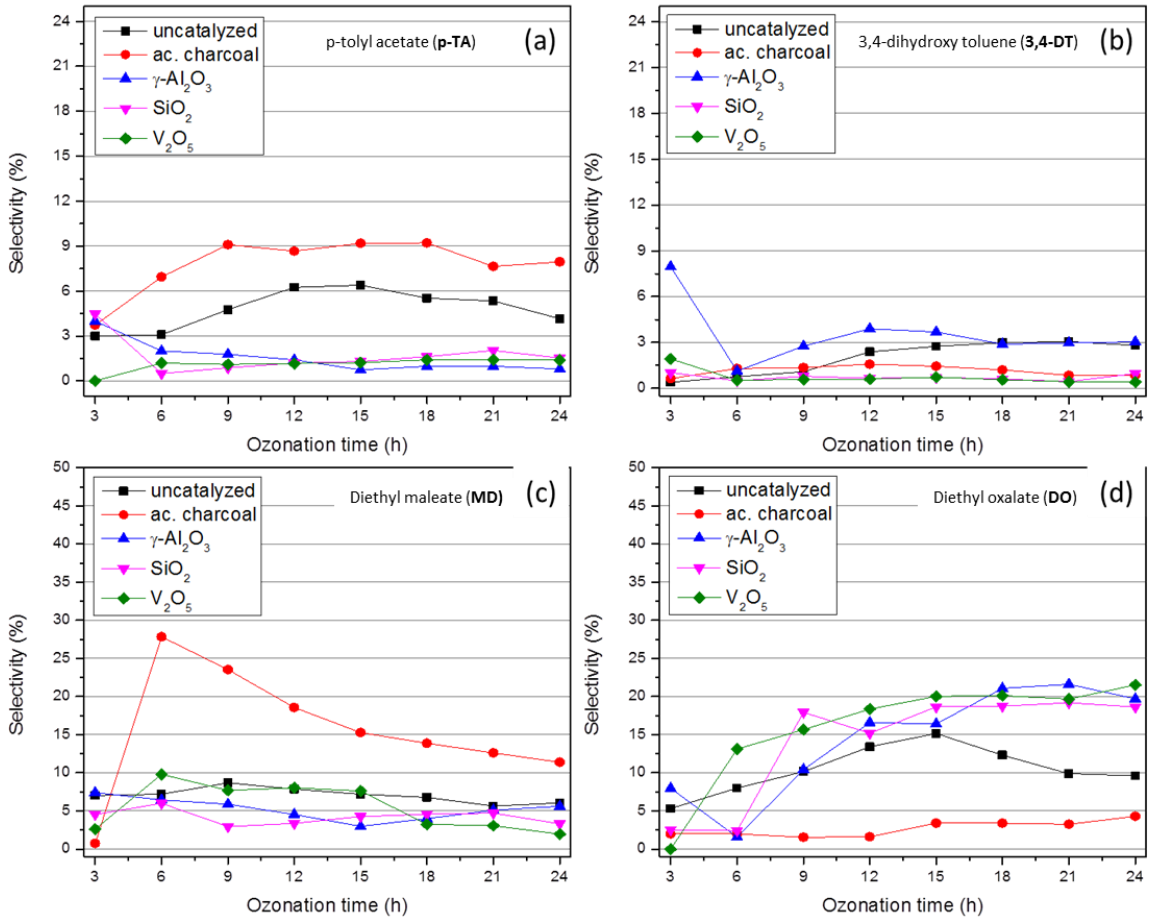

Figure 4.6. Percentage selectivities of the *p*-cresol products (a) ***p*-TA**, (b) **3,4-DT**, (c) **DM** and (d) **DO** from uncatalyzed and activated charcoal, γ-Al_2O_3, SiO_2 and V_2O_5 catalyzed ozonation reactions.

In Figure 4.6d, the γ-Al_2O_3, V_2O_5 and SiO_2 formed more of **DO** than the uncatalyzed reaction while activated charcoal formed the least, even far less than the uncatalyzed reaction. Lastly, γ-

Al_2O_3 was noted to enhance the **3,4-DT** (Figure 4.6b) formation, better than in the uncatalyzed oxidation and the rest of the catalysts formed less of **3,4-DT**, less than in the uncatalyzed oxidation of the *p*-cresol.

The exact data for the selectivities of the oxidation products from all cresol isomers, as discussed in this Section, are presented in the Appendix B (Table B1–B15, pp. 139–144). It is worth mentioning that, the oxidation products obtained during column mounted ozonation reactions were found to be the same as those from reactor reactions and this is highlighted in products characterization below.

4.3. Characterization of the oxidation products of the three cresol isomers

Cresol isomers were oxidized using ozone in a glass column and a glass reactor, through the methods presented in Section 2.4 (pp 43) and the resultant products were characterized using the FT-IR, HPLC-UV and GC-MS [see Section 2.3 (pp 34) for specific instrumentation details].

4.3.1. Fourier Transform-Infrared Spectroscopy (FT-IR) on oxidation products

Post oxidation of each cresol isomer, the crude or mixture of products was analyzed for qualitative purposes on the FT-IR and a crude product from the activated charcoal catalyzed ozonation of m-cresol after 24 h was herein used as a representative of all other ozonation reactions at 24 h since they displayed similar FT-IR results. The FT-IR spectra of *m*-cresol and the oxidation products of *m*-cresol are shown in Figure 4.7. The *m*-cresol spectrum (Figure 4.7a) shows a very broad absorption peak at 3372 cm^{-1} which is characteristic to O–H bond stretching of the phenol functional group and vibration of aromatic carbons (-C=C-) can be found at ~1400 cm^{-1}, which is representative of the benzene ring.

The ozonated substrate (Figure 4.7b) displayed the presence of new functional groups, marking the formation of the oxidation products. An absorption at 1765 cm^{-1} can be assigned to the stretching of the O=C< bond, either from the esters, anhydrides or ketones. The O–H stretching frequency can still be seen in the product mixture and it serves as both a confirmation of incomplete conversion of the substrate to products and formation of alcohols and carboxylic acids. Furthermore, the sharp absorption peak at 2977 cm^{-1} denotes the Sp^3, C–H bond stretching, implying an increased number of the C–H bonds present [**10**]. In comparison to the

spectrum of the substrate (Figure 4.7a), the product mixture (Figure 4.7b) shows an absorption peak that could be assigned to the alkoxy (1047 cm^{-1}, C–O–) functional group instead of a noisy fingerprint region.

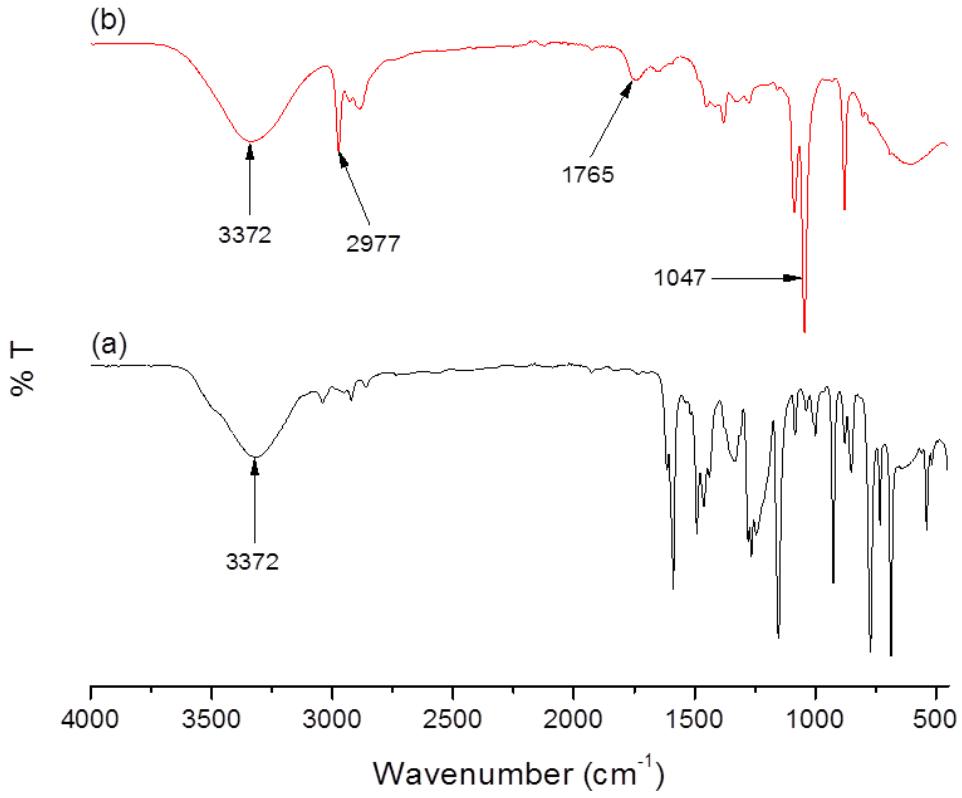

Figure 4.7. FT-IR spectra, showing both the (a) unreacted and (b) ozonated *m*-cresol substrate in the presence of activated charcoal catalyst at 24 h of reaction.

4.3.2. High performance liquid chromatography (HPLC) on oxidation products

The FT-IR results suggested the formation of similar oxidation products from substrate to substrate and the HPLC analysis gave clarity in this regard. The HPLC chromatograms of the oxidation product mixtures of *m*-, *o*- and *p*-cresol are shown in Figure 4.8. Cresol substrates were observed to share similar retention times on the HPLC column plausibly due to their isomeric nature, and this effect can be further seen on their oxidation products, marked by asterisk (*) in

Figure 4.8 which may be due to cresols forming the similar number of oxidation products or the isomeric nature of the resultant products.

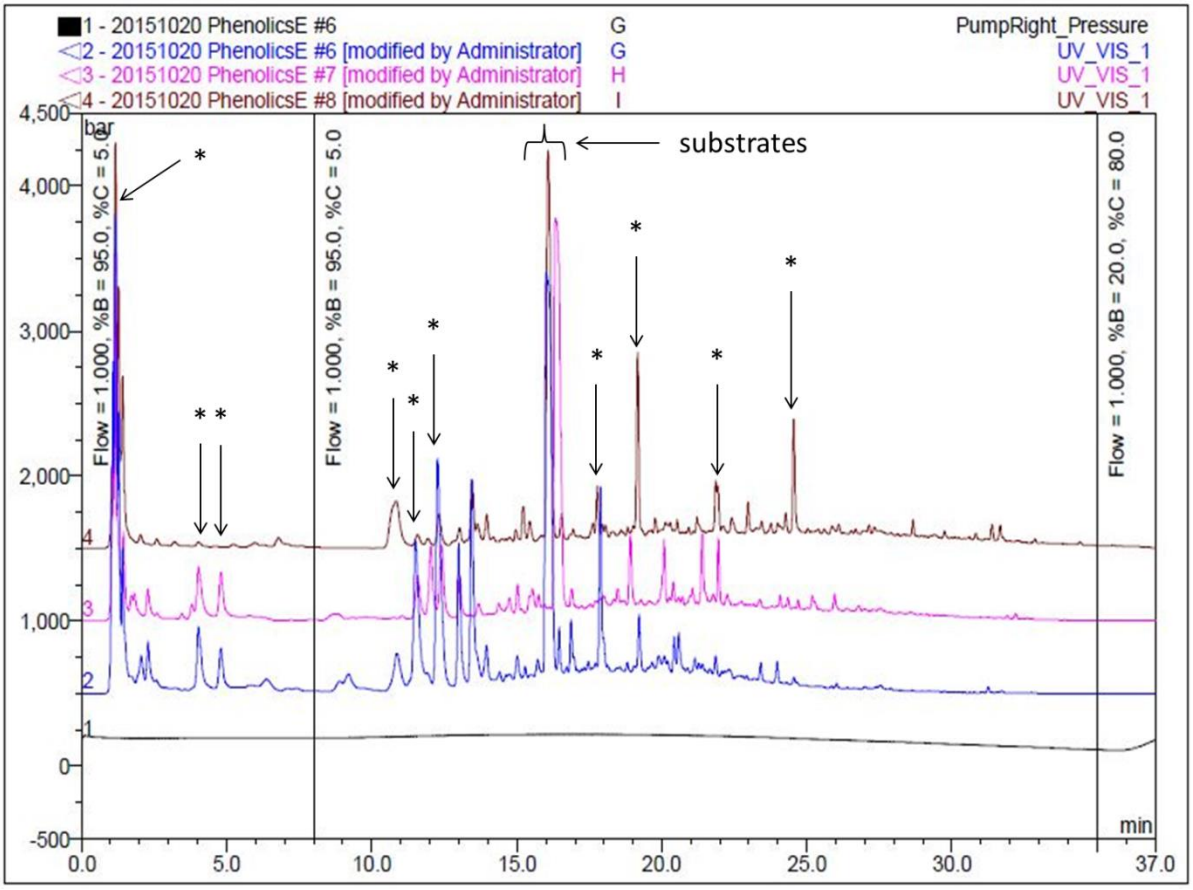

Figure 4.8. HPLC chromatograms of the oxidized (G) *m*-cresol, (H) *o*-cresol and (I) *p*-cresol, showing their (*) isomeric oxidation products at 24 h using γ-Al_2O_3 as a catalyst.

4.3.3. Gas chromatography with Mass Spectrometer (GC-MS) on oxidation products

The gas chromatography, coupled with mass spectrometer was used to analyze the product mixture and identify the products. Figure 4.9 shows a chromatogram of *m*-cresol oxidation products obtained from the column oxidation of the substrate at 3 h, which is typical of all cresols product mixtures. However, the number of peaks tends to increase over time since O_3 continually attack substrate as well as the formed products. The inserted chromatogram is that of the *m*-cresol ozonated in a glass reactor for 12 h, and apparently, the column reactions produced a similar number of oxidation products to those produced in reactor reactions (uncatalyzed/

catalyzed). The Figure 4.9 displays the unreacted *m*-cresol, resultant ***m*-TA**, **DM** and **3,4-DT** products and the rest of the chromatographic peaks could not be identified.

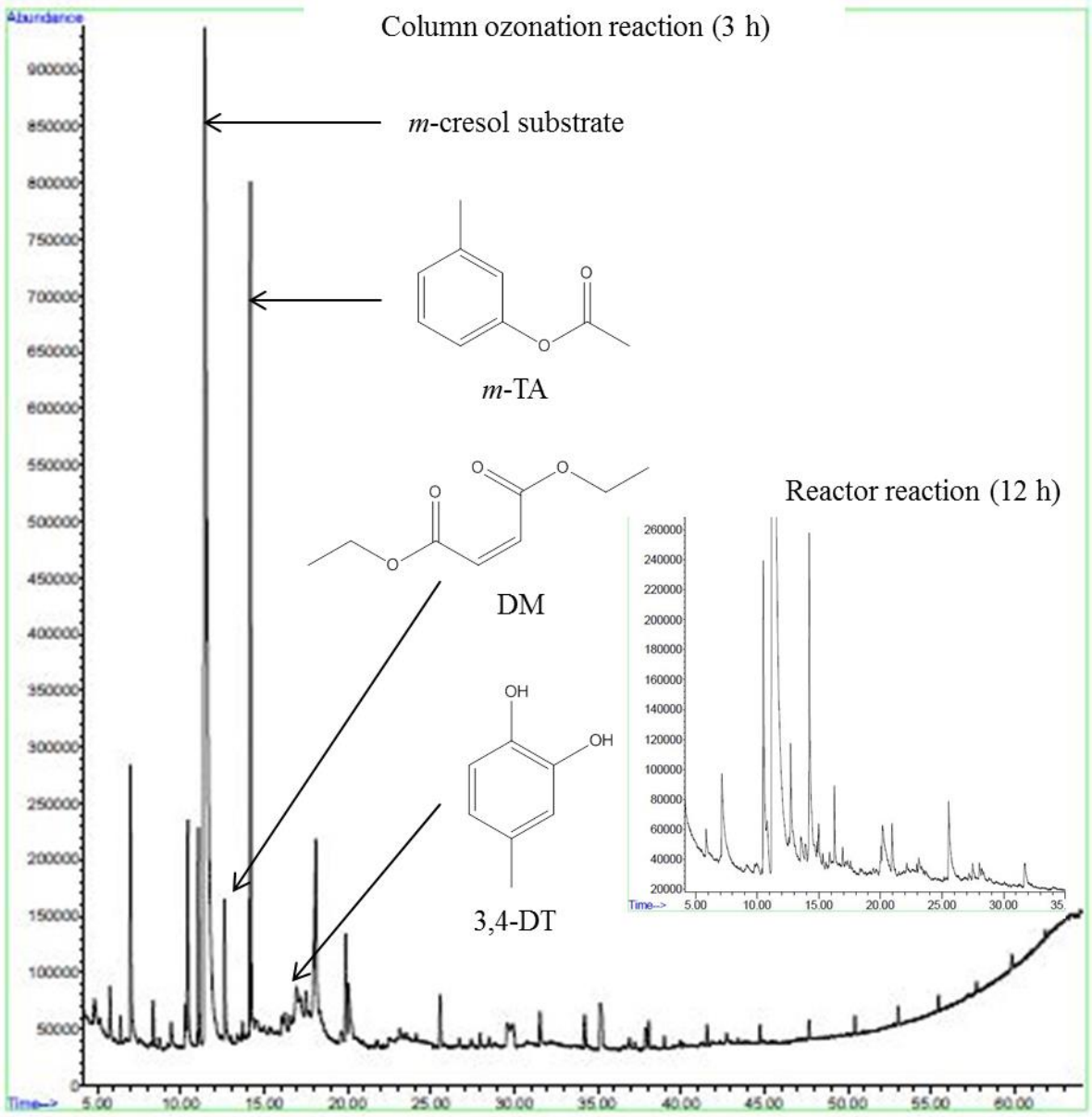

Figure 4.9. Chromatogram of ozonated *m*-cresol using column ozonation reaction (3 h reaction time), where γ-Al_2O_3 was used as adsorbent (insert, reactor ozonated *m*-cresol for 12 h).

A positive identification was made by Mass Spectrometry analyses for **2,3-DT** product as seen in Figure 4.10. The **2,3-DT** product was achieved from the O_3 mediated oxidation of the *m*-cresol both in the absence and presence of different catalyst materials. In literature, cresol isomers are

readily oxidized by either O_2/ O_3 to produce dihydroxy toluenes and usually, more than one of **DTs** tends to be present in a product mixture of each cresol [**8,11**]. However, there are some cases where other degradation methods have been utilized to yield the **DTs** from these isomers, especially in the photocatalytic study that was done by Abdollahi *et al.* [**12**]. Mass spectral signals at *m/z* 16, 18, 78 and 124 strongly confirms the product to contain a methyl, hydroxyl, benzyl and 2,3-dihydroxy tolyl fragments, respectively. It is worth mentioning that **2,3-DT** have been reported as one of oxidation products of the *m*-cresol [**8**].

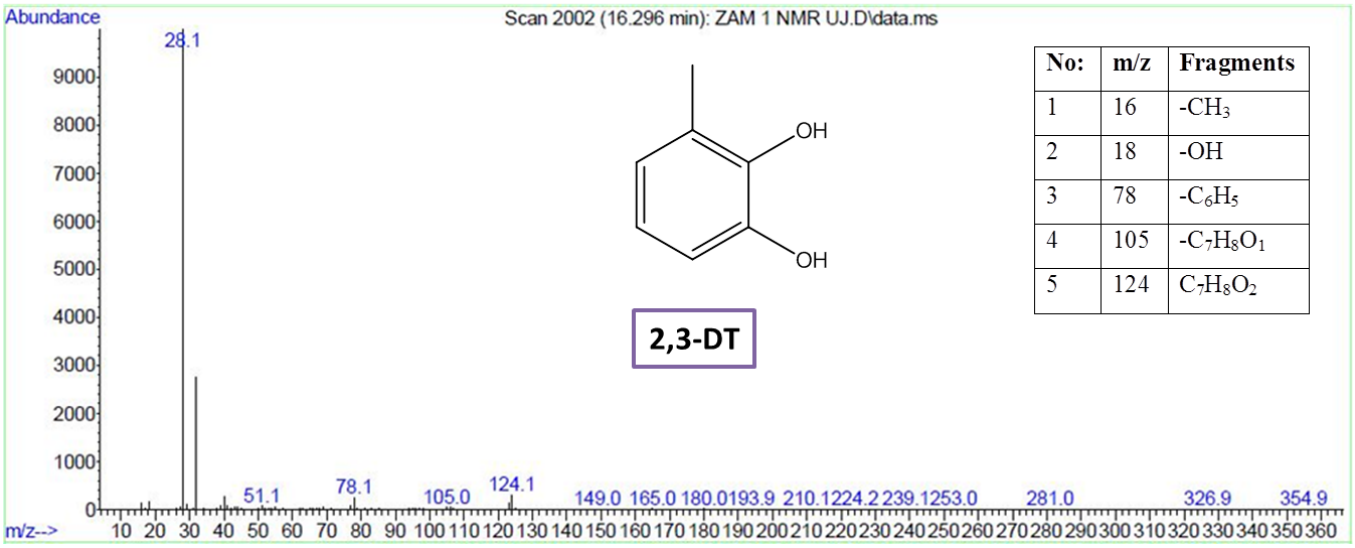

No:	m/z	Fragments
1	16	$-CH_3$
2	18	-OH
3	78	$-C_6H_5$
4	105	$-C_7H_8O_1$
5	124	$C_7H_8O_2$

Figure 4.10. Mass spectrum of the **2,3-DT** oxidation product and its fragmentation.

The **3,4-DT** (Figure 4.11) was also detected as an oxidation product of *m*-cresol in few instances but mainly as a product from *p*-cresol oxidation and the **3,4-DT** formation from *p*-cresol oxidation have been reported previously [**11**]. The detected MS signals includes *m/z* 16, 18, 107 and 124, which corresponds to the methyl, hydroxyl, methylphenoxyl and the molecular weight of **3,4-DT**, respectively. Even though there was no sound evidence of the hydroxyl radical ($HO^{\cdot}$) formation pursued in this work, the possibility of its production can be considered. The latter would be in agreement with O_3 ability to decompose and form $HO^{\cdot}$ in water [**13**], but in this regard a hydroxyl group functionalized toluene (cresol isomer). This would further propose that,

the highly reactive HO$^{\cdot}$ species were formed during the early stages of the ozonation reaction and subsequently initiated a hydroxylation of cresols resulting in dihydroxy toluenes.

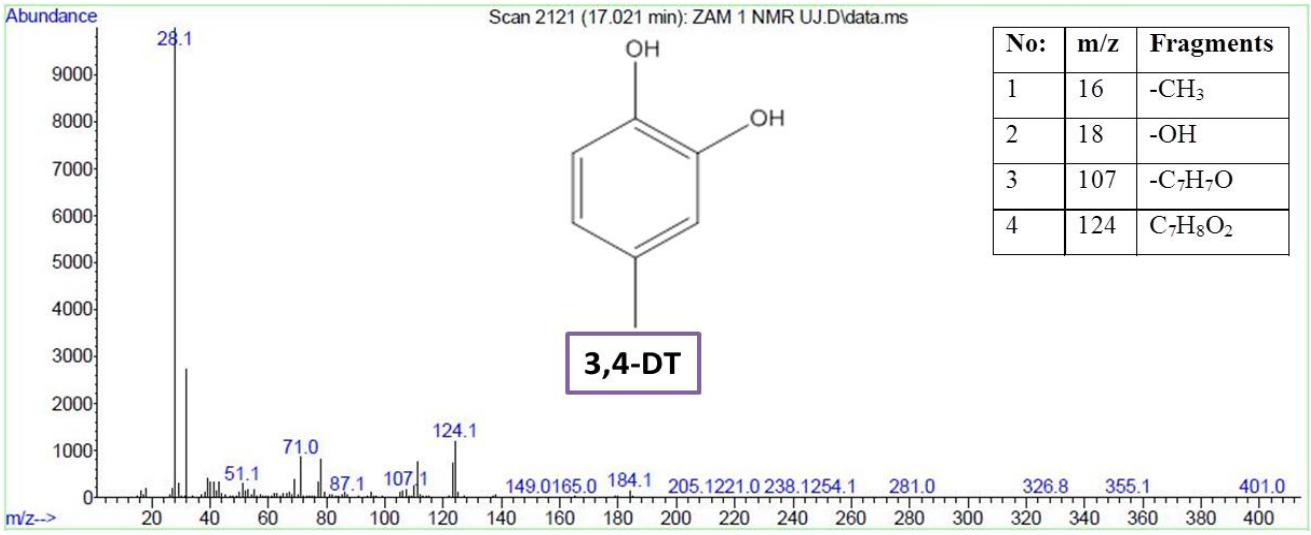

No:	m/z	Fragments
1	16	-CH_3
2	18	-OH
3	107	-C_7H_7O
4	124	$C_7H_8O_2$

Figure 4.11. Mass spectrum of the **3,4-DT** oxidation product and its fragmentation.

The *o*-cresol was no exception, since the **2,5-DT** (Figure 4.12) oxidation product was identified after its ozonation in the absence and presence of a catalyst system. The strong electron-donating nature of the hydroxyl group of the *o*-cresol than the methyl counterpart of the substrate is believed to have activated the position *para*- to the hydroxyl for hydroxyl radical attack, resulting in **2,5-DT** (*i.e.* the hydroxyl and methyl groups are *ortho-para* directors) in Figure 4.12.

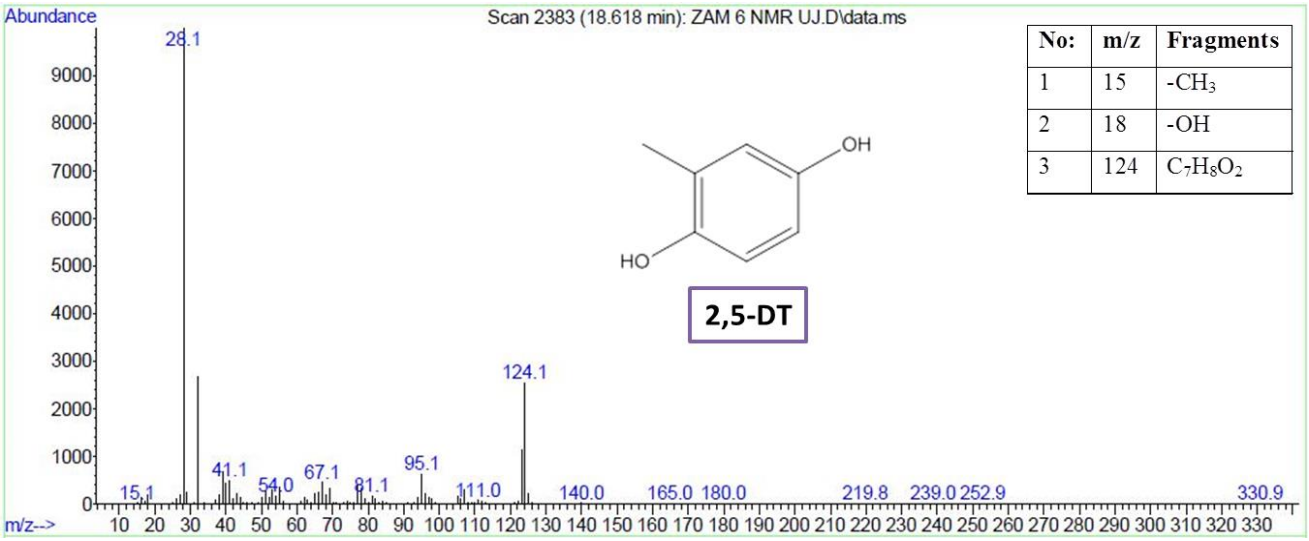

Figure 4.12. Mass spectrum of the **2,5-DT** oxidation product and its fragmentation.

Cresol isomers are merely, well-known phenol derivatives containing a single methyl functional group. However, their proposed O_2/ O_3 mediated oxidation reaction path-ways have shown great similarities from the previous studies. For instance, Kulkarni and Dixit [**14**] proposed a phenol degradation mechanism that begins by hydroxylation of the benzene ring followed by ring breakage that further forms 2,5-dioxo-3-hexenedioic acid, muconic acid and consequently maleic acid and more. More than two decades later, Valsania *et al.* [**8**] distinctively proposed a cresol degradation mechanism that follows the similar order to that of phenol but interestingly resulted in maleic acid formation over time. The literature emphasizes the production of the maleic acid as one of the oxidation products of cresols and their parent phenol compound.

In this work, a maleic acid ester, **DM** (Figure 4.13) was detected nearly in all ozonation and catazone reactions of cresol isomers. This may have resulted from immediate dissolution of the collected ozonated sample in ethanol (see Section 2.4, pp 43), consequently initiating the esterification of maleic acid to yield the diethyl maleate (**DM**) ester. In Figure 4.13, the MS signals seen are *m/z* 127 (M^+), 112 (M^+ - 15), 99 (100%, M^+ - 28), 54 and 18.

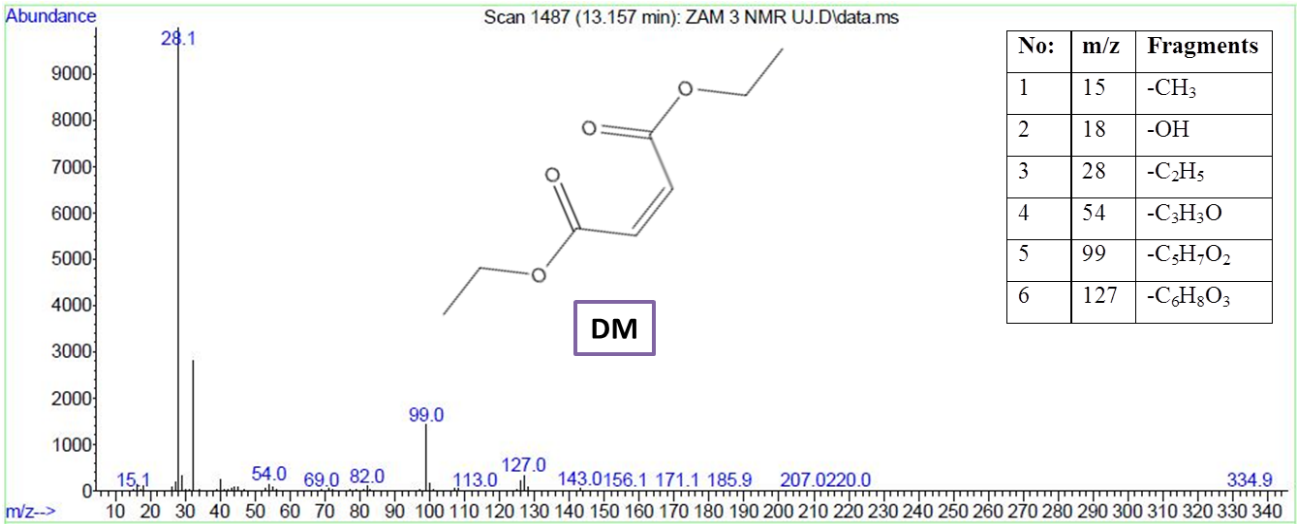

No:	m/z	Fragments
1	15	$-CH_3$
2	18	-OH
3	28	$-C_2H_5$
4	54	$-C_3H_3O$
5	99	$-C_5H_7O_2$
6	127	$-C_6H_8O_3$

Figure 4.13. Mass spectrum of the **DM** oxidation product and its fragmentation.

The oxidation of both phenol and cresols does not end at the production of the maleic acid and other similar products, but it proceeds to the formation of shorter chain carboxylic acids such as acetic, oxalic and formic acid before reaching the mineralization products (CO_2 and H_2O) [**8, 14**]. Figure 4.14 presents the diethyl oxalate (**DO**), an ester of oxalic acid that was produced through the esterification reaction of oxalic acid by ethanol. The Mass spectrometer analyses detected signals at *m/z* 74 (M^+), 45 (100%, M^+ - 29) and 58 (M^+ - 16) which corresponds to the **DO** oxidation product.

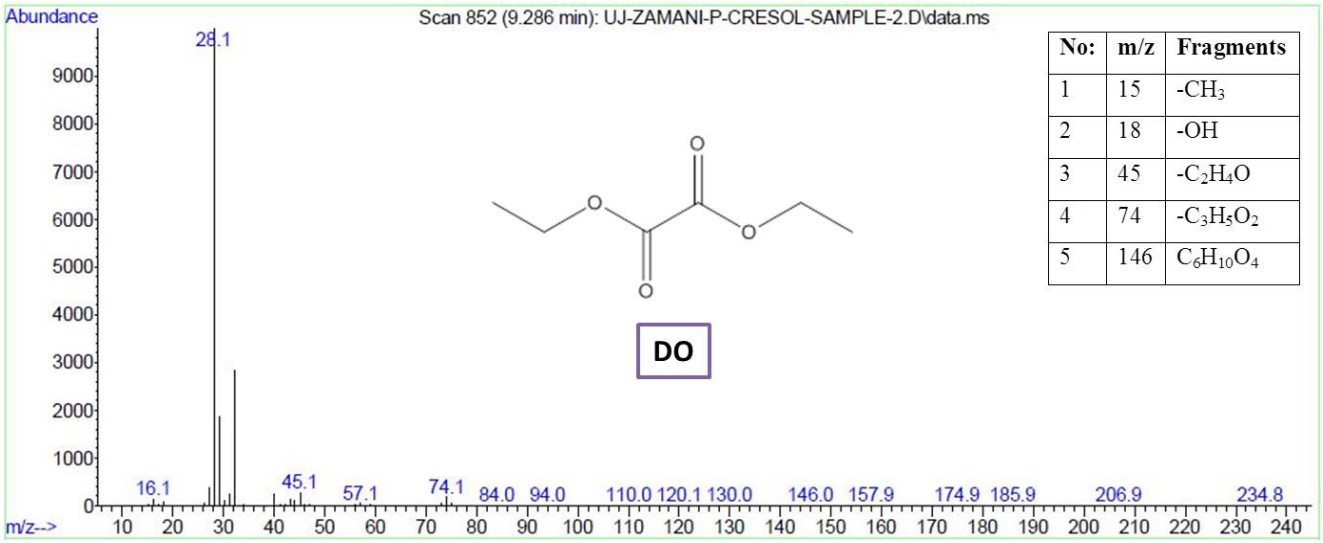

Figure 4.14. Mass spectrum of the **DO** oxidation product and its fragmentation.

During the GC-MS analyses, tolyl acetates (**TAs**) were detected and at first were thought to be the oxidation products of the cresol isomers. The latter would have been an exclusive discovery since none of these products have been identified in the oxidation cresol isomers and thus prompted further investigation on how the **TAs** were formed. A brief experiment, which is later discussed in this Chapter, was conducted. The **TAs** are neither direct ozonation products of cresols nor products of the reaction between cresols and ethanol. However, there have been studies where cresols were reacted with tertiary alcohols, merely resulting in alkylation of these isomers, separately [**15,16**].

The **TAs** were thus resolved to be post oxidation products, but their considerable increase in selectivity percentages suggests that, an intermediate that easily initiates their production was formed during the oxidation and was stable enough to exist until the collected sample was dissolved and stored in ethanol. The MS data suggesting a tolyl acetate shows signal *m/z* 150 (M^+), 136 (M^+ - 15), 122 (M^+ - 28), 108 (100%, M^+ - 42), 92, 77 and 61 for all three isomers (Figures 4.15–4.17). Had the alkylation of cresols occurred? The MS *m/z* values that would be expected are 136 (M^+) and 164 (M^+) for mono-alkylation and di-alkylation, respectively.

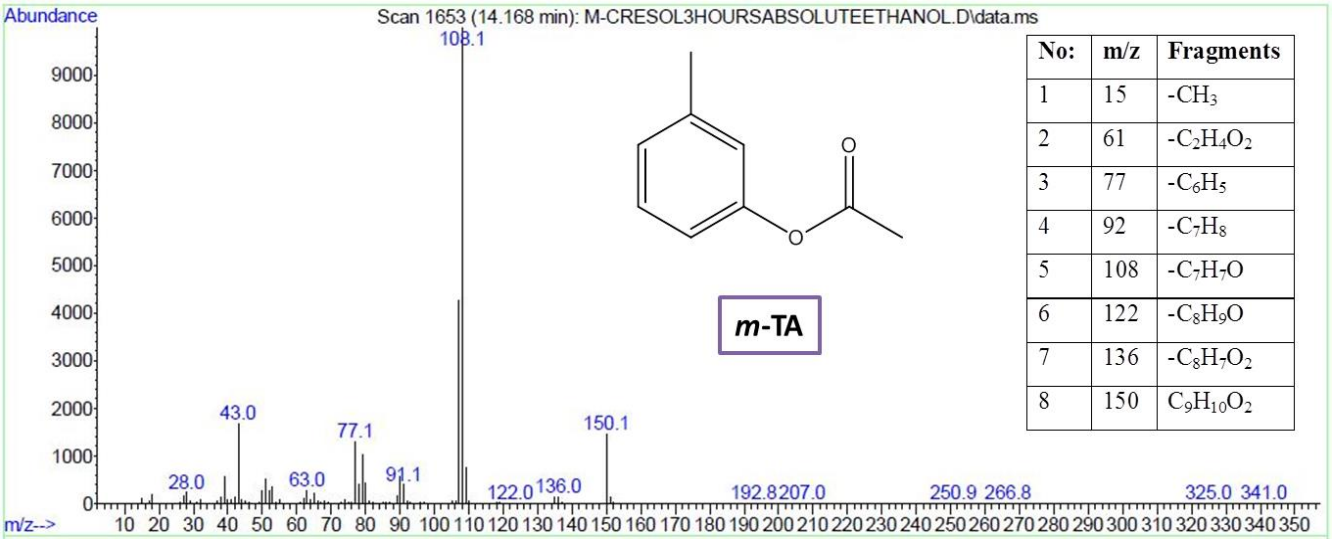

No:	m/z	Fragments
1	15	$-CH_3$
2	61	$-C_2H_4O_2$
3	77	$-C_6H_5$
4	92	$-C_7H_8$
5	108	$-C_7H_7O$
6	122	$-C_8H_9O$
7	136	$-C_8H_7O_2$
8	150	$C_9H_{10}O_2$

Figure 4.15. Mass spectrum of the ***m*-TA** oxidation product and its fragmentation.

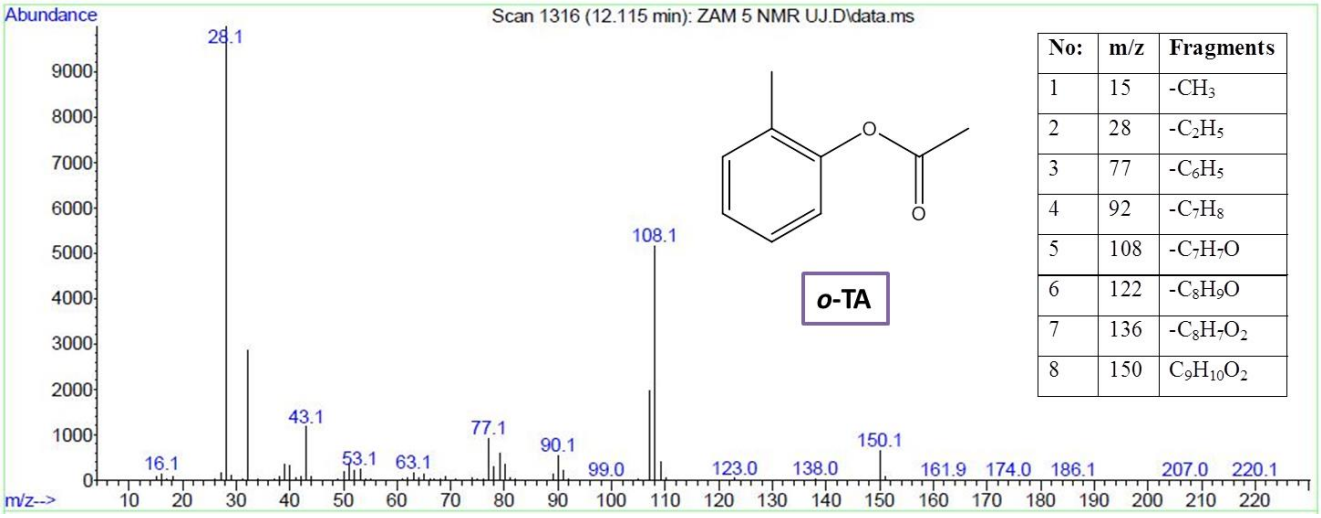

No:	m/z	Fragments
1	15	$-CH_3$
2	28	$-C_2H_5$
3	77	$-C_6H_5$
4	92	$-C_7H_8$
5	108	$-C_7H_7O$
6	122	$-C_8H_9O$
7	136	$-C_8H_7O_2$
8	150	$C_9H_{10}O_2$

Figure 4.16. Mass spectrum of the ***o*-TA** oxidation product and its fragmentation.

The variation in selectivities of the tolyl acetate products is believed to be an indirect representation of relatively stable radicals over time, plausibly the methylphenoxyl radicals [**17**]. Hypothetically, these radicals are stable enough to exist until the collected sample is dissolved in ethanol.

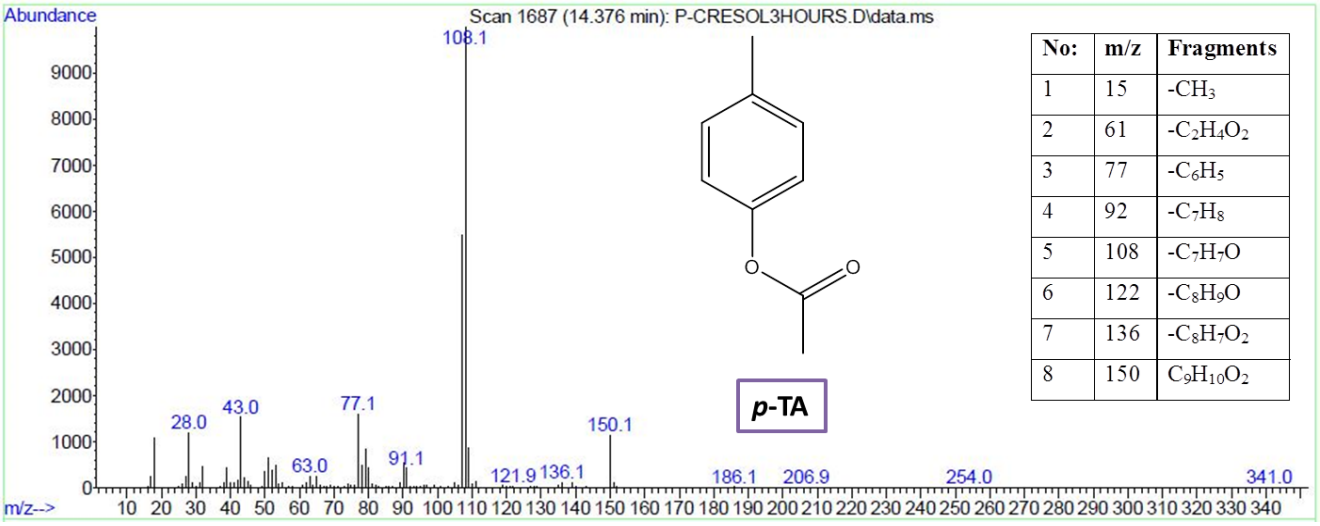

Figure 4.17. Mass spectrum of the ***p*-TA** oxidation product and its fragmentation.

A reaction mechanism was proposed based on literature [**8**], showing how the cresol isomers were converted into other products through O_3 mediated oxidation reaction as illustrated in Scheme 4.1. The oxidation products contained in boxes are the ones that could be identified in the current work. It is tempting to assume ***m*-TA** for a product of *m*-cresol and ethanol (EtOH) even though it is specifically a post oxidation product. In light of the latter, considerable experimental evidence was acquired and discussed later in this Chapter, eliminating baseless presumptions.

Furthermore, O_3 reacts with the *m*-cresol, leading to the yield of $HO^{\cdot}$ radical that subsequently attacks the *ortho*-position, activated by the methyl and hydroxyl group to give **2,3-DT**. Ozone continues attacking the Sp^2-carbons within the ring, forming an ozonide intermediate that rearranges and produce unsaturated carboxylic acid chains *i.e.* 2-methyl muconic acid. Eventually, products like citraconic and maleic acid (reacted with EtOH to give **DM**) were produced and later the oxalic acid, which reacted with EtOH to give **DO.**

Beyond this level, no other products were proved to have formed in the current work though the possibility of slight mineralization is considered.

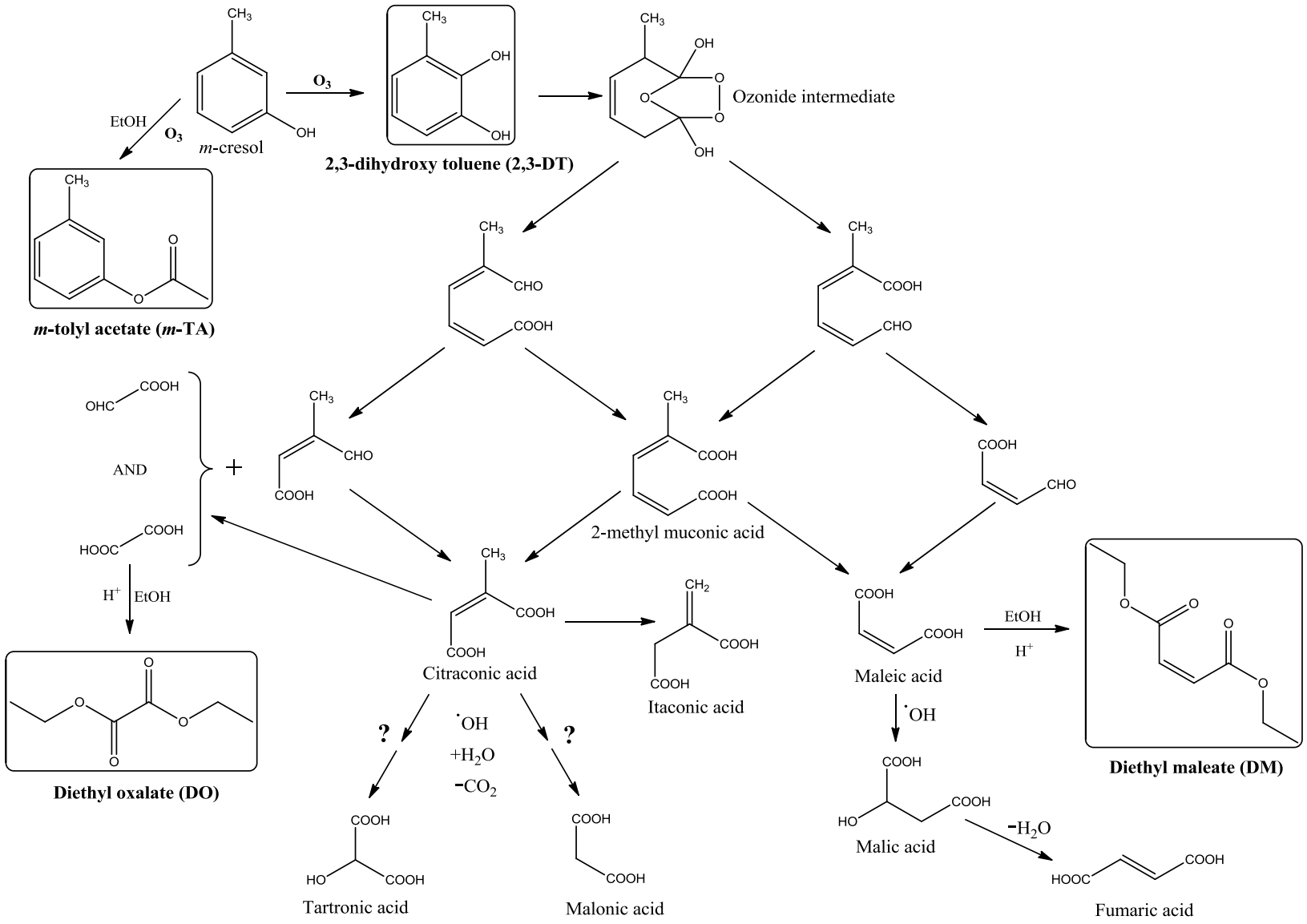

Scheme 4.1. A proposed mechanism for cresols oxidation which is a slight variation of the one reported in literature [8].

The formation of tolyl acetates from the oxidation of cresol isomers is either not documented or hardly accessible since it could not be found in literature during the period of the present work. To confirm and/ or eliminate the idea of direct reaction between *m*-cresol and EtOH, three reactions were done, (i) 5 mL of *m*-cresol was dissolved in excess ethanol and stirred overnight in air, (ii) the same reaction was done under inert conditions and (iii) 5 mL of *m*-cresol was dissolved in excess EtOH and ozonated in a glass reactor for 5, 10, 30 and 60 min. Both reaction (i) and (ii) showed no yield of any product while the FT-IR spectra of samples (10–60 min) collected from reaction (iii) showed a development of chemical species containing a O=C< bond at 1728 cm^{-1} (Figure B1, p. 145) which was later confirmed on GC-MS to be traces of ***m*-TA**. It is thus believed herein, that the formation of *m*-tolyl acetate (Scheme 4.1) was driven by the presence of ethanol and this idea is further supported by the ability of O_3 to react with ethanol to give acetaldehyde, ethylene, ethyl acetate and diethyl ether as reported by Oyama and co-workers [**18**]. The formation of acetaldehyde was confirmed in the current work in Section 2.3.2.3 (p. 38).

Although the reaction pathway for ***m*-TA** production demands a dedicated attention to best deduce, it is plausible that O_3 first activated the *m*-cresol by forming the *m*-methylphenoxyl radical [**17**] that further reacted with acetaldehyde to yield ***m*-TA** in excess EtOH. Moreover, the formation of ***o*-TA** and ***p*-TA** is thought to proceed in a similar manner. Be this the case, then the percentage selectivities of **TAs** (Figures 4.4–4.6) suggests that the methylphenoxyl radicals are reactive, either with O_3 or other species in a reaction matrix.

The application of activated charcoal, γ-Al_2O_3, SiO_2 and V_2O_5 as catalysts in the oxidation of cresols (*m*-, *o*-, *p*-cresol) and identification of resultant oxidation products in this Chapter, have in part laid a foundation for a rather more catalytic study covered in the successive Chapter 5. In Chapter 5, cresol isomers are ozonated in the presence of catalysts that were prepared by loading metals (Ni, Fe, Mn & V) on γ-Al_2O_3, SiO_2 and V_2O_5 which are termed as supports.

4.4. References

1. M. Sui, L. She; Review on research and application of mesoporous transitional metal oxides in water treatment. *Front. Environ. Scie. Eng*. 7(6) (**2013**) 795–802.
2. M. A. Vuurman, I. E. Wachs, D. J. Stufkens, A. Oskam; Characterization of chromium oxide supported on Al_2O_3, ZrO_2, TiO_2 and SiO_2 under dehydrated conditions. *J. Mol. Catal*. 80 (**1993**) 209–227.
3. C. R. Dias, M. F. Portela, G. C. Bond; Oxidation of *o*-Xylene to Phthalic Anhydride over V_2O_5/TiO_2Catalysts: I. Influence of catalyst composition, preparation method and operating conditions on conversion and product selectivities. *J. Catal*. 157 (**1995**) 344–352.
4. M. O. Corapcioglu, C. P. Huang; The surface acidity and characterization of some commercial activated carbons. *Carbon* 25(4) (**1987**) 569–578.
5. S. B. Lima, S. M. Borges, M. D-C. Rangel, S. G. Marchetti; Effect of Iron content on the catalytic properties of activated carbon–supported magnetite derived from biomass. *J. Braz. Chem. Soc*. 24(2) (**2013**) 344–354.
6. D. S. Maciver, H. H. Tobin, R. T. Barth; Catalytic aluminas I. Surface chemistry of eta and gamma alumina. *J. Catal.* 2 (**1963**) 485–487.
7. G. J. Young; Interaction of water vapor with silica surfaces. *J. Colloid Sci*. 13 (**1958**) 67–85.
8. M. C. Valsania, F. Fasano, S. D. Richardson, M. Vincenti; Investigation of the degradation of cresols in the treatment with ozone. *Water Res.* 46 (**2012**) 2795–2804.
9. R. Criegee; Mechanism of ozonolysis. *Angew. Chem. Int. Edit*. 14 (11) (**1975**) 745–752.
10. Y. N. Khonsari, S. A. Mirshokrael, A. Abdolkhani; Dissolution of wood flour and lignin in 1-butyl-3-methyl-1-imidazolium chloride. *Orient. J. Chem.* 29(3) (**2013**) 889–904.
11. A. Santos, P. Yustos, S. Rodriguez, F. Garcia-Ochoa; Wet oxidation of phenol, cresols and nitrophenols catalyzed by activated carbon in acid and basic media. *Appl. Catal. B-Environ.* 65 (**2006**) 269–281.
12. Y. Abdollahi, A. Zakaria, N. A. Sairi; Degradation of High Level m-Cresol by Zinc Oxide as Photocatalyst. *Clean – Soil Air Water* 42 (9) (**2014**) 1292–1297.

13. J. Hoigné, H. Bader; The role of hydroxyl radical reactions in ozonation processes in aqueous solutions. *Water Res.* 10 (**1976**) 377–386.
14. U. S. Kulkarni, S. G. Dixit; Destruction of phenol from wastewater by oxidation with SO_3^{2-}-O_2. *Ind. Eng. Chem. Res*. 30 (**1991**) 1916–1920.
15. G. D. Yadav, S. B. Kamble; Synthesis of carvacrol by Friedel–Crafts alkylation of *o*-cresol with isopropanol using superacidic catalyst UDCaT-5. *J Chem. Technol. Biotechnol.* 84 (**2009**) 1499–1508.
16. Pandian Elavarasan, Kishore Kondamudi, Sreedevi Upadhyayula; Comparative Kinetic Study on Alkylation of *p*-cresol with *tert*-butyl Alcohol using Different SO_3-H functionalized Ionic Liquid Catalysts. *International Journal of Chemical, Molecular, Nuclear, Materials and Metallurgical Engineering.* 4(6) (**2010**) 384–389.
17. L. S. Richard, C. E. S. Bernardes, H. P. Diogo, J. P. Leal, M. E. Minas da Piedade; Energetics of cresols and of methylphenoxyl radicals. *J. Phys. Chem. A* 111 (**2007**) 8741–8748.
18. S. T. Oyama, W. Li, W. Zhang; A comparative study of ethanol oxidation with ozone on supported molybdenum and manganese oxide catalysts. *Stud. Surf. Sci. Catal*. 121 (**1999**) 105–110.

Chapter 5

OXIDATION OF *meta-, ortho-* AND *para*-CRESOL USING OZONE IN THE PRESENCE OF METAL-LOADED CATALYSTS

5.0. Introduction

The importance of supported metal catalyst materials in heterogeneous catalysis has been widely emphasized [**1–4**]. They have earned great efficacy in hydrogenation, oxidative desulfurization, traditional oxidations and other reactions. These catalyst systems have shown enhanced performance due to (in most cases) the presence of catalytically active metal/ metal-oxides and support material. The utilized metals in this regard, include but not limited to noble metals [**5**] and transition metals *i.e.* Cr, Ti, Mn, Fe [**6–8**] V, Ni [**3,9,10**] and many more.

The Ni based catalysts for instance, have been studied by Swaan *et al.* [**11**] supported on La_2O_3, MgO, ZrO_2, TiO_2, SiO_2, as bimetallic catalysts coupled with K and Cu and suspended on dual Al_2O_3-SiO_2 supports in a reforming reaction of methane. However, among the latter, the Ni/SiO_2 system was found to be the most active and stable catalyst at elevated temperatures. There have also been reports of V based catalysts supported on mesoporous carbon, named as CMK-3, which displayed an increase in activity for the therein chosen reactions with increase in vanadium loading on the support [**3,12**]. Furthermore, metals like Fe and Mn have also seen used in catalytic oxidation reactions, improving degradation of aliphatic and aromatic organics that pose any form of hazard to the environment in the presence of ozone or any other suitable oxidant [**13–15**].

This Chapter aims at studying the catalytic oxidation of cresol isomers that are environmentally unfriendly. It encompasses the use of metal-loaded catalyst materials that are prepared by separately loading (wet impregnation) each metal (Ni, Fe, Mn and/ or V) on γ-Al_2O_3, SiO_2 and V_2O_5 supports. The synthesis of these various catalysts and their characterization were discussed in Section 2.2 (p. 33) and Sections 3.1–3.7 (pp. 49–76), respectively. All ozonation reactions were undertaken on a glass reactor (Impinger) in the present Chapter and dimensions of the reactor are provided in the previous Section 2.4.2 (p. 44). Considering the catalytic activity of supports established in the previous Chapter 4, ozonation reactions were performed for 24 h and samples were collected in every 6 h of reaction (6, 12, 18 and 24 h) in the present Chapter.

5.1. Effect of metal loaded γ-Al_2O_3 catalysts in oxidation of cresol isomers

The activity of pure γ-Al_2O_3 as a catalyst was studied in the oxidation of *m*-, *o*- and *p*-cresol as discussed in Section 4.2 (p. 86). Pure γ-Al_2O_3 proved to be catalytically active only in the oxidation of *m*-cresol. Thus, the catalytic activity of various metals (Ni, Fe, Mn, and V) loaded on γ-Al_2O_3 was studied in detail in the current Section and these materials are labeled herein as 'metal-loaded γ-Al_2O_3 catalysts'. The oxidation of cresol isomers was affected greatly by the introduction of metal loaded catalysts and their conversion percentages improved significantly using various metal loaded γ-Al_2O_3 catalysts. Figure 5.1 display the percentage conversions of all three isomers under the influence of Ni, Fe, Mn and V loaded on γ-Al_2O_3.

The Ni/γ-Al_2O_3 catalyst was found to be dominant in activity during oxidative degradation of *m*-cresol (Figure 5.1a-b) over other catalyst materials at 2.5 % of metal dopant, the order of performance deduced was Ni > Mn > Fe > V. The activity of this Ni catalyst may plausibly be attributed to existence of Ni in its zero oxidation state, Ni^0, in a supposedly formed $NiAl_2O_4$ spinel, which is reportedly detectable in XRD at Ni loadings that are much higher than 7.5 wt.% [**16**]. The surface area also plays a vital role pertaining the activity of a Ni-loaded catalyst, although this could not be inferred in the current work. However, the latter activity order was observed to have changed at 7.5 % metal content (Figure 5.1b), it became Ni > Fe > Mn > V and this may be due to decrease in catalyst surface area which is in agreement with BET results presented in Section 3.8 (Table 3.4, p. 76).

It is apparent that at higher metal content on γ-Al_2O_3 surface, Fe-loaded catalyst converted more of *m*-cresol than Mn and V materials. This can be attributed to the particle sizes that were calculated from TEM in the present work and activity of the resultant metal oxides, individually. Altogether, the catalysts at 2.5 wt.% of dopant (Figure 5.1a) converted a small percentage of the substrate at 6 h, spanning a conversion range of 14–72% from 6–24 h of reaction time. It is worth pointing out that the catalyst that showed low conversion at 6 h was Ni(2.5%)/γ-Al_2O_3 which is typical of time induced activity of Ni/γ-Al_2O_3 catalyst. Whereas, at 7.5 wt.% (Figure 5.1b), the range was 17–69%.

The above mentioned catalyst system was further employed in the oxidation of *o*-cresol (Figure 5.1c–d). The relatively high activity of Ni/γ-Al_2O_3 was witnessed and the resultant order of

catalytic performance was Ni > Mn > V > Fe at 2.5 wt.% (Figure 5.1c) of each metal loading which altered to Ni > Fe > Mn > V for 7.5% (Figure 5.1d) metal-loaded catalysts at the end of each reaction set (24 h). It is again worth pointing out that the increased activity of catalyst systems at low dopant amounts, converting up to 66% of *o*-cresol whereas, while only 62% of the substrate was oxidized at higher metal content. This may also be due to the aggregation of metal/ metal oxide particles on the surface of a γ-Al_2O_3 support, which can be clearly seen from the point-mapping on EDX results as seen in Appendix A (Figures A2–A12, pp. 132–137).

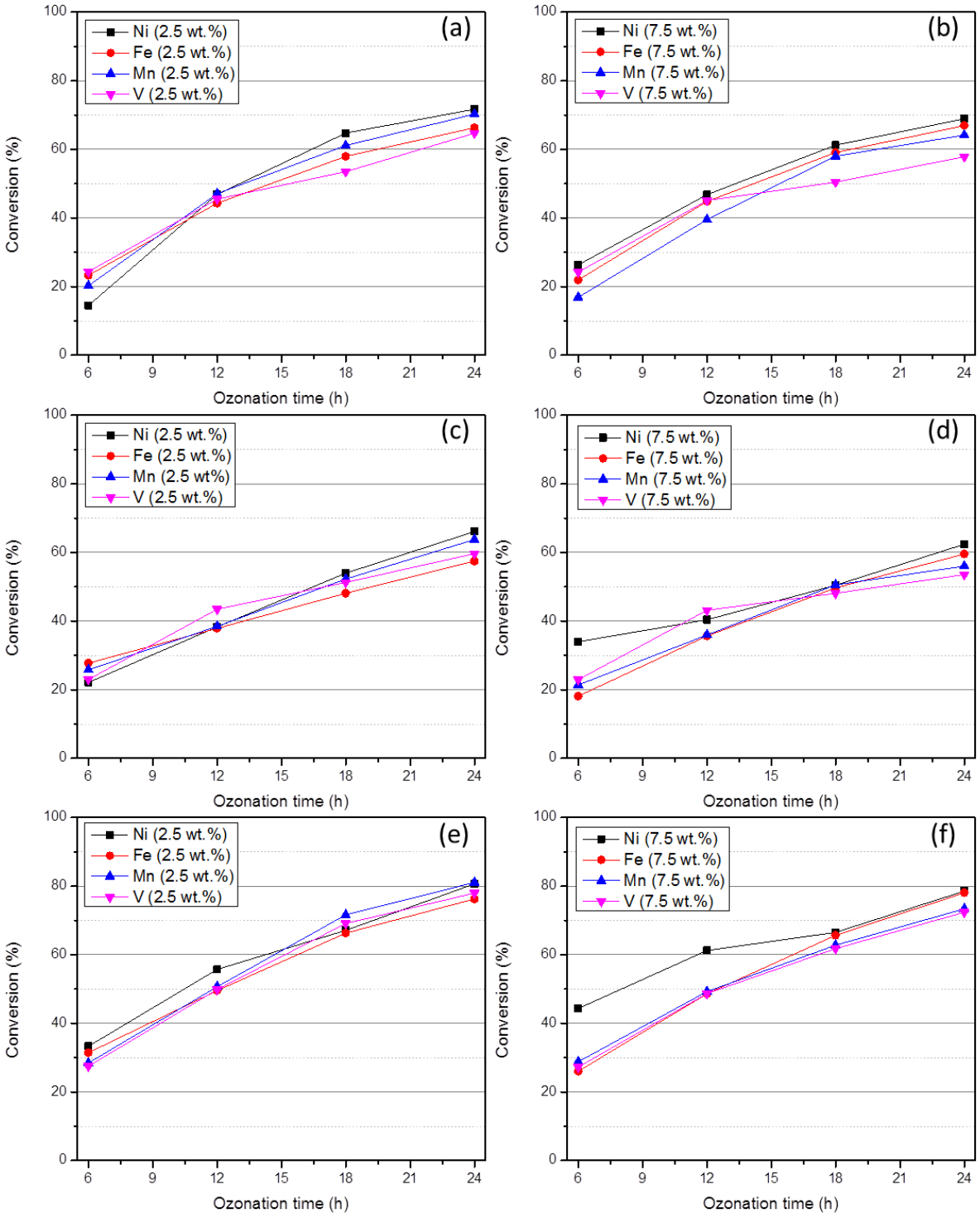

Figure 5.1. Percentage conversions of *m*-cresol (a-b), *o*-cresol (c-d) and *p*-cresol (e-f) from catalyzed oxidation reactions, using metal (Ni, Fe, Mn, V) loaded γ-Al_2O_3 catalysts at 2.5 and 7.5 wt.% metal loadings.

The 7.5 wt.% metal-loaded catalysts were found to be less active compared to the 2.5 wt.% materials. This can be seen from percentage conversions of *o*-cresol in Figure 5.1 (c-d), especially at 24 h of reaction time.

Furthermore, when the catalytic oxidation of *p*-cresol was investigated, metal supported γ-Al_2O_3 catalysts performed uniquely in Figure 5.1 (e-f). The Mn loaded γ-Al_2O_3 catalyst was observed to convert more of the *p*-cresol from 18–24 h (Figure 5.1e) of ozonation while the Ni loaded γ-Al_2O_3 catalyst had outperformed all the materials from 6–12 h at 2.5 wt.% of metal loading for both catalysts. The activity trend resulted in Mn > Ni > V > Fe at low metal content (Figure 5.1e) and Ni > Fe > Mn > V at higher metal content (Figure 5.1f) at the end of the reaction (24 h). Among the 7.5 wt.% metal-loaded γ-Al_2O_3 set of catalysts, the activity of Mn/γ-Al_2O_3 in the degradation of *p*-cresol strongly depends on its surface area (Table 3.4, p. 76). At 2.5 wt.% Mn loading (surface area, 167.6 m^2/g) the catalyst is the most active whereas at 7.5 wt.% of Mn loading (surface area, 107.8 m^2/g) the catalyst becomes the second least active.

It is clear that the *p*-cresol was the most converted substrate of all three in the presence metal-loaded on γ-Al_2O_3 catalysts, reaching up to 81% of percentage conversion in 24 h. The decrease in substrate conversion with increase in dopant amount on the surface of the support could be due to the decrease in BET surface area and pore sizes of the materials witnessed from 2.5–7.5 wt.% loaded metal catalysts (Table 3.4, p. 76). Increasing the metal loading on a support may improve the catalytic activity of a metal-loaded system but only to a certain extent and then reduce the activity of a catalyst [**17–19**]. A typical scenario to explain the latter would be, loading small amounts of catalytically active metals on inactive/ less active supports tend to result in good metal dispersion and thus utmost exposure to reactants in a reaction, which ultimately yields high catalytic activity [**20**]. Increasing the loadings increases these active sites but eventually results in metal particle aggregation (less exposure of active metals to reactants) and thus decreased catalytic activity [**20**].

The discussion so far has been mainly based on catalyst enhanced substrate conversion at final ozonation stages (24 h) of each reaction, which best caters for showing the catalyst performance at the end of the reaction but not the accurate catalyst activity results. An attempt to best comprehend (for comparison purposes) each catalyst activity towards cresols oxidation was made by calculating average percentage conversion of each substrate in the presence of 2.5 and

7.5 % of Ni, Fe, Mn and V-loaded on γ-Al_2O_3 catalysts. This was achieved by adding and calculating the average of percentage conversions for each substrate at 6, 12, 18 and 24 h in oxidation reactions that were catalyzed by various metal-loaded γ-Al_2O_3 catalysts at 2.5 and 7.5 wt.% of metal loadings. For example, the use of Ni(2.5 wt.%)/γ-Al_2O_3 catalyst in the oxidation of *m*-cresol converted 14.5% in 6 h, 46.9% in 12 h, 64.8% in 18 h and 71.7% in 24 h of the substrate. These percentage conversions were summed up and divided by 4 to get 49.5% of average percentage conversion and the same was done for all other reactions that are presented herein (see Section 2.5, p. 46).

In a period of 24 h of catalytic ozonation reactions, the average percentage conversions of 2.5 wt.% and 7.5 wt.% Ni/γ-Al_2O_3 catalysts were higher for all cresol isomers oxidations (Figure 5.2). The activity sequence over the entire reaction period (6–24 h) was Ni > Mn > V > Fe at 2.5 % of metal-loadings and Ni > Fe > Mn > V for 7.5 % of a loaded metal. Notably, the catalytic activity of Fe loaded catalyst improved greatly at 7.5 % loading, outperforming Mn and V-based catalysts, emphasizing the existence of catalytically active Fe_2O_3 in large amount [21]. This could partly be attributed to a plausibly decrease in the surface area, from Ni to V loaded γ-Al_2O_3 catalysts.

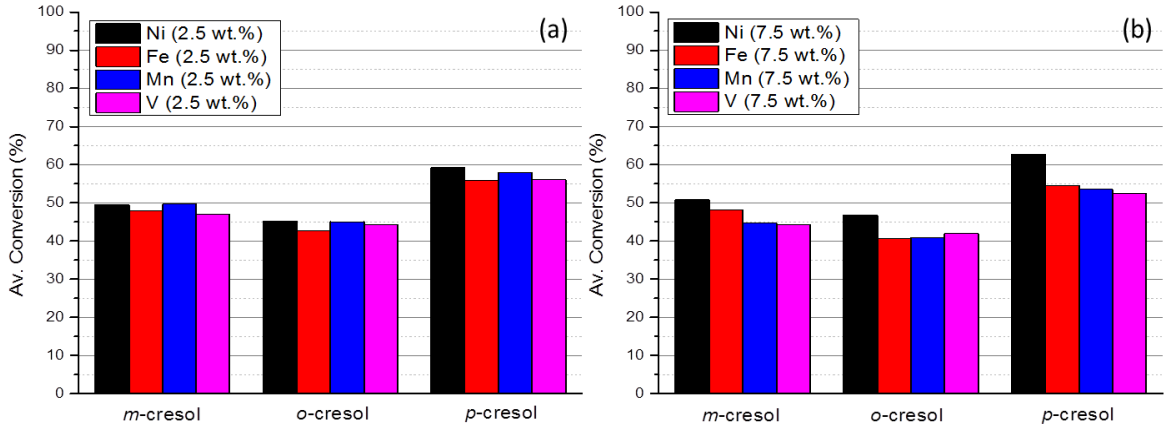

Figure 5.2. Average percentage conversion of cresol isomers in the presence of (a) 2.5 wt.% and (b) 7.5 wt.% of Ni, Fe, Mn and V-loaded γ-Al_2O_3 catalysts.

Apparently, the Ni/γ-Al_2O_3 was observably the most active metal-loaded γ-Al_2O_3 catalyst and thus, a closer attention was then paid to its selectivity towards the formation of oxidation products. The Figure 5.3 illustrates percentage selectivities of **TAs**, **DTs**, **DM** and **DO** production in the presence of Ni(2.5%)/γ-Al_2O_3 and Ni(7.5%)/γ-Al_2O_3 catalysts. A 2.5 % Ni-loaded catalyst (Figure 5.3a) yielded a relatively large amount **DO**, followed by **DM**, **2,3-DT** and the least, with diminishing selectivity over time being ***m*-TA** from m-cresol degradation. Using the 7.5% Ni-loaded (Figure 5.3b) catalyst the formation of **2,3-DT** which appeared to decrease with time, ***m*-TA** and **DM** were produced at comparable amounts and **DO** was relatively minor. The weakening of selectivity curves may suggest two incidents; (i) minor physical changes on a catalysts surface or (ii) products susceptibility to ozone attack, leading to their partial and/or complete degradation.

The Ni(2.5%)/γ-Al_2O_3 catalyst (Figure 5.3c) was observed to be more selective towards **DM** during *o*-cresol oxidation followed by **2,5-DT**, ***o*-TA** and lastly **DO**. Increasing the Ni loading to 7.5% (Figure 5.3d) promoted the yield of **DM** significantly over the **2,5-DT** product and the low selectivities were recorded for both ***o*-TA** and **DO.** Furthermore, some similarities were observed in the oxidation of *p*-cresol (5.3e-f) to that of *o*-cresol (5.3c-d). The 2.5% Ni-loaded catalyst (Figure 5.3e) favored the formation of **DM** which could also be seen from the Ni(7.5%)/γ-Al_2O_3 catalyzed (Figure 5.3f) oxidation of *p*-cresol. The ***p*-TA**, **3,4-DT** and **DO** oxidation products from the latter reactions showed comparable selectivities. Diethyl maleate (**DM**) is reasonably the major product of Ni/γ-Al_2O_3 catalyzed oxidative degradation of *m*-, *o*- and *p*-cresols collectively. Moreover, it is worth noticing that Figure 5.3 strongly supports the proposal made in Section 4.4.3 (p. 96), that the **TAs** or the radicals responsible for their formation are formed and further reacts with O_3 to form other oxidation products within 24 h of reaction duration.

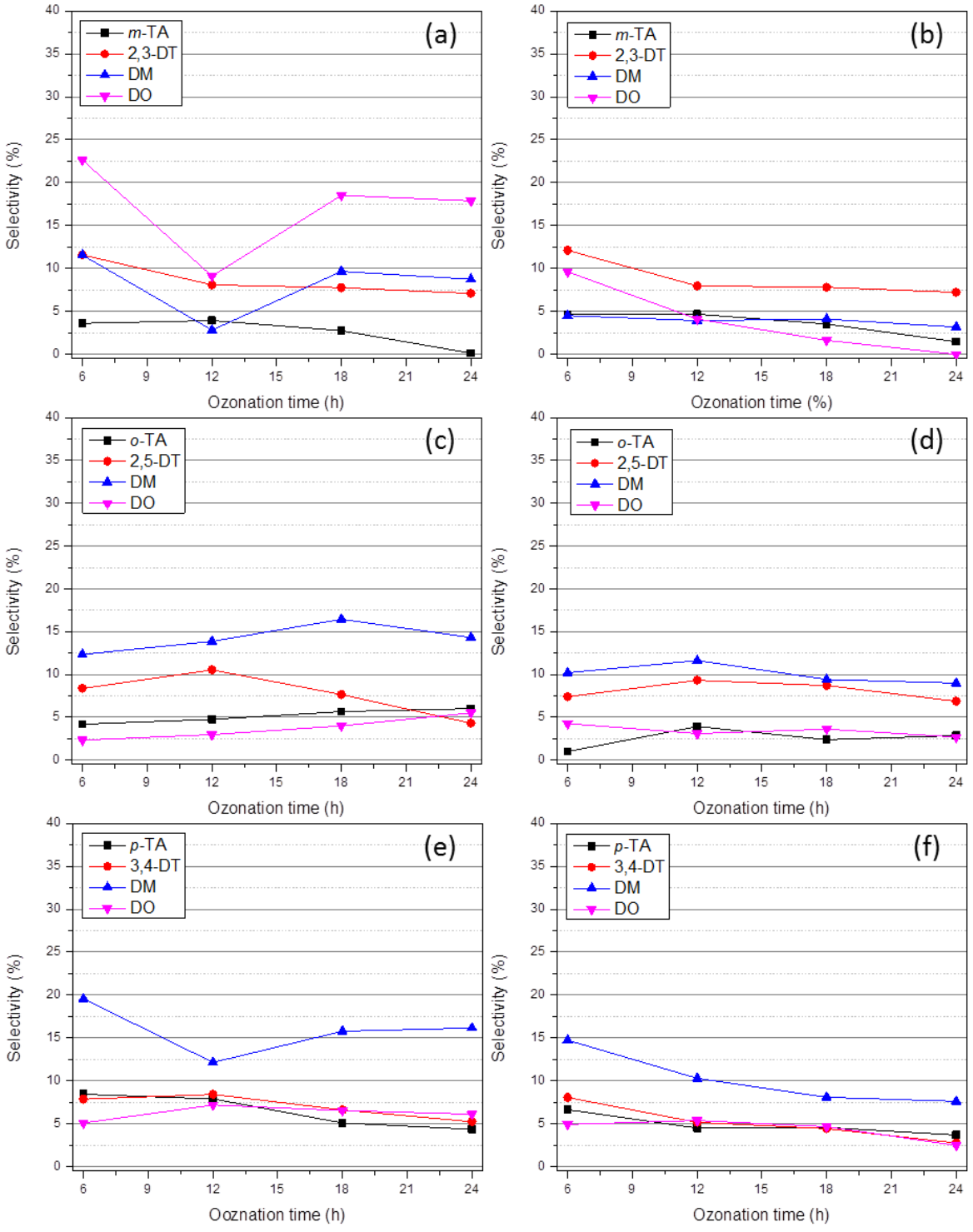

Figure 5.3. Percentage selectivities of Ni/γ-Al_2O_3 catalysts towards formation of **TAs**, **DTs**, **DM** and **DO** from *m*-cresol (a–b), *o*-cresol (c–d) and *p*-cresol (e–f) ozonation in the presence of (a, c, e) 2.5 and (b, d, f) 7.5 wt.% of Ni loadings on γ-Al_2O_3 catalysts.

5.2. Effect of metal loaded SiO_2 catalysts in the oxidation of cresol isomers

Investigation of the scope of metal supported SiO_2 catalysts in the oxidation of *m*-, *o*- and *p*-cresol was done in the current work. The percentage conversions of the cresol isomers in the presence at 2.5 and 7.5 wt.% of Ni, Fe, Mn and V-loaded catalysts over 6–24 h of ozonation period are presented in Figure 5.4.

The Ni(2.5%)/SiO_2 catalyst (Figure 5.4a) was observed to have converted most of *m*-cresol at 24 h, however, 2.5 % Fe-loaded catalyst had dominated in percentage conversions from the early stages of the reaction (6–18 h) in the Figure 5.4. The 2.5 wt.% of Mn and V-loaded SiO_2 (Figure 5.4a) displayed comparable activities and the collective activity order of the above mentioned catalysts at 24 h, was found to be Ni > Fe > Mn > V and in overall, substrate conversion range was 21–85 %. The metal loadings of 7.5 % (Figure 5.4b), converted 20–80% of *m*-cresol over the period of 6–24 h and the recorded activity at 24 h for each catalyst yielded the sequence of Ni > Mn > Fe > V.

In the oxidation of *o*-cresol, it is clearly evident that the Fe(2.5%)/SiO_2 (Figure 5.4c) is more active, giving the highest percentage of conversions than other catalysts. At 2.5 % metal loading, Ni, Mn and V–based catalyst produced similar substrate conversion, but the resultant activity was Fe > Ni > V > Mn and the percentage conversion for *o*-cresol was 19–76% from 6–24 h altogether. The 7.5 wt.% Fe catalyst (Figure 5.4d) further led to achieve relatively high conversions as compared to other catalysts and the catalysts performance assumed Fe > Ni > V > Mn sequence at 24 h of reaction time.

Percentage conversion values are in some instances close to one another, *i.e*. conversion of *m*-cresol (Figure 5.4a–b) to that of *p*-cresol (Figure 5.4e-f) at 24 h. Thus, the exact values of percentage conversions are provided in Appendix C (Table C1, p. 146). At 24 h, Fe(2.5%)/SiO_2 catalyst (Figure 5.4e) had oxidized most of *p*-cresol into oxidation products, followed by 2.5 wt.% Ni, Mn and the least conversion was found in the V-loaded SiO_2 catalyst. The catalysts with 7.5 % of metal loadings, *p*-cresol was converted mostly by Ni(7.5%)/SiO_2 catalyst and the activity order of catalysts was Ni > Mn > Fe > V. The *p*-cresol conversion rate in overall was found to be 24–87 % and 29–80 % under 2.5 and 7.5 wt.% metal loaded SiO_2 catalysts, respectively.

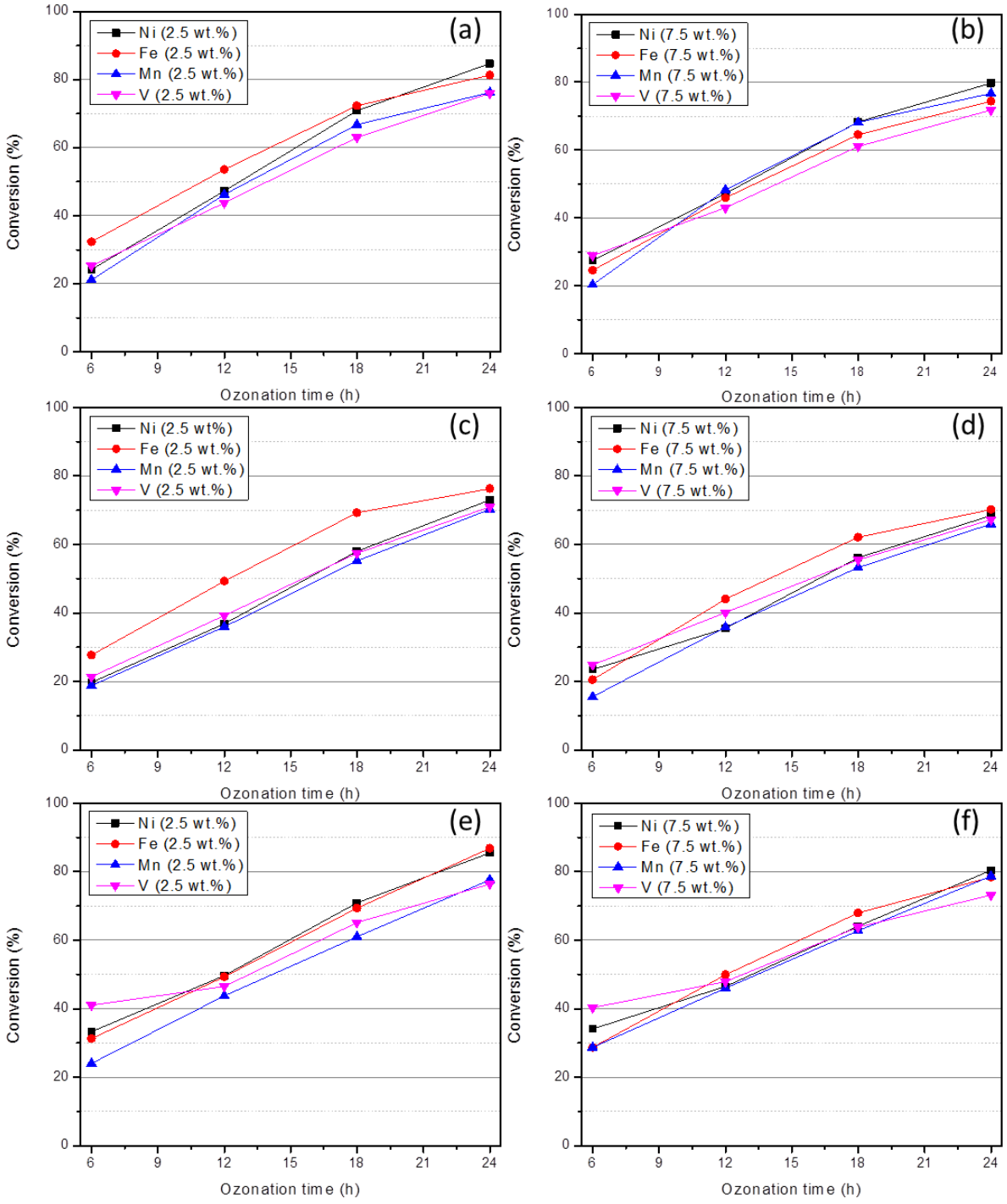

Figure 5.4. Percentage conversions of *m*-cresol (a-b), *o*-cresol (c-d) and *p*-cresol (e-f) from catalyzed oxidation reactions, using metal (Ni, Fe, Mn, V) loaded SiO_2 catalysts at 2.5 and 7.5 wt.% metal loadings.

It is apparent that, metal-loaded SiO_2 catalysts converts more of cresol substrates at lower metal loading (2.5 wt.%) and the least in presence of 7.5 % metal loaded catalysts. This could be due to the aggregation of the metal loaded on the SiO_2 support which is discussed in SEM–EDX results (Section 3.4.2 and 3.5) and also attributed to less active surface area available for the substrate to get oxidized.

Calculating accurate catalytic activity of SiO_2 supported catalysts can not only be based on their performance at a particular hour *i.e.* 24 h, although studying activities at the last hour of reaction has a potential to provide predictions of further catalyst performance. Figure 5.5 displays the average percentage conversion of each cresol isomer in the presence of 2.5 and 7.5 % metal-loaded SiO_2 catalysts, revealing accurate activity of each catalyst over the full course of the catazone reactions (6–24 h). Notably, within the 2.5 % metal loaded materials (Figure 5.5a), Fe(2.5%)/SiO_2 catalyst was relatively the most active catalyst in oxidation of cresol isomers drawing an average performance order of Fe > Ni > V > Mn. Increasing the dopant amount to 7.5 % (Figure 5.5b) may have resulted in lower substrate conversion in total but the aforementioned catalyst activity sequence was maintained and the Fe loaded catalyst showed similar activity to that of Ni.

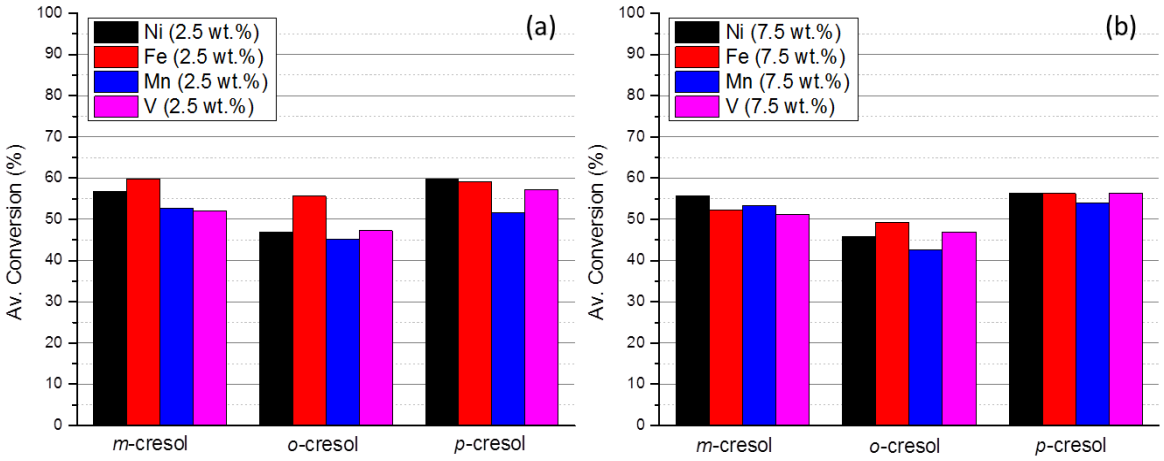

Figure 5.5. Average percentage conversion of cresol isomers in the presence of (a) 2.5 wt.% and (b) 7.5 wt.% of Ni, Fe, Mn and V-loaded SiO_2 catalysts.

Based on observations from the percentage conversion results, it is clear that Fe-loaded SiO_2 catalyst can be used to achieve utmost oxidation of cresol isomers, especially at low metal loading. The activity of Fe-loaded SiO_2 catalyst may be due to its relatively large specific surface area [**22**] (see Table 3.4, p. 76). Moreover, XRD results showed the formation of a catalytically active Fe_2O_3 on the surface of SiO_2 on Fe-loaded catalysts whereas SEM displayed iron oxide particles aggregation on the silica support. In correlation with catalytic activity of Fe, SiO_2 is believed to co-exist with Fe_2O_3 aggregates on the surface of SiO_2 support, resulting in independent catalytic participation, which however, enhanced the overall activity. The dependence on specific surface area of metal-loaded SiO_2 catalysts is obvious in this work [**20**]; catalytic activity (Fe > Ni > V > Mn) decreased with the decrease in BET measured surface area (Table 3.4, p. 76).

The oxidation products obtained from the degradation of cresol isomers were ***m*-TA**, **2,3-DT**, **DM** and **DO** from *m*-cresol, ***o*-TA**, **2,5-DT**, **DM** and **DO** for *o*-cresol and ***p*-TA**, **3,4-DT**, **DM** and **DO** from *p*-cresol. Regrettably, the selectivity curves for the comparatively more Fe-loaded SiO_2 catalysts could not be plotted due to limited sufficiency of data (gaps designated by "-" in Appendix C, Table C1, p. 146). The gaps marked by "-", are due to the absence of the particular product in the gas chromatogram, suggesting the product had formed in smaller quantities but further reacted to complete mineralization or it is formed at later stages due to the ozonation reaction of the substrate.

5.3. Effect of metal-loaded V_2O_5 catalysts in oxidation of cresol isomers

The activities of metal (Ni, Fe, Mn) loaded on vanadium pentoxide catalyst materials were studied. Unlike the pattern followed in Sections 5.1–5.2 (pp 110–117), a V loaded V_2O_5 catalyst was not prepared nor studied in the present work, mainly since the V precursor may produce V_2O_5 on the surface of a support. Figure 5.6 presents the resultant percentage conversion curves that were deduced from the O_3 facilitated oxidative degradation of *m*-, *o*- and *p*-cresol. The Mn(2.5%)/V_2O_5 catalyst (Figure 5.6a) may have been the least active catalyst at the beginning of *m*-cresol conversion but it matured during the course of reaction and recorded the relatively high percentage conversion when compared to Ni and Fe loaded catalysts in 24 h, all at 2.5 wt% loadings. The elevated activity of Mn(2.5%)/V_2O_5 can at most be attributed to the presence of

MnO_x species in the catalyst material [**23**] since V_2O_5 alone could barely convert more than 50 % of *m*-cresol (Figure 4.2, p. 87).

The catalyst activity sequence at the end of the reaction (24 h) was Mn > Ni > Fe for 2.5 wt.% of metal loaded catalyst and percentage conversion rate of *m*-cresol was 18–71% from 6–24 h of reaction. Increasing each metal loading on V_2O_5 surface to 7.5% (Figure 5.6b) did not affect the aforementioned activity order but achieved less m-cresol conversions covering a range of 19–67 % in 24 h. It is reported in the literature that, increasing Mn loading on a metal oxide support reportedly results in less catalyst activity [**23**]. Even though Ni or Ni_xO_n species are known to possess pronounced catalytic activities [**10,16**], loaded Ni may be less compatible with the V_2O_5 support used in the present work, which disfavored its activity as seen in Figure 5.6. The low activity of Fe-loaded catalysts was apparent and could be due to the ability of Fe to poison the active catalyst sites of the V_2O_5 support [**24**].

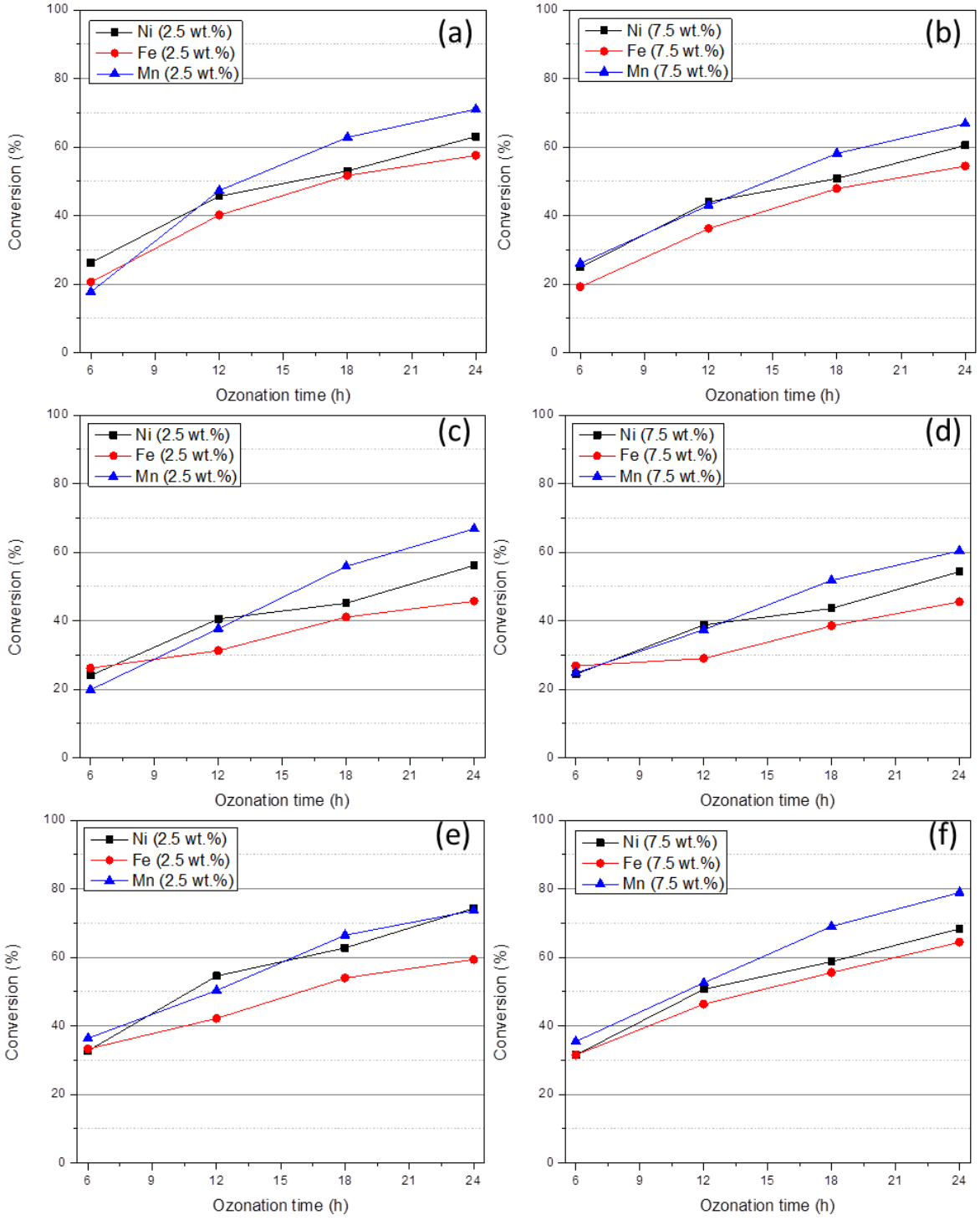

Figure 5.6. Percentage conversions of *m*-cresol (a-b), *o*-cresol (c-d) and *p*-cresol (e-f) from catalyzed oxidation reactions, using metal (Ni, Fe, Mn) loaded V_2O_5 catalysts at 2.5 and 7.5 wt.% metal loadings.

The o-cresol oxidation in the presence of V_2O_5 metal-loaded catalysts further emphasized the Mn > Ni > Fe order of catalysts activity, which was observed both in 2.5 (Figure 5.6c) and 7.5 % (Figure 5.6d) of each loaded metal on V_2O_5 support. This trend continued, and it can be seen on degradation of *p*-cresol as well, though at 24 h, Ni(2.5%)/V_2O_5 (Figure 5.6e) converted more of the substrate than the rest of the catalysts. Mn(7.5%)/V_2O_5 uniquely outperformed the Fe and Ni-based catalysts in Figure 5.6f through converting most of *p*-cresol to oxidation products, even more than the percentage conversions attained with Mn(2.5%)/V_2O_5.

Figure 5.7 best provides the averaged percentage conversions of cresol isomers in the presence of Ni, Fe, Mn-loaded V_2O_5 catalysts, both at 2.5 and 7.5 wt.% loadings of the metals. A catalyst that promoted most conversion of all three methyl phenols was apparently Mn(2.5%)/V_2O_5 followed by Ni(2.5%)/V_2O_5 and lastly, Fe(2.5%)/V_2O_5 at 2.5% loaded metal (Figure 5.7a) and exactly same activity trend was observed with 7.5% metal-loaded V_2O_5 catalysts (Figure 5.7b). The latter renders Mn-loaded V_2O_5 as the most active catalyst on average in the present work. The average activity sequence can be as follows, Mn > Ni > Fe.

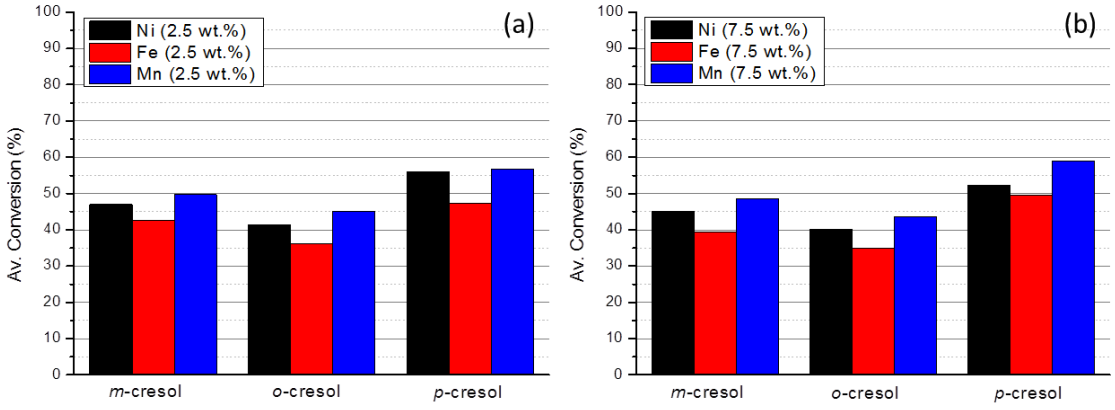

Figure 5.7. Average percentage conversion of cresol isomers in the presence of (a) 2.5 wt.% and (b) 7.5 wt.% of Ni, Fe and Mn-loaded V_2O_5 catalysts.

5.4. Comparison of the most active metal loaded γ-Al_2O_3, SiO_2 and V_2O_5 catalysts in oxidation of cresol isomers.

Collectively, the *m*-, *o*- and *p*-cresol have been observed to get more converted into products when the Ni/γ-Al_2O_3, Fe/SiO_2 and Mn/V_2O_5 catalyst systems are respectively used in the oxidative degradation of these isomers, especially at low metal loadings (2.5%) as seen in the current work. Table 5.1 summarizes the catalysts performance that led to high conversions of each cresol isomers. **Entry 1**, the *m*-cresol got converted more into products with the Mn-loaded γ-Al_2O_3 whereas the *o*-cresol and the *p*-cresol were converted into products mostly by Ni-loaded γ-Al_2O_3 catalysts at 2.5 % of metal loadings and the order of substrate reactivity could be drawn to be *p*-cresol > *m*-cresol > *o*-cresol and the similar sequence have been observed in literature [25,26].

Table 5.1. Average performances of highly active metal-loaded catalysts in cresol isomers oxidation.

Entry no.	Support material	Converted isomer	Loaded metal + %	Average % conversion (i)[†††]	Average % conversion(ii)[‡‡‡]
1	γ-Al_2O_3	*m*-	Mn (2.5%)	49.68	51.33
		o-	Ni (2.5%)	45.12	
		p-	Ni (2.5%)	59.20	
2	SiO_2	*m*-	Fe (2.5%)	59.87	58.44
		o-	Fe (2.5%)	55.63	
		p-	Ni (2.5%)	59.82	
3	V_2O_5	*m*-	Mn (2.5%)	49.70	48.06
		o-	Mn (2.5%)	45.03	
		p-	Fe (7.5%)	49.45	

On **Entry 2**, Fe(2.5%)/SiO_2 proved dominant to other metals, converting most of both the *m*-cresol and the *o*-cresol during catazone reactions. The *p*-cresol on the other hand, was mostly

[†††] Average calculated from all percentage conversions at 6, 12, 18 and 24 h of reaction time in the presence of a catalyst.
[‡‡‡] Average calculated from conversion (i) values.

oxidized in the presence of Ni(2.5%)/SiO_2 catalyst and altogether the substrates response to catalyzed ozonation was in the sequence of *m*-cresol > *p*-cresol > *o*-cresol.

The above mentioned cresols reactivity order may be different from the one deduced from **Entry 1** calculations but it makes sense to a greater extent as far as cresols susceptibility to ˙OH radical attack is concerned [25]. Both the hydroxyl (*) and methyl (^{o}) functional groups are *ortho-para* activators as shown in Figure 5.8. The *m*-cresol has position 2, 4 and 6 activated by both the hydroxyl and a methyl group and is more prone to ozone initiated attack, *p*-cresol has two pairs of activated positions and each pair is either *ortho* to the hydroxyl or methyl group. The *o*-cresol has position 2, 3, 4 and 5 activated where the both methyl and hydroxyl groups activated one *ortho*- and one *para*- position separately. Thus, the substrate reactivity sequence is generally expected to be *m*- > *p*- > *o*-cresol [25].

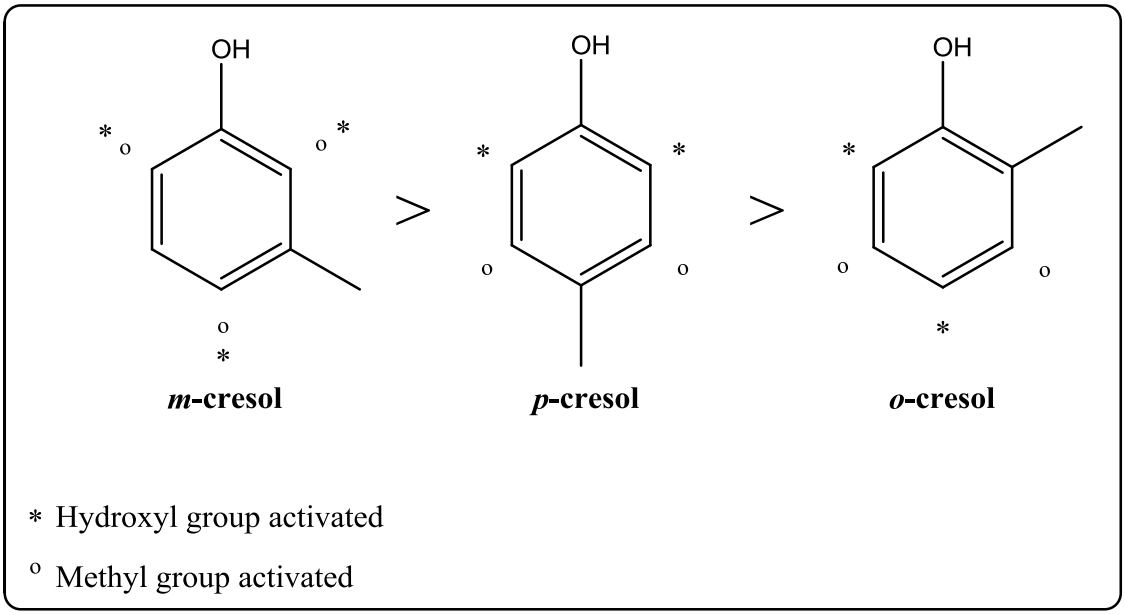

Figure 5.8. Most plausible reactivity order of cresol isomers under O_3 facilitated oxidation, deduced from the discussion made in reference [25].

In Table 5.1, **Entry 3** shows V_2O_5 supported metal catalysts that relatively displayed high catalytic performance during oxidation of the cresol isomers. The Mn(2.5%)/V_2O_5 catalyst converted both the *m*-cresol and *o*-cresol comparably more than other metal-loaded V_2O_5

catalysts. The *p*-cresol was uniquely converted the most when Fe(7.5%)/V_2O_5 catalyst was used and the overall substrate reactivity order deduced was *m*-cresol > *p*-cresol > *o*-cresol.

The conversion (ii) values in Table 5.1 illustrates the performance of tabulated catalysts per support and metals loaded on SiO_2 catalysts were found to be more active, followed by metals on γ-Al_2O_3 and the least were metals on V_2O_5, on average.

The current Chapter marks the end (based on set objectives) of the present study of the catalytic oxidation of different cresol isomers. However, the following Chapter 6 provides detailed conclusion remarks, challenges encountered and possible extension of this study in particular.

5.5. References

1. M. G. Musolino, C. V. Caia, F. Mauriello, R. Pietropaolo; Hydrogenation versus isomerization in the reaction of cis-2-butene-1,4-diol over supported catalysts: The role of Group VIII transition metals in driving the products selectivity. *Appl. Catal. A-Gen.* 390 (**2010**) 141–147.
2. C. G. A. Morisse, A. R. McInroy, C. Anderson, C. J. Mitchell ,S. F. Parker, D. Lennon; Structure/ activity relationships applied to the hydrogenation of α,β-unsaturated carbonyls: The hydrogenation of 3-butyne-2-oneover alumina-supported palladium catalysts. *Catal. Today* 283 (**2017**) 110–118.
3. L. Rivoira, J. Juárez, H. Falcón, M. G. Costa, O. Anunziata, A. Beltramone; Vanadium and titanium oxide supported on mesoporous CMK-3 as new catalysts for oxidative desulfurization. *Catal. Today* 282 (**2017**) 123–132.
4. J. Xu, J. Zhang, H. Peng, X. Xu, W. Liu, Z. Wang, N. Zhang, X. Wang; Ag supported on meso-structured SiO_2 with different morphologies for CO oxidation: On the inherent factors influencing the activity of Ag catalysts. *Micropor. Mesopor. Mat.* 242 (**2017**) 90–98.
5. W. X. Li, C. Stampfl, M. Scheffler; Why is a noble metal catalytically active? The role of the O-Ag interaction in the function of Silver as an oxidation catalyst. *The American physical society* 90 (25) (**2003**) 1–4.
6. M. A. Vuurman, I. E. Wachs, D. J. Stufkens, A. Oskam; Characterization of chromium oxide supported on Al_2O_3, ZrO_2, TiO_2 and SiO_2 under dehydrated conditions. *J. Mol. Catal.* 80 (**1993**) 209–227.
7. F. J. Beltrán, F. J. Rivas, R. Montero-de-Espinosa; A TiO_2/Al_2O_3 catalyst to improve the ozonation of oxalic acid in water. *Appl. Catal. B-Environ.* 47 (**2004**) 101–109.
8. M. G. A. Cruz, F. A. N. Fernandes, A. C. Oliveira, J. M. Filho, A. C. Oliveira, A. F. Campos, E. Padron-Hernandeze, E. Rodríguez-Castellón; Effect of the calcination temperatures of the Fe-based catalysts supported on polystyrene mesoporous carbon for FTS Synthesis. *Catal. Today* 282 (**2017**) 174–184.
9. Y. Kim, P. Kim, C. Kim, J. Yi; A novel method for synthesis of a Ni/Al_2O_3 catalyst with a mesoporous structure using stearic acid salts. *J. Mater. Chem.* 13 (**2003**) 2353–2358.

10. T. Zhang, M. D. Amiridis; Hydrogen production via the direct cracking of methane over silica-supported nickel catalysts. *Appl. Catal. A-Gen.* 167 (**1998**) 161–172.
11. H. M. Swaan, V. C. H. Kroll, G. A. Martin, C. Mirodatos; Deactivation of supported nickel catalysts during reforming of methane by carbon dioxide. *Catal. Today* 21 (**1994**) 571–578.
12. M. D. Amiridis, I. E. Wachs, G. Deo, J. M. Jehng, D. S. Kim; Reactivity of V_2O_5 catalysts for the selective catalytic reduction of NO by NH_3: Influence of Vanadia loading, H_2O, and SO_2. *J. Catal.* 161 (**1996**) 247–253.
13. J. A. Zimbron, K. F. Reardon; Fenton's oxidation of pentachlorophenol. *Water Res*. 43 (**2009**) 1831–1840.
14. T. Turan-Ertas, M. D. Gurol; Oxidation of diethylene glycol with ozone and modified Fenton processes. *Chemosphere* 47 (**2002**) 293–301.
15. L. Qi, H. You, Z. Zhang, C. Feng, S. Van Agtmaal; Degradation of 4-Chlorophenol by catalytic ozonation using γ-Al_2O_3/TiO_2 supported manganese oxides in aqueous solution. *Int. J. Electrochem. Sci.* 8 (**2013**) 5457–5468.
16. Y. Song, H. Liu, S. Liu, D. He; Partial oxidation of methane to syngas over Ni/Al_2O_3 catalysts prepared by a modified Sol-Gel method. *Energ. Fuel.* 23 (**2009**) 1925–1930.
17. Z. Q. Liu, J. Ma, Y. H. Cui; Carbon nanotube supported platinum catalysts for the ozonation of oxalic acid in aqueous solutions. *Carbon* 46 (**2008**) 890–897.
18. S. Maddila, V. D.B.C. Dasireddy, S. B. Jonnalagadda; Ce-V loaded metal oxides as catalysts for dechlorination of chloronitrophenol by ozone. *Appl. Catal. B-Environ.* 150–151 (**2014**) 305–314.
19. L. Li, W. Ye, Q. Zhang, F. Sun, P. Lu, X. Li; Catalytic ozonation of dimethyl phthalate over cerium supported on activated carbon. *J. Hazard. Mater.* 170 (**2009**) 411–416.
20. G. C. Bond; The origins of particle size effect in heterogeneous catalysis. *Surf. Sci.* 156 (**1985**) 966–981.
21. S. C. Kim; The catalytic oxidation of aromatic hydrocarbons over supported metal oxide. *J. Hazard. Mater. B* 91 (**2002**) 285–299.
22. C. A. Sierra-Pereira, E. A. Urquieta-González; Reduction of NO with CO on CuO or Fe_2O_3 catalysts supported on TiO_2 in the presence of O_2, SO_2 and water steam. *Fuel* 118 (**2014**) 137–147.

23. Y. Liu, M. Luo, Z. Wei, Q. Xin, P. Ying, C. Li; Catalytic oxidation of chlorobenzene on supported manganese oxide catalysts. *Appl. Catal. B-Environ.* 29 (**2001**) 61–67.
24. C. H. Bartholomew; Mechanisms of catalyst deactivation. *Appl. Catal. A-Gen.* 212 (**2001**) 17–60.
25. M. C. Valsania, F. Fasano, S. D. Richardson, M. Vincenti; Investigation of the degradation of cresols in the treatment with ozone. *Water Res.* 46 (**2012**) 2795–2804.
26. W. J. Smolenski, J. M. Suflita; Biodegradation of cresol isomers in anoxic aquifers. *Appl. Environ. Microb.* 53 (4) (**1987**) 710–716.

Chapter 6

CONCLUSIONS AND FUTURE WORK

6.0. Conclusions

Various metals (Ni, Fe, Mn, V) loaded on γ-Al_2O_3, SiO_2 and V_2O_5 supports were prepared and characterized before being used as catalysts. The powder XRD analysis provided no accurate results with respect to the phase of nickel/ nickel oxide that formed on the surface of each support, though along the study, a possibility of $NiAl_2O_4$ spinel formation on γ-Al_2O_3 was considered. Iron was found to be deposited as Fe_2O_3 on γ-Al_2O_3 and SiO_2 supports, whereas as Fe_3O_4 on V_2O_5 support. Manganese was detected as Mn_3O_4 only on V_2O_5 surface and not on other supports. There was no phase of vanadium/ vanadium oxide that could be detected in all supports and whether detected on XRD or not, EDX analysis confirmed the presence of all the metals that were loaded on the supports such as γ-Al_2O_3, SiO_2, V_2O_5. However, preparation and use of V loaded on V_2O_5 as a catalyst was not considered, due to the ability of V to form as V_2O_5 on the surface of a support. Only in the case of γ-Al_2O_3 support, a slight phase transformation was observed with calcination and calcination temperatures were thus kept minimal (300 ^oC).

Metals were loaded on supports at varied weight percentages, 2.5 and 7.5 wt.% which were confirmed by ICP-OES and EDX analyses. Aggregation of metal particles on surface of the supports was shown in SEM, TEM and EDX analyses. The aggregation of metal particles was influenced by increase in metal loading from 2.5 to 7.5 wt.% which also resulted in the decrease in BET surface areas of each catalyst.

Oxidation of cresols, adsorbed on γ-Al_2O_3 and/ or SiO_2 mounted on a glass column (for 5 h) was studied. The SiO_2 adsorbent was concluded to be more active than γ-Al_2O_3 in the degradation of cresols during column reactions, especially at 3 h of reaction time. Column ozonation reactions yielded promising results when compared to support (γ-Al_2O_3, SiO_2) catalyzed reactions by correlation *i.e.* up to 65% of *m*-cresol was converted in 24 h in a column reaction (adsorbed in γ-Al_2O_3) whereas up to 47% was converted in a glass reactor (catalyzed by γ-Al_2O_3). However, the use metal loaded catalysts produced better results *i.e.* Mn(2.5)/γ-Al_2O_3 led to a conversion of up to 70% of *m*-cresol in 24 h. As mentioned above, cresols were oxidized in a glass reactor without any catalyst and in the presence of activated charcoal, support (γ-Al_2O_3, SiO_2, V_2O_5) and metal (Ni, Fe, Mn, V) loaded supports as catalysts. Identified oxidation products include tolyl acetates (**TAs**), dihydroxy toluenes (**DTs**), diethyl maleate (**DM**) and diethyl oxalate (**DO**) of the

respective cresols (*m*-, *o*-, *p*-cresol). Both column and reactor reactions yielded same oxidation products per individual cresol isomer.

Catalytically, pure γ-Al_2O_3 found to be inactive in the oxidative degradation of cresols while V_2O_5 showed moderate activity and SiO_2 found as highly active. Catalytic activity order of pure supports was found to be $SiO_2 > V_2O_5 >$ γ-Al_2O_3. Moreover, metal loaded SiO_2 materials are the most active catalysts in the oxidative degradation of cresols followed by metal loaded γ-Al_2O_3 then metal loaded V_2O_5. A slight phase transformation of γ-Al_2O_3 with calcination is believed to enhance the activity of metal loaded γ-Al_2O_3 catalysts. The activity order of metal loaded catalysts with respect to support was $SiO_2 >$ γ-$Al_2O_3 > V_2O_5$. However, increasing metal loadings from 2.5 to 7.5 wt.% decreased the activities of catalysts due to elevated aggregation of metal particles, lowered BET surface areas and minimized access of reactants to catalytically active sites.

The Fe(2.5%)/SiO_2 catalyst was concluded to be the most active catalyst in the oxidative degradation of *m*- and *o*-cresol, yielding percentage conversions of up 76% and 70%, respectively. The Ni(2.5%)/SiO_2 catalyst was concluded to be most active in the oxidative degradation of *p*-cresol, by converting 85% of the substrate. Percentage selectivities of all metal loaded catalysts varied with the loaded metal (Ni, Fe, Mn, V), metal loading (2.5 wt.%, 7.5 wt.%) and the support (γ-Al_2O_3, SiO_2, V_2O_5) material but there were no conclusive trends that could be deduced from these parameters.

6.1. Future Work

There are different scientific goals as far as the treatment of organic chemical pollutants is concerned. The goal may either be to degrade the species to complete mineralization or transform them to value added products. The work presented in this thesis has demonstrated the ability of ethanol to participate in controlling the resultant oxidation products of aromatic compounds. Thus, studying the influence of solvents that have well established degradation mechanisms on driving the oxidation products of aromatic organic pollutants could be of benefit to the science community in the future.

APPENDIX

Appendix A

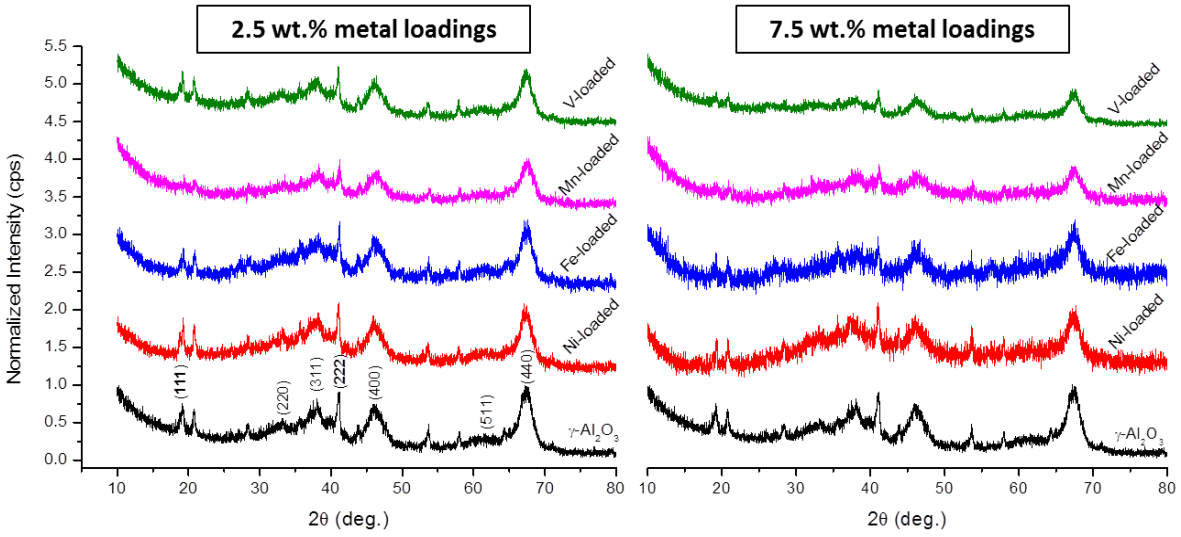

Figure A1. XRD results for the uncalcined metal-loaded γ-Al_2O_3 catalysts.

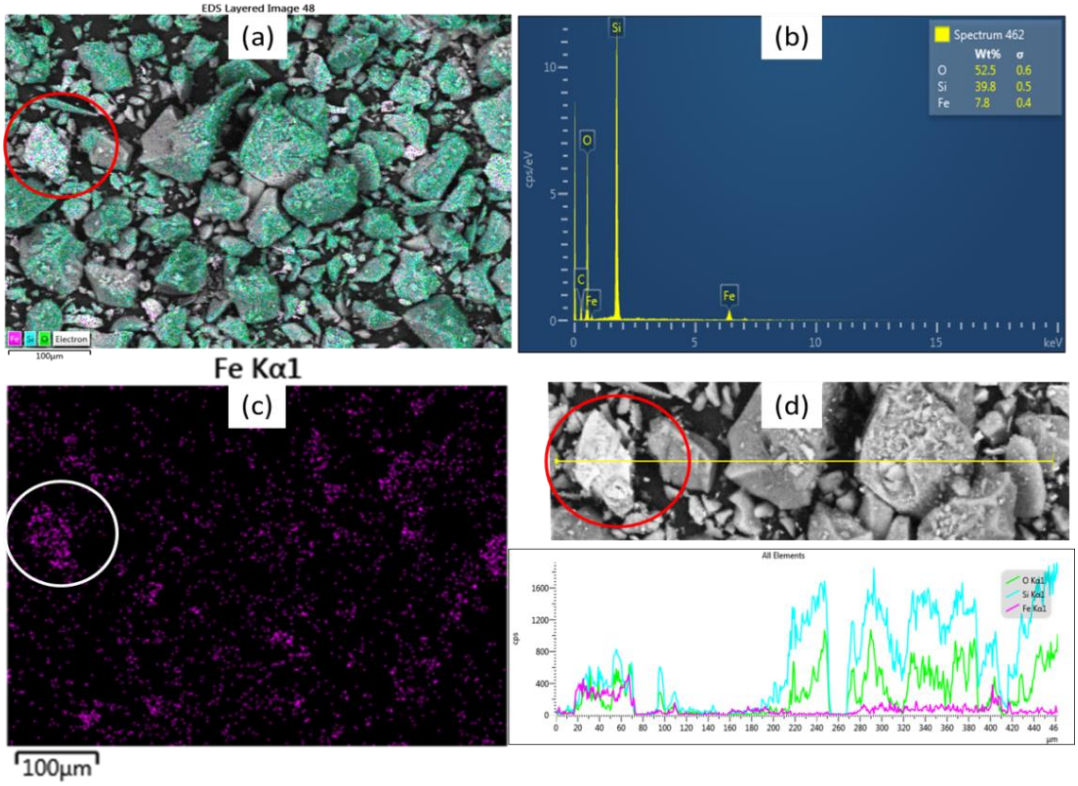

Figure A2. EDX results for Fe(2.5%)/SiO_2 catalyst, showing (a) surface scan, (b) EDX spectrum, (c) point-mapping and (d) line-mapping.

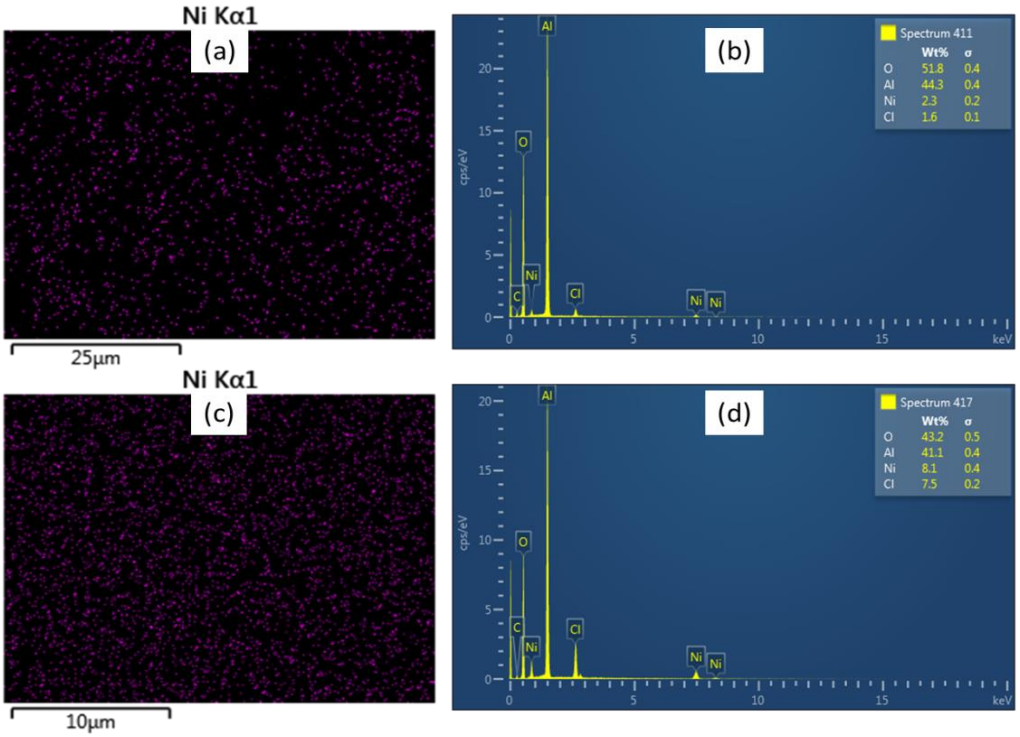

Figure A3. EDX results showing (a - b) point-mapping, EDX spectrum for Ni(2.5%)/γ-Al_2O_3 and (c - d) point-mapping, EDX spectrum for Ni(7.5%)/γ-Al_2O_3 calcined catalysts.

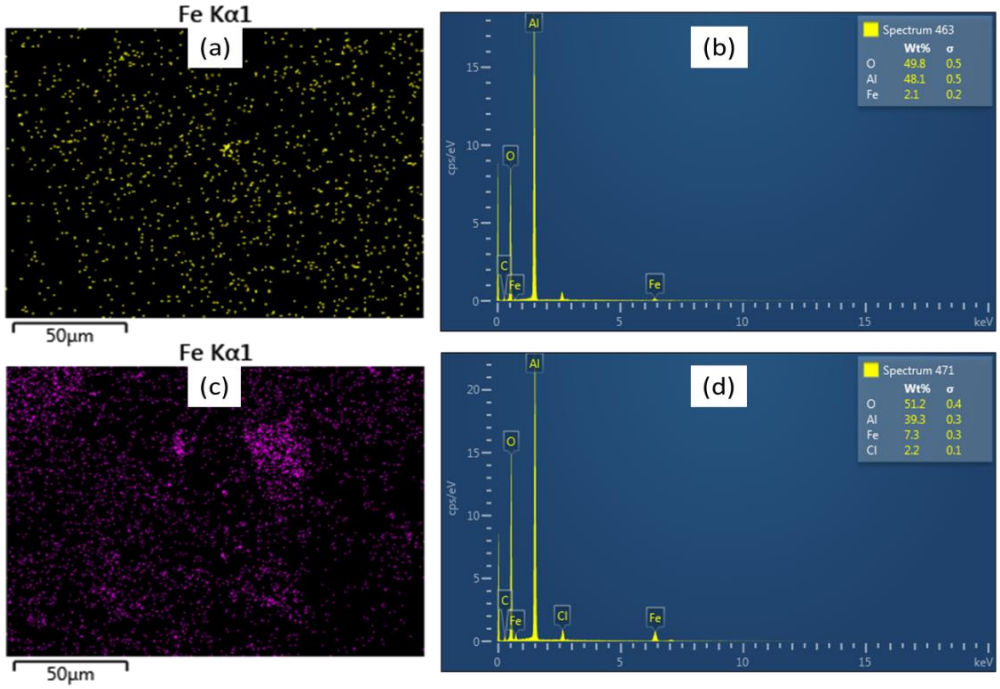

Figure A4. EDX results showing (a - b) point-mapping, EDX spectrum for Fe(2.5%)/γ-Al_2O_3 and (c - d) point-mapping, EDX spectrum for Fe(7.5%)/γ-Al_2O_3 calcined catalysts.

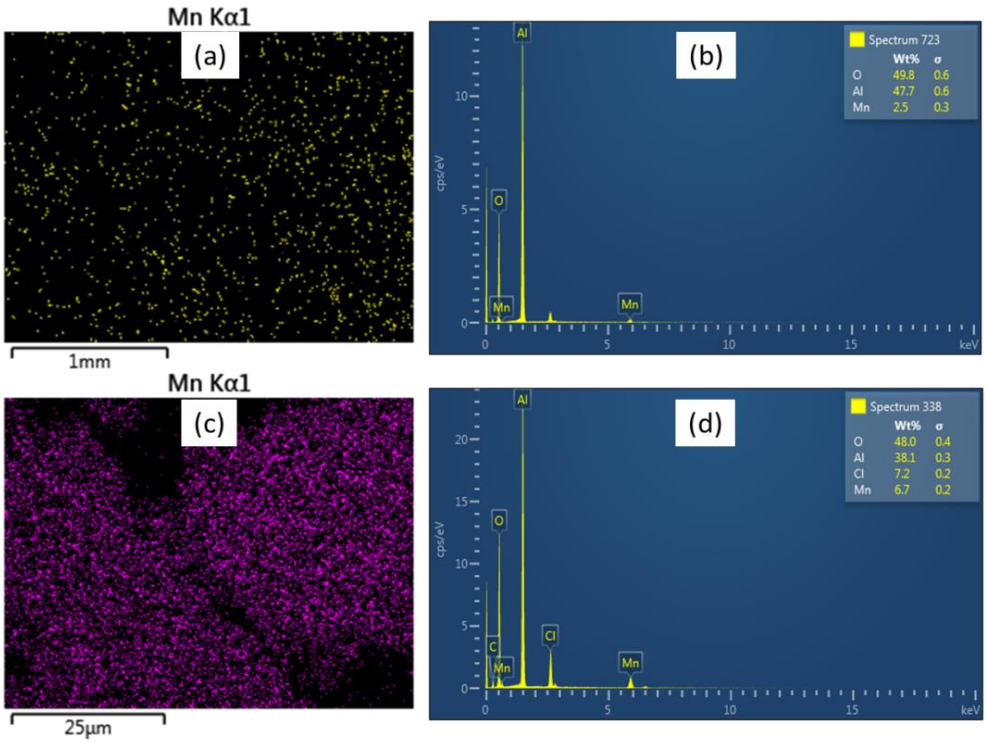

Figure A5. EDX results showing (a - b) point-mapping, EDX spectrum for Mn(2.5%)/γ-Al_2O_3 and (c - d) point-mapping, EDX spectrum for Mn(7.5%)/γ-Al_2O_3 calcined catalysts.

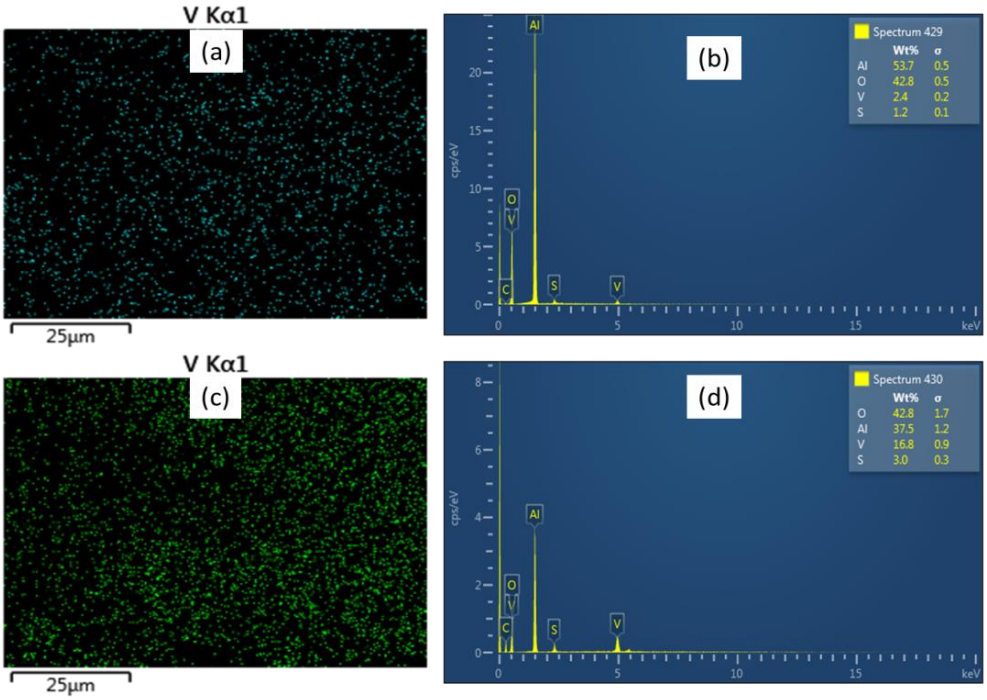

Figure A6. EDX results showing (a - b) point-mapping, EDX spectrum for V(2.5%)/γ-Al_2O_3 and (c - d) point-mapping, EDX spectrum for V(7.5%)/γ-Al_2O_3 calcined catalysts.

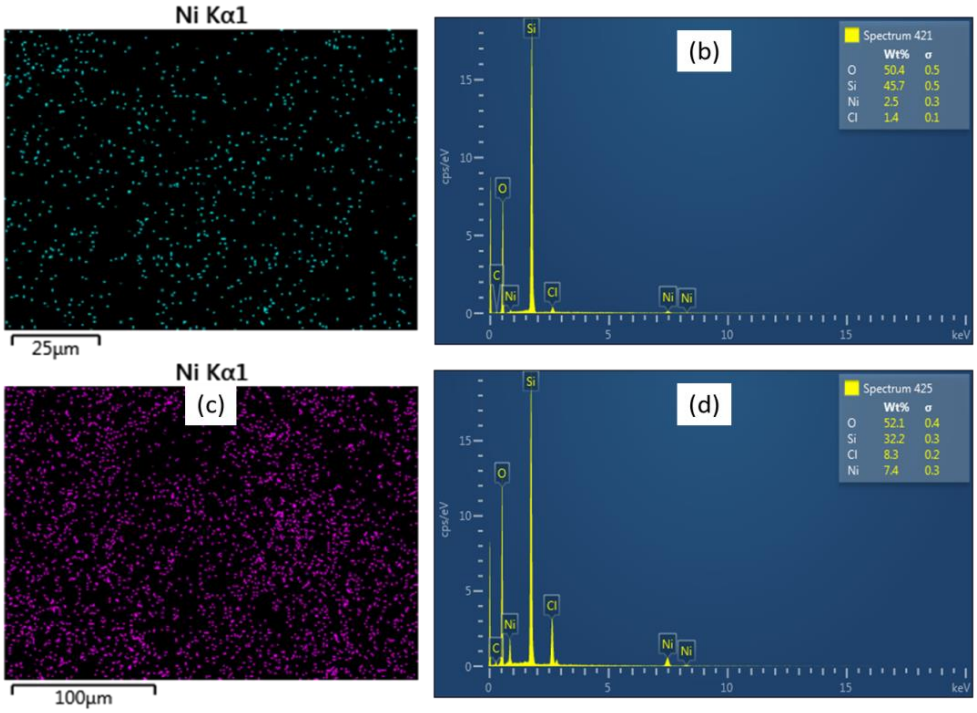

Figure A7. EDX results showing (a - b) point-mapping, EDX spectrum for Ni(2.5%)/SiO_2 and (c - d) point-mapping, EDX spectrum for Ni(7.5%)/SiO_2 calcined catalysts.

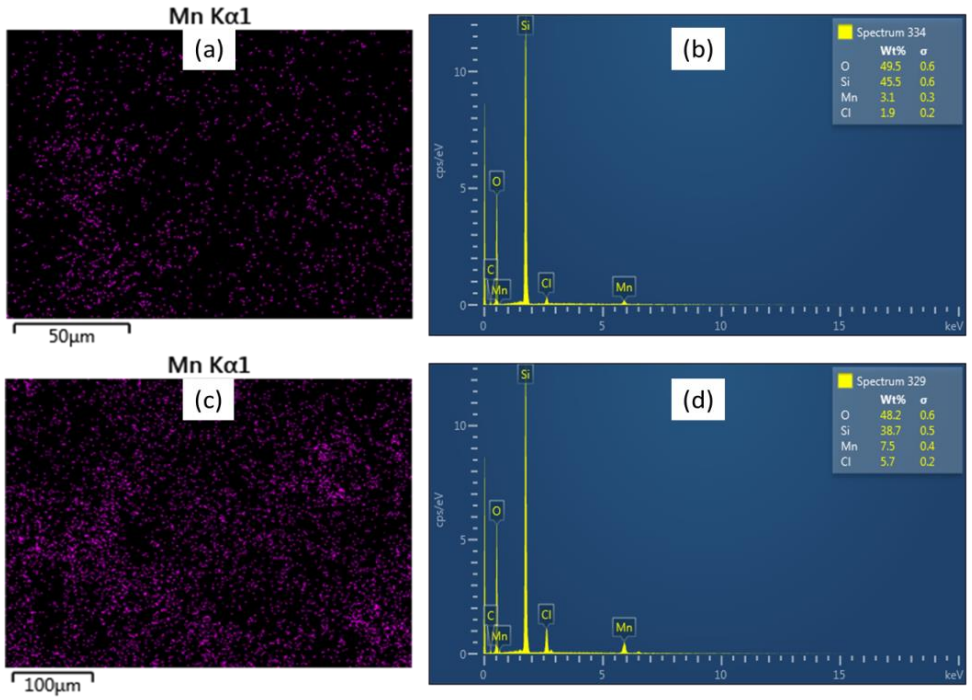

Figure A8. EDX results showing (a - b) point-mapping, EDX spectrum for Mn(2.5%)/SiO_2 and (c - d) point-mapping, EDX spectrum for Mn(7.5%)/SiO_2 calcined catalysts.

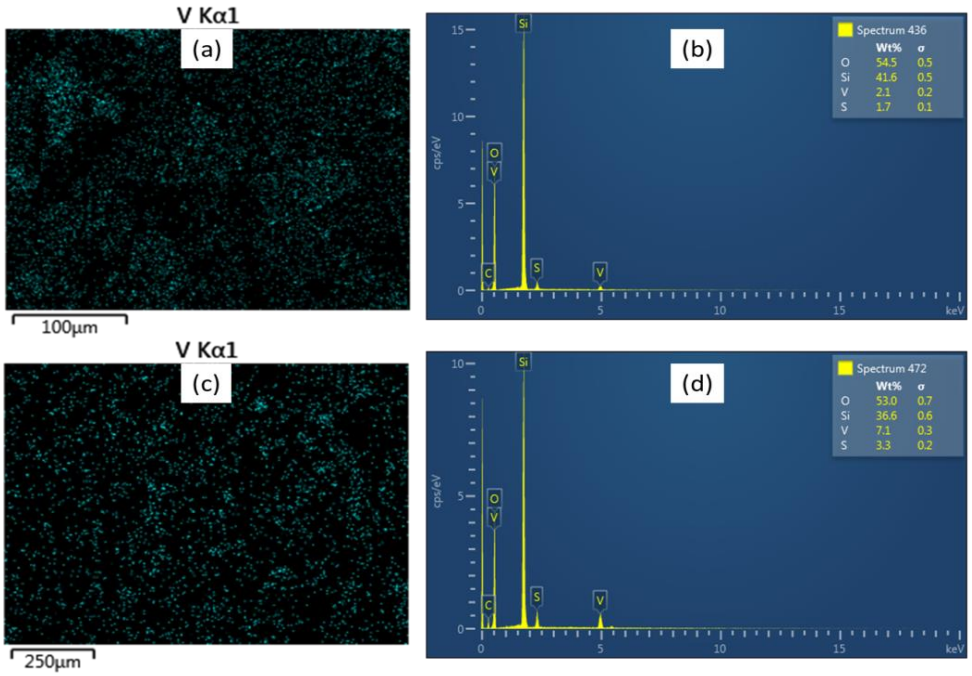

Figure A9. EDX results showing (a - b) point-mapping, EDX spectrum for V(2.5%)/SiO_2 and (c - d) point-mapping, EDX spectrum for V(7.5%)/SiO_2 calcined catalysts.

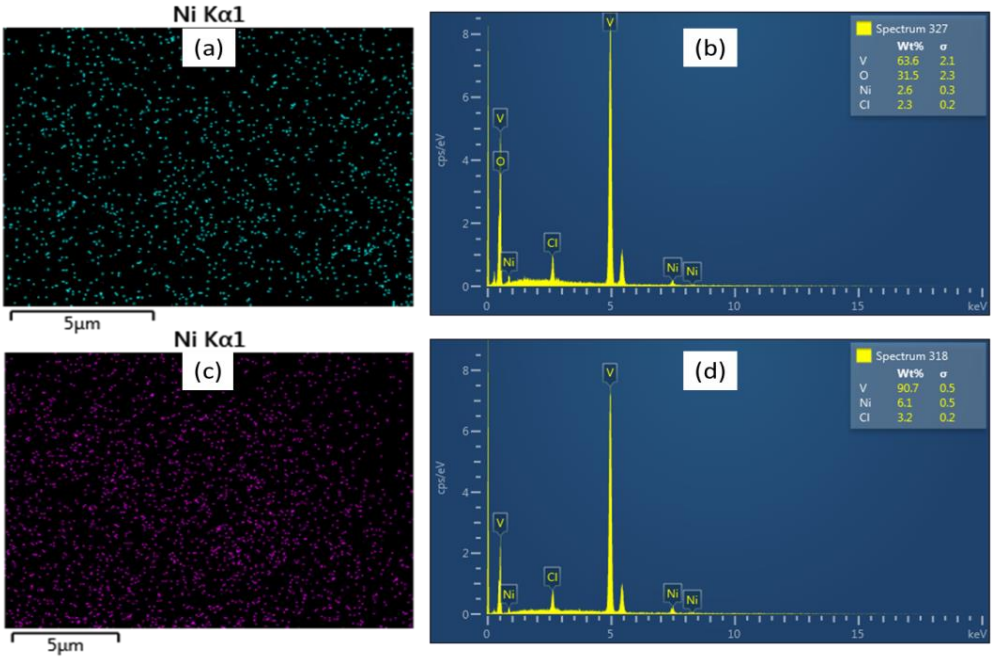

Figure A10. EDX results showing (a - b) point-mapping, EDX spectrum for Ni(2.5%)/V_2O_5 and (c - d) point-mapping, EDX spectrum for Ni(7.5%)/V_2O_5 calcined catalysts.

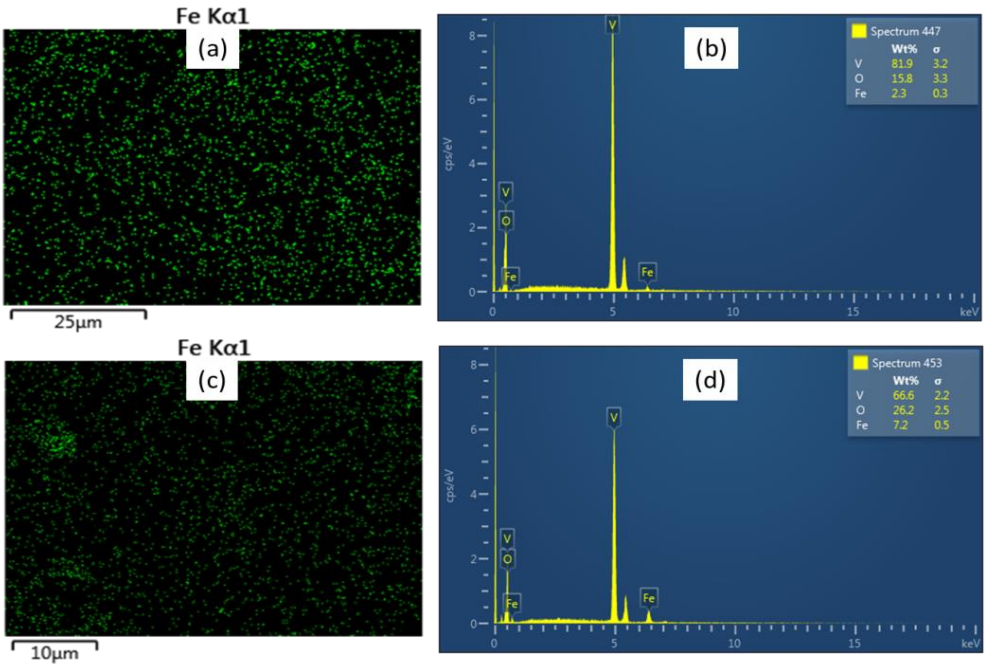

Figure A11. EDX results showing (a - b) point-mapping, EDX spectrum for Fe(2.5%)/V_2O_5 and (c - d) point-mapping, EDX spectrum for Fe(7.5%)/V_2O_5 calcined catalysts.

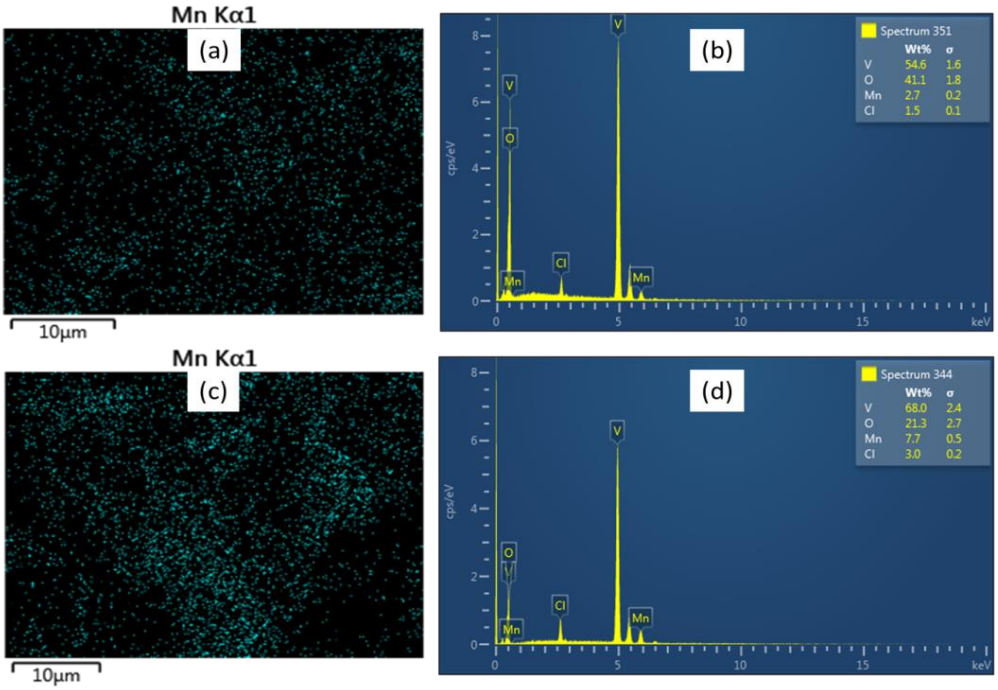

Figure A12. EDX results showing (a - b) point-mapping, EDX spectrum for Mn(2.5%)/V_2O_5 and (c - d) point-mapping, EDX spectrum for Mn(7.5%)/V_2O_5 calcined catalysts.

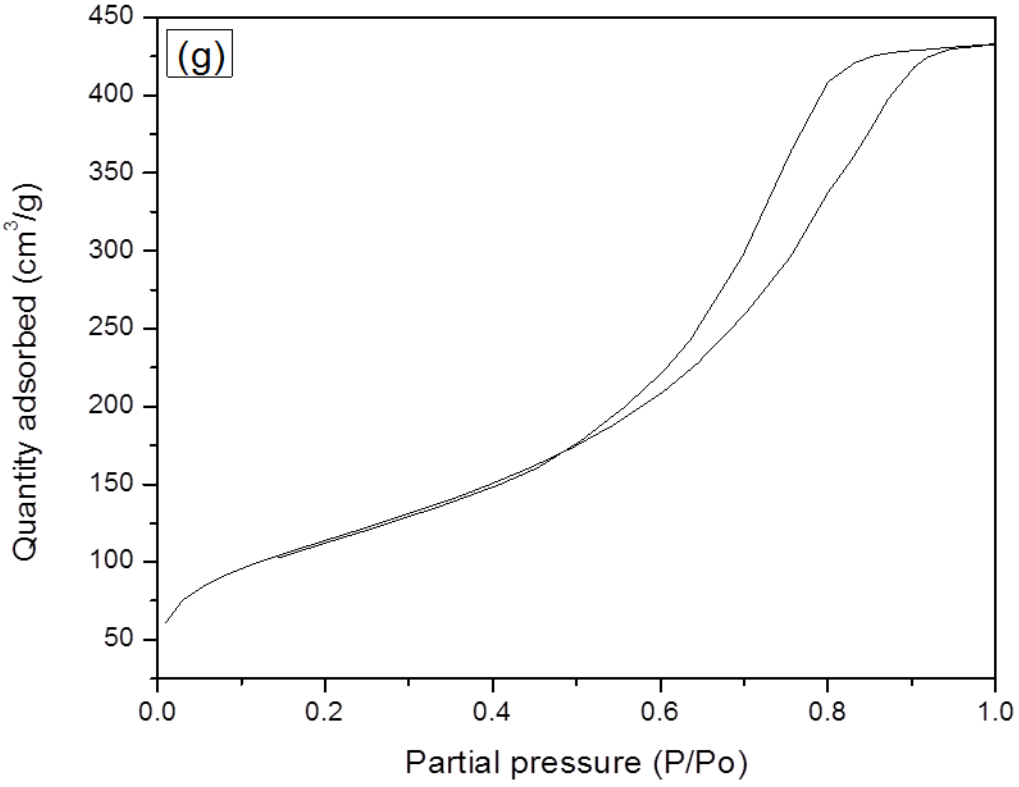

Figure A13. N_2 sorption isotherm of the Fe(7.5%)/SiO_2 calcined catalyst. (extension of Figure 3.20).

Appendix B

Table B1. Uncatalyzed *m*-cresol oxidation; percentage conversions and percentage selectivities towards various products.

Time (h)	*m*-cresol (uncat.) Conversion, %	Selectivity, %			
		***m*-TA**	**2,3-DT**	**DM**	**DO**
3	1.79	10.67	4.81	0	0
6	5.99	15.60	2.29	6.79	0
9	9.62	23.79	3.23	6.56	0
12	11.76	22.63	3.33	6.07	0
15	12.53	25.11	2.67	3.41	0
18	13.91	27.48	2.33	2.27	0.32
21	18.23	28.72	1.24	4.53	0.98
24	22.54	30.61	0.82	6.94	1.57

Table B2. Activated charcoal catalyzed *m*-cresol oxidation; percentage conversions and percentage selectivities towards various products.

Time (h)	*m*-cresol (ac. ch) Conversion, %	Selectivity, %			
		***m*-TA**	**2,3-DT**	**DM**	**DO**
3	1.66	6.87	16.87	5.24	6.32
6	3.81	9.19	4.54	5.77	3.18
9	7.37	16.30	2.21	5.96	15.09
12	9.05	21.07	5.39	7.96	19.16
15	15.07	20.48	1.63	7.07	17.58
18	26.37	12.75	6.41	2.14	21.64
21	35.23	11.88	6.08	1.14	19.36
24	43.42	9.90	4.55	0.79	21.32

Table B3. γ-Al_2O_3 catalyzed *m*-cresol oxidation; percentage conversions and percentage selectivities towards various products.

Time (h)	*m*-cresol, γ-Al_2O_3 Conversion, %	Selectivity, %			
		***m*-TA**	**2,3-DT**	**DM**	**DO**
3	3.48	2.82	2.44	1.72	0
6	6.76	4.26	4.10	1.18	0
9	12.35	5.12	0.62	1.51	0.14
12	16.56	7.53	0.66	1.63	12.54
15	22.76	7.73	1.23	1.38	12.20
18	27.06	8.38	0.86	1.22	13.72
21	41.95	5.87	0.87	0.66	9.16
24	47.11	6.22	0.85	0.50	10.90

Table B4. SiO_2 catalyzed *m*-cresol oxidation; percentage conversions and percentage selectivities towards various products.

Time (h)	*m*-cresol (SiO_2) Conversion, %	Selectivity, %			
		***m*-TA**	**2,3-DT**	**DM**	**DO**
3	0.51	8.63	7.25	0	0
6	5.25	6.32	3.03	0	0
9	10.32	5.27	2.42	0.87	16.41
12	17.84	5.20	2.30	1.32	15.25
15	25.26	5.21	2.26	2.00	12.36
18	33.98	4.80	2.01	1.60	15.86
21	43.33	5.16	2.47	1.72	14.68
24	51.87	5.52	2.49	1.97	14.55

Table B5. V_2O_5 catalyzed *m*-cresol oxidation; percentage conversions and percentage selectivities towards various products.

Time (h)	*m*-cresol (V_2O_5) Conversion, %	Selectivity, %			
		***m*-TA**	**2,3-DT**	**DM**	**DO**
3	4.50	1.33	1.96	1.42	3.42

6	10.75	1.63	3.34	0.70	7.91
9	18.53	6.07	4.20	1.44	8.10
12	25.87	6.50	4.61	2.36	9.24
15	33.03	5.84	4.86	2.40	9.84
18	37.72	5.23	4.27	2.14	10.24
21	39.77	5.22	4.08	2.05	10.01
24	40.86	5.30	4.97	2.00	8.15

Table B6. Uncatalyzed *o*-cresol oxidation; percentage conversions and percentage selectivities towards various products.

Time (h)	**o-cresol (uncat.) Conversion, %**	**Selectivity, %**			
		***o*-TA**	**2,5-DT**	**DM**	**DO**
3	2.23	16.44	0.63	13.72	7.80
6	9.83	14.00	0.74	16.36	10.43
9	17.04	13.89	0.98	14.15	12.39
12	24.25	11.98	1.00	15.13	13.53
15	27.72	10.22	1.52	9.84	15.07
18	29.27	6.19	2.03	11.69	15.45
21	32.92	8.57	1.65	12.18	14.30
24	34.29	7.62	1.34	13.03	13.11

Table B7. Activated charcoal catalyzed *o*-cresol oxidation; percentage conversions and percentage selectivities towards various products.

Time (h)	***o*-cresol (ac. ch.) Conversion, %**	**Selectivity, %**			
		***o*-TA**	**2,5-DT**	**DM**	**DO**
3	2.14	9.21	0.48	8.00	0
6	5.29	14.01	1.45	11.55	0.65
9	8.66	17.70	3.29	13.05	2.52
12	13.87	16.73	0.83	13.66	3.04
15	20.00	16.53	0.80	12.98	3.20
18	22.77	17.80	0.45	13.03	3.45
21	29.67	16.64	0.28	11.95	4.55
24	35.01	14.27	0.37	12.01	4.47

Table B8. γ-Al_2O_3 catalyzed *o*-cresol oxidation; percentage conversions and percentage selectivities towards various products.

Time (h)	*o*-cres., γ-Al_2O_3 Conversion, %	Selectivity, %			
		***o*-TA**	**2,5-DT**	**DM**	**DO**
3	2.64	6.89	1.06	6.40	0
6	5.39	9.70	0.39	9.15	0
9	10.16	5.14	0.36	4.73	0
12	15.30	10.92	0.32	11.46	2.93
15	22.50	10.57	0.64	11.01	3.27
18	25.07	11.32	0.85	9.86	4.20
21	28.22	13.97	0.92	10.66	4.54
24	31.24	13.42	1.02	13.20	6.24

Table B9. SiO_2 catalyzed *o*-cresol oxidation; percentage conversions and percentage selectivities towards various products.

Time (h)	*o*-cresol (SiO_2) Conversion, %	Selectivity, %			
		***o*-TA**	**2,5-DT**	**DM**	**DO**
3	2.42	32.15	0.03	0	0
6	9.32	6.38	4.17	9.23	0.96
9	16.21	2.32	0.97	12.63	3.87
12	25.72	2.83	2.27	13.38	5.28
15	32.69	2.09	2.32	12.71	6.42
18	36.51	2.22	2.00	13.36	8.21
21	42.72	1.94	1.01	13.30	9.27
24	43.17	1.78	1.62	11.29	8.33

Table B10. V_2O_5 catalyzed *o*-cresol oxidation; percentage conversions and percentage selectivities towards various products.

Time (h)	*o*-cresol (V_2O_5) Conversion, %	Selectivity, %			
		***o*-TA**	**2,5-DT**	**DM**	**DO**
3	4.46	0.72	2.56	2.89	5.52

6	9.54	1.67	0.33	4.26	3.94
9	13.53	1.80	0.77	8.48	5.40
12	20.33	1.62	1.85	7.91	5.33
15	26.81	1.54	2.33	7.41	5.25
18	30.37	1.98	2.11	8.02	6.64
21	31.32	2.37	1.87	7.94	7.20
24	31.66	1.73	2.08	7.81	7.72

Table B11. Uncatalyzed *p*-cresol oxidation; percentage conversions and percentage selectivities towards various products.

Time (h)	***p*-cresol (uncat.) Conversion, %**	**Selectivity, %**			
		***p*-TA**	**3,4-DT**	**DM**	**DO**
3	3.45	2.99	0.40	7.03	5.32
6	11.23	3.08	0.76	7.21	8.00
9	19.79	4.77	1.08	8.68	10.17
12	26.84	6.24	2.39	7.84	13.43
15	34.23	6.39	2.74	7.19	15.15
18	43.06	5.52	2.98	6.77	12.30
21	51.90	5.34	3.06	5.64	9.88
24	53.06	4.16	2.80	6.07	9.62

Table B12. Activated charcoal catalyzed *p*-cresol oxidation; percentage conversions and percentage selectivities towards various products.

Time (h)	***p*-cresol (ac. ch.) Conversion, %**	**Selectivity, %**			
		***p*-TA**	**3,4-DT**	**DM**	**DO**
3	5.39	3.73	0.63	0.74	2.00
6	11.80	6.95	1.30	27.84	1.99
9	18.82	9.10	1.35	23.53	1.55
12	29.19	8.67	1.58	18.57	1.61
15	38.12	9.18	1.44	15.28	3.41
18	44.41	9.22	1.20	13.88	3.39
21	54.03	7.65	0.84	12.62	3.26
24	55.26	7.95	0.83	11.39	4.29

Table B13. γ-Al_2O_3 catalyzed *p*-cresol oxidation; percentage conversions and percentage selectivities towards various products.

Time (h)	*p*-cres., γ-Al_2O_3 Conversion, %	Selectivity, %			
		***p*-TA**	**3,4-DT**	**DM**	**DO**
3	1.23	3.98	7.97	7.40	7.97
6	7.32	2.00	1.13	6.44	1.57
9	8.99	1.78	2.76	5.89	10.43
12	11.56	1.41	3.89	4.52	16.58
15	13.34	0.74	3.69	2.98	16.41
18	17.12	0.99	2.90	3.99	21.09
21	23.43	0.98	2.97	5.09	21.62
24	29.24	0.80	3.04	5.62	19.70

Table B14: SiO_2 catalyzed *p*-cresol oxidation; percentage conversions and percentage selectivities towards various products.

Time (h)	*p*-cresol (SiO_2) Conversion, %	Selectivity, %			
		***p*-TA**	**3,4-DT**	**DM**	**DO**
3	5.86	4.47	1.02	4.54	2.54
6	14.77	0.49	0.48	6.00	2.42
9	25.94	0.88	0.78	2.96	17.94
12	39.09	1.20	0.65	3.36	15.17
15	44.92	1.31	0.71	4.26	18.65
18	52.34	1.62	0.61	4.56	18.75
21	56.14	2.03	0.44	4.71	19.18
24	57.01	1.53	0.97	3.31	18.61

Table B15. V_2O_5 catalyzed *p*-cresol oxidation; percentage conversions and percentage selectivities towards various products.

Time (h)	*p*-cresol (V_2O_5) Conversion, %	Selectivity, %			
		***p*-TA**	**3,4-DT**	**DM**	**DO**
3	7.57	0	1.92	2.62	0

6	20.07	1.19	0.53	9.79	13.11
9	27.38	1.10	0.58	7.71	15.67
12	33.42	1.17	0.60	8.02	18.35
15	39.45	1.23	0.73	7.61	20.03
18	39.97	1.41	0.56	3.24	20.12
21	40.16	1.43	0.43	3.06	19.68
24	42.93	1.40	0.41	1.96	21.53

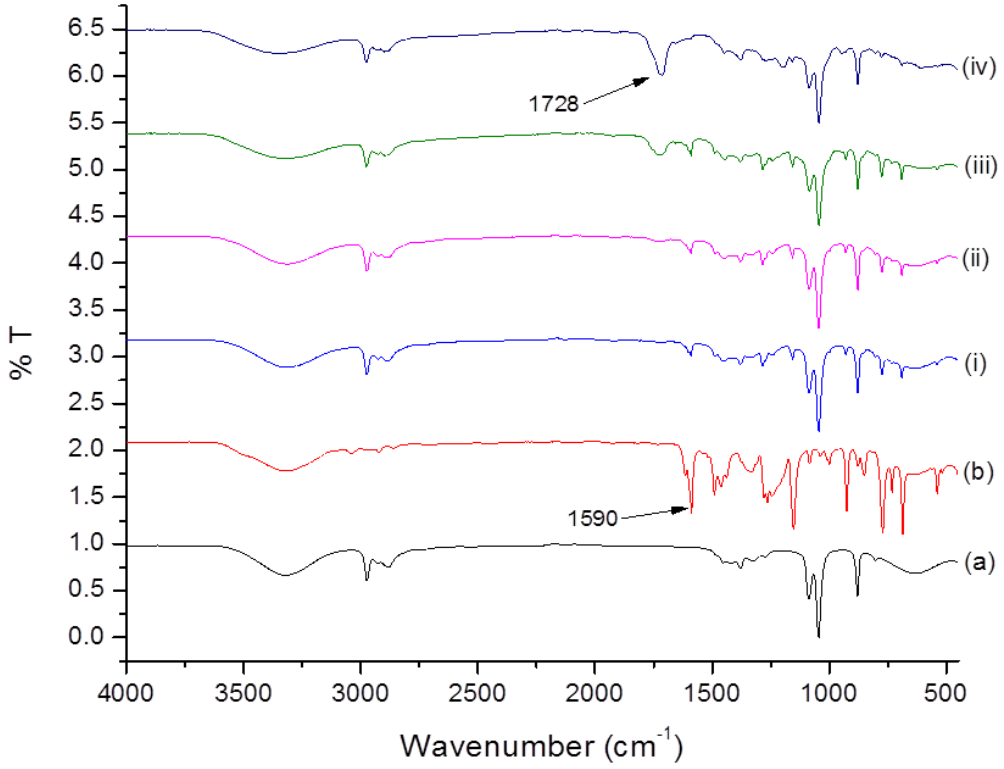

Figure B1. FT-IR spectra of (a) absolute ethanol, (b) *m*-cresol and 5 mL of *m*-cresol in excess ethanol, ozonated for (i) 5, (ii) 10, (iii) 30, (iv) 60 min. in a glass reactor.

Appendix C

Table C1. Substrate conversion and products selectivities from each oxidized cresol isomer in the presence of metal loaded catalysts.

M-CRESOL SUBSTRATE							
Catalyst	**Loaded metal (%)**	**Reaction time (h)**	**Conversion (%)**	**Selectivity (%)**			
				***m*-TA**	**DO**	**DM**	**2,3-DT**
$Mn/\gamma\text{-}Al_2O_3$	2.5	6	20.23	3.30	13.47	8.55	12.30
		12	47.07	2.40	11.91	3.89	13.68
		18	61.13	3.29	12.74	3.15	11.85
		24	70.27	-	11.00	2.70	9.60
$Mn/\gamma\text{-}Al_2O_3$	7.5	6	16.92	2.30	15.02	4.54	14.68
		12	39.52	3.33	9.05	3.43	14.97
		18	58.01	3.53	12.76	8.13	10.95
		24	64.17	2.52	11.03	1.41	12.73
$Fe/\gamma\text{-}Al_2O_3$	2.5	6	23.29	5.80	10.30	2.98	8.51
		12	44.26	5.23	12.74	3.32	6.12
		18	57.94	4.73	13.38	5.41	6.03
		24	66.28	3.98	11.12	4.01	4.65
$Fe/\gamma\text{-}Al_2O_3$	7.5	6	21.94	3.81	9.56	4.49	11.14
		12	44.83	-	15.54	3.24	9.86
		18	59.08	5.39	16.07	3.12	8.68
		24	66.91	4.11	14.09	2.90	7.32
$Ni/\gamma\text{-}Al_2O_3$	2.5	6	14.49	3.61	22.64	11.57	11.59
		12	46.86	3.95	9.13	2.83	8.10
		18	64.77	2.75	18.52	9.66	7.77
		24	71.69	0.13	17.89	8.74	7.09
$Ni/\gamma\text{-}Al_2O_3$	7.5	6	26.31	4.63	9.62	4.52	12.12
		12	46.79	4.69	4.11	3.94	7.97
		18	61.24	3.53	1.64	4.10	7.81
		24	68.91	1.47	0	3.18	7.23
$V/\gamma\text{-}Al_2O_3$	2.5	6	24.36	6.13	9.29	2.27	9.49
		12	45.50	4.86	9.50	3.42	8.52
		18	53.47	2.37	9.69	4.46	7.19
		24	64.71	2.19	7.74	4.78	6.66

$V/\gamma\text{-}Al_2O_3$	7.5	6	24.20	4.13	9.72	6.56	6.83
		12	45.13	3.68	7.63	7.11	5.04
		18	50.42	2.46	6.57	7.85	4.90
		24	57.82	1.10	6.22	6.81	4.00
Mn/SiO_2	2.5	6	21.09	3.52	6.26	4.04	9.24
		12	46.23	4.37	11.65	3.67	9.17
		18	66.72	3.70	12.33	3.15	8.23
		24	76.20	2.84	10.45	2.64	7.32
Mn/SiO_2	7.5	6	20.37	2.99	11.00	3.03	8.78
		12	48.28	4.08	10.80	3.76	10.47
		18	68.18	3.95	10.17	4.52	9.36
		24	76.67	2.47	8.36	2.89	8.93
Fe/SiO_2	2.5	6	32.33	3.05	3.34	3.33	6.38
		12	53.57	4.50	9.67	4.40	9.56
		18	72.30	5.44	8.57	3.12	10.00
		24	81.29	4.28	7.01	2.64	8.81
Fe/SiO_2	7.5	6	24.60	4.23	5.13	5.14	8.89
		12	45.95	3.09	12.60	4.30	9.18
		18	64.49	3.63	10.86	3.92	9.95
		24	74.38	-	9.88	3.60	8.02
Ni/SiO_2	2.5	6	24.18	4.40	4.78	4.03	5.82
		12	47.25	3.96	12.66	2.87	7.76
		18	70.83	3.77	12.28	3.08	7.11
		24	84.72	3.23	10.60	2.44	6.36
Ni/SiO_2	7.5	6	27.46	2.48	5.03	3.47	4.49
		12	47.22	2.71	4.01	5.52	2.52
		18	68.26	3.24	3.75	6.20	2.13
		24	79.68	2.69	2.94	4.72	1.09
V/SiO_2	2.5	6	25.22	-	3.75	3.70	6.77
		12	43.76	0.57	8.02	2.79	3.99
		18	63.01	1.56	9.66	2.41	5.50
		24	75.96	0.84	7.38	1.97	4.82
V/SiO_2	7.5	6	28.94	-	5.92	3.36	1.73
		12	43.02	2.85	7.34	-	0.79
		18	61.07	3.33	8.20	2.68	-
		24	71.77	2.18	7.86	1.90	-
Mn/V_2O_5	2.5	6	17.71	-	11.96	6.26	2.67

		12	47.29	2.75	5.65	4.86	4.20
		18	62.81	4.04	10.41	3.30	5.11
		24	71.00	3.68	9.87	0.87	4.51
Mn/V_2O_5	7.5	6	26.05	-	8.60	4.76	2.94
		12	43.00	2.57	7.28	3.97	1.78
		18	58.11	2.96	6.70	2.55	0.66
		24	66.80	2.12	6.23	-	-
Fe/V_2O_5	2.5	6	20.60	3.96	6.92	5.43	2.73
		12	40.09	4.22	7.01	4.80	2.08
		18	51.70	4.87	6.30	4.21	0.85
		24	57.54	3.05	5.77	3.48	-
Fe/V_2O_5	7.5	6	19.19	3.43	5.14	3.64	1.99
		12	36.20	4.12	6.36	4.39	1.65
		18	47.88	3.60	5.82	3.72	0.44
		24	54.44	2.84	4.91	2.52	-
Ni/V_2O_5	2.5	6	26.24	6.19	4.96	2.55	1.41
		12	45.61	8.38	4.44	1.89	0.93
		18	53.04	7.00	3.62	1.30	0.52
		24	63.06	6.64	2.07	0.86	-
Ni/V_2O_5	7.5	6	24.85	10.15	4.81	2.16	2.08
		12	44.00	8.11	5.47	2.64	1.73
		18	50.82	6.95	3.10	1.80	0.86
		24	60.48	6.29	2.68	1.21	0.30

P-CRESOL SUBSTRATE

Catalyst	Loaded metal (%)	Reaction time (h)	Conversion (%)	Selectivity (%)			
				DO	DM	*p*-TA	3,4-DT
$Mn/\gamma\text{-}Al_2O_3$	2.5	6	28.42	0.68	1.98	3.44	7.01
		12	50.66	11.68	3.08	2.20	5.05
		18	71.59	13.21	4.34	2.02	6.53
		24	81.04	10.09	2.75	0.89	4.77
$Mn/\gamma\text{-}Al_2O_3$	7.5	6	28.79	0.87	2.45	1.72	7.38
		12	49.24	4.62	1.73	1.98	5.59
		18	62.75	7.40	-	2.66	6.95

		24	73.37	5.23	-	1.82	4.76
Fe/γ-Al_2O_3	2.5	6	31.44	5.98	13.92	4.24	10.60
		12	49.56	7.33	15.01	5.85	9.77
		18	66.26	8.81	18.73	6.11	7.83
		24	76.22	8.22	16.12	5.36	7.62
Fe/γ-Al_2O_3	7.5	6	26.04	6.64	12.88	4.57	13.14
		12	48.60	9.63	15.29	6.30	12.16
		18	65.63	10.80	19.07	8.15	9.87
		24	78.06	8.17	18.79	7.00	-
Ni/γ-Al_2O_3	2.5	6	33.33	5.11	19.58	8.46	7.89
		12	55.74	7.20	12.16	7.91	8.42
		18	67.08	6.55	15.80	5.10	6.63
		24	80.66	6.13	16.18	4.38	5.26
Ni/γ-Al_2O_3	7.5	6	44.32	4.93	14.75	6.66	8.07
		12	61.23	5.38	10.31	4.52	5.17
		18	66.52	4.67	8.11	4.58	4.45
		24	78.56	2.49	7.62	3.71	2.78
V/γ-Al_2O_3	2.5	6	27.52	8.54	12.99	3.61	11.19
		12	49.88	7.86	11.67	5.82	9.55
		18	69.07	-	11.53	8.60	9.29
		24	77.94	-	10.48	8.47	5.00
V/γ-Al_2O_3	7.5	6	27.29	6.11	10.16	6.30	8.63
		12	48.68	5.70	7.33	8.04	6.04
		18	61.77	3.15	7.02	10.94	5.82
		24	72.35	-	5.40	9.83	3.27
Mn/SiO_2	2.5	6	23.96	3.94	3.12	2.89	9.37
		12	43.73	1.28	3.27	1.22	5.25
		18	60.98	0.88	4.50	0.67	4.82
		24	77.63	-	2.89	-	4.12
Mn/SiO_2	7.5	6	28.68	2.03	2.88	1.04	8.92
		12	45.98	9.98	3.09	1.82	5.48
		18	62.76	11.14	2.65	2.11	5.00
		24	78.71	10.20	2.15	1.37	4.54
Fe/SiO_2	2.5	6	31.25	1.64	3.89	3.15	7.77
		12	49.35	14.19	3.00	1.76	4.23
		18	69.38	14.87	3.46	1.20	5.37
		24	86.89	10.18	2.28	0.69	3.28

Fe/SiO_2	7.5	6	28.69	2.39	1.34	2.22	4.72
		12	49.93	14.63	2.99	1.36	4.29
		18	68.00	15.23	5.11	-	3.34
		24	78.44	11.49	3.45	-	2.96
Ni/SiO_2	2.5	6	33.24	7.90	6.33	4.26	3.18
		12	49.66	15.16	8.19	3.43	3.95
		18	70.90	16.38	7.82	3.00	2.63
		24	85.49	13.93	5.99	1.94	1.87
Ni/SiO_2	7.5	6	34.10	9.78	4.60	4.97	5.69
		12	46.53	13.04	5.96	4.50	6.06
		18	64.08	14.85	4.17	3.24	5.74
		24	80.42	12.09	3.52	2.10	4.25
V/SiO_2	2.5	6	40.97	9.53	4.06	3.27	5.05
		12	46.51	12.66	3.87	-	-
		18	65.19	13.93	2.91	2.46	4.02
		24	76.42	11.78	2.42	1.59	3.14
V/SiO_2	7.5	6	40.29	5.44	5.24	-	-
		12	47.94	11.32	4.94	-	-
		18	63.83	12.29	4.27	3.70	3.22
		24	73.21	10.86	3.64	2.83	2.65
Mn/V_2O_5	2.5	6	36.34	13.94	6.40	4.16	0.85
		12	50.30	14.97	1.95	2.76	2.13
		18	66.43	16.42	5.17	3.77	4.09
		24	73.68	11.11	3.23	2.36	2.65
Mn/V_2O_5	7.5	6	35.45	13.66	6.83	1.45	0.82
		12	52.55	11.79	2.49	1.94	1.23
		18	69.04	10.22	5.76	2.03	3.57
		24	78.86	7.32	4.10	1.54	2.55
Fe/V_2O_5	2.5	6	33.28	9.88	5.52	2.94	1.03
		12	42.16	16.48	2.19	2.13	0.77
		18	53.98	17.21	4.65	1.78	0
		24	59.35	13.33	3.92	-	-
Fe/V_2O_5	7.5	6	31.51	10.16	3.04	3.26	0.87
		12	46.34	14.67	5.66	-	0
		18	55.54	16.01	4.89	2.44	0
		24	64.42	11.99	2.57	1.52	0.98
Ni/V_2O_5	2.5	6	32.74	14.90	3.17	1.42	0.41

		12	54.56	14.83	3.99	1.30	-
		18	62.75	13.94	5.25	0.98	-
		24	74.34	11.61	5.03	-	-
Ni/V_2O_5	7.5	6	31.50	18.85	3.51	1.36	-
		12	50.67	13.06	5.35	2.21	2.39
		18	58.70	11.07	7.18	1.53	3.11
		24	68.34	8.69	4.40	1.06	1.73

O-CRESOL SUBSTRATE

Catalyst	Loaded metal (%)	Reaction time (h)	Conversion (%)	Selectivity (%)			
				DO	DM	*o*-TA	2,5-DT
$Mn/\gamma\text{-}Al_2O_3$	2.5	6	25.78	3.56	8.74	7.91	3.86
		12	38.46	4.35	8.99	13.69	5.63
		18	52.27	6.30	7.13	14.04	5.37
		24	63.74	5.67	6.91	10.86	4.66
$Mn/\gamma\text{-}Al_2O_3$	7.5	6	21.42	3.70	10.25	6.44	5.39
		12	35.97	5.83	12.76	9.69	6.78
		18	50.53	7.93	12.08	10.34	7.02
		24	56.00	6.11	9.00	-	6.22
$Fe/\gamma\text{-}Al_2O_3$	2.5	6	27.76	3.34	9.80	4.74	5.00
		12	37.88	4.11	9.98	5.12	5.72
		18	48.09	2.86	11.66	3.22	6.15
		24	57.48	1.90	10.31	1.06	3.08
$Fe/\gamma\text{-}Al_2O_3$	7.5	6	18.13	2.46	6.09	1.28	8.24
		12	35.67	4.11	7.21	4.92	6.79
		18	49.70	-	7.35	5.33	7.24
		24	59.55	6.79	6.60	2.43	7.08
$Ni/\gamma\text{-}Al_2O$	2.5	6	22.13	2.35	12.34	4.20	8.39
		12	38.27	2.98	13.87	4.78	10.55
		18	53.95	4.02	16.45	5.67	7.66
		24	66.12	5.54	14.33	6.04	4.32
$Ni/\gamma\text{-}Al_2O$	7.5	6	33.97	4.28	10.22	1.01	7.40
		12	40.39	3.11	11.65	3.94	9.33

		18	50.42	3.63	9.43	2.40	8.72
		24	62.41	2.71	9.00	2.88	6.89
V/γ-Al_2O_3	2.5	6	23.01	2.73	7.04	-	5.37
		12	43.46	4.18	8.77	-	6.22
		18	51.29	4.94	6.92	3.22	6.96
		24	59.64	3.30	6.55	5.72	7.05
V/γ-Al_2O_3	7.5	6	22.91	-	11.04	2.01	2.18
		12	43.19	-	9.58	3.75	5.46
		18	48.09	0.83	9.16	5.90	4.44
		24	53.53	2.32	7.54	6.31	4.20
Mn/SiO_2	2.5	6	18.79	2.25	10.50	6.84	3.69
		12	35.96	2.76	11.32	11.92	4.22
		18	55.19	3.80	13.77	11.31	6.68
		24	70.29	3.27	10.65	9.99	7.02
Mn/SiO_2	7.5	6	15.47	2.04	9.37	4.57	2.48
		12	35.82	1.62	9.58	7.61	3.16
		18	53.26	-	7.12	6.52	6.00
		24	66.01	-	6.06	6.33	6.51
Fe/SiO_2	2.5	6	27.69	5.58	5.19	6.20	9.17
		12	49.24	7.76	11.82	7.44	10.39
		18	69.27	6.32	8.35	5.56	12.74
		24	76.33	4.60	7.78	4.88	9.50
Fe/SiO_2	7.5	6	20.45	6.87	6.11	5.67	7.87
		12	44.03	5.66	15.54	8.48	10.00
		18	62.14	5.14	13.06	7.32	10.83
		24	70.22	4.04	10.32	5.05	9.21
Ni/SiO_2	2.5	6	19.70	2.73	10.32	7.24	9.47
		12	36.81	4.76	9.45	6.30	7.96
		18	57.99	4.23	9.94	6.97	7,78
		24	73.02	3.70	7.41	-	6.52
Ni/SiO_2	7.5	6	23.46	5.03	12.58	2.12	4.33
		12	35.48	7.64	14.66	5.31	3.57
		18	56.12	9.22	14.19	6.04	3.28
		24	68.44	9.57	15.32	4.87	3.98
V/SiO_2	2.5	6	21.32	1.88	2.46	4.93	4.53
		12	39.24	2.64	7.11	4.42	5.22
		18	57.41	3.19	9.20	3.31	5.01

		24	70.94	3.02	8.83	2.17	3.56
V/SiO_2	7.5	6	24.82	2.76	3.92	-	2.71
		12	40.11	3.31	6.95	-	3.34
		18	55.47	4.40	7.66	3.80	2.86
		24	67.30	3.28	7.03	3.19	-
Mn/V_2O_5	2.5	6	19.80	-	9.28	10.03	4.56
		12	37.72	2.87	10.27	9.26	4.04
		18	55.83	4.03	12.81	8.47	3.59
		24	66.78	3.64	11.11	8.70	2.41
Mn/V_2O_5	7.5	6	24.77	3.76	9.32	6.22	5.59
		12	37.34	5.40	12.19	7.51	5.18
		18	51.80	6.32	13.80	7.84	3.98
		24	60.33	5.87	15.12	7.03	3.00
Fe/V_2O_5	2.5	6	26.17	4.25	8.47	12.51	6.32
		12	31.26	6.66	9.53	14.08	5.24
		18	41.05	7.38	8.29	15.40	4.17
		24	45.67	9.60	7.55	18.91	4.05
Fe/V_2O_5	7.5	6	26.83	7.15	9.10	7.62	3.46
		12	28.99	9.38	10.36	7.54	3.21
		18	38.50	10.45	8.82	8.70	2.17
		24	45.53	13.77	8.43	9.18	-
Ni/V_2O_5	2.5	6	23.96	5.32	7.94	4.22	6.58
		12	40.54	5.74	8.40	3.78	4.69
		18	45.12	6.82	6.73	5.67	3.19
		24	56.11	7.11	6.15	7.01	3.08
Ni/V_2O_5	7.5	6	24.32	2.10	8.23	-	4.04
		12	38.76	4.87	9.65	-	5.75
		18	43.59	5.05	7.07	3.45	5.30
		24	54.29	6.71	6.43	5.94	3.21